

The Pennsylvania State University

The Graduate School

Department of Mechanical and Nuclear Engineering

**MULTI SCALE MODELING OF IGNITION AND COMBUSTION  
OF MICRO AND NANO ALUMINUM PARTICLES**

A Dissertation in

Mechanical Engineering

by

Puneesh Puri

© 2008 Puneesh Puri

Submitted in Partial Fulfillment  
of the Requirements  
for the Degree of

Doctor of Philosophy

December 2008

The dissertation of Puneesh Puri was reviewed and approved\* by the following:

Vigor Yang  
Professor of Mechanical Engineering  
Dissertation Advisor  
Chair of Committee

Richard Yetter  
Professor of Mechanical Engineering

Daniel Haworth  
Professor of Mechanical Engineering

Robert Kunz  
Associate Professor of Aerospace Engineering

Steve Son  
Special Member  
Associate Professor of Mechanical Engineering at Purdue University

Karen A. Thole  
Head of the Department of Mechanical and Nuclear Engineering

\*Signatures are on file in the Graduate School

## ABSTRACT

With renewed interest in nano scale energetic materials like aluminum, many fundamental issues concerning the ignition and combustion characteristics at nano scales, remain to be clarified. The overall aim of the current study is the establishment of a unified theory accommodating the various processes and mechanisms involved in the combustion and ignition of aluminum particles at micro and nano scales. A comprehensive review on the ignition and combustion of aluminum particles at multi scales was first performed identifying various processes and mechanisms involved. Research focus was also placed on the establishment of a Molecular Dynamics (MD) simulation tool to investigate the characteristics of nano-particulate aluminum through three major studies. The general computational framework involved parallelized pre-processing, post-processing and main code with capability to simulate different ensembles using appropriate algorithms. Size dependence of melting temperature of pure aluminum particles was investigated in the first study. Phenomena like dynamic co-existence of solid and liquid phase and effect of surface charges on melting were explored. The second study involved the study of effect of defects in the form of voids on melting of bulk and particulate phase aluminum. The third MD study was used to analyze the thermo-mechanical behavior of nano-sized aluminum particles with total diameter of 5-10 nm and oxide thickness of 1-2.5 nm. The ensuing solid-solid and solid-liquid phase changes in the core and shell, stresses developed within the shell, and the diffusion of aluminum cations in the oxide layer, were explored in depth for amorphous and crystalline oxide layers. In the limiting case, the condition for pyrophoricity/explosivity

of nano-particulate aluminum was analyzed and modified. The size dependence of thermodynamic properties at nano scales were considered and incorporated into the existing theories developed for micro and larger scales. Finally, a phenomenological theory for ignition and combustion of aluminum particles was proposed. The whole time history from ignition till particle burnout was divided into five stages. An attempt was made to explore different modes of ignition based on the effect of pressure, temperature, oxidizer, oxide thickness and particle diameter and was investigated using length and time scales involved during ignition and combustion.



## TABLE OF CONTENTS

LIST OF FIGURES .....	viii
LIST OF TABLES .....	xiv
NOMENCLATURE .....	xvi
ACKNOWLEDGEMENTS .....	xxii
<b>Chapter 1</b> Introduction .....	1
1.1 Background and Motivation .....	1
1.2 Issues Concerning Metal Particle Combustion .....	4
1.2.1 Heterogeneous vs. Homogeneous Combustion .....	5
1.2.2 Limiting Flame Temperature .....	8
1.2.3 Diffusion vs. Kinetically Controlled Mechanism .....	10
1.2.4 Mode of Ignition .....	13
1.3 Objectives .....	14
<b>Chapter 2</b> Micro Scale Aluminum Combustion .....	17
2.1 Aluminum .....	17
2.2 Experiments at Micro Scales .....	19
2.2.1 Particle Generation .....	20
2.2.2 Characteristics at Micro Scales .....	20
2.2.3 Three Stages of Micron-sized Particle Combustion .....	22
2.2.4 Asymmetric Burning .....	24
2.2.5 Diffusion of Ions within the Oxide Layer .....	25
2.2.6 Phase Transformations .....	27
2.2.7 Experimental Data .....	32
2.3 Thermodynamics and Transport Properties .....	39
2.4 Burning Rate .....	40
2.5 Theoretical Modeling at Micro Scales .....	41
2.6 Chemical Kinetics .....	46
2.7 Summary and Conclusions .....	49
<b>Chapter 3</b> Nano Scale Aluminum Combustion .....	51
3.1 Unique features at Nano Scales .....	51
3.2 Oxide Thickness .....	52
3.3 Literature Survey .....	53
3.4 Existing Simplified Models .....	59
3.5 Comparison with Micro Scale Combustion .....	67

3.5.1 Heterogeneous vs. Homogeneous Mechanism.....	67
3.5.2 Diffusion vs. Kinetically Controlled Mechanism.....	68
3.5.3 Mode of Ignition.....	70
3.5.3.1 Cracking vs. Melting of Oxide Layer.....	71
3.5.3.2 Thermodynamic Explanation .....	72
3.6 Summary and Conclusions .....	73
<b>Chapter 4 Nano Scale Simulations .....</b>	<b>75</b>
4.1 Molecular Dynamics Simulation Framework.....	75
4.2 Potential Functions .....	78
4.3 Equations of Motion .....	89
4.4 Boundary Conditions .....	94
4.5 Statistical Ensembles .....	99
4.6 Structural and Thermodynamic Properties .....	104
4.7 Parallel Numerical Framework.....	106
4.8 Code Validation.....	110
<b>Chapter 5 Thermo-Mechanical Behavior of Pure Aluminum at Nano Scales.....</b>	<b>119</b>
5.1 Background.....	119
5.2 Objectives .....	121
5.3 Results and Discussion .....	123
5.4 Conclusions.....	131
<b>Chapter 6 Effect of Voids and Pressure on Melting of Nano-Particulate and Bulk Aluminum.....</b>	<b>133</b>
6.1 Background.....	133
6.2 Objectives .....	136
6.3 Results and Discussion .....	137
6.4 Conclusions.....	152
<b>Chapter 7 Thermo-Mechanical Behavior of Nano Aluminum Particles with Oxide Layers .....</b>	<b>154</b>
7.1 Background.....	154
7.2 Objectives .....	156
7.3 Results and Discussion .....	157
7.4 Conclusions.....	172
<b>Chapter 8 Pyrophoricity of Aluminum at Nano Scales .....</b>	<b>174</b>
8.1 Background.....	174
8.2 Size Dependence of Properties at Nano Scales .....	177

8.2.1 Thermodynamic Properties .....	177
8.2.2 Ignition Characteristics.....	181
8.3 Pyrophoricity of Nascent Aluminum Particles .....	181
8.4 Pyrophoricity of Oxide-Coated Aluminum Particles .....	185
8.4.1 Particles with Thin Oxide Shell.....	185
8.4.2 Particles with Thicker Oxide Shell.....	188
8.5 Glassman's Criterion for Pyrophoricity.....	190
8.6 Conclusions.....	192
<b>Chapter 9 Unified Theory of Aluminum Particle Combustion.....</b>	<b>193</b>
9.1 Ignition and Combustion at Multi Scales .....	193
9.2 Stages of aluminum oxidation .....	198
9.2.1 Stage I.....	202
9.2.2 Stage II.....	207
9.2.3 Stage III .....	210
9.2.4 Stage IV .....	211
9.2.5 Stage V .....	215
9.3 Modes of ignition.....	216
9.4 Ignition Formulation using Phase Transformations .....	222
9.5 Conclusions.....	224
<b>Chapter 10 Summary and Future Work .....</b>	<b>226</b>
10.1 Summary.....	226
10.2 Recommendations for Future Work .....	230
10.2.1 Ignition Behavior of Metal-Coated Aluminum Particles .....	230
10.2.2 Oxidation of Aluminum in Flow Environments.....	232
10.2.3 Flame Speed Calculations in Particle Laden Flows .....	233
<b>Bibliography .....</b>	<b>233</b>

## LIST OF FIGURES

Figure 1.1: CEC Calculation for crossover pressures .....	6
Figure 2.1: Different techniques adopted to calculate ignition point of aluminum (Trunov et al., 2005b) .....	33
Figure 2.2: Sequence of true color image showing evolution of aluminum particle flame structure upon transition from spherically symmetric to non-symmetric combustion regime (Dreizin, 1999b) .....	38
Figure 2.3: Modeling in Combustion Science .....	42
Figure 3.1: SEM micrograph of Alex Aluminum particles (Risha, 2005) .....	52
Figure 3.2: (a) TEM (light field) and SAED of aluminum nanoparticles within Al/PPK nano-composite (b) Al particle size distribution (Pivkina et al., 2004) ..	56
Figure 3.3: Burning rate vs. pressure for propellant with different Al size (Meda et al., 2005) .....	57
Figure 3.4: Effect of aluminum content on detonation velocity for TNT/Al mixes at a charge diameter of 25.4 mm (Brousseau and Anderson, 2002) .....	57
Figure 3.5: Chains of clusters in the cloud of low gravity combustion (60 atm, O <sub>2</sub> +Ar) (Assovskiy, 2002) .....	58
Figure 3.6: XRD patterns for partially oxidized aluminum powder samples (Trunov et al., 2005) .....	59
Figure 3.7: Comparison of kinetic data for aluminum nanoparticles obtained from SPMS and TGS methods; $k$ is diffusion limited rate constant (Park et al., 2005) .....	60
Figure 3.8: Experimental and calculated dependences of ignition delay on particle diameter (Fedorov and Kharlamova, 2003) .....	61
Figure 3.9: (a) Snapshot of structure of pure aluminum nanoparticle at 500 K (b) Radial distribution function for nanoparticle (c) Charge distribution for aluminum particle from Streitz-Mintmire potential (Alavi et al., 2005) .....	62
Figure 3.10: A 20 nm aluminum particle with 4 nm oxide thickness .....	63
Figure 3.11: SEM images of Al-1 and Alex (Eisenreich et al., 2004) .....	64

Figure 3.12: Experimentally observed aluminum particle burning time as a function of particle diameter (Huang et al., 2006).....	70
Figure 3.13: Ignition temperature of aluminum particle as function of particle diameter .....	71
Figure 4.1: Lennard-Jones potential for aluminum.....	82
Figure 4.2: Glue potential for aluminum .....	83
Figure 4.3: Sutton-Chen potential for aluminum.....	85
Figure 4.4: Streitz-Mintmire potential for aluminum .....	88
Figure 4.5: Flow chart of a typical MD simulation .....	90
Figure 4.6: Various lattice types for crystalline structures .....	94
Figure 4.7: FCC Lattice for aluminum .....	96
Figure 4.8: Supercell for alumina .....	97
Figure 4.9: Schematic diagram showing periodic boundary condition for Cartesian coordinates .....	98
Figure 4.10: Expand and fold operations showing communications among 8 processors in three steps (Plimpton, 1995).....	107
Figure 4.11: Speed-up and efficiency vs. number of processors for the MD code.....	108
Figure 4.12: Parallel computing facility at Penn State .....	109
Figure 4.13: Comparison with results of Solca et al. for Validation .....	112
Figure 4.14: Variation in Potential energy during melting for an Argon crystal at 44.56 kbar .....	113
Figure 4.15: Validation for NPT ensembles using argon at 0.25 kbar, time step of 8.6 fs .....	113
Figure 4.16: Simulation of a liquid droplet of argon at 100 K (a) argon droplet in its saturated vapor at 100 K; (b) density contour at 100 K.....	114
Figure 4.17: Radial distribution functions for liquid argon using NVE simulations...	115
Figure 4.18: Gaseous phase argon at 200K and 7.5 MPa .....	116

Figure 4.19: Radial distribution functions for Al-Al, Al-O, and O-O interactions .....	117
Figure 4.20: Fragmentation and decomposition of $\text{Al}_2\text{O}_3$ from an alumina particle when heated beyond 4000 K; initial diameter of 5 nm.....	118
Figure 5.1: Variations of thermodynamic and structural properties during melting of bulk aluminum in vacuum; the glue potential .....	124
Figure 5.2: Variations of thermodynamic and structural properties during melting of nano-sized aluminum particle; the glue potential.....	125
Figure 5.3: A 4 nm aluminum particle in solid state; the glue potential.....	126
Figure 5.4: Melting point of nano-sized aluminum particle as function of particle size .....	127
Figure 5.5: Spherical shape assumed by nano-scale aluminum particles after melting .....	129
Figure 5.6: Variation of equilibrium potential energy with temperature for 2 nm sized particle (256 atoms).....	130
Figure 5.7: Surface charge development for 3 nm aluminum particle using the embedded-atom and Streitz-Mintmire potentials .....	131
Figure 6.1: Variations of structural and thermodynamic properties during melting of bulk aluminum; perfect crystal of 864 atoms without defects .....	138
Figure 6.2: Different void geometries considered for bulk aluminum with 864 atoms.....	139
Figure 6.3: Effect of void size on melting of bulk aluminum with 864 atoms .....	140
Figure 6.4: Variations of structural and thermodynamic properties during melting of bulk aluminum; crystal of 864 atoms with $1.05 \text{ nm}^3$ void .....	141
Figure 6.5: Variations of structural and thermodynamic properties of bulk aluminum showing lattice collapse; crystal of 864 atoms with $4.0 \text{ nm}^3$ void .....	142
Figure 6.6: Temporal evolution of atomic positions, showing mechanisms of melting and structural collapse for bulk aluminum with 864 atoms (a) without defect, (b) with a void size of $1.05 \text{ nm}^3$ , and (c) with a large void size of $4 \text{ nm}^3$ .....	144
Figure 6.7: Effect of void size on melting of bulk aluminum with 2048 atoms .....	145

Figure 6.8: Variation of critical void size for lattice collapse as a function of bulk aluminum volume .....	146
Figure 6.9: Different void geometries considered for a spherical 5.5 nm aluminum particle .....	147
Figure 6.10: Effect of void size on melting for a spherical 5.5 nm aluminum particle .....	147
Figure 6.11: Time evolution of atomic positions, showing mechanism of melting for a 5.5 nm nanoparticle (a) without defect, (b) with a void size of $0.98 \text{ nm}^3$ , (c) with a large void size of $8.2 \text{ nm}^3$ .....	148
Figure 6.12: Time evolution of density contours, showing mechanism of melting for a 5.5 nm nanoparticle (a) without defect, (b) with a void size of $0.98 \text{ nm}^3$ , (c) with a large void size of $8.2 \text{ nm}^3$ .....	149
Figure 6.13: Effect of void size on melting of a spherical 8.5 nm aluminum nanoparticle.....	150
Figure 6.14: Time evolution of atomic positions, showing mechanism of melting for a 8.5 nm nanoparticle (a) without defect, (b) with a void size of $5.0 \text{ nm}^3$ , (c) with a large void size of $20.0 \text{ nm}^3$ .....	151
Figure 6.15: Time evolution of density contours, showing mechanism of melting for a 8.5 nm nanoparticle (a) without defect, (b) with a void size of $5.0 \text{ nm}^3$ , (c) with a large void size of $20.0 \text{ nm}^3$ .....	152
Figure 7.1: Schematic of a spherical nanoparticle with aluminum core and oxide shell.....	156
Figure 7.2: Aluminum nanoparticles with crystalline oxide layer at room temperature .....	158
Figure 7.3: Equilibration calculations for 5 nm particle (3 nm core diameter and 1 nm crystalline oxide thickness) .....	159
Figure 7.4: Evolution of Lindemann indices for aluminum core and crystalline oxide layer; 5 nm particle (3 nm core diameter and 1 nm oxide thickness).....	160
Figure 7.5: Density distributions at various temperatures during heating of 5 nm particle .....	161
Figure 7.6: Evolution of Lindemann indices for aluminum core and crystalline oxide layer; particle size of 5-10 nm (3-8 nm core diameter and 1.0 oxide thickness).....	162

Figure 7.7: Evolution of Lindemann indices for aluminum core and crystalline oxide layer; particle size 7-10 nm (5 nm core diameter and 1.0-2.5 nm oxide thickness) .....	163
Figure 7.8: Variation of melting points as function of core size and oxide layer thickness .....	163
Figure 7.9: Evolution of Lindemann index during heating of 5 nm pure crystalline alumina particle .....	164
Figure 7.10: Evolution of Lindemann indices during heating of 5 nm particles with crystalline and amorphous oxide layers (3 nm core diameter and 1 nm oxide thickness) .....	165
Figure 7.11: Snapshots of 5-8 nm nano aluminum particles with crystalline oxide layer, showing diffusion of aluminum cations (core size of 3-6 nm and oxide thickness of 1 nm).....	168
Figure 7.12: Snapshots of 7-9 nm nano aluminum particles with crystalline oxide layer, showing diffusion of aluminum cations (core size of 5 nm and oxide thickness of 1-2 nm) .....	169
Figure 7.13: Snapshot showing diffusion of aluminum cations in crystalline and amorphous oxide layers for 5 nm particle (oxide thickness of 1 nm) .....	170
Figure 7.14: Domain for application of continuum laws based on particle diameter and Pressure .....	171
Figure 8.1: Size dependence of melting point and heat of fusion for nano-particulate aluminum .....	179
Figure 8.2: Size dependence of vaporization temperature for nano-particulate aluminum .....	180
Figure 8.3: Pyrophoricity at nano scales with melting of aluminum core as primary mechanism of ignition.....	182
Figure 8.4: Time evolution of temperature for nascent aluminum particles.....	185
Figure 8.5: Time evolution of temperature and oxide thickness for particle with 10 nm core diameter and 0.3 nm oxide thickness using ion transport in non-adiabatic conditions .....	187
Figure 8.6: Time evolution of temperature and oxide thickness using ion transport for particle with 10 nm core diameter and 0.3-0.4 nm oxide thickness in adiabatic conditions .....	188



Figure 8.7: Evolution of temperature and oxide thickness for particle with 10 nm core diameter and 0.5 nm oxide thickness.....	190
Figure 9.1: Al-O phase diagram (Goldsmith et al., 1960) .....	199
Figure 9.2: A schematic showing aluminum oxide thickness on a nanoparticle .....	200
Figure 9.3: Various Stages of Aluminum Particle Ignition and Combustion .....	202
Figure 9.4: Fourier Analysis based on characteristic time and length scales associated with oxide layer .....	208
Figure 9.5: Regimes of Diffusion vs. Kinetically controlled mechanism as a function of different pressures and particle size .....	212
Figure 9.6: Different modes of ignition based on length and time scales.....	217
Figure 9.7: Schematic of different modes of ignition for oxide coated aluminum particles.....	220
Figure 9.8: Effect of Pressure on Characteristic Time Scale Study.....	221
Figure 9.9: Effect of Temperature on Characteristic Time Scale Study.....	222
Figure 9.10: Predicted temperature histories and overall thickness of oxide layers for 100 nm particle introduced in air at 1250 K .....	223
Figure 9.11: Predicted temperature histories and overall thickness of oxide layers for 500 nm particle introduced in air at 1750 K .....	224
Figure 9.12: Predicted temperature histories and overall thickness of oxide layers for 5 $\mu\text{m}$ particle introduced in air at 2100 K.....	224

## LIST OF TABLES

Table 1.1: Properties of metal and metal oxides.....	7
Table 2.1: Properties of aluminum.....	18
Table 2.2: Properties of aluminum oxide.....	18
Table 2.3: Adiabatic temperature of aluminum combustion with different oxidizers.....	19
Table 2.4: Values of kinetic parameters used in models for aluminum oxidation and ignition.....	30
Table 2.5: Existing experimental data on aluminum at micro-scale.....	33
Table 2.6: Existing numerical models for micro-scale aluminum combustion (Brooks and Beckstead, 1995).....	42
Table 2.7: Reactions involved in aluminum combustion along with rate constants....	46
Table 3.1: Existing data on aluminum at nano scales.....	54
Table 4.1: Various length and time scales in physical world (material science).....	76
Table 4.2: Coordinates for $\text{Al}_2\text{O}_3$ lattice.....	95
Table 5.1: Cohesive energies for bulk aluminum.....	126
Table 5.2: Melting points of nano-scale aluminum particles as function of particle diameter.....	128
Table 7.1: Stresses developed inside the oxide shell due to melting.....	166
Table 8.1: Thermo physical properties of bulk aluminum and alumina.....	179
Table 8.2: Kinetic parameters determined for phase transformations.....	189
Table 8.3: Constants used in expression for growth of oxide layer.....	189
Table 8.4: Properties used in determination of pyrophoricity.....	191
Table 9.1: Thermo-physical properties of aluminum and alumina.....	201
Table 9.2: Kinetic parameters determined for phase transformations.....	204

Table 9.3: Constants used in expression for growth of oxide layer.....	215
Table 9.4: Various regimes of particle behavior during ignition.....	216

## NOMENCLATURE

### *Symbols*

$A$	surface area, pre-exponential factor
$a$	half distance from one potential minimum to the next
$Al$	aluminum
$Al_2O_3$	aluminum oxide
$b, c, d$	constants
$c, c_p, c_v$	specific heat
$C$	molar concentration
$d_i$	scaled coordinates
$d, D$	diameter of particle, particle size
$Da$	Damkohler number
$D$	gas mass diffusivity
$E$	activation energy, total energy of a particle
$E_0$	Electric field due to Mott's potential, $V_M$
$f$	ratio of structural to thermodynamic melting point, probability, fraction
$F$	force, activation energy, energy required to embed an atom in an environment with given electron density
$g$	constant
$J$	second derivative associated with self-Coulomb repulsion
$h, H$	enthalpy
$h$	critical thickness, heat transfer constant

$H$	Hamiltonian
$K$	kinetic energy, activation energy
$k$	rate constant, conductivity
$k_B$	Boltzmann's constant
$L$	latent heat of fusion/vaporization, Lagrangian, length scale of simulation
$l$	length of Al-Al atomic bond
$MW$	molecular weight
$\dot{m}$	mass flow rate
$m, M$	mass
$n$	number of cations per unit area, mole number, reaction order
$N$	number of atoms/molecules
$N_A$	Avogadro's number
$P, p$	pressure
$p$	momentum
$q_i$	scaled coordinates, charges
$q$	heat loss
$Q$	heat release
$r_0$	mean free path
$r_i$	coordinates for a particular location
$r_{ij}$	distance between two atoms
$r, R$	particle radius
$R_K$	reaction front location

$R_u$	Universal gas constant
$s$	scaling factor
$S$	surface area
$t$	time
$T$	temperature
$U$	potential energy, energy barrier
$V$	volume, potential
$V_M$	Mott's potential
$W$	molecular weight
$X$	mole fraction
$x$	coordinates, oxide thickness
$Y_i$	mass fraction of species $i$
$Z_D$	frequency factor
$Z$	pre exponential constant

### ***Greek Symbols***

$\alpha$	energy accommodation constant, material constant, alpha phase for alumina
$\beta$	constant, heating rate
$\gamma$	gamma phase for alumina
$\delta$	oxide thickness, Lindemann index
$\varepsilon$	epsilon (constant for LJ potential), mass fraction of reacting species

$\zeta$	decay length for atomic orbital, friction length
$\xi$	constant used in Streitz-Mintmire potential
$\kappa$	lattice vector
$\kappa$	lattice vector
$\lambda$	translational order parameter, mean free path
$\mu$	viscosity, constant used for charge evolution, molecular weight
$\nu$	potential, velocity, Stoichiometric ratio, electrostatic interaction energy
$\nu_1$	monomer volume calculated using density of aluminum
$\rho$	density
$\sigma$	sigma (constant for LJ potential), surface tension, stress
$\tau$	burn time
$\nu$	attempt frequency of cation jump
$\varphi$	pair wise atomic interactions, potential function
$\chi$	electro-negativity, mole fraction
$\psi$	wave function
$\dot{\omega}$	production/oxidation/reaction rate
$\hbar$	Planck's constant
$\Gamma$	phase space
$Z$	core charge
$\Lambda$	wavelength
$\Omega$	entropy, volume of oxide formed per cation

***Subscripts***

<i>0</i>	initial condition
<i>Al</i>	aluminum
<i>Al<sub>2</sub>O<sub>3</sub></i>	aluminum oxide
<i>bpt</i>	boiling point
<i>b</i>	bulk properties
<i>c</i>	condensed phase
<i>cr</i>	critical
<i>diff</i>	diffusion
<i>el</i>	electron
<i>fus</i>	fusion
<i>g</i>	gaseous phase
<i>i, j, k</i>	indices
<i>kin</i>	kinetic
<i>LJ</i>	Lennard Jones
<i>m</i>	melting point
<i>n</i>	nucleus
<i>o</i>	oxidizer
<i>ox</i>	oxidation
<i>p</i>	particle
<i>s</i>	surface



$SC$  Sutton Chen

$vap$  vaporization

***Superscripts***

$\overrightarrow{(\cdot)}$  vector

$(\cdot)'$  first derivative

$(\cdot)''$  second derivative

## ACKNOWLEDGEMENTS

With deep gratitude, first I wish to express my sincere thanks to my advisor, Dr. Vigor Yang, for giving me an opportunity to work under him and kindly providing guidance throughout the development of the study. He has been the source of inspiration and his support, encouragement, and comments have been of greatest help at all times.

Sincere thanks also go to Dr. Dan Haworth, Dr. Robert Kunz, Dr. Steve Son and Dr. Richard Yetter for serving as my committee members. They took effort in reading and gave me valuable suggestions on the earlier versions of this thesis. I would also like to thank Dr. Barbara Garrison, Dr. Saman Alavi and Dr. Leonid V. Zhigilei for their advise and interactions during the early stages of my learning of nano scale simulations.

This work was sponsored by the U.S. Army Research Office under the Multi-University Research Initiative under Contract No. W911NF-04-1-0178. The financial support and encouragement provided by Drs. David Mann, Kevin L. McNesby, and Ralph Anthenien are gratefully acknowledged.

I also wish to express thanks to all my friends and research mates for their company and support. I take this opportunity to express my love and sincere thanks to my parents, grandparents and my sister for their endless love and support. They taught me the value of hard work and provided me enormous support all my life. I owe this accomplishment to The Almighty who has given me the mind, intellect, body and energy to accomplish such a task.

## Chapter 1

### Introduction

#### 1.1 Background and Motivation

Energetic materials are substances that can store large amounts of chemical energy and are characterized by a very high rate of energy release on burning. Nano-phase materials and composites, characterized by ultra fine grain size, have especially attracted widespread interest in recent years due to their unusual energetic properties. Such nano-sized metallic and explosive powders have been used with solid propellant and explosive mixtures to increase the overall efficiency. Excess energy of surface atoms and reduced activation energy values for chemical reactions contribute to the extraordinary chemical activity of nanoparticles (Pivkina et al., 2004).

It has been found that addition of aluminum nanoparticles in particular can enhance the burning rate of propellants by 5-10 times as compared to conventional aluminum particles (Mench et al., 1998). Aluminum nanoparticles have been used as an ingredient in solid rocket propellants because of their high density, high heat release during oxidation, and low cost. The addition of aluminum has resulted in an increase in specific impulse of around 10%. It also suppresses combustion instability. Some disadvantages of using aluminum are smoky, luminous exhaust trails, contamination with  $\text{Al}_2\text{O}_3$ , and potential of increase metal fire damage in case of a launch failure. The first experiments with aluminized propellants were conducted in mid-1950s. Nothing much

was known about aluminum combustion and only some thermo chemical calculations suggested substantial power gains. Aluminum was also used in several tactical rockets in 1960s and for long-range ballistic missiles, use of aluminum became a must if missiles were to be of practical size. Suppression for combustion instability has always been a concern for aluminum combustion.

Many fundamental issues concerning the ignition and combustion characteristics at nano scales, however, remain to be clarified. Before moving to a full multi-scale modeling with simulations of the generation, transport, and combustion of nano-sized energetic materials in flow environments, good understanding of the combustion of a single particle in a quiescent medium is required. Moreover, the theories developed for micron-sized particles cannot be directly applied to study the ignition and combustion of nano-sized particles. The combustion mechanisms at such scales can no longer be controlled by transport rates and are speculated to be kinetically controlled. Also, the mode of combustion may switch to heterogeneous reactions because of the small length scales. There is a diversity of opinions regarding the ignition of nanoparticles as well. The overall aim of the current study is the establishment of a unified theory accommodating the various processes and mechanisms involved in the combustion and ignition of aluminum particles at micro and nano scales. Such a theory helps understand the single particle behavior with high fidelity, and can also act as a sub-model in predicting the collective behavior of particles at large scales.

Another critical issue relevant to the future development of nano-structured energetic materials is the basic understanding of structures that provide desirable performance, thermo-mechanical, and ignition and combustion characteristics. In light of

the inconsistency and uncertainties of existing theories concerning the particle behavior at nano scales, fundamental research based on well-calibrated techniques appeared to be imperative, in order to achieve improved understanding of the effects of particle size on the ignition and combustion behavior.

With this point of view a comprehensive review of work done on aluminum particles at micro-scale and nano scale has been performed ([Glassman, 2001](#); [Bucher et al., 1998](#); [Bucher et al., 1999](#); [Bucher et al., 2000](#); [Brooks and Beckstead, 1995](#); [Babuk et al., 2001b](#); [Price and Sigman, 2001](#)). Various processes and mechanisms involved were identified. Research focus was placed on the continued development of a unified theory for particle ignition and combustion, and on the establishment of a Molecular Dynamics (MD) simulation tool to handle the problems at nano scales.

Once the theoretical and computational tools were established, the main objective was then to investigate the characteristics of bulk and nano-particulate aluminum by means of MD simulations using three major studies. The general computational framework involved parallelized pre processing, post processing and main solvers with capability to simulate different ensembles using appropriate algorithms. Size dependence of melting temperature of pure aluminum particles up to 9 nm was investigated in the first study. Phenomena like dynamic co-existence of solid and liquid phase and the effect of surface charges on melting were also explored. The second study involved the study of effect of defects in the form of voids on melting of bulk and particulate phase aluminum. The third MD study was used to study the thermo-mechanical behavior of nano aluminum particles coated with crystalline and amorphous oxide layers during melting. The effect of particle size in the range of 5-10 nm with oxide thickness in the range of 1-

2.5 nm was investigated. Various fundamental processes, including structural changes, stress development, and phase transformations in both the aluminum core and the oxide shell, were examined and quantified systematically. The diffusion of aluminum cations through the oxide layer was also explored. In addition, a structural analysis was applied to determine the stress field in the oxide shell due to the volume dilatation in the aluminum core. In a following theoretical study, the condition for pyrophoricity and explosivity of nano-particulate aluminum was analyzed and modified. The size dependence of thermodynamic properties at nano scales, including melting and vaporization temperatures, heat of fusion and heat of vaporization were considered and incorporated into the existing theories developed for micro and larger scales. Finally, a phenomenological theory for ignition and combustion of aluminum particles was proposed. The whole time history from ignition till particle burnout was divided into five stages. An attempt was made to explore different modes of ignition based on the effect of pressure, temperature, oxidizer, oxide thickness and particle diameter. This was investigated using time and length scales involved during ignition and combustion.

## **1.2 Issues Concerning Metal Particle Combustion**

Due to their high ignition temperatures, metals were often not thought as being combustible. Once ignited, they release more heat on burning as compared to other fuels. Burning metal particles is different than hydrocarbons because of the presence of condensed species. This is a very challenging scientific research topic and these days it is being used in some important practical applications. One of the reasons for their

widespread use is the high energy densities as compared to hydrocarbons. Metal cutting, welding, metal fires like the oxygen generator fire on Mir, and self propagating high-temperature synthesis of materials are some examples of metal combustion. In propulsion systems however, the combustion of metals typically occurs via small diameter particles which can be either of micro or nano size.

Since the phase transition temperatures vary with the chemical composition of atmosphere and pressure, the resulting combustion mechanism is dependant on the oxidizer type and pressure. The transport phenomenon through the condensed and gas phase further complicates the combustion mechanism. Due to the formation of high temperature condensed-phase products, radiation effects also play a role in energy conservation of burning particles. Moreover, inter solubility of metal and its products can also affect the combustion behavior and can lead to disruption or break up of solid metal (Yetter and Dryer, 2001).

### **1.2.1 Heterogeneous vs. Homogeneous Combustion**

Three factors influence the mode of metal combustion in a major way:

1. Volatility of metal relative to that of the oxide
2. The comparison between the energy required to gasify the metal or its oxide with the overall energy available from the oxidation reaction
3. Size of the particle

On the basis of the first two thermodynamic factors, metal combustion is classified as heterogeneous or homogeneous. The process can either occur with the metal

and oxidizer in gas phase for a volatile metal, leading to vapor phase reaction or with metal and a condensed phase, leading to a heterogeneous reaction.

The limiting flame temperatures, boiling points of pure metals, and hence the mode of combustion are also a strong function of pressure. At a particular limit called the crossover pressure, the boiling point of the metal equals adiabatic flame temperature of the system under consideration. If the pressure is increased further, the boiling temperature exceeds the adiabatic flame temperature and combustion proceeds via reactions on particle surface. Figure 1.1 shows the cross over pressures for different systems. It can be seen that the oxidation with oxygen always occurs in the gas phase for all practical purposes. For Al-H<sub>2</sub>O and Al-CO<sub>2</sub> systems, cross over pressures of 1.4 atm and 4.6 atm were obtained, respectively. This can be done through CEC calculations and Clausius-Claperyon equation to obtain variation of boiling point with pressure.

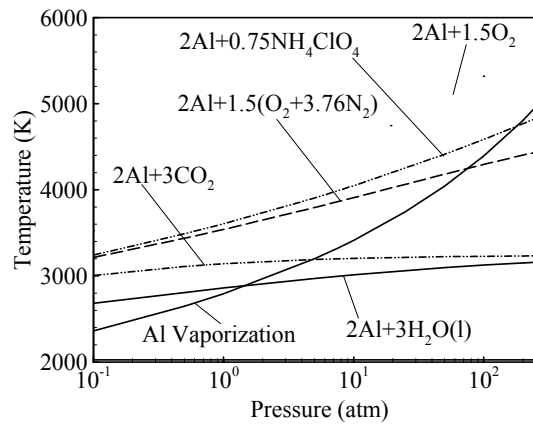


Figure 1.1: CEC Calculation for crossover pressures

Table 1.1 shows the properties of various metals and their oxides (Glassman, 2001). The table lists metal, its boiling point, the oxide formed during oxidation, the oxide's properties like volatilization temperature, heat of formation, heat of volatilization,



and the sum total of energy required to heat the oxide to its volatilization temperature and dissociate. As can be seen from the table, since for metals like Al, Be, Ti etc. the boiling point of the metal is significantly below the decomposition temperature of their oxides, the combustion proceeds via formation of a detached flame in the gas phase. But in metals like boron that have a very high boiling point, the combustion proceeds via heterogeneous reactions. In terms of enthalpy, the chemical energy released is sufficient to vaporize the metal oxide but insufficient to change the phase of metal. From the table, since boiling point of aluminum is significantly below decomposition of aluminum oxide, it will proceed with a detached diffusion flame.

Table 1.1: Properties of metal and metal oxides

Metal	$T_{bp}$ (K)	Oxide	$T_{vol}$ (K)	$\Delta H_{f,298}$ (kJ/mol)	$\Delta H_{vol}$ (kJ/mol)	$H_{T_{vol}} - H_{298} + \Delta H_{vol}$ (kJ/mol)
Al	2791	$Al_2O_3$	4000	-1676	1860	2550
B	4139	$B_2O_3$	2340	-1272	360	640
Be	2741	BeO	4200	-608	740	1060
Cr	2952	$Cr_2O_3$	3280	-1135	1160	1700
Fe	3133	FeO	3400	-272	610	830
Hf	4876	HfO <sub>2</sub>	5050	-1088	1014	1420
Li	1620	$Li_2O$	2710	-599	400	680
Mg	1366	MgO	3430	-601	670	920
Ti	3631	$Ti_3O_5$	4000	-2459	1890	2970
Zr	4703	$ZrO_2$	4280	-1097	920	1320

Unlike hydrocarbons, the temperature profile for most of the metals is like a flat top distribution, over a significant range of radial distances above the particle surface, where the oxide vaporization takes place. However, in some cases if due to radiation losses the temperature drops below the boiling point of metal, then combustion proceeds on the surface of the particle.

### 1.2.2 Limiting Flame Temperature

In case of metal combustion the flame temperature is fixed by the vaporization-dissociation temperature (volatilization/limiting temperature) of the metal oxide product formed as a result of oxidation. This is because the heat required to vaporize/decompose the oxide is greater than the heat available to raise the oxide above its boiling point (Glassman, 1977). The flame temperature can exceed the limiting temperature only when the heat released during the reaction exceeds the combined heat required to raise the products to the volatilization temperature and that required for dissociation. As mentioned before in addition to the boiling temperature, the volatilization temperature, and the heat of formation, Table 1.1 also shows the heat of volatilization and a combined sum of heat of volatilization with the enthalpy required to raise the product to the volatilization temperature. This issue should be taken care of while simulating metal particles. Due to limiting flame temperatures, Glassman's criterion for vapor phase combustion states that for a metal to burn as vapor, the oxide volatilization temperature must be greater than the metal boiling point. At steady state the temperature at the surface of the metal is a few degrees below its boiling point.

Thermodynamic calculations show that adiabatic flame temperature does not vary much with the equivalence ratio and this is attributed mostly to the fact that the temperature is limited by the vaporization-decomposition temperature of aluminum oxide. It can be exceeded if initial temperature is higher than the ambient. Off stoichiometric for metal oxygen systems, temperature varies minimally as stoichiometric ratio is approached and that too if equilibrium of decomposed metal oxide species is

influenced by excess of one of the reactants. The enthalpy of vaporization-decomposition can be calculated using isobaric-isoenthalpic numerical simulations and for  $\text{Al}_2\text{O}_3$  the value is 1860 kJ/mol. However such calculations hold only for stoichiometric conditions. The enthalpy of reaction for oxidation of aluminum is 1676 kJ/mol. The enthalpy required to heat  $\text{Al}_2\text{O}_3$  in liquid state to its volatilization temperature is 688 kJ/mol. Furthermore, we can have distinction between volatilization temperature and decomposition temperature if the product species of oxide decomposition are in condensed phase.

There is a subtle difference between vaporization temperature and decomposition temperature of metal oxides. In practice metal oxides always decompose to more than one species close to the boiling temperature reported in thermodynamic property tables. The term vaporization would be the temperature at which free energies of liquid and gaseous phases are equal and strictly speaking heat of vaporization can be calculated from the standard heat of formations of liquid and gaseous phases. However, both the terms have different meanings and definitions, if the oxide decomposes instead of vaporizing. Recently, the term volatilization has been used to replace vaporization-decomposition ([Brewer, 1953](#)).

During volatilization of  $\text{Al}_2\text{O}_3$ ,  $\text{AlO(g)}$  is the major species, and  $\text{Al}_2\text{O}_3 \rightarrow 2\text{AlO} + \text{O}$  is one of the primary reactions. As the pressure is increased for Al-O system, by Le Chatelier's principle, dissociation is reduced. As a result heat required to volatilize the oxide reduces and adiabatic temperature increases. A ten fold increase in pressures results in 15% increase in the temperature and 7% reduction in the heat of volatilization.

### 1.2.3 Diffusion vs. Kinetically Controlled Mechanism

Combustion of metal particles also involves chemical and transport time scales. These can be compared to further classify the mode of combustion mechanism. If the reaction rates are slow as compared to the rates of mass and energy diffusion, the spatial non-uniformities can be eliminated and the process is kinetically controlled. But fast reaction chemistry leads to temperature and species spatial gradients, which cause conduction and diffusion of heat and species, respectively. This leads to diffusion controlled mechanism.

Pressure and particle diameter play a very important role in determining the type of combustion mechanism by affecting the characteristic diffusion time relative to the kinetic times. For diffusion controlled mechanism the combustion time can be derived as:

$$t_{b,diff} = \frac{\rho_p d_0^2}{8\rho D \ln(1 + \nu Y_{O,\infty})} \quad (1.1)$$

where  $d_0$  is the initial particle diameter,  $\rho_p$  the particle density,  $\rho$  the gas density,  $D$  the gas mass diffusivity,  $\nu$  the mass stoichiometric fuel-oxidant ratio, and  $Y$  the mass fraction. In case of a kinetically controlled mechanism the mass consumption rate is given by:

$$\frac{\dot{m}}{4\pi r_p^2} = MW_p k P X_{O,s} \quad (1.2)$$

where  $X_o$  is the oxidizer mole fraction,  $P$  the pressure,  $r$  the radius,  $MW$  the molecular weight, and  $k$  the surface reaction rate with the oxidizer. This on integration gives a characteristic time of

$$t_{b,kin} = \frac{\rho_p d_0}{2MW_p kPX_{o,\infty}} \quad (1.3)$$

To determine the dominant combustion mechanism (Yetter and Dryer, 2001) the Damkohler number,  $Da$ , for surface reaction is defined as:

$$Da = \frac{t_{b,diff}}{t_{b,kin}} = \frac{MW_p k P d_0 X_{o,\infty}}{4\rho D \ln(1 + \nu Y_{o,\infty})} \quad (1.4)$$

This implies that small particles at low pressures generally burn under kinetically controlled conditions.

From a different perspective, the Surface kinetics is given by  $\dot{\omega}'' = kM_{Al}[O_{2s}]$  where  $\dot{\omega}''$  is  $\text{kg/s.m}^2$ ,  $M$  is molecular weight of aluminum,  $k$  is rate coefficient expressed as  $k = Ae^{-E_a/R_u T_s}$ ,  $[O_{2s}]$  is oxygen concentration in  $\text{kmol/m}^3$  which can be written as  $[O_{2s}] = \frac{M_{mix}}{M_{o_2}} \frac{P}{R_u T_s} Y_{O_{2,s}}$ . Here,  $R_u$  is the universal gas constant, and  $T$  is the temperature. This yields,

$$\dot{m}_{Al} = 4\pi r_s^2 k M_c \frac{M_{mix}}{M_{o_2}} \frac{P}{R_u T_s} Y_{O_{2,s}} \quad (1.5)$$

where  $r_s$  is the radius of the surface. From flux balance we can derive that

$$\dot{m}_{Al} = 4\pi r_s \rho D \ln \left[ 1 + \frac{Y_{O_{2,\infty}} - Y_{O_{2,s}}}{Y_{O_{2,s}} + \nu} \right] \approx 4\pi r_s \rho D \frac{Y_{O_{2,\infty}} - Y_{O_{2,s}}}{Y_{O_{2,s}} + \nu} \quad (1.6)$$

The above two expressions can be combined to obtain

$$\dot{m}_{Al} = \frac{Y_{O_{2,\infty}} - 0}{\frac{\nu R_u T_s}{4\pi r_s^2 k M_{mix} P} + \frac{Y_{O_{2,s}} + \nu}{4\pi r_s \rho D}} \quad (1.7)$$

The above equation can also be interpreted using circuit analogy as a relation of resistances due to diffusion/kinetics and the potential difference. And we can express them as

$$R_{kin} = \frac{\nu R_u T_s}{4\pi r_s^2 k M_{mix} P} \quad R_{diff} = \frac{Y_{O_2,s} + \nu}{4\pi r_s \rho D} \quad (1.8)$$

At large  $r_s$ , and high pressures, the process is diffusion controlled because  $R_{diff} > R_{kin}$ . At high temperatures,  $k$  increases rapidly compared to  $T$  and hence we have diffusion controlled mechanism (Turns, 1996).

Such characteristic time scales can also be used to look at ignition and explosion using well established theories by Semenov and Frank-Kamenetskii. If the reaction proceeds at a constant rate the characteristic reaction time can be defined as

$$\tau_r = \rho / \left[ \rho^n \varepsilon^n A \exp(-E/R_u T_0) \right] \quad (1.9)$$

for the reaction rate  $\dot{\omega} = AC^n \exp(-E/R_u T) = A\rho^n \varepsilon^n \exp(-E/R_u T)$ . Here  $\rho$  is the density,  $\varepsilon$  the mass fraction of reacting species,  $A$  the pre-exponential factor,  $E$  the activation energy,  $n$  the overall reaction order, and  $R_u$  the universal gas constant. Also, a characteristic heat loss time can be expressed as

$$\tau_l = V \rho c_v / hS \quad (1.10)$$

where  $V$  is the volume of vessel,  $c_v$  the specific heat,  $h$  the heat transfer coefficient, and  $S$  the surface area. The limit of thermal explosion is given by using Semenov's criteria, implying if  $\tau_r/\tau_l$  is greater than a particular value, thermal explosion is not possible.

According to non stationary solution by Frank-Kamenetskii, a similar result can be

derived and we can obtain the induction time associated with the whole system before ignition

$$\tau_{ind} = \frac{c_v \rho}{Q} \frac{R_u T_0^2}{E} \frac{1}{Z} e^{E/R_u T_0} \quad (1.11)$$

Here,  $Z$  is the pre exponential factor and  $Q$  is the heat thermal heat release during reaction.

#### 1.2.4 Mode of Ignition

Particle size plays a significant role in determining the characteristics of ignition and combustion of aluminum particles and there is a diversity of opinion regarding the ignition. For micron-sized and larger aluminum particles, the ignition temperature coincides with the melting point of the surface oxide ( $\text{Al}_2\text{O}_3$ ) layer at 2327K (Bucher et al., 2000). The impervious nature of aluminum oxide inhibits the ignition of aluminum. Once the layer melts, it coalesces to form an oxide cap, and the aluminum core is then exposed to the ambient gases for oxidation. Researchers like Ermakov et al., Boiko et al., Lokenbakh et al., Boiko et al., Rozenband and Vaganova (Lokenbakh et al., 1985; Boiko et al., 1989), however have concluded that ignition of aluminum in particular occurs due to the failure of oxide shell integrity at micro scales. At nano scales (less than 100 nm), the ignition occurs near the melting point of aluminum at 940 K by cracking of the oxide shell, possibly caused by the pressure buildup (Rai et al., 2004; Rozenband and Vaganova, 1992) and/or phase transformations (Dreizin, 2003; Trunov et al., 2006) inside the shell. According to Rai et al., oxidation of alumina-coated nano-sized aluminum

particles is initiated by melting of the aluminum core. The resultant volume dilatation causes a pressure build-up inside the shell formed by the oxide layer. Because of the higher curvature as compared to micron-sized particles, the stress developed due to the pressure becomes unsustainable and the shell subsequently ruptures. This concept was originally introduced by Rozenband (Rozenband and Vaganova, 1992), who developed a model taking into account the mechanical stresses at the metal-oxide interface. Trunov et al. (Trunov et al., 2006) attributed the observed low ignition temperature of nano-sized particles to the transformation from the amorphous to the gamma and alpha phases in the oxide layer. As a consequence of the density variations in different phases, the layer develops cracks, which permit direct oxidation of aluminum in the core. A proper justification of all the processes leading to ignition, which covers a broad range of scales, needs to be developed.

### 1.3 Objectives

Summarizing the previous works, it was realized that a lot of work needs to be done to develop a theory for micro and nanoparticle combustion which is applicable at all scales. The primary objectives are:

- To obtain fundamental understanding of the physics and reactive behavior of a single particle at different length scales, particularly with regard to sensitivity, ignition, burning characteristics, and mechanical properties. Thus, enabling design optimization for nano-structured energetic materials



- To systematically investigate essential difference between physiochemical mechanisms under micro and nano regime
- To establish the nano scale simulation framework and validate it extensively with existing literature data
- To explore the size-dependence of properties at nano scales and focus on the melting phenomena for bulk and particulate phase using pure aluminum particles
- To investigate the thermo mechanical characteristics of oxide coated aluminum particles
- To explore the pyrophoricity and explosivity of aluminum at nano scales
- To provide an explanation for different modes of ignition based on detailed study of length and time scales associated with different processes

The approach follows three steps:

- Investigation of the existing literature on micro-particle combustion and observations made by experimentalists at nano scales
- Establishing nano scale simulation framework on a parallel computing platform to observe key thermo-mechanical characteristics based on literature survey using molecular dynamics simulations
- Performing detailed theoretical studies like pyrophoricity of particulate aluminum, explanation of modes of ignition based on length and time scales and establishing a five stage theory

The following Chapter 2 introduces the work done in literature for micro-particle burning. It includes major experimental observations and numerical models which exist

at micro-scale. Chapter 3 discusses the work done so far in the area of nanoparticle combustion. Chapter 4 presents the nano scale simulation framework and other finer details related to code development and validation. Chapter 5, 6, and 7 present the results of three major molecular dynamics studies performed using the framework discussed in Chapter 4. Chapter 8 explores the pyrophoricity of aluminum at nano scales. Chapter 9 summarizes all the key results and also discusses the five stage theory using the study of different length and time scales. A brief summary of the current research and proposed future work are provided in Chapter 10.

## Chapter 2

### Micro Scale Aluminum Combustion

#### 2.1 Aluminum

Aluminum is the most abundant metal and the third most abundant element in the Earth's crust, after oxygen and silicon. It makes up about 8% by weight of the Earth's solid surface and is chemically too reactive to occur in nature as a free metal. Instead, it is found in combined state in over 270 different minerals. The chief ore of aluminum is bauxite, a mixture of hydrated aluminum oxide ( $\text{Al}_2\text{O}_3 \cdot x\text{H}_2\text{O}$ ) and hydrated iron oxide ( $\text{Fe}_2\text{O}_3 \cdot x\text{H}_2\text{O}$ ). Another mineral important in the production of aluminum metal is cryolite ( $\text{Na}_3\text{AlF}_6$ ). However, cryolite is not used as an ore i.e. aluminum is not extracted from it. The commercial process allowing its recovery economically was not discovered until around the turn of the 20th century.

Aluminum metal is silvery white, has a low specific gravity (2.70) and a low melting temperature (933 K). Except for iron and steel, aluminum is probably used for more purposes than any other metal. Aluminum as a metal has light weight – about one-third that of steel. Pure aluminum is soft and ductile. Other reasons of its use in industry are the ease with which the metal can be cast, machined, rolled, forged, extruded, and drawn. It has high electrical conductivity and significant resistance to atmospheric corrosion. Aluminum paint, beverage cans, baseball bats, high-voltage power lines, house siding, boats, and airplanes are just a few examples of aluminum in use as a metal. As an

energetic material, it can be used as very good source of energy with the heat of reaction as high as 32 kJ/g. Various properties of aluminum and its oxide alumina are shown in Table 2.1 and 2.2, respectively

Table 2.1: Properties of aluminum

Atomic Number	13
Atomic Weight	26.98 kg/kmol
Density	2700 kg/m <sup>3</sup>
Molar Volume	10 cm <sup>3</sup>
Young Modulus	70 GPa
Rigidity Modulus	26 GPa
Elastic Modulus	70-79 GPa
Bulk Modulus	76 GPa
Tensile Strength	230-570 MPa
Yield Strength	215-505 MPa
Poisson Ratio	0.35, 0.33
Melting Point	933 K
Boiling Point	2740 K
Specific Heat	938 J/kg K
Latent heat of fusion	397 kJ/kg
Thermal Conductivity	0.5 cal/s cm K
Van der wall Radius	0.143 nm
Ionic Radius	0.05 nm
Thermal expansion coefficient	20.4-25.0 *10 <sup>-6</sup> /K

Table 2.2: Properties of aluminum oxide

Molecular Weight	101.961 kg/kmol
Melting Point	2327 K
Boiling Point	3273 K
Density	4000 kg/m <sup>3</sup>
Flexural Strength	330 MPa
Elastic Modulus	300 GPa
Shear Modulus	124 GPa
Bulk Modulus	165 GPa
Poisson's Ratio	0.21
Compressive Strength	2100
Hardness	1175 kg/mm <sup>2</sup>
Fracture Toughness	3.5 MPa/m <sup>0.5</sup>
Thermal Conductivity	18 W/m K
Specific Heat	880 J/ kg K

The adiabatic flame temperatures for aluminum and products obtained from different oxidizers are shown in Table 2.3 (Yetter and Dryer, 2001). Unlike combustion

in oxygen or  $\text{H}_2\text{O}$ , fluorination is a vigorous and highly exothermic reaction and Glassman's criterion for vapor-phase combustion does not apply here. Due to the sublimation of  $\text{AlF}_3$ , aluminum particle combustion in fluorine is similar to hydrocarbon droplet combustion. It also provides maximum flame temperature in excess of 4000 K. The adiabatic flame temperature with pure oxygen is also around 3900 K. This further proves the high energy density of a metal particle like aluminum.

Table 2.3: Adiabatic temperature of aluminum combustion with different oxidizers

Reactants	Adiabatic temperature (K)	Products > 1 mol% at $T_{\text{ad}}$	Products
$2\text{Al(s)} + 1.5\text{O}_2$	3977.0	$\text{Al, AlO, Al}_2\text{O}_3, \text{O}, \text{O}_2, \text{Al}_2\text{O}_3(\text{l})$	$\text{Al}_2\text{O}_3(\text{a})$
$2\text{Al(s)} + 1.5(\text{O}_2 + 3.76\text{Ar})$	3624.8	$\text{Al, AlO, Al}_2\text{O}_3, \text{Ar, O, Al}_2\text{O}_3(\text{l})$	$\text{Al}_2\text{O}_3(\text{a})$
$2\text{Al(s)} + 1.5(\text{O}_2 + 3.76\text{N}_2)$	3546.5	$\text{Al, AlO, NO, N}_2, \text{O, Al}_2\text{O}_3(\text{l})$	$\text{Al}_2\text{O}_3(\text{a})$
$2\text{Al(s)} + 3\text{N}_2\text{O}$	3746.9	$\text{Al, AlO, Al}_2\text{O}_3, \text{NO, N}_2, \text{O, O}_2, \text{Al}_2\text{O}_3(\text{l})$	$\text{Al}_2\text{O}_3(\text{a})$
$2\text{Al(s)} + 3\text{H}_2\text{O}$	3052.8	$\text{H, H}_2, \text{H}_2\text{O, Al}_2\text{O}_3(\text{l})$	$\text{Al}_2\text{O}_3(\text{a})$
$2\text{Al(s)} + 3\text{CO}_2$	3144.4	$\text{CO, CO}_2, \text{Al}_2\text{O}_3(\text{l})$	$\text{Al}_2\text{O}_3(\text{a})$
$2\text{Al(s)} + 3\text{CO}$	2277.2	$\text{Al, Al}_2\text{O}_3, \text{CO, Al(l), Al}_2\text{O}_3(\text{a}), \text{C(cr)}$	$\text{Al}_2\text{O}_3(\text{a})$
$2\text{Al(s)} + 1.5\text{F}_2$	4414.5	$\text{AlF, AlF}_2, \text{AlF}_3, \text{Ar, F}$	$\text{AlF}_3(\text{a})$
$2\text{Al(s)} + 1.5(\text{F}_2 + 3.76\text{Ar})$	3873.5	$\text{AlF, AlF}_2, \text{AlF}_3, \text{Ar, F}$	$\text{AlF}_3(\text{a})$

## 2.2 Experiments at Micro Scales

This section summarizes different characteristics associated with micron-sized aluminum particle combustion. Generation of aluminum particles, unique characteristics during the flame front formation, three stages of combustion, asymmetric burning, diffusion of ions through the layer, phase transformations, and burning data under different experimental conditions are discussed in detail.

### 2.2.1 Particle Generation

There are diverse techniques reported in literature that are used to generate aluminum particles and analyze their combustion characteristics. For example, at JNIT the study has been conducted using generator of mono-disperse metal droplets also referred to as GEMMED (Dreizin, 1995). 150 microns diameters droplets are produced up to velocities of 3 m/s using this technique. Other techniques like milling, DC arc discharge, and laser ablation also exist. During the study of aluminum particles, droplets/particles are either burned completely or quenched in inert gases like Argon and Helium. In most of the experimental studies, the burned particles are quenched and micro-sections are prepared on glass slides at different combustion times to study the composition and structure of particles. Even the shape of smoke traces surrounding the quenched particles can be investigated. Electron Probe micro analyzer, energy dispersive spectroscopy detector and wavelength dispersive spectroscopy scan are utilized to determine the particle internal compositions. The emission due to combustion is monitored using brightness pyrometer transducer and is generally used as an indicator of the combustion process. The temperatures are measured using the wavelength pyrometer or optical pyrometry.

### 2.2.2 Characteristics at Micro Scales

For micron-sized particles, aluminum ignites at the melting point of oxide i.e. 2323 K. In combustion of a metal like aluminum there are gas phase reactions and also surface oxidation resulting in volatile and non volatile products which include oxide and

sub oxide species. Some current models allow for deposition of non volatile products (Dreizin, 2000). After ignition, due to the high flame temperature, aluminum starts evaporating and a detached flame front is formed. The species/oxides produced at the flame front are transported back to the aluminum surface. The oxygen is transported in the form of AlO, Al<sub>2</sub>O and Al<sub>2</sub>O<sub>2</sub> species. In air, NO is the main species involved. NO reactivity is negligible in the vapor phase Al-O reaction mechanism. Because of the low reactivity and longer lifetimes, the oxide cap for cases with aluminum oxidation in air is larger as compared to the other oxidizers. Molecular and atomic oxygen are less likely to reach the surface because of the high probability of reaction with Al and sub oxide vapors. The species like AlO, Al<sub>2</sub>O and Al<sub>2</sub>O<sub>2</sub>, and NO react in a heterogeneous mode and also add to the oxygen content inside the particle. The dissolution of oxygen in the droplet results in a three phase equilibrium between the liquid Al<sub>2</sub>O<sub>3</sub>, liquid Al-O solution and the gas. The composition of evaporated species is also affected due to the formation of the Al-O liquid. Aluminum sub oxide vapor is generated at oxygen rich locations at the particle surface, in addition to aluminum. This also results in the change in boiling point of aluminum at different places inside the particle, based on the composition. The ongoing heterogeneous reactions can increase or decrease the burning time. It can lead to faster consumption of aluminum or on the other hand can block aluminum vaporization.

Micron-sized particle combustion is characterized by some well known features such as brightness oscillations, disruptive burning, burning droplet speed variations, oxygen build-up within the molten particle, micro-explosions, asymmetric combustion, and follows  $d^2$  burning rate law. Most of these were investigated by Dreizin et al. (Dreizin, 1995). The main conclusions from the preliminary studies performed on

micron-sized aluminum particles suggested that the oxide is not formed on the burning particle surface during initial period of combustion and gas dissolves in particles causing internal holes. The disruptive events change the combustion time significantly and also aluminum particles agglomerate after ignition. Micro-explosions are generally associated with temperature jumps.

### **2.2.3 Three Stages of Micron-sized Particle Combustion**

The combustion of micron-sized aluminum particles can be further divided into three stages corresponding to different temperatures, internal compositions and flame shapes. The first stage involves spherically symmetric vapor phase combustion, consistent with the metal vapor phase burning model. The second stage is associated with an increase in the size and the density of the smoke cloud, non symmetric burning regime, strong oscillations in particle radiation, flame distortion and spinning. The asymmetric burning is attributed to the dissolution of oxygen and other gases, internal phase changes ensuring eutectic, monotectic and peritectic phase transitions and will be discussed in detail in the following sections. The third stage involves oxide cap formation and its growth. This stage is also characterized by oscillations but decrease in radiation intensity. In addition to exploring these three stages, measurements of flame shape, particle diameter, and temperature histories during the entire process of particle combustion in air was done in an experimental study by Dreizin et al. (Dreizin, 1996). Using transfer number at 3000 K and 1500 K, theoretical burning time was evaluated



using  $d^2$  law. A significant discrepancy was found between predicted and experimental results due to the heterogeneous reactions.

The transition between three stages can be explained in detail through the formation of different Al-O phases (Dreizin, 2000). Aluminum ignites at temperature close to the melting point of  $Al_2O_3$  (2327 K). Because the adiabatic flame temperature is so high, the particle self heats to aluminum boiling point (2730 K). This marks the onset of Stage I with the formation of flame front. The gaseous oxides  $Al_2O$ ,  $AlO$ ,  $Al_2O_2$  and  $NO$  are transported back to the surface. Molten aluminum can dissolve up to 0.1 atomic percent oxygen, and produce liquid phase L1. Oxygen solubility in this L1 phase increases with the decrease in temperature. On particle cooling the solution cannot become super saturated like other metals. Hence, the solution boiling temperature decreases from 2730 for pure aluminum to 2510 for L1, as concentration of oxygen in L1 increases. At 2510, a new oxygen rich L2 phase forms and there is a three phase equilibrium. This starts Stage II. L1 and L2 are immiscible and hence non-uniformity occurs. The boiling point of L2 is 3250 K as compared to that of 2510 for L1. This reduces the aluminum evaporation rate. When particle size decreases, heat flux from the flame becomes smaller than required for the aluminum to boil, and temperature drops. Stage II begins when the particle temperature decreases from 2510 K and combustion rate drops as well due to the decrease in the aluminum vaporization rate. When the temperature decreases to 2323 K, a monotectic phase transition occurs. L1 and L2 phases combine to form  $Al_2O_3$  and it precipitates out to form an oxide cap.

Pressure affects the formation of L1 phase. The monotectic reaction is independent of pressure but the temperature of L1-L2-gas equilibrium increases at higher

pressures. Thus in case of high radiative/convective losses, it is probable that the boiling point of even L1 might not be reached under some conditions, and monotectic phase transition would play the role similar to aluminum surface reactions. This all qualitatively explains experimentally observed phenomena. The particle can explode in the cases if oxygen solubility decreases with temperature, the solution becomes super saturated and heat release can cause particle temperature to increase. Gaseous species like  $N_2$  can also be released.

#### **2.2.4 Asymmetric Burning**

Microgravity eliminates the effects of buoyancy and convection as compared to the normal conditions. Experiments are performed in microgravity by different researchers to explore the physics behind various phenomena associated with the aluminum particle combustion (Yetter and Dwyer, 2001; Dreizin, 1999). Through such experiments, it was concluded that the flame asymmetry is an intrinsic feature of the aluminum particle burning. Al-O solution is formed inside the particle during combustion. The onset of non symmetric burning is accompanied by formation of highly radiative condensed products at several locations within the particle flame zone. Spinning is also observed and explained on the basis of flame asymmetry and torque exerted on the particle by gases. There are combustion models which ascribe non symmetry to accumulation of condensed oxide on particle surface. Dreizin conducted experiments at high and low Reynolds number. The bulk gas velocity due to aluminum evaporation

correlated well with the gas velocity needed to accelerate particle experimentally (Dreizin, 1999b).

To explore and identify the conditions under which asymmetric combustion develops, single aluminum particles have also been burned in  $N_2/O_2$ ,  $Ar/O_2$  and  $He/O_2$  environments. It was found that oxide caps in  $O_2/Ar$  are smaller than other environments. No brightness oscillations were observed in  $O_2/Ar$  either. Nitrogen intensifies oxide dissolution especially through NO. Diffusion in He is faster than Ar, and as a result the asymmetry was more prominent in the former. Smaller drops are more asymmetric. A combination of all these phenomena can increase or decrease burning time (Dreizin, 1999). Free falling metal droplets are formed using pulsed micro arc discharge ignited using a cold tool cathode and a consumable wire anode in work by Dreizin et al. (Dreizin, 2003). Experiments were aimed at identifying correlations between burning particle temperature and composition histories. Most experiments were conducted in microgravity and in air, argon-oxygen, helium-oxygen, and carbon di oxide environments.

### **2.2.5 Diffusion of Ions within the Oxide Layer**

Jeurgens et al. have studied the structure and morphology of thin aluminum oxide films (Jeurgens et al., 2002b), determined the chemical composition and chemical state of the Al and O ions (Jeurgens et al., 2002c), and devised a novel method to determine the thickness of film using XPS (X-ray photoelectron spectroscopy) spectra (Jeurgens et al., 1999). A more mathematical approach followed to determine the total metallic primary zero loss (PZL) intensity and total oxidic PZL intensity for aluminum oxide films. In

recent work by Jeurgens (Jeurgens et al., 2002) the growth kinetics of aluminum oxide films formed by dry thermal oxidation of aluminum, at partial oxygen pressure of  $1.33 \times 10^{-4}$  Pa, and in a temperature range of 373-773 K, was studied using x-ray photoelectron spectroscopy. For temperatures less than 573 K, an amorphous oxide film develops and attains limiting thickness. For temperatures greater than 573 K, there is no limiting thickness. At higher temperatures the initial rate is faster and in comparison to the low temperature case where the thickness is self limiting, the oxide layer grows slowly. The initial regime of very fast growth is followed by slower stage. The second stage is only observed at high temperatures ( $>673$  K). The transition occurs at around 3 nm for study performed at 773 K. The fast growth rate is realized by outward migration of aluminum cations into and through the close packing of oxygen anions in developing oxide film. However, the decrease of oxygen sticking coefficient with increase in temperature may indirectly (due to a low Mott's potential, cation transport rate determining) or directly (supply rate of chemisorbed oxygen is rate determining) lead to lower growth rate during the initial stage, as compared to corresponding rate at lower temperatures. During the second slow oxidation stage, the initially aluminum-enriched amorphous oxide film attains stoichiometric composition of  $\text{Al}_2\text{O}_3$  and becomes crystalline  $\gamma$ - $\text{Al}_2\text{O}_3$ .

Simulations conducted using thermodynamic equilibrium code for Al-air system also show high concentration of ions like  $\text{Al}^+$  and  $\text{AlO}^-$  and electrons. Experimentally the researchers observed distortion in smoke cloud in the external electric field. Also the temperature history and combustion time changed in presence of electric field suggesting that transport processes are affected due to the electric field.

The growth rate is quantified through Mott's potential using Mott-Cabrera model. It is assumed that no net charge is transported through the oxide and no space charge builds up in the film. The cation movement is the rate determining step in oxidation at low temperatures. The rate of electron transport across the developing oxide film by tunneling decreases exponentially with increasing oxide thickness. This results in the limiting oxide thickness. The free electron movement results in establishment of an electric potential which lowers the energy barriers for interstitial movement of cations from metal into the oxide film. The mathematical equation governing the process is given by

$$\frac{dx}{dt} = \Omega n \nu \exp\left(\frac{-U + qaE_0}{kT}\right) \quad (2.1)$$

where  $\Omega$  is the volume of oxide formed per cation,  $n$  the number of cations per unit area which may jump the energy barrier  $U$ ,  $\nu$  the attempt frequency of cation jump,  $q$  the charge of migrating cation,  $2a$  the distance from potential minimum to next potential minimum,  $k$  the Boltzmann constant,  $T$  the temperature,  $E_0$  the electric field due to Mott's potential  $V_M$ , and  $x(t)$  denotes the oxide film thickness at time  $t$ . The constants are given in detail in work by Jeurgens et al. (Jeurgens et al., 2002).

### 2.2.6 Phase Transformations

Trunov and his co-workers established a numerical framework to simulate ignition using correlations/kinetic parameters obtained through thermal analysis. The melting point of alumina is chosen as the criteria for ignition. The methodology proposed

by Trunov (Trunov et al., 2006) treats heterogeneous oxidation as an exothermic process leading to ignition. The ignition is assumed to occur when the particle's temperature exceeds alumina melting point. This model also analyzes the process of simultaneous growth and phase transformations in the oxide. The kinetic parameters for both, direct oxidative growth and phase transformations, are determined from the thermal analysis. The model can be used to predict the ignition for particles of different sizes.

The entire oxidation stage till ignition is divided into different stages. In the model, the growth of three phases of alumina namely, amorphous,  $\gamma$ , and  $\alpha$  and their transformations from one form to the other have been considered. The oxidation process starts with the growth of natural amorphous alumina layer. The rate of this process is controlled by outward diffusion of Al cations. The energy of oxide metal interface stabilizes the oxide only up to a critical thickness of about 5 nm. When the temperature is sufficiently high, the amorphous oxide transforms to  $\gamma$  phase. If prior to the phase change, the thickness of amorphous layer is less than 5 nm, gamma alumina no longer forms a continuous layer covering the surface, due to its higher density. As a result, oxidation rate increases rapidly because of the direct attack of oxidizer. These openings heal gradually and the oxidation rate decreases. As discussed before, this is an alternative explanation of cracking. Cracking was also mentioned to be occurring due to thermal expansion by Rai et al. in previous sections (Rai et al., 2005). The growth of  $\gamma$  alumina continues and the oxidation is limited by inward grain boundary diffusion of oxygen anions. This is also accompanied by transformations from  $\gamma$  phase to  $\theta$  and  $\delta$  phases, which do not affect the oxidation rate significantly. This  $\gamma$  phase alumina finally

transforms to a coarse and dense  $\alpha$  phase alumina. Thus the processes, in order of their occurrence at increasing temperatures, are given by

1. Growth of amorphous oxide
2. Amorphous to  $\gamma$ -alumina phase change
3. Growth of  $\gamma$ -alumina
4.  $\gamma$ -Alumina to  $\alpha$ -alumina phase change
5. Growth of  $\alpha$ -alumina

The kinetic parameters were obtained from TGA experiments. The absolute value of diffusion rate during the growth of layers is given by the solution of radial diffusion equation:

$$\dot{N}_A = \frac{|C_A^{ox} - C_A^{Al}| 4\pi D_A}{\frac{1}{r_{Al}} - \frac{1}{r_{ox}}} \quad (2.2)$$

where  $D_A$  is the diffusion coefficient,  $C_A^{ox}, C_A^{Al}$  the molar concentrations of species  $A$  on the interfaces of oxide with aluminum and oxidizing gas respectively,  $r$  the radius and subscripts  $Al$ , and  $ox$  refer to the aluminum core and oxide layer. With the help of experiments, the rate of diffusion limited oxidation for a spherical oxide layer was given by:

$$m_i^{ox} = \frac{C_i \exp(-E_i / RT_p)}{\frac{1}{r_{i-1}} - \frac{1}{r_i}} \quad (2.3)$$

where,  $C_i$  is the coefficient describing diffusion of a species obtained from TGA experiments. The subscript  $i$  refers to specific phase of oxide and  $i-1$  refers to

underlying layer. The fraction of aluminum surface,  $f$  exposed to direct oxygen is calculated using density ratio of parent and a newly formed (higher density) oxide phase. Thus,  $f = 1 - \rho_{am} / \rho_{\gamma} = 0.17$  when the amorphous phase changes to  $\gamma$  phase. An additional assumption was made regarding the diffusion resistance. It was assumed that the newly formed  $\gamma$  and  $\alpha$  phases provide negligible resistance. There exists a critical thickness at which these layers stop behaving as individual crystallites producing no resistance and start behaving as polycrystalline oxide scales. Based on the literature data, this was chosen as 5 nm for  $\gamma$  phase and 30 nm for  $\alpha$  phase. In this period, till the critical thickness is reached, the constant  $C_i$  is replaced by an effective constant  $C_i^e$ , based on oxide thickness using the relation:

$$C_i^e = \left[ X_i - \frac{h_i - h_i^m}{h_i^e - h_i^m} (X_i - 1) \right] C_i \quad (2.4)$$

where  $X_{\gamma} = 200$ ,  $X_{\alpha} = 150$ ,  $h_{\gamma}^m = 5nm$  and  $h_{\alpha}^m = 30nm$ . Also,  $h_i^e = 2h_i^m + G_i \exp(-L_i\beta)$  where  $G_{\gamma} = 7.71nm$ ,  $G_{\alpha} = 116nm$ ,  $L_{\gamma} = 1.066s/K$  and  $L_{\alpha} = 0.439s/K$ .  $\beta$  is defined as the heat rate, given by  $dT/dt$  with units of K/s. All other constants obtained from experimental study are tabulated in Table 2.4.

Table 2.4: Values of kinetic parameters used in models for aluminum oxidation and ignition

Kinetic Parameter	Value
$E_{am}$	120 kJ/mol
$E_{\gamma}$	227 kJ/mol
$E_{\alpha}$	306 kJ/mol
$C_{am}$	$5.098 \times 10^{-8}$ kg/m-s
$C_{\gamma}$	$4.0784 \times 10^{-3}$ kg/m-s
$C_{\alpha}$	$2.3791 \times 10^{-2}$ kg/m-s



$E_{am \rightarrow \gamma}$	458 kJ/mol
$E_{\gamma \rightarrow \alpha}$	394 kJ/mol
$K_{am \rightarrow \gamma}$	$1 \times 10^{12}$ J/mol-m
$K_{\gamma \rightarrow \alpha}$	$1 \times 10^8$ J/mol-m
$F_{am \rightarrow \gamma}$	$2 \times 10^{15}$ m/s-K
$F_{\gamma \rightarrow \alpha}$	$5 \times 10^6$ m/s-K

For phase transformations the rate of mass increase,  $\dot{m}_{(i-1) \rightarrow i}^{tr}$  of the oxide phase  $i$  transformed from oxide phase  $i-1$  is described as:

$$\dot{m}_{(i-1) \rightarrow i}^{tr} = 4\pi r_{i-1}^2 \rho_i \nu_{(i-1) \rightarrow i} \quad (2.5)$$

$$\nu_{i-1 \rightarrow i} = F_{i-1 \rightarrow i} T_p \left\{ 1 - \exp\left(-\frac{K_{i-1 \rightarrow i} h_{i-1}}{RT_p}\right) \right\} \exp\left(-\frac{E_{i-1 \rightarrow i}}{RT_p}\right) \quad (2.6)$$

where  $T_p$  is the temperature of the particle,  $h_{i-1}$  the oxide thickness, and  $F$ ,  $K$ , and  $E$  are determined experimentally. For direct attack of oxygen at the surface, and assuming diffusion controlled mechanism, using Stefan's law the rate of oxidation has been computed as

$$\dot{m}_{O_2}^{ox} = -\ln\left(1 - \chi \frac{\mu_{O_2}}{\mu_{gas}}\right) \frac{8\pi \mu_{Al_2O_3}}{3\mu_{O_2}} \rho_{gas} D_{O_2} r_p f \quad (2.7)$$

where  $D_{O_2}$  is the diffusion coefficient in air,  $\rho_{gas}$  the density of gas,  $\mu$  the molar mass, and  $\chi$  is the molar fraction of oxygen in gaseous environment. In a separate experiment, in which aluminum particles are heated in oxygen up to 1500 °C, during 300-550 °C, the thickness of natural amorphous layer on particle surface increases. The oxide transforms to gamma at about 4 nm and 550 °C. Later on gamma grows and transforms to alpha and theta polymorphs. Previously too such studies have been performed to obtain activation energies of phase transformations between alumina polymorphs. The model predicts

different ignition temperatures based on particle size but values are a little over predicted compared to lower ignition temperatures of nanoparticles.

### **2.2.7 Experimental Data**

Various sources of Aluminum combustion data, along with a brief summary of their experimental conditions will be discussed in subsequent sections. Different techniques like gas burner, laser, flash, shock, etc have been used to ignite aluminum particles. All these experiments have been directed with an aim to find the burning rate for aluminum. Figure 2.1 below summarizes different techniques adopted in literature to calculate the ignition point of aluminum under different physical and experimental conditions.

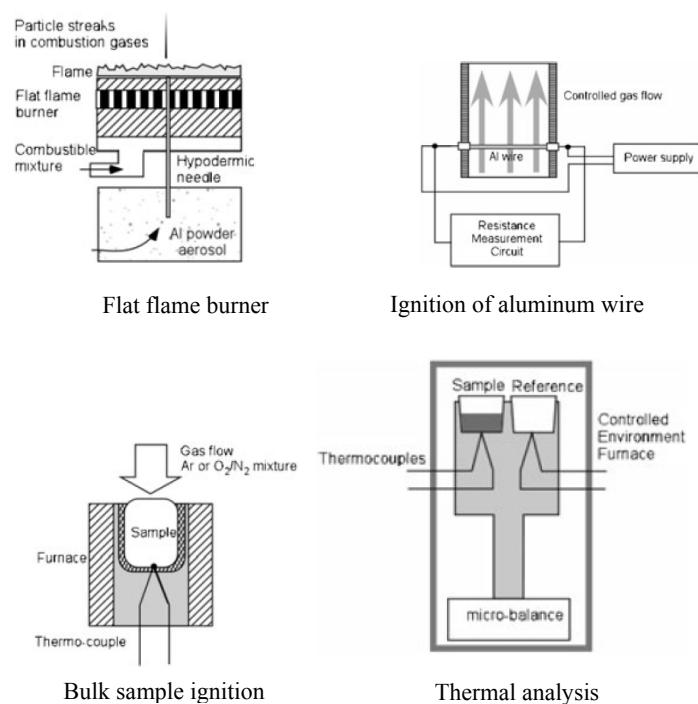


Figure 2.1: Different techniques adopted to calculate ignition point of aluminum (Trunov et al., 2005b)

Table 2.5: Existing experimental data on aluminum at micro-scale

Author	Date	$D_0(\mu\text{m})$	Ambient		Gas Concentrations (%)						
			$T_0(\text{K})$	P(atm)	H <sub>2</sub> O	O <sub>2</sub>	CO <sub>2</sub>	CO	N <sub>2</sub>	Ar	HCl
Friedman & Macek (Friedman and Maeck, 1962; Friedman and Maeck, 1963)	1962-63	15-67	2510	1	17-18	5-6	12-14	0	63-65	0	0
Davis (Davis, 1963)	1963	60-96	2200-3200	1-204	0.5-50	0-27	9-50	9-41	9-41	0	0-21
Macek (Maeck, 1967)	1967	32-49	2500	1	0-17	8-16	13-43	0	40-58	0	0
Hartman (Hartman, 1971)	1971	23-94	3000-3189	25.5	27-34	0-4	17-23	9-30	13-20	0	0-8

Wilson & Williams (Wilson and Williams, 1971)	1971	24-74	298	2-5	0	10-30	0	0	70-90	90	0
Prentice (Prentice, 1974)	1974	250-400	298	1	0-3	15-75	0-50	0	0-80	0-85	0
Turns & Wong (Wong and Turns, 1987; Turns et al., 1987)	1987	300-760	1809-1827	1	29-31	10-25	27-30	15-49	46-64	0	0
Roberts et al. (Roberts et al., 1993)	1993	20	2225-2775	1-34		99			1		
Marion (Marion and Gokalp, 1995; Marion and Gokalp, 1996)	1995	35-40	298	1-39	0	21	0	0	79	0	0
Olsen & Beckstead (Olsen and Beckstead, 1996)	1996	40-70	3000	1	66-89	11-16	0-18	0	0	0	0
Melcher et al. (Melcher et al., 1999)	1999	106	2300	13-22	38-41	0-11	12-16	2-9	10	0	18
Dreizin (Dreizin, 1999; Dreizin, 1999b)	1999	90-200	298	1		5-100			5-90	0-95	
Zenin (Zenin et al., 1999; Zenin et al., 2000)	2000	185-500	298	1-40	0	0-20	0-100	0	0-80	0-80	0

Table 2.5 summarizes existing experimental data at micro-scales. Davis (Davis, 1963) prepared ammonium per chlorate and para-formaldehyde propellants with less than 1% aluminum by mass. The propellants were ignited in a ‘bomb’ apparatus with pressures up to 200 atm. Using aluminum particles with initial diameters ranging from 53-103  $\mu m$ , an exponent of 1.8 for a burning time expression of  $\tau = CD^n$  was shown, where C is a constant depending on concentrations of various products in gas phase. An

increase in burning rate was also observed as pressure was increased from 20 to 70 atm. Davis also ignited aluminum particles with a carbon monoxide flame and observed a flame front several diameters larger than the particle size thus providing evidence for vapor phase diffusion.

Similar to Davis, Friedman and Macek (Friedman and Maeck, 1962; Friedman and Maeck, 1963), and Maeck (Maeck, 1967) also created aluminized propellant samples which burned with pressures ranging up to 135 atm. They noticed production of hollow spheres for burning at atmospheric pressures and provided some of the first reported burning time data for aluminum particle combustion. The experiments showed consistent fragmentation during vigorous burning in oxygen rich environments. In both the studies a fine oxide smoke and porous or hollow oxide spheres were formed.

Hartman (Hartman, 1971) chose particle distributions with mean diameters of 23, 54, and 94  $\mu m$ . In these experiments, modified double base propellants were used to provide a wider range of oxidizer environments in which aluminum could burn. For pressures of 19, 26 and 50 atm, he found pressure and environment dependence of burning rate similar to Davis. He also gave a pressure exponent of 0.4.

Wilson and Williams (Wilson and Williams, 1971) ignited single aluminum particles with a laser in argon and oxygen atmospheres. They found that argon suppressed oxide cap formation and without a cap the particles burn in accordance with vapor phase model, as suggested by Glassman.

Prentice et al. (Prentice, 1974) used lasers to ignite individual particles. In addition a Xenon flash tube was used to ignite small aluminum foils. Oxide caps did not

form in argon and oxygen environment, similar to observations made by Wilson and Williams.

Wong and Turns ([Wong and Turns, 1987](#); [Turns et al., 1987](#)) added aluminum powder to jet fuel (JP-10) to create slurry droplets with diameters ranging from 500 to 1100  $\mu m$ . Upon burnout of Jet fuel, the aluminum agglomerated forming particles of diameters 300-800  $\mu m$ . Using high speed cinematography, they observed smaller flame fronts for methane flame where water would be present, as compared to dry environment of carbon monoxide flame.

Robert et al. ([Roberts et al., 1993](#)) used a shock tube to ignite aluminum and its alloys with magnesium at pressures up to 34 atm in almost pure oxygen. Here, the researchers concluded that the burning time for aluminum was not a strong function of pressure although a slight decrease in burning time was noticed for an increase in pressure.

Marion et al. ([Marion and Gokalp, 1995](#); [Marion and Gokalp, 1996](#)) measured burning time of 40  $\mu m$  aluminum at pressures of 1 to 40 atm in air using laser for ignition. Burning times were observed to decrease slightly with pressure increasing from 1 to 4 MPa. They predicted a residual oxide particle approximately 70% the size of original aluminum particle, increasing slightly with pressure. With nitrogen/oxygen atmospheres, particles fragmented irrespective of the amount of water vapor present.

Olsen and Beckstead ([Olsen and Beckstead, 1996](#)) used a carbon monoxide/hydrogen flame to ignite aluminum particles one at a time. Particles ranging in size from 40-80  $\mu m$  were chosen under a microscope. They concluded that oxidizer

concentration has a strong effect on the particle's burning rate. They also found that burning rate exponent changed during the combustion history of particle, ranging from approximately two at ignition and decreasing towards one at burnout. They explained it on the basis of increasing fraction of aluminum oxide covering the molten aluminum sphere.

In addition to the above data, Price et al. (Price et al., 1966) performed a number of aluminum particle combustion experiments, many of them qualitative, but some of them quantitative. Their burners used hydrogen, carbon monoxide, and cyanogen combined with oxygen. Particles ranged in size from 30-400  $\mu\text{m}$ . Foelsche (Foelsche et al., 1998) used photodiodes to measure the burning time of a small cloud of aluminum powder (approx. 22  $\mu\text{m}$ ) inside a combustion bomb with pressure ranging from 38 to 145 atm. His data compared favorably well with Davis and others but showed a greater pressure dependency.

Dreizin and Trunov (Dreizin, 1999b) ignited 150 micron Aluminum droplets in air at room temperature, similar to Prentice's work. They reported a region of spherically symmetric burning, followed by two oscillatory regions, with particles giving off smoke jets and spiraling as shown in Figure 2.2. Dreizin has published a series of papers explaining this oscillatory phenomenon for micro-aluminum particle (Dreizin, 1995; Dreizin, 1996; Dreizin, 1999; Dreizin, 1999b; Dreizin, 2000; Dreizin, 2003). The explanation of asymmetric burning has been given on the basis of deposition of condensed phase on aluminum surface, extent of dissolution of oxygen at different places, and hence asymmetric vaporization rate of aluminum, based on thermodynamic

phase diagrams. It was also concluded that asymmetric burning is not due to convection or buoyancy.

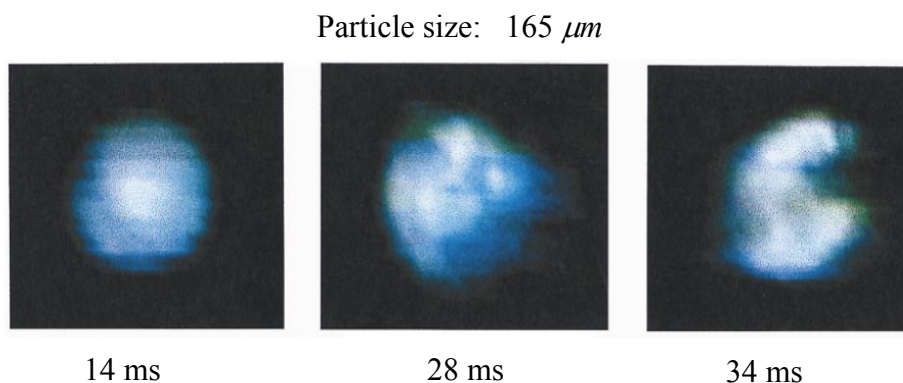


Figure 2.2: Sequence of true color image showing evolution of aluminum particle flame structure upon transition from spherically symmetric to non-symmetric combustion regime (Dreizin, 1999b)

Orlandi made an interesting observation (Orlandi and Fabignon, 2000) that as  $X_{\text{O}_2}$  increases, the gaseous phase reaction approaches aluminum liquid surface. The concentration of aluminum vapor at the surface is a function of surface temperature. When the ejection velocity at aluminum surface is small, the vaporization rate depends on the concentration gradient in the gas phase. As  $X_{\text{O}_2}$  increases, diffusion rate of oxygen increases. Corresponding to this the vaporization rate of aluminum increases. To meet this increase in vaporization rate, the flame region naturally approaches the liquid surface to steepen the concentration gradient of aluminum in the gas phase near surface. As temperature increases the flame zone moves away from the surface and also results in an increase in the burning rate due to an increased vaporization rate.

Most of the work for aluminum has so far been done at micro-scale where aluminum unlike other particles, like boron or magnesium, burns with a detached flame.



## 2.3 Thermodynamics and Transport Properties

The transport phenomenon has been explained by Jeurgens et al. (Jeurgens et al., 1999; Jeurgens et al., 2000; Jeurgens et al., 2000b; Jeurgens et al., 2002; Jeurgens et al., 2002b; Jeurgens et al., 2002c) in terms of aluminum cation motion through the amorphous film and inward diffusion of oxygen along the grain boundaries in crystalline films. An explanation is also given regarding the growth kinetics and mechanisms of thin aluminum-oxide layer on a bare Al substrate in the temperature range of 373-773 K. The concepts of limiting oxide thickness at temperatures less than 573 K and slower oxidation stage at temperatures above 573 K can contribute to the development of theory of heterogeneous oxidation of aluminum nano and micro- sized particles.

Unlike micron-sized particles, the oxidation of a nanoparticle is speculated to be more of a surface phenomenon. This involves collision of oxygen molecules with the surface of particle and transport of oxygen through the oxide shell that is being formed as the reaction progresses. As a result, the diffusion properties of Al and O through oxide layer are also needed. A survey was done to obtain the diffusion coefficient of various species in the oxide layer as a function of temperature. Gall et al. (Gall et al., 1995) have obtained the expressions for diffusion coefficients of Al and O in alumina but in the temperature range of 1700-2000 K. Further experimental/numerical work needs to be done to get the variation of these coefficients over the whole temperature range of concern for use in theory or simulations.

## 2.4 Burning Rate

The aluminum combustion is assumed to follow a  $d^n$  law. This exponent lies between 1 and 2. As discussed before, the characteristic burning time follows  $d^1$  law and is inversely proportional to pressure under kinetically controlled mechanism. It is independent of pressure, following a  $d^2$  law in a diffusion controlled mechanism. Typically for aluminum, the values lie between 1.5~1.8. Beckstead et al. have (Beckstead, 2002) proposed an equation that can be used to estimate the burning times of aluminum particles based on a compilation of data from various sources.

$$t_b = \frac{aD^n}{X_{eff}P^{0.1}T_0^{0.2}} \quad (2.8)$$

where  $X_{eff} = C_{O_2} + 0.6C_{H_2O} + 0.22C_{CO_2}$ ,  $a = 41$  for  $n = 1.5$ , and  $a = 136$  for  $n = 1.8$ . Here  $p$  is the pressure in atm,  $T$  the temperature in K,  $D$  the diameter in  $\mu m$ , and  $t$  the time in ms. The formula for  $X_{eff}$  was suggested by Brooks to consider the relative effectiveness of various oxidizers based on experiments.

For experimental studies at micro scales, the main reason for a value of exponent between 1 and 2 was attributed to the fact that the droplet does not regress uniformly. There is an inherent assumption in the diffusion controlled model that the spherical droplet is regressing uniformly. Secondly, it is assumed that the particle burns out to a diameter of zero, which in practice is not consistent with experimental observations. Burning time should decrease with a decrease in the oxidizer concentration because in a diffusion flame, the concentration gradient is the principle driving force for the flame and so higher concentrations should result in shorter burning times.

Changes in the ambient temperature have very little effect on the burning time and the flame can be seen as a thermal barrier that protects the droplet from ambient conditions. Flame is closer to the surface with an increase in pressure. Reduction in the droplet diameter leads to thickening of the flame and increased vaporization mass flow rate.

## **2.5 Theoretical Modeling at Micro Scales**

Combustion of metals involves the study of chemical and physical processes simultaneously occurring in three phases i.e. solid, liquid and gas. The assumption of spherical symmetry simplifies the complexity for the problem and as a result the combustion can be viewed as a one-dimensional system, allowing full chemical kinetics and transport processes. To study this complex phenomenon of metal combustion, gas phase and condensed phase can be modeled and validated separately. After accommodating the interfacial surface processes through sub models, the full particle combustion can then be simulated as shown in Figure 2.3

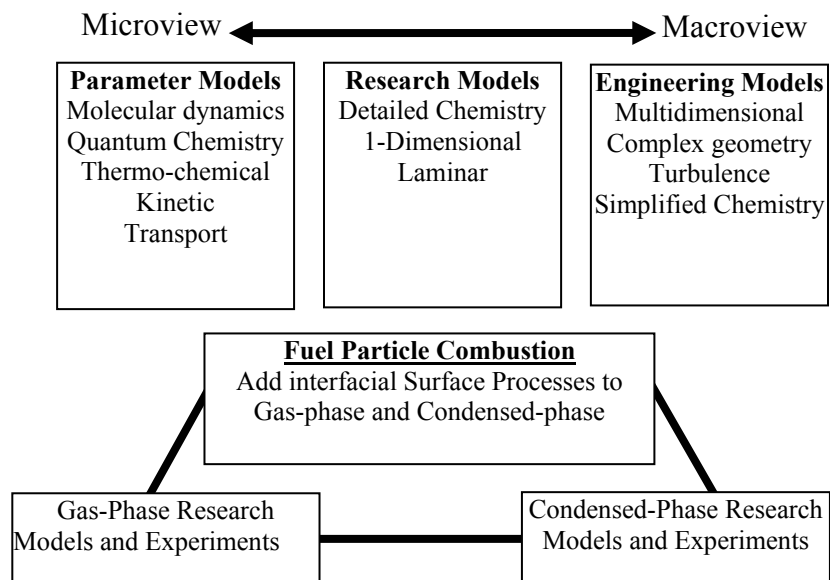


Figure 2.3: Modeling in Combustion Science

Several analytical and numerical models have been developed to gain an in-depth understanding of aluminum particle combustion. Table 2.6 shows the comparison between different models introduced and unique contributions of each model (Brooks and Beckstead, 1995).

Table 2.6: Existing numerical models for micro-scale aluminum combustion (Brooks and Beckstead, 1995)

Model	Analytical Solution	Diffusion through condensate	Flame temperature = f(oxide condensation)	Product condensation on surface	Condensed buildup on surface	Extended condensation zone	Kinetics of Al+CO <sub>2</sub>	Variable transport properties	Multiple oxidizers	Flame temperature = f(oxidizers)	Radiation effects	Convective effects
Brzustowski (Brzustowski and Glassman, 1964)	•	•	•								•	
Law (Law, 1973)	•		•	•								
Law (Law and Williams, 1974)	•		•	•		•						
King (King, 1977)							•					

Micheli (Micheli and Schmidt, 1977)		•	•					•	•	•		
Kudryavtsev (Kudryavtsev et al., 1979)	•	•				•						•
Gremyachkin (Gremyachkin et al., 1979)	•											•
Turns and Wong (Turns et al., 1987)	•		•	•	•					•		
Bhatia and Sirignano (Bhatia and Sirignano, 1993)	•		•	•						•		
Brooks (Brooks and Beckstead, 1991)	•		•	•	•			•	•	•	•	•

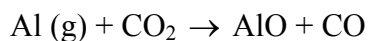
Very early phenomenological models by Glassman (Glassman, 1977) and Brzustowski (Brzustowski and Glassman, 1964) have been based on hydrocarbon droplet combustion for volatile metals. They assumed vapor phase diffusion flame. The model takes into account infinitely fast flame sheet, with fuel and oxidizer reacting in stoichiometric proportions. Diffusion processes were assumed to limit the rate of combustion. The maximum gas phase temperature was constrained to the decomposition temperature of metal oxide.

To include the effects of accumulation of oxide and surface condensation, models have been proposed by Law (1973), Williams (1974), King (1978), Brooks and Beckstead (1995), and Marion et al. (1996). Law allowed for diffusion of dissociated product species like AlO, Al<sub>2</sub>O from the flame sheet to the particle surface. He later included an extended oxide condensation zone which was found to be important for low temperature surroundings. Law's combustion model accurately predicts the vapor phase diffusion flame and surface formation of aluminum oxide due to diffusion of sub oxides

from the flame. Assumptions include pseudo steady state burning, spherical symmetry, negligible viscous forces, isobaric conditions, infinitely thin flame zone, Fick's and Fourier's laws, and burning aluminum particles at their boiling points.

Brooks and Beckstead (Brooks and Beckstead, 1991) accounted for accumulation of surface oxide as an inhibition to the surface processes. The aluminum burning-rate constant has been found to be a strong function of the oxidizer. Burning was also found to be a strong function of oxidizer concentration and particle size (Brooks and Beckstead, 1995). The transport properties are calculated by using a weighing factor in this model. In order to account for change in combustion rate, due to surface coverage, the burning rate is proportioned according to the surface area covered by oxide to a surface area if no oxide is present. Oxide cap has been approximated as fractions of attached spheres. The growth rates are related to volumetric changes which in turn are converted to change in surface area. However, the size of the oxide cap is to be calculated using the density corresponding to ambient conditions. Transport property evaluation and diffusion parameters are found to have a large influence on the burning rate.

King (King, 1977) relaxed the assumption that the kinetics of the reaction was infinite. He predicted a value of 1.35-1.9 for the exponent  $n$  in burning rate law. King's numerical studies have indicated that combustion process may be partially kinetically controlled. He developed a numerical model using the rate data for the reaction:



Aluminum monoxide produced was permitted to react infinitely fast with liquid aluminum on the surface to form  $\text{Al}_2\text{O}$ . The location of aluminum oxide condensation is determined by specification of condensation temperature. The burning rate exponent was

predicted to range from 1.35 to 1.9. Models emphasizing convective effects have been published in Russian Literature (Kudryavtsev et al., 1979; Gremyachkin et al., 1979)

Bucher et al. (Bucher et al., 1998) have included a full detailed species transport and didn't invoke thin condensation sheet approximation. It was also assumed that the gas-phase kinetics between the particle surface and the flame are much faster as compared to the mass transport, thus a spatial local equilibrium exists. As a result, there is no need of kinetic parameters and the process is assumed to be diffusion controlled. However, the transient processes such as ignition, and extinction cannot be studied with this assumption. Assuming no buoyancy effects, no forced convection, no Dufoir effects, and negligible dissipation, a one dimensional model can be established for the particle combustion. Condensation process and growth of condensed phase have not been included in this model. They have only assumed vaporization of aluminum at the surface and radiation heat transfer has been neglected. A quasi steady model is taken into consideration where the particle radius is not allowed to regress. Differences were found between experimental and simulation results, due to absence of finite rate chemistry and treatment of  $\text{Al}_2\text{O}_3$  as a gas phase species.

Bhatia and Sirignano's (Bhatia and Sirignano, 1993) model is analogous to Law's model and also determines flame and surface temperature from thermodynamics and vapor pressure data. They also allow for transient heating of particle.

Beckstead et al. have formulated a comprehensive model for the burning behavior of spherical aluminum particles at several length scales and have proposed mechanisms of oxide lobe formation, particle regression rate, and ignition criteria. They have extended the Law's steady state aluminum combustion model to include the effects of

multiple oxidizers, oxide accumulation on the surface, and convection. Assumption of unity Lewis number is also relaxed by calculating the transport and thermodynamic properties internally.

A similar study of heterogeneous combustion has been done by King (1993), Li and Williams (1991), and Kuo (1996) but for boron particles. Detailed models for metal combustion are limited due to the lack of fundamental data on kinetic rates and transport properties in gas and condensed phases.

Barlett et al. (Bartlett et al., 2004) studied the combustion of aluminum particles in methane-oxygen flame and postulated that the combustion of aluminum particles was not necessarily controlled by a gas phase diffusion mechanism, but instead it was controlled by the diffusion of aluminum vapor through the oxide shell. This is very similar to what is observed at the nano scales.

## 2.6 Chemical Kinetics

Table 2.7 lists the chemical kinetic mechanisms for gas phase reactions of  $\text{Al}_2\text{O}_3$ . These have been collected from various sources and compiled together. For some reactions, there might be two kinetic expressions depending on the source.

Table 2.7: Reactions involved in aluminum combustion along with rate constants

No.	Reactions	A ( $\text{cm}^3/\text{mol-s}$ )	n	E (cal/mol)	
1	$\text{Al} + \text{O}_2 = \text{AlO} + \text{O}$	9.72E13	0.	159.95	Dr. Catorie (Catorie, 2004)
2	$\text{Al} + \text{O} + \text{M} = \text{AlO} + \text{M}$	3.0E17	-1.	0.	Dr. Catorie (Catorie, 2004) Kuo (Tatum and Kuo,



					2003)
3	$\text{AlO} + \text{O}_2 = \text{OAlO} + \text{O}$	4.62E14	0.	19885.9	Dr. Catorie (Catorie, 2004)
4	$\text{Al}_2\text{O}_3 = \text{AlOAlO} + \text{O}$	3.0E15	0.	97649.99	Dr. Catorie (Catorie, 2004)
5	$\text{Al}_2\text{O}_3 = \text{OAlO} + \text{AlO}$	3.0E15	0.	126999.89	Dr. Catorie (Catorie, 2004)
6	$\text{AlOAlO} = \text{AlO} + \text{AlO}$	1.0E15	0.	117900	Dr. Catorie (Catorie, 2004)
7	$\text{AlOAlO} = \text{Al} + \text{OAlO}$	1.0E15	0.	148900	Dr. Catorie (Catorie, 2004)
8	$\text{AlOAlO} = \text{AlOAl} + \text{O}$	1.0E15	0.	104249.94	Dr. Catorie (Catorie, 2004)
9	$\text{OAlO} = \text{AlO} + \text{O}$	1.0E15	0.	88549.86	Dr. Catorie (Catorie, 2004)
10	$\text{AlOAl} = \text{AlO} + \text{Al}$	1.0E15	0.	133199.94	Dr. Catorie (Catorie, 2004)
11	$\text{AlOH} = \text{AlO} + \text{H}$	1.0E15	0.	114700	Dr. Catorie (Catorie, 2004)
12	$\text{AlOH} = \text{Al} + \text{OH}$	1.0E15	0.	132000	Dr. Catorie (Catorie, 2004)
13	$\text{Al} + \text{H}_2\text{O} = \text{H} + \text{AlOH}$	1.14E12	0.	879.8	Dr. Catorie (Catorie, 2004)
14	$\text{Al} + \text{H}_2\text{O} = \text{AlO} + \text{H}_2$	9.6E13	0.	5700	Dr. Catorie (Catorie, 2004)
15	$\text{AlO} + \text{CO}_2 = \text{OAlO} + \text{CO}$	1.50E10	0.	-794.8	Dr. Catorie (Catorie, 2004)
16	$\text{Al} + \text{CO}_2 = \text{AlO} + \text{CO}$	1.74E14	0.	6400	Dr. Catorie (Catorie, 2004)
17	$\text{AlH}_3 + \text{H} = \text{AlH}_2 + \text{H}_2$	4.75E09	0.	0.0	Dr. Catorie (Catorie, 2004)
18	$\text{AlH}_2(+\text{M}) = \text{AlH} + \text{H}(+\text{M})$	1.46E15	0.	46448.	Dr. Catorie (Catorie, 2004)
	LOW	9.68E14	0.	39664.	
	TROE/5.1 21.6 493. 942./				
19	$\text{AlH}_3(+\text{M}) = \text{AlH} + \text{H}_2(+\text{M})$	1.48E13	0.	61112.	Dr. Catorie (Catorie, 2004)
	LOW	1.01E15	0.	53826.	
	TROE/0.06 885. 552. 3807/				
20	$\text{Al} + \text{H} + \text{M} = \text{AlH} + \text{M}$	1.6E17	-0.34	0.	Dr. Catorie (Catorie, 2004)
21	$\text{AlH} + \text{H} = \text{Al} + \text{H}_2$	1.0E13	0.	0.	Dr. Catorie (Catorie, 2004)
22	$\text{AlH}_2 + \text{H} = \text{AlH} + \text{H}_2$	2.0E13	0.	0.	Dr. Catorie (Catorie, 2004)
23	$\text{Al} = \text{Al}(\text{l})$	1.0E14	0.	0.	Ying et al. (Huang et al., 2005)
24	$\text{Al}_2\text{O}_3 = \text{Al}_2\text{O}_3(\text{l})$	1.0E14	0.	0.	Ying et al. (Huang et al., 2005)
25	$\text{Al}(\text{g}) + \text{H}_2\text{O}(\text{g}) = \text{AlO} + \text{H}_2$	60.5	3.59	525	NISTDatabase (Mallard et al., 1994) (298-1174 K)
26	$\text{Al}(\text{g}) + \text{CO}_2 = \text{AlO} + \text{CO}$	6.75E15	0.	-10689	NISTDatabase (Mallard et al., 1994) (1500-1880 K)
27	$\text{Al}(\text{g}) + \text{O}_2 = \text{AlO} + \text{O}$	2E13	0.	0.	NISTDatabase (Mallard et al., 1994) (300-2000 K)
28	$\text{Al}(\text{g}) + \text{HCl} = \text{AlCl} + \text{H}$	3.3E11	0.	-3925	NISTDatabase (Mallard et al., 1994) (1000-4000 K)

29	$\text{Al(l)}=\text{Al(g)}$				Beckstead et al. (Widener et al., 1999) Kuo (Tatum and Kuo, 2003) (Surface Reaction)
30	$\text{Al(l)}+\text{AlO(g)}=\text{Al}_2\text{O(g)}$  $\text{Al(l)}+\text{AlO(g)}=\text{Al}_2\text{O(g)}$				Beckstead et al. (Widener et al., 1999) Kuo (Tatum and Kuo, 2003) (Surface Reaction)
31	$\text{Al(g)}+\text{O}_2=\text{AlO}+\text{O}$	9.76E13	0.	-80	Bucher et al. (Bucher et al., 1996) (Gas Phase) Kuo (Tatum and Kuo, 2003)
32	$\text{AlO}+\text{O}_2=\text{OAlO}+\text{O}$	4.63E14	0.	-10008	Bucher et al. (Bucher et al., 1996) (Gas Phase) Kuo (Tatum and Kuo, 2003) (Surface Reaction)
33	$\text{O}+\text{O}+\text{M}=\text{O}_2+\text{M}$	6.17E15	-0.5	0.	Bucher et al. (Bucher et al., 1996) (Gas Phase) Kuo (Tatum and Kuo, 2003)
34	$\text{Al}_2\text{O}_3=2\text{AlO}+1/2\text{O}_2$				Bucher et al. (Bucher et al., 1996) (Dissociation)
35	$2\text{AlO}+1/2\text{O}_2=\text{Al}_2\text{O}_3(\text{l})$ $2\text{AlO}+\text{CO}_2=\text{Al}_2\text{O}_3(\text{l})+\text{CO}$ $2\text{AlO}+\text{H}_2\text{O}=\text{Al}_2\text{O}_3(\text{l})+\text{H}_2$				Bucher et al. (Bucher et al., 1996) (Condensation, High rate constants)
36	$\text{Al}_2\text{O}+\text{O}_2=\text{Al}_2\text{O}_3(\text{l})$ $\text{Al}_2\text{O}+2\text{CO}_2=\text{Al}_2\text{O}_3(\text{l})+2\text{CO}$ $\text{Al}_2\text{O}+2\text{H}_2\text{O}=\text{Al}_2\text{O}_3(\text{l})+2\text{H}_2$				Bucher et al. (Bucher et al., 1996) (Condensation)
37	$\text{AlO}_2+\text{AlO}_2=\text{Al}_2\text{O}_3(\text{l})+1/2\text{O}_2$				Bucher et al. (Bucher et al., 1996) (Condensation)
38	$\text{Al}+\text{CO}_2=\text{AlO}+\text{CO}$	1.5E11(A1) 8.4E14(A2) 2.5E-13(A1) 1.4E-9(A2)	0.5(n1) 0.5(n2) 0.5(n1) 0.5(n2)	-2050(E1) -27800(E2) -1030(E1) -14000(E2)	Fontijn&Felder (Fontijn and Felder, 1977) (300-1900K) Kuo (Tatum and Kuo, 2003)
39	$\text{Al}+\text{H}_2\text{O}=\text{AlO}+\text{H}_2$	1.1E12(A1) 9.6E13(A2) 1.9E-12(A1) 1.6E-10(A2)	0.(n1) 0.(n2) 0.(n1) 0. (n2)	880(E1) 570(E2) 443(E1) 2868(E2)	McClean et al.(McClean et al., 1993) (298-1174K) Kuo (Tatum and Kuo, 2003)
40	$\text{Al}_2\text{O}=\text{Al}+\text{AlO}$				Kuo (Tatum and Kuo, 2003)
41	$\text{Al}_2\text{O}_2=\text{AlO}+\text{AlO}$				Kuo (Tatum and Kuo, 2003)
42	$\text{H}+\text{H}+\text{M}=\text{H}_2+\text{M}$				Orlandi et al. (Orlandi and Fabignon, 2000)
43	$\text{O}_2+\text{M}=\text{O}+\text{O}+\text{M}$				Orlandi et al. (Orlandi and Fabignon, 2000)
44	$\text{H}+\text{OH}+\text{M}=\text{H}_2\text{O}+\text{M}$				Orlandi et al. (Orlandi and Fabignon, 2000)
45	$\text{O}+\text{N}_2=\text{NO}+\text{O}$	1.8E12	0.	-38345	Kuo (Tatum and Kuo, 2003)
46	$\text{N}+\text{O}_2=\text{NO}+\text{O}$	6.4E9	0.	-3125	Kuo (Tatum and Kuo, 2003)
47	$2\text{AlO}=\text{AlO}_2+\text{Al}$				Kuo (Tatum and Kuo, 2003)
48	$\text{Al}_2\text{O}+\text{O}=2\text{AlO}$				Kuo (Tatum and Kuo, 2003)
49	$\text{Al}_2\text{O}+\text{O}_2=\text{AlO}+\text{AlO}_2$				Kuo (Tatum and Kuo, 2003)

50	$2\text{AlO}+\text{M}=\text{Al}_2\text{O}_2+\text{M}$				Kuo (Tatum and Kuo, 2003)
51	$\text{Al}+\text{AlO}_2+\text{M}=\text{Al}_2\text{O}_2+\text{M}$				Kuo (Tatum and Kuo, 2003)
52	$\text{O}+\text{Al}_2\text{O}+\text{M}=\text{Al}_2\text{O}_2+\text{M}$				Kuo (Tatum and Kuo, 2003)
53	$\text{Al}_2\text{O}+\text{O}_2=\text{Al}_2\text{O}_2+\text{O}$				Kuo (Tatum and Kuo, 2003)
54	$\text{AlO}+\text{Al}_2\text{O}=\text{Al}_2\text{O}_2+\text{Al}$				Kuo (Tatum and Kuo, 2003)

## 2.7 Summary and Conclusions

Micron-sized aluminum particles ignite at the melting point of oxide i.e. 2323 K. In metal combustion like aluminum there are gas phase reactions and also surface oxidation resulting in volatile and non volatile products which include oxide and sub oxide species. Micron-sized particle combustion is characterized by some well known features such as brightness oscillations, disruptive burning, burning droplet speed variations, oxygen build-up within the molten particle, micro-explosions, asymmetric combustion, and follows  $d^n$  burning rate law. The exponent typically lies between 1.5~2.0.

These unique characteristics, along with techniques for generation of aluminum particles, three stages of combustion, asymmetric burning, diffusion of ions through the layer, phase transformations, and burning data under different experimental conditions have been studied and discussed in detail.

Literature on combustion of aluminum indicates that ignition can take place via two potential pathways. One is the destruction of oxide layer due to cracking, and the other is self heating due to oxidizer diffusion through the oxide layer, and hence melting

of the layer. Various factors like the particle diameter, oxidizing species, pressure, and temperature affect the burning rate of the particle. It can be concluded that, the difference in the burning rate exponent among different researchers is as much due to varied data reduction techniques used, as it is due to the diverse physical conditions of each experiment. The oxygen concentration has a very pronounced effect on the burning rate. Higher the concentration of oxide, shorter is the burning time. This is expected because in the diffusion flame, concentration gradient is the principal driving force for the flame. Russian work suggests that pressure has very small effect on the burning rate, at least till 20 atm. The differential equation for diffusion contains the product of diffusivity and density. The product is almost independent of pressure and since diffusivity is proportional to a 1.65 power of temperature, it is slightly dependent on temperature (0.65 power). All these phenomena and physics at micro-scale are to be used to develop and extend the theory at nano scales. The explanation of asymmetric burning has been given on the basis of deposition of condensed phase on aluminum surface, extent of dissolution of oxygen at different places, and hence asymmetric vaporization rate of aluminum based on thermodynamic phase diagrams. It was also concluded that asymmetric burning is not due to convection or buoyancy.

## Chapter 3

### Nano Scale Aluminum Combustion

#### 3.1 Unique features at Nano Scales

Most of the work so far has been done at micro-scale where aluminum unlike other particles, like boron or magnesium, burns with a detached flame. However, at nano scales again depending on the mode of ignition, it is possible that the oxide layer does not melt. In such a case, the ignition will be heterogeneous till all the molten aluminum is consumed. At micro-scales there is an issue of diffusion controlled or kinetically controlled burning. But at nano scales, if the rate limiting step is just diffusion through the oxide layer, then the whole process is always diffusion controlled. During direct heterogeneous oxidation at crack site, the process will be kinetically controlled due to low Damkohler numbers. Phenomena associated with detached flame like spinning of droplet, instabilities, etc. might not be observed at nano scales at all. After the ignition, the question of particle burning heterogeneously or with a detached flame is also to be answered. Nanoparticle oxidation is a very open ended research problem and in this chapter some key aspects and existing literature on nanoparticle burning will be discussed.

### 3.2 Oxide Thickness

The aluminum particle is covered with a layer of aluminum oxide. The oxide layer acts as a passivation layer and protects the aluminum particle from getting ignited. During ignition, this layer either cracks or melts and hence, the thickness is an important parameter. The layer has been observed to be of the order of 3~5 nm. In the case of nanoparticles the thickness of the layer is very important because it reduces the active aluminum content of the particle. Figure 3.1 shows the Scanning Electron Microscope (SEM) micrograph of Alex aluminum particles. The particle size ranges from 50 to 250 nm and the oxide layer thickness is around 3.1 nm.

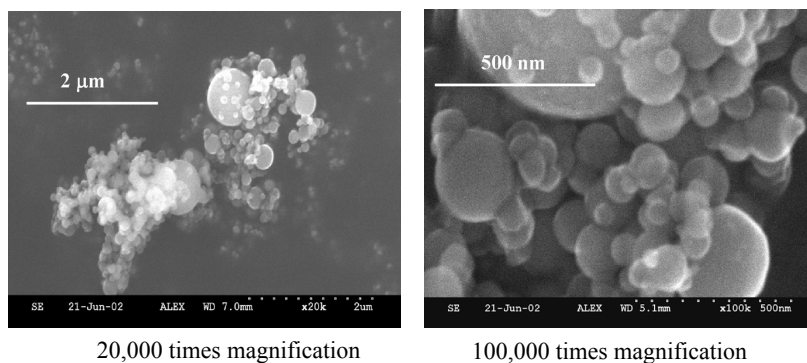


Figure 3.1: SEM micrograph of Alex Aluminum particles (Risha, 2005)

In later sections, an attempt has been made to explain and hence predict the thickness using thermodynamics. A lot of work has been done by Dreizin (Dreizin, 1995; Dreizin, 1996; Dreizin, 1999; Dreizin, 1999b; Dreizin, 2000; Dreizin, 2003) emphasizing the reactions and phase changes occurring within the burning metal in addition to those occurring on and above the metal surface. The explanation is given on the basis of Al-O binary phase diagrams. Gas dissolution within the burning metal, ensuing phase changes, and their effects on combustion are discussed. It also explains the transition from

spherically symmetric to non-symmetric combustion regime as discussed in Chapter 2. The familiar concept of phase-diagrams has been applied here to predict the initial thickness of passive oxide layer, which is about 3-5 nm.

For experimental work done at nano scales, mostly researchers have used particles of the range of 50-100 nm and hence have quoted a thickness of the order of 3-5 nm. In the experimental work done by Eisenreich et al. (Eisenreich et al., 2004), total increase in the mass of aluminum nanoparticles after oxidation was calculated. This data was used to obtain the fraction of aluminum particle unavailable for oxidation, which basically is the fraction of oxide layer. According to their analysis, a value of 0.2 was obtained. Moreover, the value of 0.2 is a bit over predicted because it has been obtained using only one type of sample which had a weight increase of 71%. With other samples, they obtained a weight increase of 85-88%, implying an averaged value 82.75%. This gives the fraction occupied by aluminum oxide as 0.12, it being in agreement with 0.13 (calculated in the present study using phase diagrams), assuming experimental uncertainties. This simple correlation using thermodynamics can be used to get a very good initial guess of the oxide thickness based on particle size. This will be discussed in detail in Chapter 9.

### 3.3 Literature Survey

Table 3.1 summarizes some key studies performed on nano-sized aluminum over a period of past few years.

Table 3.1: Existing data on aluminum at nano scales

Researchers/ Authors	Particle Size	Ambient Conditions	Experimental Set up	Comments/Summary
Eckert et al. (1992)	$< 100 \mu m$	Powders milled in argon, hydrogen and oxygen atmospheres	Ball milling used to synthesize particles, Contamination levels studied using EDX, WDX, X ray diffraction and TEM also used for analysis	Synthesis mechanisms, structure and melting behavior at nano scales studied
Dreizin et al. (1995-2003)	100-500 $\mu m$	Burned in air and oxygen environments	Aluminum droplets produced using GEMMED in free fall, emission measured using brightness pyrometer, quenched in Ar/He, wavelength pyrometer, Electron Probe micro analyzer, energy dispersive spectroscopy detector and a wavelength dispersive spectroscopy	Brightness oscillations, burning droplet speed variations, micro explosions, spinning smoke cloud shape, mini jets small secondary particle satellites observed at micro scales and explored the similar phenomena at nano scales
Jeurgens et al. (2000-2002)	aluminum substrates and alumina films	Vacuum, oxygen and air	Low temperature oxidation and structures of alumina studied using x ray photoelectron spectroscopy,	Investigated growth kinetics of alumina on aluminum substrates, structure of alumina films, movement of ions across the film
Assovski (2002)	50 nm - 3 $\mu m$	Combustion in $O_2$ and $CO_2+Ar$	Normal and low gravity experiments performed. SEM, TEM combined with X ray diagnostics used	Study of clusters and nano-agglomerates in aluminum droplet combustion
Brousseau et al. (2002)	100-200 nm	Cast cured plastic bonded explosives, TNT based melt cast and ammonium nitrate fuel oil formulations tested	Velocity of detonation measured using ionization probes. Heat of detonation measured using detonation bomb calorimeter	Detonation properties of aluminum studied and aluminum content was varied
Kwon et al. (2003)	100 nm	Superrfine powders in air	Powders produced by exploding heated wires, SEM, X ray diffraction, chemical analysis performed	Formation of AlN studied, combustion of aluminum in air, reaction mechanisms, and heat release studied
Eisenreich et al. (2004)	20-100 nm	Oxygen environment	Particles visualized using SEM, weight analysis using TGA,	Low temperature oxidation of particles studied in oxygen, oxidation occurs in two steps, kinetic parameters determined using TG curves
Risha et al. (2005)	5-8 $\mu m$ +100nm	Aluminum particles and air, dust concentration varied from 263-448 g/m <sup>3</sup>	Laminar flame speed calculation using Bunsen burner dust cloud apparatus, Energy dispersion spectroscopy performed	Laminar flame speed (~22 cm/s) independent of equivalence ratio, increases with introduction of $H_2$ ,
Meda et al. (2005)	0.17-50 $\mu m$	Aluminum used in AP/HTPB binder	Samples burned in nitrogen flushed window bomb to measure burning rates, XPS, XRD, SEM analyses done	Different propellant formulations investigated by varying aluminum content



Park et al. (2005)	19-150 nm	Particles oxidized in aerosol flow reactor at (25-1100 °C)	Aluminum particles produced using DC arc, Oxidation rate studied using single particle mass spectrometer	Size dependant diffusion rates and kinetic rate constants measured
Rai et al. (2005)	100 nm	Oxidation in air inside a tube furnace	Aluminum particles generated using DC arc discharge plasma method or laser ablation, Oxidation rate studied using single particle mass spectrometer	Phenomenological model developed to describe oxidation of aluminum nanoparticle based on free molecule formulation
Risha et al. (2006)	5-8 $\mu\text{m}$	Liquid water and steam	Bunsen burner dust cloud apparatus	Burning rates measurements, burning rate 8.6 cm/s, pressure exponent 0.47, lower flame temperature
Trunov et al. (2005-2006)	50 nm-10 $\mu\text{m}$	Oxygen, air	Thermal analysis, TGA, heating rates from 5-40 K/min	Focused on polymorphic phase transformations inside alumina and its role in ignition
Risha et al. (2007)	38-130 nm	Aluminum and water	Measurements of linear and mass burning rates as a function of pressure, mixture composition, particle size	Linear burning rate of 8.6 cm/s, mass burning rate per unit area increased from 1.0-5.8 for equivalence ratio of 0.5-1.25, inversely proportional to particle diameter

Nano-sized aluminum and other metallic particles can be extensively used in many propulsion and energy-conversion applications due to their unusual energetic properties, such as increased catalytic activity and higher reactivity. The application of nano aluminum particles for propulsive and energetic application has been explored in many studies (Ilyin et al., 2001; Kwon et al., 1996; Mench et al., 1998). Pivikina et al. (Pivkina et al., 2004) investigated the effects of nano-sized materials on combustion characteristics as compared to micro-sized particles in terms of heat release and mode of combustion. They introduced a new approach for production of nano-composites of some energetic materials like ammonium nitrate, RDX, and aluminum using vacuum co-deposition technique. Excess energy of surface atoms, and reduced activation energy values for chemical reactions contributed to extraordinary chemical activity of nanoparticles. They also proposed a reduction in time scales of chemical reactions because of smaller distances. According to this study, the oxidation and other chemical

properties of aluminum were determined by cooperative effects arising in Al/polymer. Figure 3.2 shows the TEM of Al nanoparticles within Al/PPX (poly-para xylene) composite.

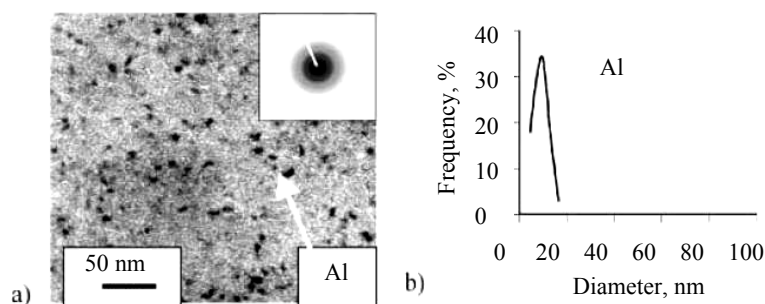


Figure 3.2: (a) TEM (light field) and SAED of aluminum nanoparticles within Al/PPK nano-composite (b) Al particle size distribution (Pivkina et al., 2004)

Meda et al. (Meda et al., 2005) also looked at the effect of adding nano-aluminum to solid rocket propellants. The aim of their work was to study different components (binder and aluminum powders) of solid propellants to improve performance. Figure 3.3 shows the effect of adding different size aluminum on the burning rate. The propellants were burned in a nitrogen flushed window bomb and were ignited by hot nickel chrome wire. The composition of the propellant was 68% ammonium perchlorate, 17% HTPB and 15% aluminum. The burning rate increased by an order of magnitude by reducing aluminum particle size.

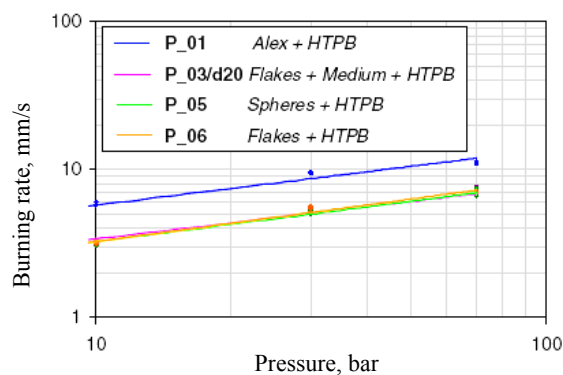


Figure 3.3: Burning rate vs. pressure for propellant with different Al size (Meda et al., 2005)

Brousseau et al. (Brousseau and Anderson, 2002) looked at the detonation properties of certain explosives after the addition of aluminum powder. No enhancement was found for plastic-bonded explosives. However, for nano-powder, the increase was significant. It was also concluded that nano-aluminum reacts faster than regular micron-sized particles in TNT/Al composites. Figure 3.4 shows the effect of nano-aluminum on detonation velocities for TNT.

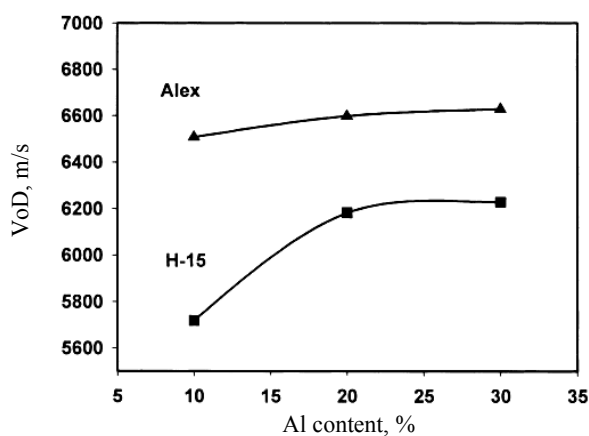


Figure 3.4: Effect of aluminum content on detonation velocity for TNT/Al mixes at a charge diameter of 25.4 mm (Brousseau and Anderson, 2002)

Assovskiy (Assovskiy, 2002) presented some experimental and theoretical evidences of the important role of clusters and nano-aggregates in the mechanism of aluminum droplet combustion. The experiments were used to determine peculiar clusters in case of high pressures. Figure 3.5 shows chains of clusters in the cloud of low gravity combustion, for a pressure of 60 atm in oxygen and argon environment.

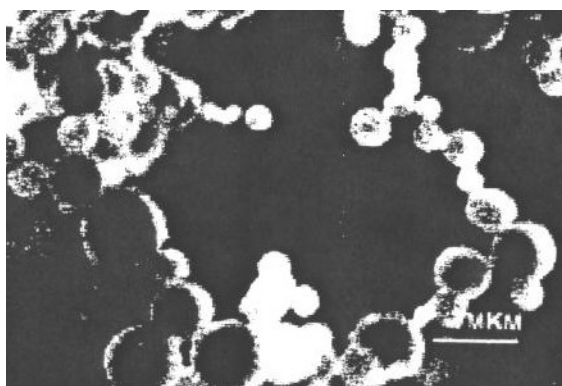


Figure 3.5: Chains of clusters in the cloud of low gravity combustion (60 atm,  $O_2 + Ar$ ) (Assovskiy, 2002)

Trunov et al. (Trunov et al., 2005) have used thermogravimetry to study oxidation of aluminum powder at elevated temperatures. The partially oxidized samples were recovered from selected intermediate temperatures and oxide phases present were analyzed by X-ray diffraction as shown in Figure 3.6. Corresponding to the peaks in diffraction pattern, presence of various oxides was observed. The aluminum powders were found to oxidize in five distinct stages: namely, growth of amorphous layer, transformation from amorphous to  $\gamma$  phase, growth of  $\gamma$  layer, transformation from  $\gamma$  to  $\alpha$ , and finally growth of  $\alpha$  layer.

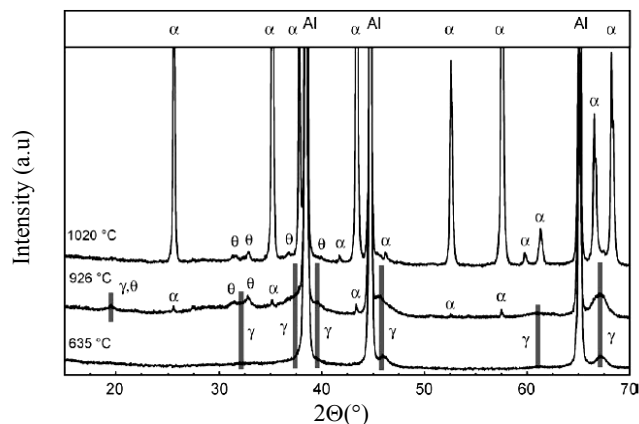


Figure 3.6: XRD patterns for partially oxidized aluminum powder samples (Trunov et al., 2005)

### 3.4 Existing Simplified Models

In addition to some key oxidation characteristics of nano-sized aluminum particles investigated by researchers, there also exist simplified numerical models to get some quantitative data. Based on heterogeneous combustion, models have been proposed by Rai et al. (Rai et al., 2005) and Park et al. (Park et al., 2005). Rai et al. have reported experimental results on the oxidation of a single aluminum nanoparticle using a quantitative single particle mass spectrometer. They also have developed a phenomenological model to describe the oxidation of aluminum nanoparticles based on free molecule formulation. It has been reiterated that burning of the nanoparticle will be different from micro-sized particle in a way that it will be heterogeneous and controlled by diffusion of oxygen through the oxide layer. Park et al. observed oxidation rates using single particle mass spectrometer. Aluminum particles were generated by DC arc

discharge or laser ablation. They performed size resolved kinetic measurements assuming diffusion through the oxide. Figure 3.7 shows the kinetic data obtained for aluminum nanoparticles using SPMS and TGS methods.

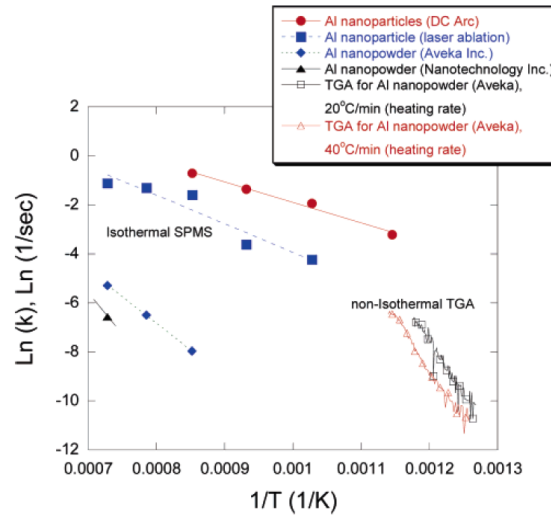


Figure 3.7: Comparison of kinetic data for aluminum nanoparticles obtained from SPMS and TGS methods;  $k$  is diffusion limited rate constant (Park et al., 2005)

Fedorov et al. (Fedorov and Kharlamova, 2003) have suggested a mathematical model for ignition of a single aluminum particle under steady state conditions based on the framework of Semenov's theory of thermal explosion. According to this model, the experimental dependences of ignition delay on radius and limiting ignition temperature are described. The growth of the oxidation layer according to this model has been described using the exponential oxidation law:

$$\frac{dh}{dt} = KC_{ox}^m e^{-E/RT} e^{-h/h_0} \quad (3.1)$$

where  $h$  is the oxide film thickness,  $h_0$  the thickness at initial time,  $E$  the activation energy,  $R$  the universal gas constant,  $K$  the pre-exponent in the oxidation law,  $C_{ox}$  the

oxidizer concentration near the particle surface, and  $m$  the order of the reaction. Another frequently used expression is:

$$\frac{dh}{dt} = \frac{KC_{ox}^m}{h^n} e^{-E/RT} \quad (3.2)$$

where  $n$  determines dependence of oxidation rate on film thickness. The constants were again determined from the curve fit and Figure 3.8 shows comparison between experimental and calculated dependences of ignition delay on particle diameter.

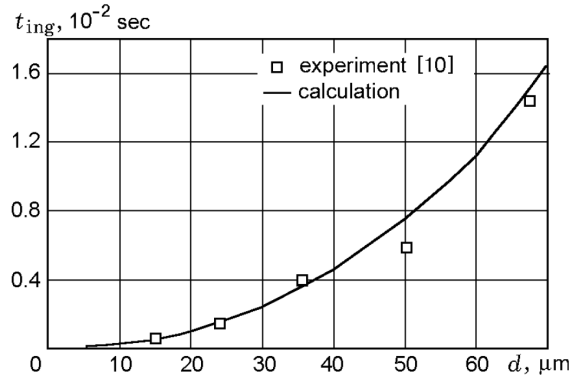


Figure 3.8: Experimental and calculated dependences of ignition delay on particle diameter (Fedorov and Kharlamova, 2003)

Alavi et al. (Alavi et al., 2005) have considered oxidation of aluminum particles from classical molecular dynamics point of view. Comparisons have been made between structures and charge distributions. They also observed the tendency towards fragmentation and oxide layer coating formation in their simulations. Figure 3.9 shows the evolution of oxidation for a nano-cluster of aluminum.

Campbell et al. investigated the oxidation of aluminum nano clusters based on dynamic charge transfer among atoms. The simulations were performed for a 20 nm aluminum particle composed of 252,158 atoms as shown in Figure 3.10. For oxidation

530,720 oxygen atoms distributed randomly outside aluminum were considered. Formation of a 4 nm thick oxide layer was simulated and structural and dynamic characteristics of the oxide layer were explored in the process (Campbell et al., 1999). The simulations consider oxygen in both O and O<sub>2</sub> forms (Campbell et al., 2005). Oxidation of aluminum single crystals was also studied by considering low index surfaces ((100), (110) and (111)) at room temperature. The mechanism of oxide growth was again explored and it was found that the growth kinetics is independent of crystallographic orientation (Hasnaoui et al., 2005). The group performs multimillion atom molecular dynamics simulations of nanostructures on parallel computers (Vashishta et al., 2003).

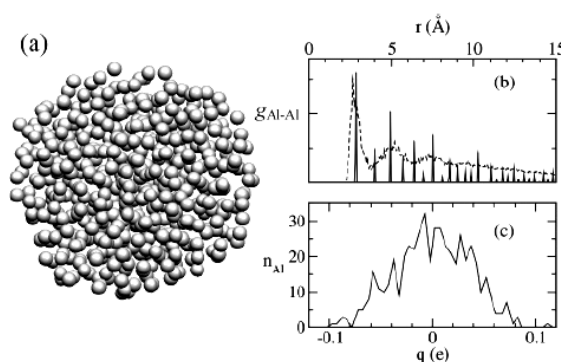


Figure 3.9: (a) Snapshot of structure of pure aluminum nanoparticle at 500 K (b) Radial distribution function for nanoparticle (c) Charge distribution for aluminum particle from Streitz-Mintmire potential (Alavi et al., 2005)



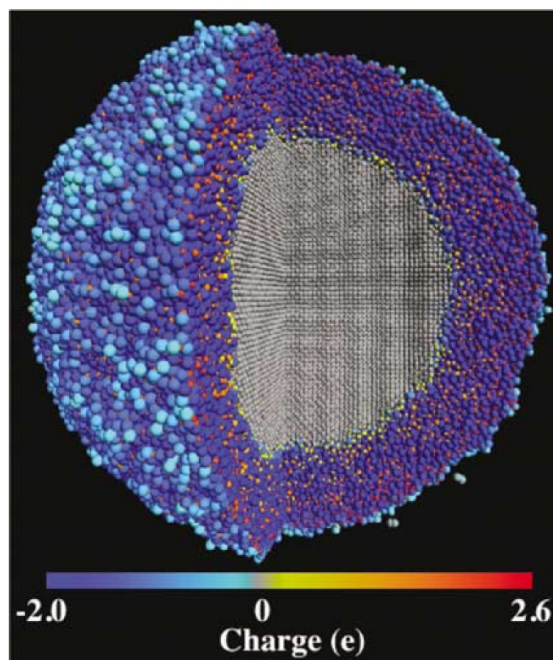


Figure 3.10: A 20 nm aluminum particle with 4 nm oxide thickness

At nano scales, pyrophoricity also becomes an issue. Glassman et al. (Glassman et al., 1992) have discussed the concept of pyrophoricity in the context with metal ignition. The study has been applied to finely powdered metals with no protective oxide coating. A metal is considered pyrophoric when, in its nascent stage, it is small enough that initial oxide coat which forms due to heterogeneous reactions with air under ambient conditions generates sufficient heat to vaporize the remaining metal. For a thickness of  $25\text{ \AA}$ , a particle of diameter 25 nm should be pyrophoric.

Eisenreich et al. (Eisenreich et al., 2004) have investigated the low temperature oxidation of Al particles. The oxidation of Al-particles down to nano scales was investigated by TG, SEM and in-situ X-ray diffraction. They have proposed that the oxidation occurs in two steps. The first step is the building up of a layer of 6 to 10 nm

thickness, where the reaction is dominated by chemical kinetics. The second step combines diffusion and chemical reaction, and proceeds slowly. The kinetic parameters are obtained using experimental results while fitting it to TG-Curves. The X-ray diffraction shows that a particle smaller than  $1\ \mu\text{m}$  builds  $\gamma\text{-Al}_2\text{O}_3$  and  $\theta\text{-Al}_2\text{O}_3$  which later transforms to  $\alpha\text{-Al}_2\text{O}_3$ . The study primarily used Alex (electro-exploded aluminum). Figure 3.11 shown below shows SEM images of nano-aluminum obtained in the study.

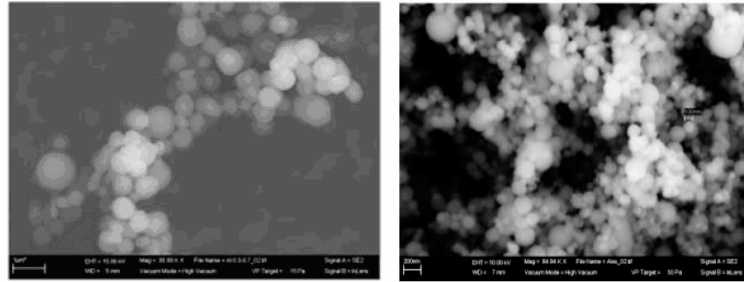


Figure 3.11: SEM images of Al-1 and Alex (Eisenreich et al., 2004)

The expressions for conversion of diffusing oxygen were given by

$$\frac{dn_o}{dt} \propto -4\pi R_K^2 k(T) c_{O,K} \quad k(T) = Z_K e^{-E_K/RT} \quad (3.3)$$

$$\frac{dn_o}{dt} \propto -4\pi R_K^2 D \left( \frac{dc_o}{dr} \right)_{r=R_K} \quad D(T) = Z_D e^{-E_D/RT} \quad (3.4)$$

where,  $n_o$  is the oxygen mole number,  $R_K$  the reaction front,  $c$  the concentration,  $Z_K$ ,  $E_K$  the frequency factor and activation energy of chemical reaction, and  $Z_D$ ,  $E_D$  are the frequency factor and activation energy of diffusion respectively. The authors conclude that over-simplification limits the applicability and there is significant mismatch between experimental results and calculated values.

Risha et al. recently performed an experimental investigation to determine laminar flame speeds of micron and nano-sized aluminum particle-laden aerosols using Bunsen burner type dust cloud apparatus (Risha et al., 2005). The particles of size 5-8 microns and 100 nm were considered. The measured flame speeds were independent of the equivalence ratio because of the independence of flame temperature. The flame speed increased with increase in oxygen concentration. The effect of addition of species like hydrogen that enhanced thermal properties also increased the flame speed. The ignition of nano-sized particles at low temperatures was supported by this study from the observation that the addition of nano-sized particles resulted in smaller cone size and less luminosity. The thickness of oxide layer of 21 nm was however, much larger than the values reported in literature (2-5 nm).

With renewed interest in under water aluminum combustion, experiments were conducted to study the effect of liquid and gas phases of water as an oxidizer on both micron and nano-sized aluminum particles. The flame temperature was lower than aluminum air or aluminum oxygen flames. Using volume optical pressure vessel, burning rates of nano aluminum and liquid water were measured. Burning rate of 8.6 cm/s and corresponding mass burning rate of 6.1 g/cm<sup>2</sup>s was observed. The pressure exponent was 0.47 and is independent of the equivalence ratio. The results were opposite to that by Ivanov et al. reporting an increase in pressure exponent due to an increase in concentration of water. The major difference between the results was the use of gelling agent used in the experiments conducted by Ivanov et al. As compared to the aluminum air case this involves heterogeneous combustion, with flame temperatures lower than aluminum vaporization temperature and close to melting point of the oxide. The work

was continued to perform linear and mass burning rate measurements of quasi-homogeneous mixtures of aluminum and liquid water as a function of pressure, mixture composition, and particle size.

Study of combustion of nano-sized aluminum particles with various oxidizers in a well-characterized laminar particle laden flow is also done through numerical and theoretical approaches. Particles are treated as large molecules in the limiting case in such a study. The particle laden flow is modeled as a one-dimensional, laminar, steady flow of premixed gas mixture and flame structure is investigated (Huang et al., 2005). In the molecular limit, the numerical results indicate that the flame speeds of an aluminum mixture with air are significantly higher than that with  $H_2O$ , mainly due to the greater reaction rate of Al with  $O_2$  versus  $H_2O$ . The kinetic bottleneck results from the  $Al_2O_3$  formation, in which O atoms play an influential role, in the aluminum-steam system. For micro-sized particles, the theoretical analysis shows that the aluminum-steam flame speed is slightly larger than that of an aluminum-air mixture. Flame propagation in a bimodal nano and micro-sized aluminum particle mixture with air is studied in a separate study (Huang et al., 2006; Huang et al., 2007). For a mono-dispersed particle laden flow, the flame speed increases with increasing particle concentration under fuel-lean conditions, but with decreasing particle size. A companion numerical model, which treats very fine aluminum particles as large molecules, is developed to obtain the flame speed at the molecular limit. For a bimodal particle laden flow, the flame structure may display either an overlapping or a separated configuration, depending on the combustion properties of aluminum particles at different scales. At low percentages of nanoparticles in the fuel formulation, the flame exhibits a separated spatial structure with a wider flame

regime. At a higher loading of nanoparticles, an overlapping flame configuration is observed. Ying et al. also proposed a burning rate correlations based on data fit for nano-sized aluminum particles.

$$\tau_b = \frac{d^{0.3}}{C_2 e^{-E_b/R_u T} X_{eff}} \quad (3.5)$$

where  $d$  is the particle diameter in  $cm$ ,  $C_2$  is  $5.5 \times 10^4$ ,  $E_b$  is 73.6 kJ/mol and  $R_u$  is the universal gas constant.

### 3.5 Comparison with Micro Scale Combustion

#### 3.5.1 Heterogeneous vs. Homogeneous Mechanism

At micro-scale, there are different types of modes of ignition. One of the modes can be like that of magnesium. Magnesium has a melting point and boiling point of 923 K and 1363 K, respectively. The oxide has a melting point of 2915 K. Thus, as the temperature rises magnesium melts, boils and builds up the pressure in the un-molten oxide shell. Finally, the shell is shattered and particles do not burn with any surface or flame temperature. In the case of boron, the melting and boiling point exceeds that of the oxide. As the temperature increases, the oxide shell melts and then vaporizes. The vaporization of boron oxide coincides with the melting of boron and the oxidizer reacts heterogeneously at the surface. The flame temperature is limited to the boiling point of the oxide that is formed.

The melting point and boiling point of aluminum are 933 and 2791 K, respectively. For the oxide, the melting and boiling points are 2327 and 4000 K. As the temperature rises, the aluminum melts first, then oxide melts and coalesces allowing the Al vapor to diffuse to a gas phase flame, and the particle ignites. Thus, aluminum burns in a gas phase reaction where flame front is at a detached distance of 1.5-4.0 times the droplet radius from the droplet surface. The hot oxide products dissociate outward, and  $\text{Al}_2\text{O}_3$  condenses and forms a smoke cloud that emits thermal radiation at a temperature of 3800K. At nano scales, due to smaller length scales, the reactions are primarily heterogeneous at the surface of the particle. The particles have been observed to ignite close to the melting point of the aluminum core and the ignition point shows a large variation in values for different experimental studies. The whole particle is consumed by the time the boiling point of the aluminum is reached, due to heterogeneous reactions, with oxygen either diffusing through the layer or directly reacting at the surface.

### **3.5.2 Diffusion vs. Kinetically Controlled Mechanism**

Combustion of metal particles also involves chemical and transport time scales. These can be compared to further classify the mode of combustion mechanism. If the reaction rates are slow compared to the rates of mass and energy diffusion, the spatial non-uniformities can be eliminated and the process is kinetically controlled. But fast reaction chemistry leads to temperature and species spatial gradients which cause conduction and diffusion of heat and species respectively, leading to diffusion controlled mechanism.

To determine the dominant combustion mechanism (Yetter and Dryer, 2001) the Damkohler number,  $Da$ , for surface reaction is defined as:

$$Da = \frac{t_{b,diff}}{t_{b,kin}} = \frac{MW_p k P d_0 X_{o,\infty}}{4 \rho D \ln(1 + \nu Y_{o,\infty})} \quad (3.6)$$

This quantitative analysis shows that very small particles at low pressures generally burn under kinetically controlled conditions. Similarly, larger particles at high pressures with a very high probability will undergo a diffusion controlled mechanism. As a result, the characteristic burning time follows  $d^1$  law and is inversely proportional to pressure under kinetically controlled mechanism. It is independent of pressure, following a  $d^2$  law in a diffusion controlled mechanism.

At micro-scale, the aluminum droplet burning rate follows  $d^2$  law which theoretically implies diffusion controlled mechanism (Beckstead, 2002). It is also speculated that because of the geometry of nano-sized particles, the oxidizer species need not diffuse across a relatively large distance before reaching the particle surface. This results in significantly shorter diffusion times and could lead to a chemical-kinetic-controlled situation. Figure 3.12 shows experimentally observed burning time for aluminum as a function of particle diameter.

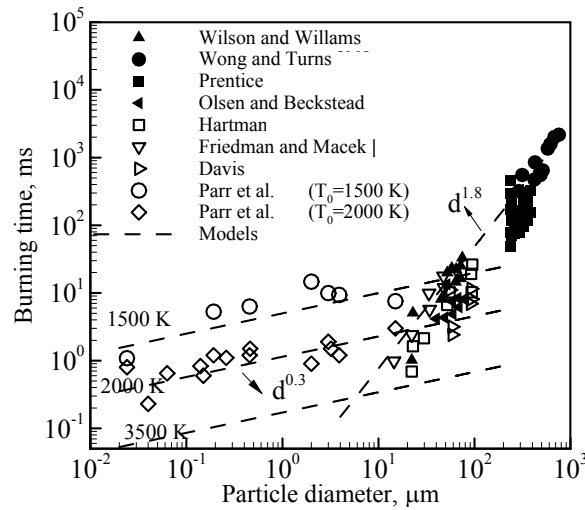


Figure 3.12: Experimentally observed aluminum particle burning time as a function of particle diameter (Huang et al., 2006)

### 3.5.3 Mode of Ignition

Figure 3.13 shows a compilation of results in literature showing the observed ignition temperature vs. particle diameter. It can be seen that the particles with size greater than approximately 1 micron show ignition at around 2327 K, which is the melting point of oxide layer. However for particle sizes below 1 microns, a wide range of observed ignition temperatures are observed down to as low as 940 K, which coincides with the melting point of aluminum core.



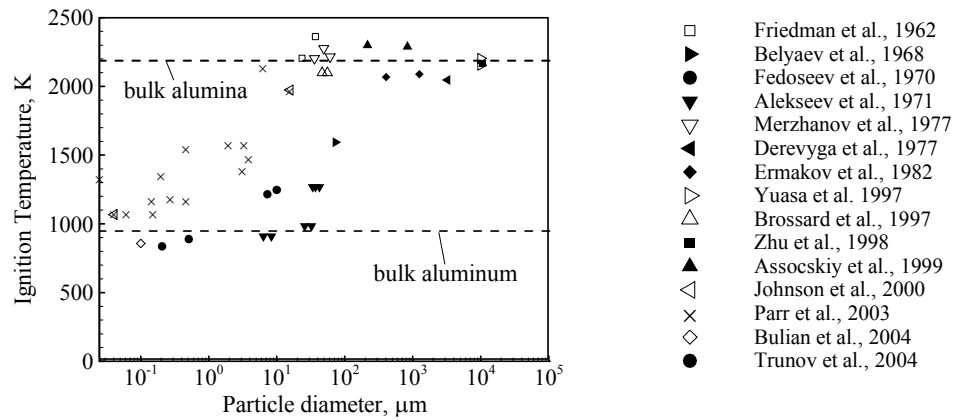


Figure 3.13: Ignition temperature of aluminum particle as function of particle diameter

### 3.5.3.1 Cracking vs. Melting of Oxide Layer

As mentioned before, there is a diversity of opinion regarding the ignition of aluminum particles. Researchers like Ermakov et al., Boiko et al., Lokenbakh et al., Boiko et al., Rozenband, and Vaganova (Lokenbakh et al., 1985; Boiko et al., 1989), all have concluded that ignition can occur due to the failure of oxide shell integrity and not necessarily melting. Ignition can occur by fracture of the oxide shell due to the mechanical stresses caused by thermal expansion.

From the experimental work done by other researchers at micro-scale, it is observed that the ignition temperature coincides with the melting point of Al<sub>2</sub>O<sub>3</sub> layer, i.e. ~2327K (Bucher et al., 2000). This is due to the impervious nature of aluminum oxide, which inhibits ignition.

However, at nano scales the particles get ignited at a much lower temperature which is near the melting point of aluminum, i.e. ~933K. Oxidation of alumina coated

nano-aluminum particles is presumably initiated by the melting of aluminum core and subsequent rupture of the oxide coating (Rai et al., 2004). This occurs when the layer is subjected to mechanical stresses caused by density differences due to rapid heating. This difference in the mode of ignition can be explained on the basis of simple heat transfer and solid mechanics analysis. The bulk modulus of Aluminum is 76 GPa and upon melting, the density changes from 2.7 g/cc to 2.4 g/cc (Rai et al., 2004). From solid mechanics, a pressure of 83340 atm is developed as a result of phase change. Comparing with ultimate tensile strength of oxide layer, it has been shown that the oxide layer cannot sustain this stress developed due to pressure inside the shell, formed by oxide layer. Chapter 8 and 9 discuss these in detail from numerical and theoretical viewpoint respectively.

### 3.5.3.2 Thermodynamic Explanation

Fourier number analysis further explains the whole phenomenon. As the particle size decreases to nano scales, this ratio increases and hence, the shell conducts heat easily. This eventually melts the aluminum core before the shell melts and results in rupture at around 933K. In the case of a micro-sized particle, the energy stored is more as compared to conduction. This high thermal resistance to conduction results in rapid heating and eventual melting of the shell before the solid core.

It has been reported recently that aluminum nanoparticles can ignite as measured by thermogravimetry (TGA) and differential thermal analysis (DTA), at a temperature of about 820 K which is close to the melting point of aluminum. Ashish et al. conducted

experiments on aluminum nanoparticles and found that for particles of 20-30 nm size with a coating of less than 3 nm, the ignition and rupture was found to occur at around 940 K which is again close to the melting point of aluminum. Such a speculation has been made because of high pressure developed inside the oxide shell which is dynamically unstable upon melting of the core. Moreover, because of higher curvature it is also under higher tension and should rupture with ease as compared to large particles. The reason for lower prediction of about 800 K by other researchers was attributed solely due to the technique used. Such dynamic thermal techniques such as thermogravimetry were thought to have high uncertainties associated with the heat and mass transfer (Ortega, 2001). A more sound explanation of cracking has been given on the basis of phase transformations of the oxide layer. According to Dreizin, the oxide layer transforms from amorphous to gamma and alpha phases. Because of the density differences during the transformation, the layer develops cracks which lead to direct oxidation and hence self heating. The current research also takes into account cracking but the cause of cracking is two fold and has been explored. All these have been explained in detail in Chapter 9 using a combined study of length and time scales involved.

### **3.6 Summary and Conclusions**

From the existing literature, it can be concluded that modeling for nano-aluminum is still in nascent stages. All the existing models agree that nano-aluminum particle burning is different from micro-size particle burning. In case of direct oxidation at the

nano scales, the process is kinetically controlled due to small diffusion scales involved. In case of heterogeneous oxidation through the oxide layer, the process is diffusion controlled due to slow diffusion of aluminum cations or oxygen anions. In case of heterogeneous oxidation through the direct attack of oxygen molecules, the process is kinetically controlled with low Damkohler numbers.

The ignition stage always starts with heterogeneous reactions and phase transformations and ignition is observed at relatively lower temperatures as compared to the micro-scale. Cracking in the oxide layer can occur either due to the phase transformation of aluminum oxide or thermal expansion caused by the melting of the solid core. This leads to ignition. Due to fast rate of heterogeneous reactions, the particles are totally consumed in a pure heterogeneous fashion till the time the boiling point of aluminum is reached and there is no detached flame front formation.

All the phenomenological models form an expression based on diffusion of oxygen and then calculate the model's parameters based on experimental data to match the observed phenomenon. There is still a lot of work to be done to explain the phenomena of agglomeration, pyrophoricity, ignition, and burning rate. A model/theory should be developed that accounts for all the issues of diffusion through the layer, pressure gradients, phase transformations, and cracking/melting of layer, rather than just calculating parameters based on experimental data.

## Chapter 4

### Nano Scale Simulations

#### 4.1 Molecular Dynamics Simulation Framework

Molecular Dynamics is a computer simulation technique that helps in predicting the time evolution of a system of interacting particles (atoms, molecules etc.). The macroscopic properties are then computed based on the aggregate particle positions and velocities. Molecular dynamics conceptually is the simplest example of stochastic/deterministic methods. A large number of atoms are chosen and assigned initial positions. Then, Newton's equations of motion are solved assuming a classical force function. The simulation is monitored and the desired properties are measured and averaged over time. First MD simulation was reported in 1957 by Alder and Wainwright investigating solid fluid transition for 500 particles at University of California Radiation Lab ([Alder and Wainwright, 1957](#)). Rahman ([Rahman, 1964](#)) in 1964 used L-J potential to simulate 864 Argon atoms at University of Illinois. Evans and Hoover also highlight in an article that Fermi began Molecular Dynamics studies with 16 particles ([Hoover, 1985](#)). Molecular Dynamics simulations gained popularity in material science in 1970s with applications in the areas of defects, interactions, fracture, melting, and alloys. It has also been used in quantum chemical models by chemists, for drug design, study of structure of membranes, dynamics of large molecules, protein folding in biochemistry, as a part of dynamical systems in theoretical physics, symplectic integrators & statistical mechanics

by mathematicians and to simulate correlated many body motions. It has also been used to support chemistry and biology research for many years.

Molecular dynamics simulations are valuable tools but they are computationally demanding. One of the requirements for efficient parallel operations is the even loading of the computations across all the processors. A three dimensional molecular dynamic code has been developed in this research for the transient studies. Before proceeding with the details of the work performed to investigate some of the issues at nano scales using molecular dynamics, a review of molecular dynamics is provided. This chapter covers fundamental concepts which were utilized to develop the simulation codes. More detailed molecular dynamic coding requirements and the implementation of parallel molecular dynamic algorithms is discussed in Section 4.7.

The length and time scales in the physical world can be divided into four major categories (Nano, Micro, Meso and Macro). Each category has its own set of applications and numerical tools to address the research issues. A detail is shown in Table 4.1.

Table 4.1: Various length and time scales in physical world (material science)

Scale	Length Scale	Time Scale	Applications	Models
Nano	$10^{-9}$ - $10^{-7}$ m	$10^{-14}$ - $10^{-10}$ s	Atomic level, dislocations, vacancies etc.	Microscopic/Atomistic Models: Classical Molecular Dynamics, Metropolis Monte Carlo, Ab Initio MD, Quantum Monte Carlo
Micro	$10^{-8}$ - $10^{-6}$ m	$10^{-11}$ - $10^{-8}$ s	Cracks, defect interactions, nucleation	Microscopic/Atomistic Models: Classical Molecular Dynamics, Metropolis Monte Carlo, Ab Initio MD, Quantum Monte Carlo
Meso	$10^{-7}$ - $10^{-4}$ m	$10^{-9}$ - $10^{-3}$ s	Grain size simulations, re-crystallization, fracture, collective dynamics of microstructure	Mesoscopic Models: Dislocation Dynamics, Cellular Automata, Kinetic Monte Carlo
Macro	$>10^{-3}$ m	$>10^{-3}$ s	Mechanics, structure etc.	Continuum models: Partial differential equations, Finite Difference Methods, FEM

Molecular dynamics simulations are used as tools for studies performed at nano and micro scales. However like any other numerical technique it has some constraints and limitations. In any MD simulation, the electrons are represented through a potential energy surface and that surface is approximated by an analytic function (discussed in detail in section 4.2). In classical description, the Schrödinger equation for nuclei is replaced with classical motion. The quantum effects can only be considered negligible if the de Broglie wavelength is much smaller than the inter particle distance. Inter atomic spacing is of the order of 1-3 Angstroms and De Broglie wavelength can be expressed using

$$\Lambda_{th} = \frac{h}{\sqrt{2\pi m k_B T}} \quad (4.1)$$

where,  $\Lambda_{th}$  is the wavelength,  $h$  the Planck's constant,  $m$  the mass of the atom,  $k_B$  the Boltzmann's constant, and  $T$  the temperature. Values for some of the elements at room temperature are

$$\Lambda_{th}^0 = 1 \text{ \AA for a H atom (300K)}$$

$$\Lambda_{th}^0 = 0.19 \text{ \AA for a Si atom (300K)}$$

$$\Lambda_{th}^0 = 0.16 \text{ \AA for an Ar atom (300K)}$$

$$\Lambda_{th}^0 = 0.07 \text{ \AA for a Au atom (300K)}$$

In terms of simulation time scale, the maximum time step is limited by the fastest motion in the system. The integration time step must also be smaller than the mean free time of atoms which can be approximated as

$$\frac{r_0}{\sqrt{3k_B T / m}} = 7.9 \times 10^{-13} s \quad (4.2)$$

where  $r_0$  is the mean free path and other symbols have their standard meanings. Since the vibrational frequencies of the order of 10 fs, the time step must be large enough to capture the effect. Due to the upper limit on time step, only few nanoseconds or picoseconds of simulation is possible because of the computational costs involved. Due to memory constraints also, it is not possible to simulate very large systems. Storing positions and velocities of atoms requires memory of the order of gigabytes. In any case, the length scale of the simulation must be large enough to simulate the physical domain without boundary conditions disrupting the behavior and must be limited by constraints involved due to computational costs.

## 4.2 Potential Functions

Intermolecular forces are computed based on intermolecular potential functions.

The classical conservation of energy using Newton's laws can be written as

$$\frac{1}{2}mv^2 + \frac{1}{2}kx^2 = E \quad (4.3)$$

which can be rewritten as

$$\frac{p^2}{2m} + \frac{1}{2}kx^2 = E \quad (4.4)$$

In making transition to a wave equation the physical variables take the form of “operators”

$$p \rightarrow \frac{\hbar}{i} \frac{\partial}{\partial x} \quad H \rightarrow -\frac{\hbar}{2m} \frac{\partial^2}{\partial x^2} + \frac{1}{2}kx^2 \quad (4.5)$$



and transforms to Schrödinger equation  $H\Psi = E\Psi$ . In order to approximate solutions to Schrödinger equation, Born-Oppenheimer Approximation is invoked (Born and Oppenheimer, 1927). According to this approximation, electronic and nuclear motion in molecules can be separated and electronic wave function depends upon nuclear positions but not on their velocities. This can be written as

$$\psi_{molecule}(\vec{r}_i, \vec{R}_i) = \psi_{electrons}(\vec{r}_i, \vec{R}_i) \psi_{nuclei}(\vec{R}_i) \quad (4.6)$$

where  $\psi$  is the wave function, and  $\vec{r}_i, \vec{R}_i$  are position vectors for electron and nuclei respectively. In general nuclear motion is so slower than electronic motion that the nuclei can be considered fixed and it sees a smeared out potential from the speedy electrons. The speed of electron and nucleus can be compared using the ratio of their masses

$$\frac{\omega_{el}}{\omega_n} \sim \sqrt{\frac{M}{m}} \sim 100 \quad (4.7)$$

The problem hence can be reformulated in terms of two separate Schrödinger equations. The equation of electronic problem gives the Eigen value of energy as a function of atomic positions, which depends parametrically on the coordinates of nuclei. This is called inter atomic potential.

In classical MD, the Schrödinger equation is replaced with the Newton equation if de Broglie thermal wavelength is small. The electrons are represented through a potential energy surface which is a solution of the electronic Schrödinger equation within Born-Oppenheimer approximation. However these surfaces are not available for most of the practical problems and approximation of actual solution of the Schrödinger equation through the potential function difficult. The potentials can have an assumed functional

form and then parameters can be optimized to reproduce by a set of experimental data e.g. structural (cohesive energies, elastic constants, elastic moduli), and thermodynamic (melting point, latent heat). These are called empirical functions like Lennard Jones. Sometimes, electronic wave function can be calculated and one can obtain semi-empirical potentials using some approximations e.g. Glue potentials. On the extreme side one can perform direct quantum mechanical calculations and these are called ab-initio MD simulations. Any potential to be used extensively should have three basic characteristics:

1. Accuracy- It should be able to reproduce properties as closely as possible
2. Transferability- It can be used to study properties for which it is not fit
3. Computational speed- it should be able to help in fast calculations

Potential function in most generalized form can be written as

$$U(\vec{r}_1, \vec{r}_2, \dots, \vec{r}_n) = \sum_i U_1(\vec{r}_i) + \sum_i \sum_{j>i} U_2(\vec{r}_i, \vec{r}_j) + \sum_i \sum_{j>i} \sum_{k>j} U_3(\vec{r}_i, \vec{r}_j, \vec{r}_k) + \dots \quad (4.8)$$

where  $U_1$  is called one body term, due to external field,  $U_2$  is called two body term and potential approximating till this point is called pair potential. This implies that interaction between a pair of atoms depends only on the spacing and not effected by other atoms.  $U_3$  is a three-body term and implies that other atoms also influence the interaction between two atoms. Thus potentials are either two body or many body. In literature aluminum has been modeled using different potentials. In this research, five potentials have been chosen on the basis of frequency of usage in literature. The potential functions considered are the two-body Lennard-Jones potential, many-body Glue potential, embedded atom potential, Sutton-Chen potential and Streitz-Mintmire potential (which also considers charges on atoms). Other than these five potentials, Vorter-Chen potentials ([Vorter and Chen, 1987](#)),

Finnis-Sinclair potential (Finnis and Sinclair, 1984) and Mei-Davenport potentials (Mei and Davenport, 1992) were also found to be commonly used in MD studies for aluminum. Vorter and Chen have been used in a numerical work done by Sebetci et al. to study clusters of aluminum (Sebetci and Guvenc, 2005). Sturgeon (Sturgeon and Laird, 2000) and Song (Song and Morris, 2003) worked on thermodynamic properties of aluminum using variations of the Mei and Davenport potential. Some potentials for aluminum are specifically developed to perform a particular numerical study. For example potentials were developed by Tomar (Tomar and Zhuo, 2006) and Johnson (Johnson, 1988; Johnson, 1989) to study mechanical strength for nano crystalline Al-Fe<sub>2</sub>O<sub>3</sub> system and alloy compositions respectively. Cleri-Rosato potential developed for transition metals and alloys has an analytical form that can be used to reproduce the thermal behavior of transition metals making use of a small set of adjustable parameters (Cleri and Rosato, 1993). Morse potential for diatomic molecules can be obtained from Schrödinger equation representing the motions of nuclei in a diatomic molecule (Morse, 1929) and Girifalco et al. describes in detail the constants used in this potential (Girifalco and Weizer, 1959). There also exist Pseudo potentials that can be used to calculate thermodynamic properties for metals like Li, Na, K and aluminum (Jones, 1973). Out of these five potentials, except the Lennard-Jones potential, all other four potentials are many-body potentials and only Streitz-Mintmire potential is capable of handling both aluminum and aluminum oxide using a method for charge equilibrium.

The Lennard-Jones potential is defined as

$$V_{LJ}(r) = 4\epsilon_{LJ} \left[ \left( \sigma_{LJ}/r \right)^{12} - \left( \sigma_{LJ}/r \right)^6 \right] \quad (4.9)$$

where  $\varepsilon_{LJ}$  and  $\sigma$  are the empirical parameters accounting for the depth of the potential well and the distance between two atoms at which the potential is zero, respectively. Their specific values of  $\varepsilon/k_B = 4551K$  and  $\sigma = 2.62\text{\AA}$  were provided by Halicioglu et al., based on the physical properties (such as lattice constants, heat capacity, and thermal expansion constant) for crystalline-state aluminum ( [Matyushov and Schmid, 1996](#); [Halicioglu and Pound, 1975](#)). Figure 4.1 shows the variation of the potential as a function of the distance between the atoms.

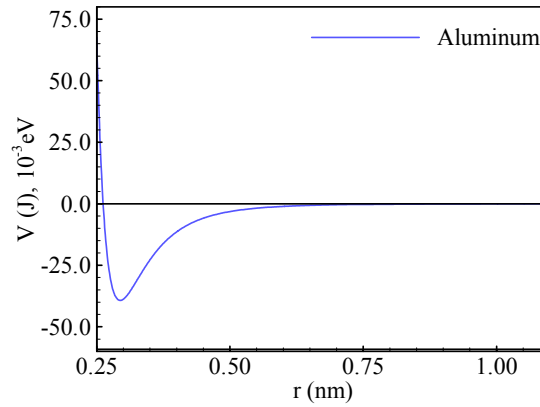


Figure 4.1: Lennard-Jones potential for aluminum

The Glue potential is defined by a pair potential,  $\phi(r)$ , an atomic density function,  $\rho(r)$ , and a Glue function,  $U(\rho)$ . Ercolessi et al. presented a scheme to extract numerically optimal inter-atomic Glue potentials from the results produced by first-principle calculations involving electronic structures ([Ercolessi and Adams, 1994](#)). The potential has also been used and well tested for other metals like gold (Au) ([Ercolessi and Tosatti, 1986](#); [Ercolessi et al., 1988](#)). The method is based on fitting the potential to ab initio atomic forces of diverse atomic configurations including surfaces, clusters, liquids,

and crystals at different temperatures. Figure 4.2 shows the three functions constituting the optimized Glue potential for aluminum. The functional form for the Glue potential is

$$V_{glue} = \frac{1}{2} \sum_{i,j} \varphi(r_{ij}) + \sum_i U \left( \sum_j \rho(r_{ij}) \right) \quad (4.10)$$

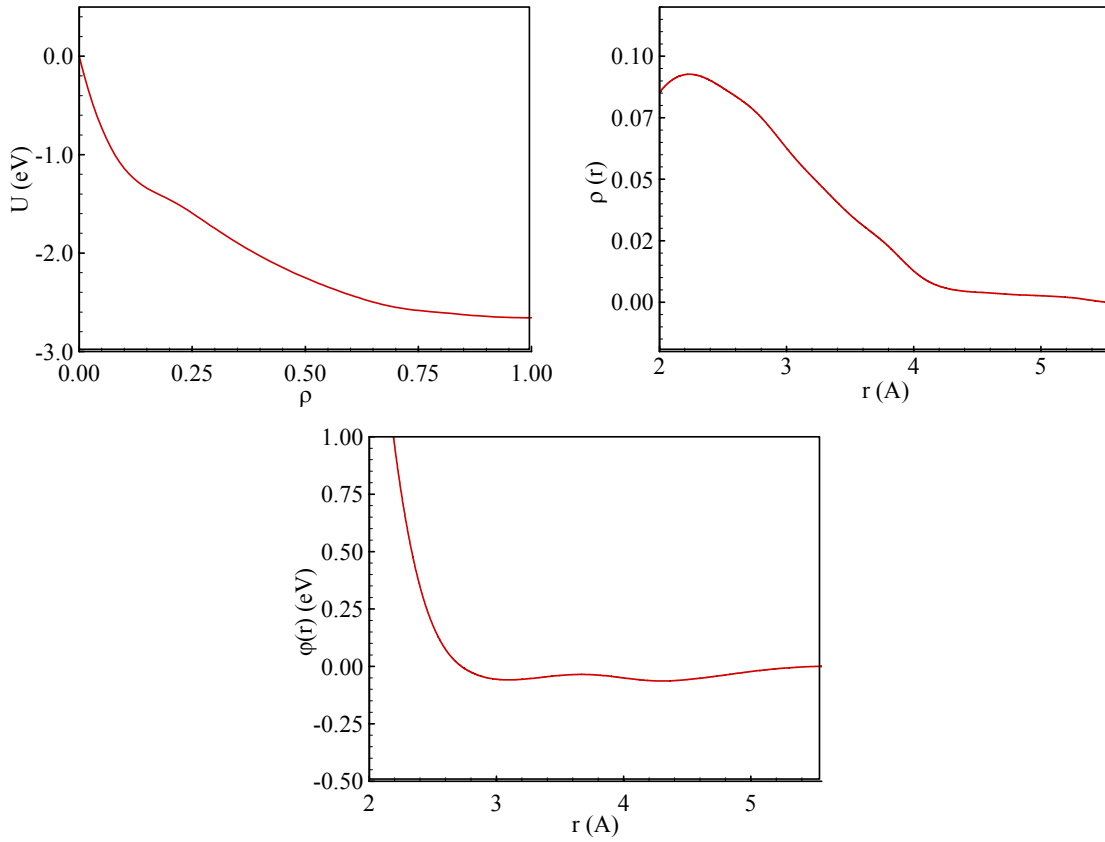


Figure 4.2: Glue potential for aluminum

The difference between the two-body Lennard-Jones and the many-body Glue potential can be analyzed by comparing Figs. 4.1 and 4.2. In the Lennard-Jones potential, the potential energy surface is represented using a single expression which captures both the attractive and repulsive forces between two atoms as a function of their separation. The Glue potential, however, consists of two functions. The first function  $\varphi(r_{ij})$  bears a

close resemblance to the Lennard-Jones potential and captures repulsive forces when the separation between atoms is small. The second part,  $U(\rho)$ , known as the Glue function, characterizes the effect of atomic density on the forces between two atoms. Since metals feature strong cohesive forces, many-body potentials can be more effective in predicting metal properties accurately than the Lennard-Jones potential. Glue potential falls under the category of a particular type of potentials called embedded atom potentials. These potentials are semi-empirical, many-atom and are used especially for metallic systems to investigate problems like point defects (Daw and Baskes, 1984), melting, thermal expansion (Foiles and Daw, 1998), other thermodynamic properties (Foiles and Adams, 1989), alloying (Foiles et al., 1986; Foiles and Daw, 1986b), grain boundary structure, dislocations, segregation (Foiles, 1985), fracture (Hoagland et al., 1990), surface structure, calculation of cohesive energies (Daw, 1989) etc. A comprehensive review of these has been provided by Daw et al. (Daw et al., 1993).

The Sutton-Chen potential extends the empirical N-body potentials, originally developed by Finnis and Sinclair for description of cohesion in metals (Joswig and Springborg, 2003), to include a long-range modification using the van der Waals tail (Sutton and Chen, 1990). This potential takes the form

$$V_{SC} = \varepsilon_{SC} \left[ \frac{1}{2} \sum_i \sum_{j \neq i} V(r_{ij}) - c \sum_i \sqrt{\rho_i} \right] \quad (4.11)$$

$$V(r_{ij}) = \left( a/r_{ij} \right)^7; \quad \rho_i = \sum_{j \neq i} \left( a/r_{ij} \right)^6$$

The constants  $\varepsilon$ ,  $c$  and  $a$  have values of  $0.033147 \text{ eV}$ ,  $16.399$ , and  $4.05 \text{ \AA}$  respectively. The functional form is similar to the Glue potential because of the presence

of pair potentials and atomic-density-dependent terms. Figure 4.3 shows the functions used in the description of Sutton-Chen Potential.

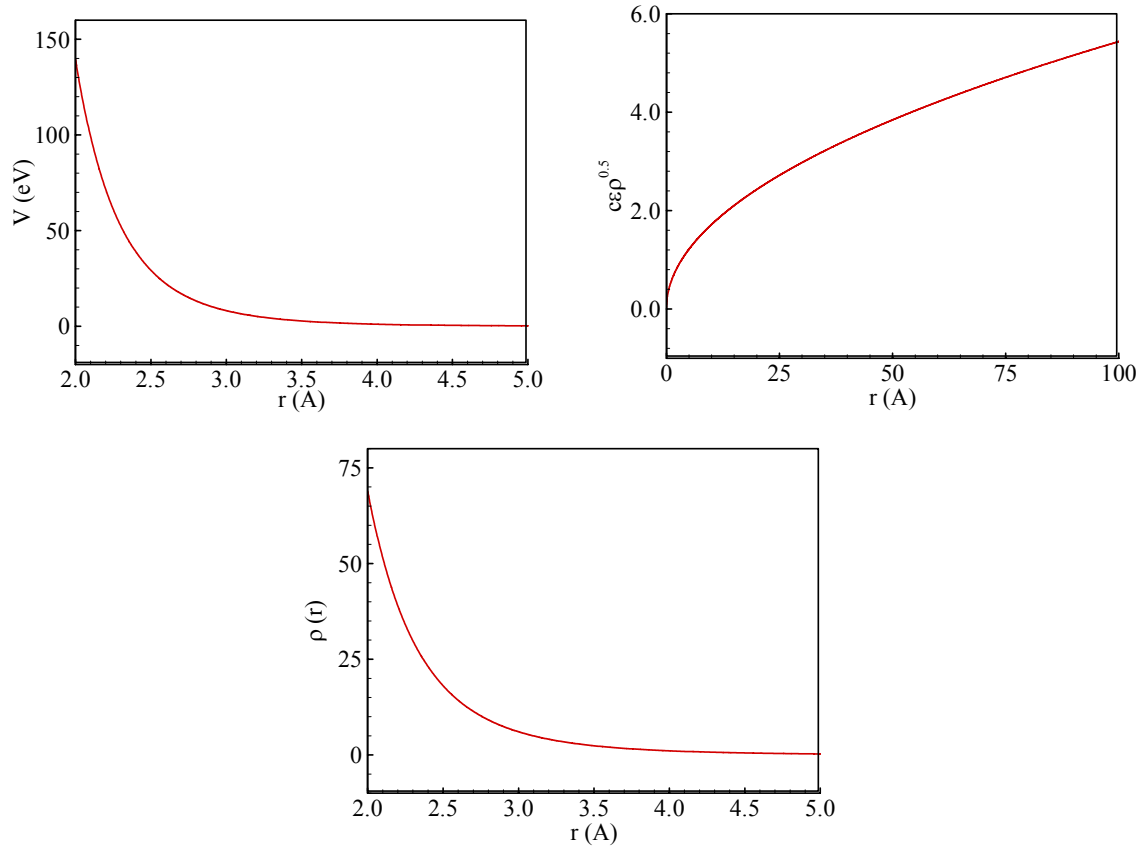


Figure 4.3: Sutton-Chen potential for aluminum

The Streitz-Mintmire potential has the same functional form as the Glue and Sutton-Chen potentials, but includes electrostatic forces due to the charges on atoms (Streitz and Mintmire, 1994; Keffer and Mintmire, 2000). It consists of two parts: an embedded-atom part and an electrostatic part accounting for charges on atoms. The embedded-atom potential used in the current study is a modification of the Streitz-Mintmire potential, consisting of only the embedded-atom part of the complete potential.

The electrostatic part and associated charge development are not considered. The embedded-atom part of the potential is defined as

$$\begin{aligned}
 V_{EAM} &= \sum_i F_i[\rho_i] + \sum_{i<j} \varphi_{ij}(r_{ij}) \\
 \rho_i(r) &= \sum_{i \neq j} \xi_j e^{-\beta_j(r_{ij}-r_j^*)} \\
 F_i(\rho_i) &= -A_i \sqrt{\frac{\rho_i}{\xi_i}} \\
 \varphi_{ij}(r) &= 2B_{ij} e^{\frac{\beta_{ij}}{2}(r-r_{ij}^*)} - C_{ij} [1 + \alpha(r-r_{ij}^*)] e^{-\alpha(r-r_{ij}^*)}
 \end{aligned} \tag{4.12}$$

where  $F_i(\rho_i)$  represents the energy required to embed atom  $i$  in electron density  $\rho_i$ , and  $\varphi_{ij}(r)$  the pair-wise interaction. The parameters used in the above functional forms for aluminum are

$$\begin{aligned}
 \xi_{Al} &= 0.147699; \xi_O = 1.0 \\
 r_{Al-Al}^* &= 3.365875 \text{ \AA}; r_{Al-O}^* = 2.358570 \text{ \AA}; r_{O-O}^* = 2.005092 \text{ \AA} \\
 \beta_{Al-Al} &= 2.017519 \text{ \AA}^{-1}; \beta_{Al-O} = 4.507976 \text{ \AA}^{-1}; \beta_{O-O} = 6.871329 \text{ \AA}^{-1} \\
 A_{Al} &= 0.763905 \text{ eV}; A_O = 2.116850 \text{ eV} \\
 B_{Al-Al} &= 0.075016 \text{ eV}; B_{Al-O} = 0.154548 \text{ eV}; B_{O-O} = 1.693145 \text{ eV} \\
 C_{Al-Al} &= 0.159472 \text{ eV}; C_{Al-O} = 0.094594 \text{ eV}; C_{O-O} = 1.865072 \text{ eV} \\
 \alpha_{Al-Al} &= 1.767488 \text{ \AA}^{-1}; \alpha_{Al-O} = 4.233670 \text{ \AA}^{-1}; \alpha_{O-O} = 8.389842 \text{ \AA}^{-1}
 \end{aligned} \tag{4.13}$$

The pair potential, as also seen in other potentials, becomes strongly repulsive at smaller distances. The functions used in embedded-atom part of Streitz-Mintmire potential are shown in Figure 4.4. The electrostatic part is given by

$$\begin{aligned}
 V_{ES} &= \sum_i v_i(q_i) + \frac{1}{2} v_{ij}(r_{ij}; q_i; q_j) \\
 v_i(q_i) &= v_i(0) + \chi_i^0 q_i + \frac{1}{2} J_i^0 q_i^2 \\
 v_{ij}(r_{ij}; q_i; q_j) &= \int d^3 r_1 \int d^3 r_2 \rho_i(r_1; q_i) \rho_j(r_2; q_j) / r_{12}
 \end{aligned} \tag{4.14}$$



where  $v_i(q_i)$  is the local atomic energy,  $\chi_i^0$  the electro negativity, and  $J_i^0$  the second derivative associated with the self-Coulomb repulsion.  $v_{ij}(r_{ij}; q_i; q_j)$  denotes the electrostatic interaction energy between atoms  $i$  and  $j$ . The charge density distribution,  $\rho_i(r; q_i)$  for a Slater 1s orbital about atom  $i$  for a charge  $q_i$ , is defined as

$$\rho_i(r; q_i) = Z_i \delta(r - r_i) + (q_i - Z_i) \left( \frac{\zeta_i^3}{\pi} \right) e^{-2\zeta_i |r - r_i|} \quad (4.15)$$

where  $\zeta_i$  is the decay length for the atomic orbital, and  $Z_i$  the effective core charge. Further simplification of the interaction energy using an analytical expression for Coulomb integrals (Roothan, 1951) yields

$$\begin{aligned} V_{ES} &= \sum_i q_i \left[ \chi_i^0 + \sum_{j \neq i} Z_j (\omega_i(r_{ij}) - v_{ij}(r_{ij})) \right] + \frac{1}{2} \sum_i q_i^2 J_i^0 + \frac{1}{2} \sum_{j \neq i} q_i q_j \left( \frac{1}{r_{ij}} + v_{ij}(r_{ij}) \right) \\ v_{ij}(r) &= -\frac{(1 - \kappa)^2}{4r} (2 + \kappa + \zeta_i r) e^{-2\zeta_i r} - \frac{(1 + \kappa)^2}{4r} (2 - \kappa + \zeta_j r) e^{-2\zeta_j r} \text{ for } \zeta_i \neq \zeta_j \\ v_{ij}(r) &= -\left\{ 1 + \frac{11}{8} \zeta_i r + \frac{3}{4} (\zeta_i r)^2 + \frac{1}{6} (\zeta_i r)^3 \right\} \frac{e^{-2\zeta_i r}}{r} \text{ for } \zeta_i = \zeta_j \\ \omega_j(r) &= -\frac{1 + \zeta_j r}{r} e^{-2\zeta_j r} \\ \kappa &= (\zeta_i^2 + \zeta_j^2) / (\zeta_i^2 - \zeta_j^2) \end{aligned} \quad (4.16)$$

The constants in the above integrals are given by

$$\begin{aligned} \chi_{Al}^0 &= 0.0 \text{ eV}; \chi_O^0 = 5.484763 \text{ eV} \\ Z_{Al} &= 0.746759; Z_O = 0.0 \\ J_{Al}^0 &= 10.328655 \text{ eV}; J_O^0 = 14.035715 \text{ eV} \\ \zeta_{Al} &= 0.968438 \text{ \AA}^{-1}; \zeta_O = 2.143957 \text{ \AA}^{-1} \end{aligned} \quad (4.17)$$

Using dynamic charge transfer, the charges  $q_i$  on each atom are calculated by minimizing the electrostatic energy (i.e., the electro negativity equalization condition) (Rappe and Goddard, 1991), subject to the charge neutrality constraint,  $\sum_i q_i = 0$ . This yields a set of linear equations

$$\sum_j V_{ij} s_j = -\chi_i; \sum_j V_{ij} t_j = -1 \quad (4.18)$$

and charges are obtained using  $\mu = \sum_i s_i / \sum_i t_i$ ;  $q_i = s_i - \mu t_i$ . Because of the functional form of the potential, and the way in which the constants are defined, the Streitz-Mintmire potential can be used for Al-O, O-O and Al-Al interactions

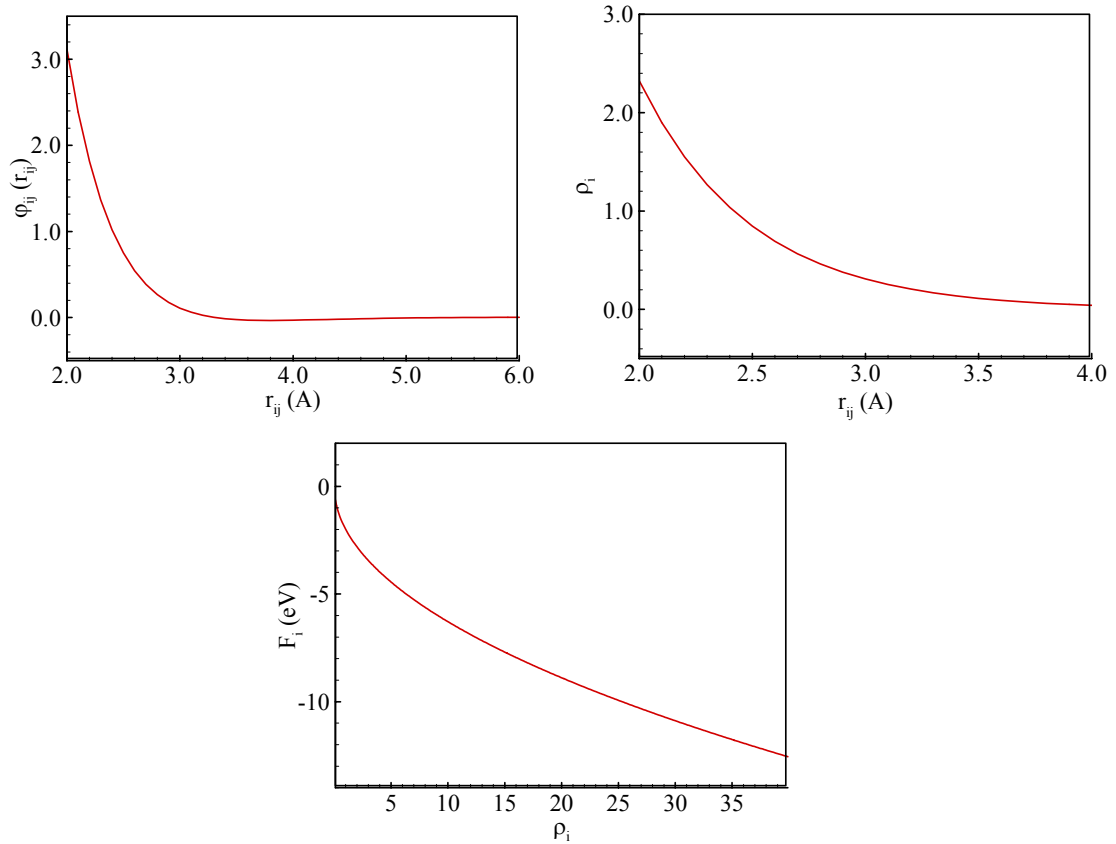


Figure 4.4: Streitz-Mintmire potential for aluminum

### 4.3 Equations of Motion

The displacement of each atom in a molecular dynamic simulation is based on Newtonian particle dynamics. The atomic accelerations are a direct function of inter-atomic forces. These forces are conservative, non-dissipative and are therefore computed as the negative gradient of the potential energy function between two atoms.

$$m_i \frac{d^2 \vec{r}_i}{dt^2} = \vec{F}_i = -\nabla_i U(r_i, v_i) \quad (4.19)$$

The problem is set up by defining initial conditions i.e. positions and velocities for all the atoms describing the system. Then the forces are calculated at the current time step. The solution stems from a common simplifying assumption for soft sphere interactions and the potentials are considered pair wise additive. This means the force on an atom due to interactions with surrounding neighbors can be computed by summing the interactions with each neighbor alone. In other words the force between two particles is considered independent of any other particles present. When pair wise additivity is assumed, the resultant force on atom  $i$  can be mathematically expressed as the sum of all the pair wise forces due to the surrounding  $j$  atoms

$$F_i = \sum_{\substack{j=1 \\ j \neq i}}^N F_{ij} \quad (4.20)$$

Utilizing the Newton's Law  $F = ma$  allows the computation of the acceleration of each particle directly from the force components. Assuming this acceleration is constant across a given time increment and is of the order of few femto-seconds, velocities and displacements can be computed using discretization in time.

$$\vec{r}_i(t_n) \rightarrow \vec{r}_i(t_{n+1}) \quad \vec{v}_i(t_n) \rightarrow \vec{v}_i(t_{n+1}) \quad (4.21)$$

Once the displacement is computed, the entire process of computing inter-atomic forces and the particle displacements can be repeated for the next time step as shown in the flow chart in Figure 4.5.

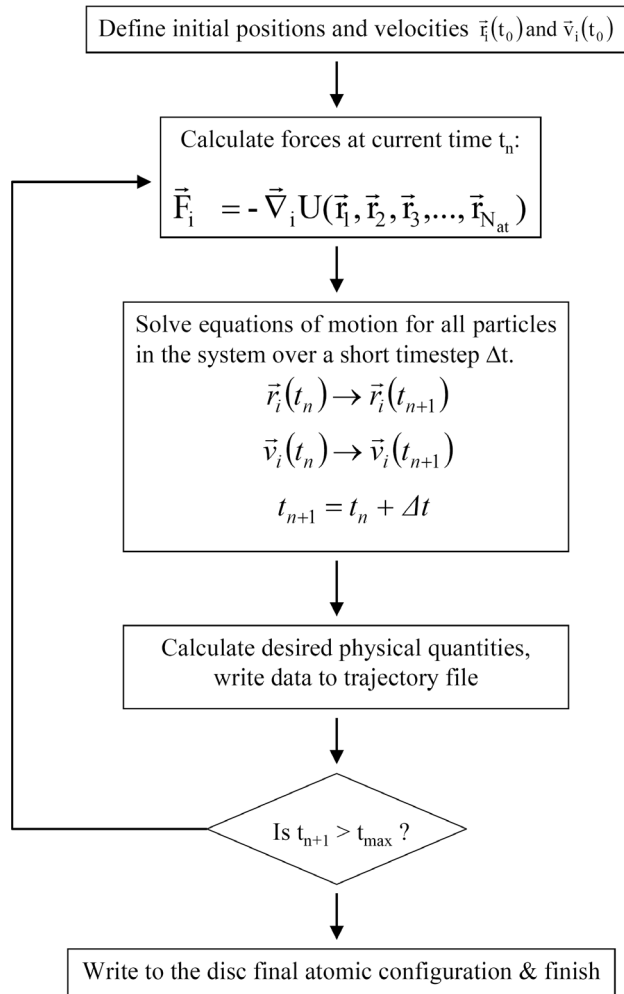


Figure 4.5: Flow chart of a typical MD simulation

So a deterministic model of molecular motions can be developed using these fairly straight forward equations. A simple time discretization can lead to instability in the code. So, special algorithms are used to update velocities and displacements at each time

step. The main algorithm of MD simulations is the integrator that calculates the trajectories with time using the equation of motion for interacting particles. There are four different types of numerical methods for integrating Newton's equations, such as Verlet, Velocity Verlet, leapfrog, and the predictor-corrector algorithm, that are used in the MD simulations discussed in this study (Allen & Tildesley, 1989; Frenkel & Smit, 2002).

#### Verlet Algorithm:

Verlet algorithm follows a simple discretization in time. After calculation of forces, the atomic positions are updated as a function of previous values, followed by calculation of velocities as a function of displacement over a period of time.

$$r(t + \delta t) = 2r(t) - r(t - \delta t) + \delta t^2 a(t) \quad (4.22)$$

$$v(t) = \frac{r(t + \delta t) - r(t - \delta t)}{2\delta t} \quad (4.23)$$

#### Velocity Verlet:

A related, and more commonly used, algorithm is the Velocity Verlet algorithm. This uses a similar approach but explicitly incorporates velocity. It can be shown that the error on the Velocity Verlet is of the same order as the basic Verlet. Velocity Verlet algorithm is less memory consuming, because it's not necessary to keep track of the velocity at every time step during the simulation. The standard implementation scheme of this algorithm is:

$$r(t + \delta t) = r(t) + \delta t v(t) + \frac{1}{2} \delta t^2 a(t) \quad (4.24)$$

$$v(t + \frac{1}{2} \delta t) = v(t) + \frac{1}{2} \delta t a(t) \quad (4.25)$$

$$v(t + \delta t) = v(t + \frac{1}{2} \delta t) + \frac{1}{2} \delta t a(t + \delta t) \quad (4.26)$$

$$v(t + \delta t) = v(t) + \frac{1}{2} \delta t [a(t) + a(t + \delta t)] \quad (4.27)$$

#### Leap frog algorithm:

Leap frog algorithm is a modified version of the Verlet algorithm as shown below

$$\begin{aligned} r(t + \delta t) &= r(t) + \delta t v(t + \frac{1}{2} \delta t) \\ v(t + \frac{1}{2} \delta t) &= v(t - \frac{1}{2} \delta t) + \delta t a(t) \\ v(t) &= \frac{1}{2} \left( v(t + \frac{1}{2} \delta t) + v(t - \frac{1}{2} \delta t) \right) \end{aligned} \quad (4.28)$$

It is computationally less expensive than the Predictor-Corrector approach, and requires less storage. This could be an important advantage in the case of large scale calculations. Moreover, the energy is conserved, even at large time steps. Therefore, the computation time could be greatly decreased when this algorithm is used. However, when more accurate velocities and positions are needed, another algorithm should be implemented, like the Predictor-Corrector algorithm.

#### Fifth order Predictor corrector:

The predictor-corrector algorithm is based on a Taylor expansion. If the position, velocity, acceleration and time derivative of the acceleration are known at time  $t$ , these quantities after time step can be predicted up to a certain order as shown in the following equations:

$$\begin{aligned}
r_i^p(t + \delta t) &= r_i(t) + v_i(t)\delta t + \frac{1}{2!}a_i(t)\delta t^2 + \frac{1}{3!}b_i(t)\delta t^3 + \frac{1}{4!}c_i(t)\delta t^4 + \frac{1}{5!}d_i(t)\delta t^5 \\
v_i^p(t + \delta t) &= v_i(t) + a_i(t)\delta t + \frac{1}{2!}b_i(t)\delta t^2 + \frac{1}{3!}c_i(t)\delta t^3 + \frac{1}{4!}d_i(t)\delta t^4 \\
a_i^p(t + \delta t) &= a_i(t) + b_i(t)\delta t + \frac{1}{2!}c_i(t)\delta t^2 + \frac{1}{3!}d_i(t)\delta t^3 \\
b_i^p(t + \delta t) &= b_i(t) + c_i(t)\delta t + \frac{1}{2!}d_i(t)\delta t^2 \\
c_i^p(t + \delta t) &= c_i(t) + d_i(t)\delta t \\
d_i^p(t + \delta t) &= d_i(t)
\end{aligned} \tag{4.29}$$

Once the forces have been evaluated, the difference between the predicted and calculated is called error. The error in acceleration can be found as

$$\delta a_i(t + \delta t) = a_i^c(t + \delta t) - a_i^p(t + \delta t) \tag{4.30}$$

Finally the corrected values are calculated using the error and constant chosen to maximize the stability of the algorithm.

$$\begin{aligned}
r_i^c(t + \delta t) &= r_i^p(t + \delta t) + c_0\delta a_i(t + \delta t) \\
v_i^c(t + \delta t) &= v_i^p(t + \delta t) + c_1\delta a_i(t + \delta t) \\
a_i^c(t + \delta t) &= a_i^p(t + \delta t) + c_2\delta a_i(t + \delta t) \\
b_i^c(t + \delta t) &= b_i^p(t + \delta t) + c_3\delta a_i(t + \delta t) \\
c_i^c(t + \delta t) &= c_i^p(t + \delta t) + c_4\delta a_i(t + \delta t) \\
d_i^c(t + \delta t) &= d_i^p(t + \delta t) + c_5\delta a_i(t + \delta t)
\end{aligned} \tag{4.31}$$

where the constants have values

$$\begin{aligned}
c_0 &= 3/20 & c_1 &= 251/360 \\
c_2 &= 1 & c_3 &= 11/18 \\
c_4 &= 1/6 & c_5 &= 1/60
\end{aligned} \tag{4.32}$$

The best choice for these coefficients depends on the order of both the differential equations and the Taylor series. These coefficients are computed based on the order of

the algorithm being used in the simulation. Verlet algorithm is fast but not accurate for long time steps. In present research work, velocity Verlet and predictor corrector have been used in various simulations. The Predictor corrector algorithm has very good local energy conservation, can be used with velocity-dependant forces, and is not time reversible. Verlet on the other hand has much better long term energy conservation compared to the predictor-corrector, and is time reversible.

#### 4.4 Boundary Conditions

As mentioned before, the initial structure is set according the crystal type. Figure 4.6 below shows different crystals structures present in metals. Aluminum takes the face-centered (fcc) shape and alumina has hexagonal closed packed structure.

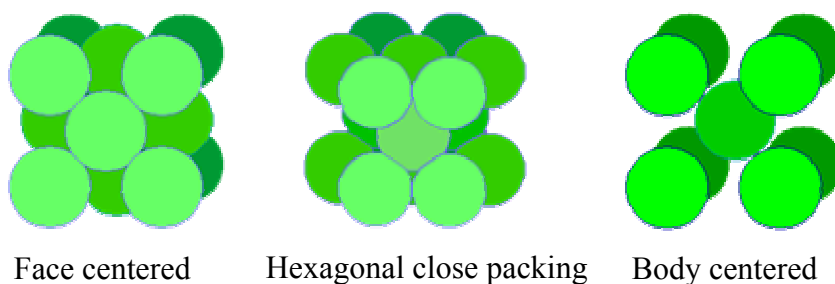


Figure 4.6: Various lattice types for crystalline structures

A separate code has been written to generate bulk or nano particulate aluminum and alumina using these lattice types as basis. For aluminum the FCC crystal structure is chosen with lattice spacing of 4.032 Angstroms. For alumina the hexagonal packed structure is used with the following unit vectors for the basis:



$$\begin{aligned}
\vec{a} &= 4.7589(1, 0, 0) \\
\vec{b} &= 4.7589\left(-\frac{1}{2}, \frac{\sqrt{3}}{2}, 0\right) \\
\vec{c} &= 12.990(0, 0, 1)
\end{aligned} \tag{4.33}$$

The fractional indices are listed in Table 4.2. This 30 atoms unit cell is repeated in three dimensions to generate any bulk or particulate alumina.

Table 4.2: Coordinates for Al<sub>2</sub>O<sub>3</sub> lattice

Atom #	Fractional coordinates			Type
1	0.306	0.000	0.250	O
2	0.000	0.306	0.250	O
3	0.694	0.694	0.250	O
4	0.694	0.000	0.750	O
5	0.000	0.694	0.750	O
6	0.306	0.306	0.750	O
7	0.000	0.000	0.352	Al
8	0.000	0.000	0.648	Al
9	0.000	0.000	0.852	Al
10	0.000	0.000	0.148	Al
11	0.639	0.667	0.917	O
12	0.333	0.973	0.917	O
13	0.027	0.361	0.917	O
14	0.027	0.667	0.417	O
15	0.333	0.361	0.417	O
16	0.639	0.973	0.417	O
17	0.333	0.667	0.019	Al
18	0.333	0.667	0.315	Al
19	0.333	0.667	0.519	Al
20	0.333	0.667	0.815	Al
21	0.973	0.333	0.583	O
22	0.667	0.639	0.583	O
23	0.361	0.027	0.583	O
24	0.361	0.333	0.083	O
25	0.667	0.027	0.083	O
26	0.973	0.639	0.083	O
27	0.667	0.333	0.685	Al
28	0.667	0.333	0.981	Al
29	0.667	0.333	0.185	Al
30	0.667	0.333	0.481	Al

If the fractional coordinates for each atom are labeled as  $q_i = (q_{1i}, q_{2i}, q_{3i})$  and unit vectors are  $(\vec{a}, \vec{b}, \vec{c})$  then Cartesian coordinates  $r = (x_i, y_i, z_i)$  are obtained from  $r_i = q_{1i} \vec{a}$

$+ q_{2i} \vec{b} + q_{3i} \vec{c}$ . For the x coordinate of  $r$ , for example,  $x_i = q_{1i} a_x + q_{2i} b_x + q_{3i} c_x$ . To make a  $(l \ m \ n)$  replica of the unit cell for the simulation super-cell, the Cartesian coordinates of unit cell are taken and multiples of the unit cell vectors are added to get additional coordinates of atoms in the super-cell. For example:  $r_\alpha(l,n,m) = q_{1\alpha} ia + q_{2\alpha} jb + q_{3\alpha} kc$ . To get all the coordinates summation is done from  $i = 1$  to  $l$ ,  $j = 1$  to  $m$  and  $k = 1$  to  $n$  and over all the atoms in the unit cell. Figures 4.7 and 4.8 show a super-cell created for aluminum and alumina respectively.

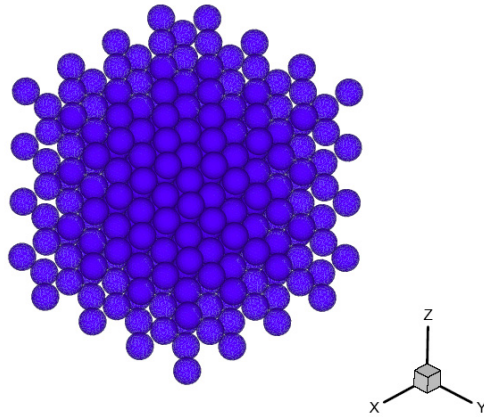


Figure 4.7: FCC Lattice for aluminum

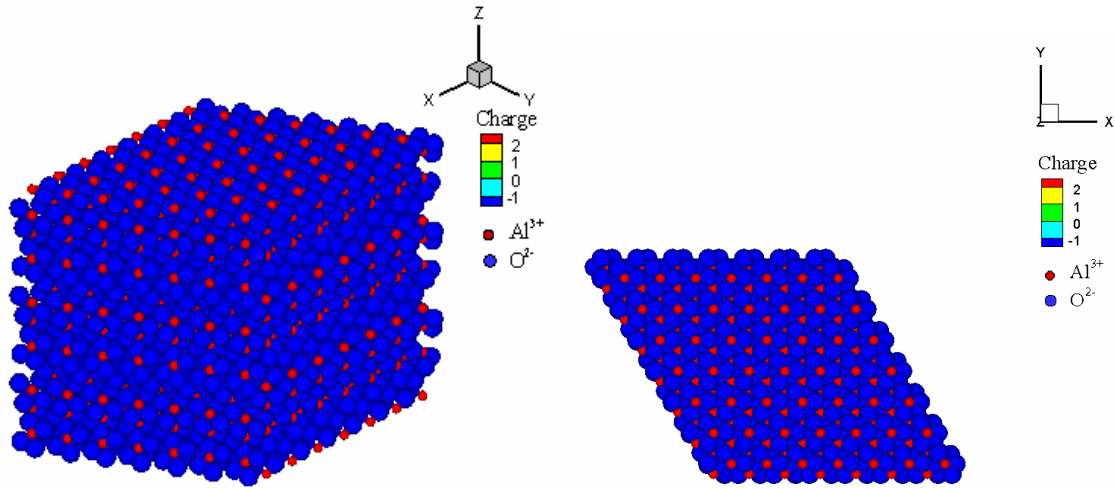


Figure 4.8: Supercell for alumina

The atoms are arranged in a crystalline structure and are given random velocities according to Maxwell Distribution.

$$f(v) = 4\pi \left( \frac{m}{2\pi kT} \right)^{3/2} v^2 \exp \left[ \frac{-mv^2}{2kT} \right] \quad (4.34)$$

The system is first equilibrated at particular temperature and then evolved in time. Boundaries can be of different types in a MD simulation:

1. Free boundaries: Used for ultrafast processes, processes in vacuum, ion bombardment etc.
2. Rigid Boundaries: Unphysical, should be carefully implemented, used in combination with others
3. Periodic Boundary Conditions: Most popular, used along with minimum image criterion, size of the cell vs. characteristic length scale

4. Mixed Boundary conditions: Non isotropic simulations, dislocations and defects

5. Stochastic Boundary Conditions: Used in special ensembles

The most common boundary condition used in molecular dynamics is the periodic boundary and can model a system as an infinitely repeating physical domain. If a molecule is close to the right side of the domain it can interact with the molecules on the left side as neighbors. Also if a molecule leaves the physical domain it will re-emerge on the opposite side as shown in Figure 4.9. However, it is good only for systems with short range forces.

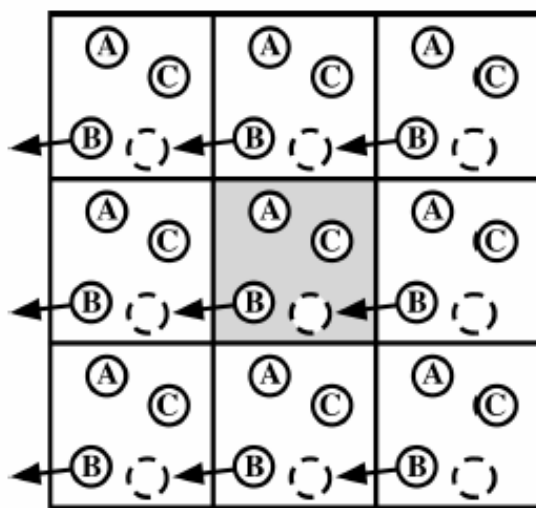


Figure 4.9: Schematic diagram showing periodic boundary condition for Cartesian coordinates

## 4.5 Statistical Ensembles

Ensemble is an idealization consisting of large number of copies of a system, considered all at once, each of which represents a possible state that the real system might be in. There are four major ensembles considered in Molecular Dynamics:

1. Microcanonical (NVE): used for constant density/equilibrium simulations
2. Canonical (NVT): used for isochoric and isothermal simulations
3. Isothermal isobaric (NPT): used for isobaric isothermal simulations
4. Isobaric isoenthalpic (NPH): used for constant pressures simulations

To simulate the system in a particular ensemble we need to derive equations using Lagrangian and Statistical Mechanics. Lagrangian Mechanics is re-formulation of classical mechanics and was introduced by Louis Lagrange in 1788. It is derived from the difference between kinetic and potential energy and simplifies many physical problems. The equations of motion thus obtained are called Lagrange's equations. It is especially useful for non Cartesian coordinate frames. The Lagrangian,  $L$ , of a dynamical system is a function that summarizes the dynamics of the system. Hamiltonian is obtained by performing Legendre transformation on Lagrangian and was invented in 1833 by William Hamilton. This is used mainly in Quantum mechanics.

For scaled coordinates defined in terms of old coordinates using

$$r = f(q, q', t); r' = f(q, q', t) \quad (4.35)$$

Lagrangian equations of motion can be derived as

$$\frac{d}{dt} \frac{\partial L}{\partial q'_i} = \frac{\partial L}{\partial q_i} \quad (4.36)$$

where  $L = T - V$ .

For Hamiltonian we define

$$p = \frac{\partial L(q, q', t)}{\partial q'} \quad p' = \frac{\partial L(q, q', t)}{\partial q} \quad (4.37)$$

The Hamiltonian can be written as

$$H(q, p) = pq' - L(q, q', t) \quad (4.38)$$

and the equations of motion can be derived using

$$\frac{\partial H}{\partial p} = q' \quad \frac{\partial H}{\partial q} = -p' \quad (4.39)$$

NVE Ensemble:

For the NVE ensemble, the Newtonian mechanics can be written as

$$\begin{aligned} F &= -\nabla V \\ mx'' &= -\nabla V \end{aligned} \quad (4.40)$$

Using the Lagrangian formulation, the Lagrangian can be written as

$$L(x, x', t) = \frac{1}{2} mx'^2 - V(x) \quad (4.41)$$

and for the subsequent equations of motion we get

$$\frac{d}{dt} \frac{\partial L}{\partial q'_i} = \frac{\partial L}{\partial q_i} \Rightarrow \frac{d}{dt} (mx') = -\nabla V(x) \Rightarrow mx'' = -\nabla V \quad (4.42)$$

The Hamiltonian can be formulated as

$$\begin{aligned} p &= \frac{\partial L(q, q', t)}{\partial q'} \Rightarrow mx' \quad p' = \frac{\partial L(q, q', t)}{\partial q} \Rightarrow -\nabla V(x) \\ H(q, p) &= pq' - L(q, q', t) \Rightarrow mx'x' - \left[ \frac{1}{2} mx'^2 - V(x) \right] = \frac{1}{2} mx'^2 + V(x) = \frac{p^2}{2m} + V(x) \end{aligned} \quad (4.43)$$

and resulting equations of motion are:

$$\begin{aligned}\frac{\partial H}{\partial p} &= q' \Rightarrow p = mx' \\ \frac{\partial H}{\partial q} &= -p' \Rightarrow p' = -\nabla V\end{aligned}\tag{4.44}$$

NPH ensemble:

In order to simulate the system in NPH ensemble, a system of  $N$  atoms is coupled to an external source by introducing additional variables into the Lagrangian. NPH ensemble was first introduced by Anderson using volume as an extra degree of freedom through mechanical coupling (Anderson, 1980). Assuming that atoms behave as classical point-like masses, the Lagrangian of the system is expressed as

$$L = \sum_i \frac{mV^{2/3}\dot{d}_i^2}{2} + \frac{M\dot{V}^2}{2} - U(V^{1/3}d_1, \dots, V^{1/3}d_{3N}) - PV\tag{4.45}$$

where  $M$  is a constant fictitious mass associated with the volume of the system,  $m$  the mass of the atom,  $V$  the volume, treated as a dynamic variable,  $P$  the pressure, and  $d_i$  the scaled position of atom  $i$ . The above equation is obtained using scaled coordinates

$r_i = V^{1/3}d_i$   $\dot{r}_i = V^{1/3}\dot{d}_i$ . The potential and kinetic energy can be written as

$$\begin{aligned}P.E. &= U(V^{1/3}d_1, \dots, V^{1/3}d_{3N}) + PV \\ K.E. &= \sum_i \frac{mV^{2/3}\dot{d}_i^2}{2} + \frac{M\dot{V}^2}{2}\end{aligned}\tag{4.46}$$

The Lagrangian equations of motion can be obtained using

$$\frac{d}{dt} \frac{\partial L}{\partial q'_i} = \frac{\partial L}{\partial q_i}\tag{4.47}$$

where  $q_i$  are generalized coordinates. Substituting  $q_i$  for  $V$  and  $d_i$  in Eqn. 4.47, the equations of motion for the case of NPH ensemble take the form

$$\begin{aligned} M\ddot{V} &= -P + \frac{1}{3V} \left[ V^{2/3} \sum_i m_i \dot{d}_i^2 + V^{1/3} \sum_i F_i d_i \right] \\ m_i \ddot{d}_i &= V^{-1/3} F_i - \frac{2m_i \dot{V} \dot{d}_i}{3V} \end{aligned} \quad (4.48)$$

where  $\dot{d}_i$  and  $\ddot{d}_i$  denote the first-order and second-order derivatives with respect to time, and  $F_i$  the net force on atom  $i$ . Equation 4.48 can be numerically integrated using a fifth-order predictor-corrector algorithm.

#### NVT Ensemble:

For NVT ensemble the temperature needs to be constant. The temperature is controlled using a parameter that also evolves with time and helps in keeping the temperature constant. The whole system can be assumed to be in contact with a reservoir that helps in maintaining the temperature constant (Nose, 1984; Nose, 1985). The scaling can be done as

$$\begin{aligned} t' &= t / s \\ \dot{x}'_i &= \dot{x}_i s \end{aligned} \quad (4.49)$$

The resultant Potential energy, kinetic energy and Lagrangian can be written as

$$\begin{aligned} P.E. &= U(x_1, \dots, x_{3N}) + gkT \ln s \\ K.E. &= \sum_i \frac{ms^2 \dot{x}_i^2}{2} + \frac{Q\dot{s}^2}{2} \\ L &= \sum_i \frac{ms^2 \dot{x}_i^2}{2} + \frac{Q\dot{s}^2}{2} - U(x_1, \dots, x_{3N}) - gkT \ln s \end{aligned} \quad (4.50)$$

Using Lagrangian mechanics we obtain:



$$\begin{aligned}
Q\ddot{s} &= s \sum_i m_i \dot{x}_i^2 - \frac{gkT}{s} \\
m_i \ddot{x}_i &= \frac{F_i}{s^2} - \frac{2m_i \dot{s} \dot{x}_i}{s}
\end{aligned} \tag{4.51}$$

which can be further simplified by using time derivative with respect to real time as

$$\begin{aligned}
Q\ddot{s} &= s \sum_i m_i \dot{x}_i^2 - sgkT + \frac{Q\dot{s}^2}{s} \\
m_i \ddot{x}_i &= F_i - \frac{m_i \dot{s} \dot{x}_i}{s}
\end{aligned} \tag{4.52}$$

Sometimes a friction constant  $\zeta$  is used to simplify the equations.

$$\begin{aligned}
\zeta &= \frac{d(\ln s)}{dt} \Rightarrow \dot{s} = \zeta s \\
Q\dot{\zeta} &= \sum_i m_i \dot{x}_i^2 - gkT \\
m_i \ddot{x}_i &= F_i - m_i \zeta \dot{x}_i
\end{aligned} \tag{4.53}$$

If the kinetic energy is greater than  $gkT$ ,  $\dot{\zeta}$  is greater than zero and  $\zeta$  increases and becomes positive. The equation for  $\ddot{x}_i$  with positive  $\zeta$  describes a system with frictional force and hence velocities and kinetic energy decrease accordingly. The opposite happen if kinetic energy is smaller than  $gkT$ .

#### NPT ensemble:

NPT ensemble is an extension of NVT and NPH ensembles. Basically the pressure and temperature are controlled by scaling the size of unit cell and velocity respectively. The scaled coordinates are given by

$$\begin{aligned}
x_i &= V^{1/3} d_i \\
\dot{x}_i &= s V^{1/3} \dot{d}_i
\end{aligned} \tag{4.54}$$

Potential, kinetic energies and Lagrangian can then be derived as

$$\begin{aligned}
P.E. &= U(V^{1/3}d_1, \dots, V^{1/3}d_{3N}) + PV + gkT \ln s \\
K.E. &= \sum_i \frac{ms^2 V^{2/3} \dot{d}_i^2}{2} + \frac{M\dot{V}^2}{2} + \frac{Q\dot{s}^2}{2} \\
L &= \sum_i \frac{ms^2 V^{2/3} \dot{d}_i^2}{2} + \frac{M\dot{V}^2}{2} + \frac{Q\dot{s}^2}{2} - U(V^{1/3}d_1, \dots, V^{1/3}d_{3N}) - PV - gkT \ln s
\end{aligned} \tag{4.55}$$

The equations of motion and thus be given by

$$\begin{aligned}
M\ddot{V} &= -P + \frac{s^2}{3V} \left[ V^{2/3} \sum_i m_i \dot{d}_i^2 - V^{1/3} \sum_i F_i d_i \right] \\
m_i \ddot{d}_i &= \frac{V^{-1/3} F_i}{s^2} - \frac{2m_i \dot{V} \dot{d}_i}{3V} - \frac{2m_i \dot{s} \dot{d}_i}{s} \\
Q\ddot{s} &= s V^{2/3} \sum_i m_i \dot{d}_i^2 - \frac{gkT}{s}
\end{aligned} \tag{4.56}$$

#### 4.6 Structural and Thermodynamic Properties

Statistical Mechanics can be used to predict bulk properties of matter in terms of the microscopic particles of which it is composed. Thermodynamics can be treated as merely statistical mechanics at macroscopic level. Boltzmann and Gibbs in late nineteenth century laid the foundation of Statistical mechanics. Using the concept of discrete energy states, Boltzmann's relation can be written as

$$S = k \ln \Omega \tag{4.57}$$

This forms the basis for extracting thermodynamic properties of the system using the motions at atomistic level. The macroscopic thermodynamic properties of the system are derived from the instantaneous values using the equation of state and statistical

mechanics. For example, the temperature can be determined from the kinetic energy of atoms according to the equi-partition principle.

$$T = \frac{2\langle K \rangle}{3Nk_B} \quad (4.58)$$

For any physical property A,  $\langle A \rangle$  denotes an average over time given by

$$\langle A \rangle = \frac{1}{N_{step}} \sum_{i=1}^{N_{step}} A(\Gamma_i) \quad (4.59)$$

where  $\Gamma_i$  represents a 6N-dimensional phase space consisting of positions and momenta of all atoms. The pressure is calculated through the virial equation of state, as a function of the temperature of the system and forces experienced by all the atoms.

$$P = Nk_B T + \left\langle \frac{1}{3} \sum_{i=1}^N r_i \cdot F_i \right\rangle \quad (4.60)$$

The melting point is identified based on the variations in the potential energy, Lindemann index, and translational order parameter. The Lindemann index, defined as (Zhuo et al., 2002),

$$\delta = \frac{2}{N(N-1)} \sum_{i < j} \frac{\sqrt{\langle r_{ij}^2 \rangle_t - \langle r_{ij} \rangle_t^2}}{\langle r_{ij} \rangle_t} \quad (4.61)$$

measures the vibrational motion of atoms, and can be calculated as a function of inter-atomic distance. The increase in vibrational motion is a characteristic of the phase change in materials, and the Lindemann index is expected to increase abruptly by a factor of more than three during melting. The translational-order parameter,  $\lambda$ , is a measure of the structure present in the solid, expressed as (Gezelter et al., 1997)

$$\lambda = \frac{1}{N} \sqrt{\left( \sum_{i=1}^N \cos(k \cdot r_i) \right)^2 + \left( \sum_{i=1}^N \sin(k \cdot r_i) \right)^2}$$

$$k = \left( \frac{(2N)^{1/3} \pi}{L} \right) (-1, 1, 1) \quad (4.62)$$

where  $k$  is an arbitrary vector of the lattice and  $L$  the side length of the simulation domain. In a solid, atoms simply vibrate about their lattice positions, and hence there is perfect order in the crystal. Such order, however, disappears in a liquid state, and the corresponding translational-order parameter is reduced by an order of magnitude.

#### 4.7 Parallel Numerical Framework

Parallel computers are essentially many processors linked together and set to operate concurrently. If a given computational task is shared evenly among the processors the task can be efficiently accomplished. Programming on parallel architectures requires considerations in terms of division of the computational workload and minimal communications between the processors. Both are important factors in generating efficient parallel code. The even division of computational work is termed load balancing. Molecular dynamic codes are especially sensitive to load imbalances. The work detailed herein is multifaceted. It involves the combining of combustion related thermo-fluid dynamics and molecular dynamics using the high speed capabilities of parallel computers.

The code developed for current Molecular Dynamics study can handle micro-canonical (NVE), isobaric-isoenthalpic (NPH), and isobaric-isothermal (NPT) ensembles

using the Verlet and predictor-corrector algorithms, respectively. These have been parallelized using the atomic decomposition method (Plimpton, 1995). This method consists of a series of expand and fold operations as shown in Figure 4.10 and makes the communications load much faster as compared to normal send and receive operations using MPI.

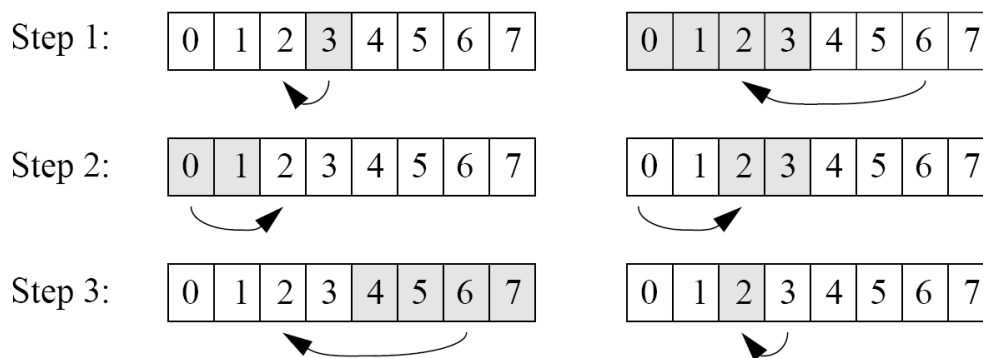


Figure 4.10: Expand and fold operations showing communications among 8 processors in three steps (Plimpton, 1995)

A separate post-processing code has also been established to superimpose the grid on the geometry under consideration, and to analyze the results using the contours of various thermodynamic properties. The code also has the capability of handling multi-atom simulations and can treat liquid and solid phases. Using the techniques mentioned by Long et al. (Long et al., 1996) and Thompson et al. (Thompson et al., 1984) a separate subroutines have been written to calculate the droplet radius in case of coexistence of liquid and gas phases.

Figure 4.11 shows the parallel speed-up obtained for 16384 atoms using up to 64 processors. The algorithmic speed-up varies almost linearly with the number of

processors, reaching up to a factor of 30 in the current case, and improves significantly with the problem size. The simulations were performed on a parallel architecture of a Beowulf system of PIII, PIV and AMD processors.

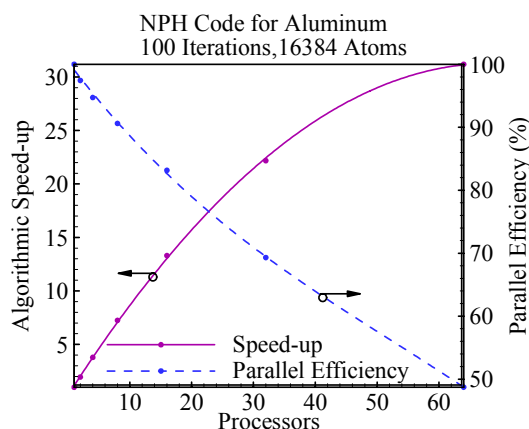


Figure 4.11: Speed-up and efficiency vs. number of processors for the MD code

A Beowulf system is a multi-computer architecture used for parallel computations. In a Beowulf system, one server computer and many other client computers are connected together via high-speed networks. It is a distributed memory, MIMD system built primarily using commodity hardware components, such as any PC capable of running the free operating system Linux, standard Ethernet adapters, and switches. The first Beowulf system was built by Donald Becker in 1994, and consisted of 16 486DX4-100MHz machines each with 16 MB of memory. The main advantage of a Beowulf system is its high performance/price ratio in comparison with other systems. Another important characteristic of the Beowulf clusters is the compatibility. Changes of hardware, including the node and network system, will not affect the programming model. A Beowulf system also uses commodity software, such as the Linux

operating system, Message Passing Interface (MPI) and other available open-source software. The work conducted for this study was implemented on an in-house Beowulf system, consisting of three Intel-based and one AMD-based Linux clusters. The parallel computing system presently includes 164 dual PIII, 173 single PIV and 160 AMD Opteron processors as shown in Figure 4.12. These computers are connected with nine 100M Fast Ethernet switches and four gigabit switches in a tree topology to facilitate parallel processing. The cumulative internal memory is 584 GB, and the total file storage is 5.5 TB. This system can sustain 1200 gigaflops total peak performance, providing substantial number-crunching capabilities for large-scale computations. The operating system was RedHat Linux. The Message Passing Interface (MPI) involving a library of functions and macros that can be used in C, FORTRAN, and C++ Program were used to exchange the information among the processors.



Figure 4.12: Parallel computing facility at Penn State

The time step for most of the simulations is chosen to be one femto-second, considering that the time scale for vibration of atoms is of the same order. Annealing is sometimes achieved using the velocity scaling, and the temperature of the nanoparticle is increased at a rate of 0.01 K per time step. A parametric study was performed on a bulk FCC crystal consisting of 2048 atoms with different temperature rises of 1, 0.1, 0.01, and 0.001 K per femto-second for each time step. A rate lower than 0.01 K/step increases the total computational time, and a higher rate gives insufficient time for particles to equilibrate at each step leading to erroneous results. An optimum rate of 0.01 to 0.1 K/step also helps in accurately predicting the melting point because it produces better resolution in the variations of thermodynamic and structural properties.

#### 4.8 Code Validation

The NVE and NPH algorithms developed in the present study have been validated against argon in different phases (solid, liquid and vapor), as well as its thermodynamic transition from the solid to the liquid phase, because of the availability of extensive and reliable experimental and numerical data (Solca et al., 1997; Solca et al., 1998; Agarwal et al., 2003). An attempt was made to fully understand the various types of numerical simulations performed for Argon at different pressures to obtain thermodynamic properties (Ermakova et al., 1994; Konning et al., 2001; Woon, 1993; Zha et al., 1986). The inter-atomic interactions were simulated using the Lennard-Jones potential. Melting was identified using the radial-distribution function, translational-order parameter, Lindemann index, and time evolution of the average potential energy. The solid-state



simulations predict an equilibrium lattice spacing of 5.26 Å, which matches exactly the values in the literature. The kinetic, potential, and total energies per atom are obtained for the system equilibrated at different random temperatures using both the NVE and NPH ensembles. With the equilibrium pressure from the NVE ensemble as a known condition, calculations were carried out using the NPH ensemble. Identical results were achieved. This was used as a validation tool for the two codes because the micro-canonical (NVE) and isobaric-isenthalpic (NPH) ensembles should be equivalent for calculations of thermodynamic quantities, without sacrificing the dynamical description of the fluid. Extensive validation tests were performed for phase transition. The predicted melting points agree well with the data in literature. The results also matched those from the molecular-dynamics simulations conducted by Agarwal et al. and Solca et al. at their respective ambient conditions.

The first simulation was conducted at a pressure of 90.0 MPa with 256 atoms, representing the bulk argon, through periodic boundary conditions. The time step chosen was 8.6 femto-seconds and heat was added to the solid crystal, by increasing the temperature at the rate of 0.001 K per step. The velocities of atoms were scaled at each time step corresponding to this increase in temperature. The phase transition was observed at around 117 K as shown in Figure 4.13 which matches perfectly with the similar NPH runs performed by Solca et al (Solca et al., 1997; Solca et al., 1998).

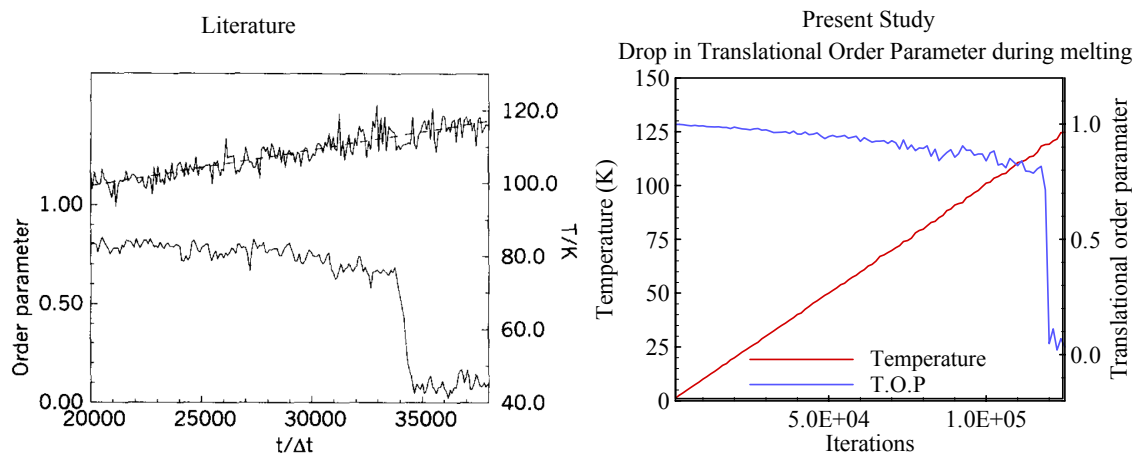


Figure 4.13: Comparison with results of Solca et al. for Validation

The second validation run was performed for simulations by Agarwal et al. for melting of argon at 44.56 kbar. The study by Agarwal was an isothermal isobaric ensemble using leapfrog Verlet algorithm. They used Melchionna modification (Melchionna et al., 1993) of Nose-Hover equations of motion. However in this study the calculations were performed in NPH ensemble which is also called isobaric-isoenthalpic trajectory. Figure 4.14 shows the plot of temperature and potential energy as the system evolves. During the time interval monitored in the simulation (I), the temperature increased from 650.0 K to 900.0 K. Melting was found to occur at 837.7 K as compared to 840.9 K by Agarwal et al. A comparison was also made with another simulation (II) in which the parameters were kept same as melting simulation, except the temperature gradient. It resulted in an isothermal isobaric trajectory with temperature fixed at 775.0 K. The purpose of this was to allow a comparison of properties generated from a standard isothermal-isobaric trajectory with those generated during a simulation having temperature gradient. The average pressure was matched perfectly with the study of

Agarwal et al. (i.e. 44.56 kbar). The average energies per atom reported in the current study were 0.956 and 0.993 eV in simulations I and II respectively. Similarly, the average atomic densities were 0.03236 and 0.03288 atoms/A<sup>3</sup> in simulations I and II respectively. These values were close to 0.1317 eV for energy per atom and 0.03403 atoms/A<sup>3</sup> for atomic density as obtained in the study done by Agarwal (Agarwal et al., 2003).

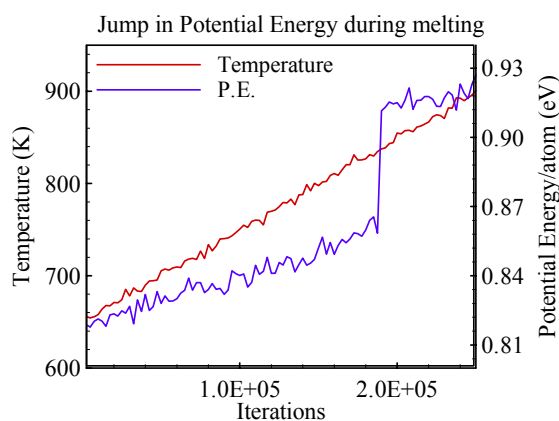


Figure 4.14: Variation in Potential energy during melting for an Argon crystal at 44.56 kbar

NPT ensembles were validated and verified by comparing the results with study performed by Nose et al. (Nose, 1985b) for argon at 0.25 kbar as shown in Figure 4.15

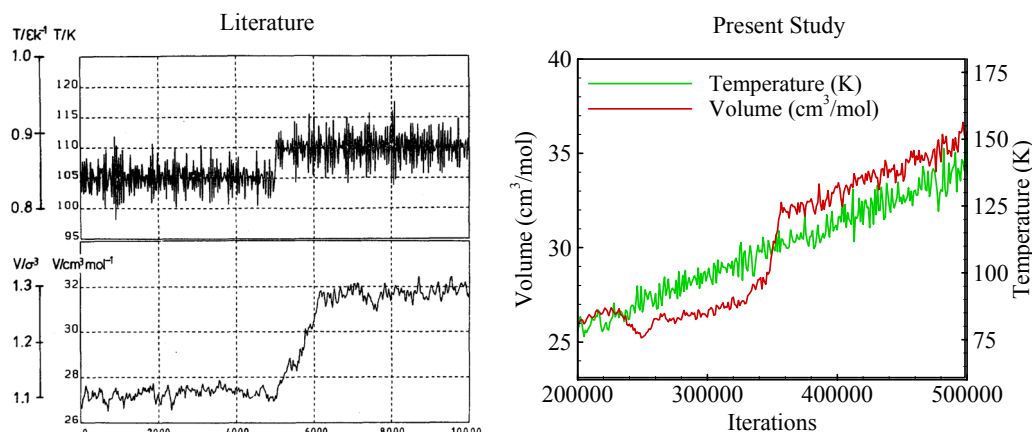


Figure 4.15: Validation for NPT ensembles using argon at 0.25 kbar, time step of 8.6 fs

The validation study for the liquid phase was conducted by simulating a liquid droplet of argon in equilibrium with its saturated vapor using the Lennard-Jones potential and NPH ensemble as shown in Figure 4.16. Different studies have been done in literature, which deal with various issues related to a liquid phase simulation and formation of droplets (Fowler et al., 1984; Powles et al., 1983; Powles et al., 1983b; Powles et al., 1984; Powles et al., 1985; Thompson et al., 1984; Long et al., 1996). The system comprising of droplet and the vapor consisted of 16384 atoms, using periodic boundary conditions. The temperature was maintained constant at 100 K. The average density of the droplet ( $1200 \text{ kg/m}^3$ ) matched the value reported at the saturation temperature in a similar research work involving Argon (Little, 1996). Figure 4.16 also shows a slice through the centre plane of the system volume and shows density contours. The spherical shape of the droplet can be easily seen and the density value inside the droplet matches with the saturated value at 100K.

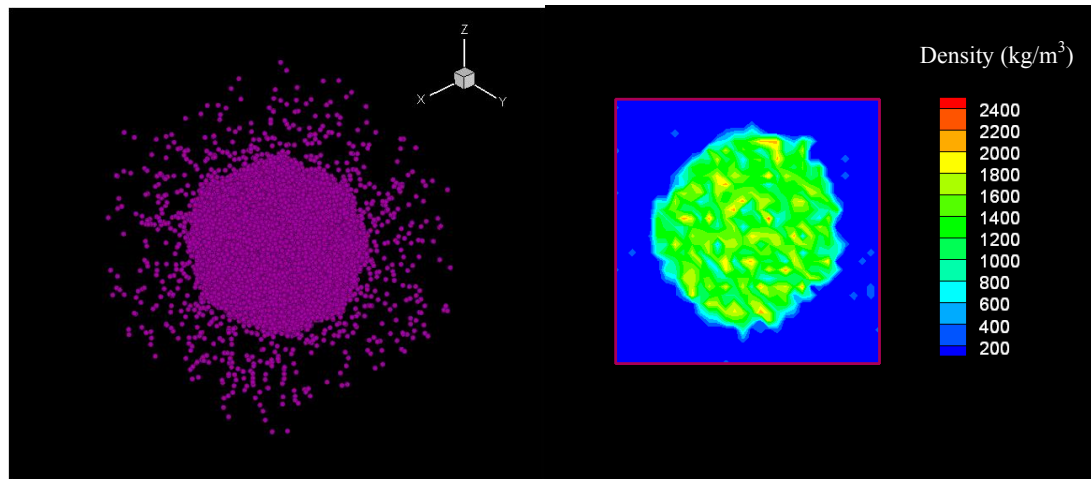


Figure 4.16: Simulation of a liquid droplet of argon at 100 K (a) argon droplet in its saturated vapor at 100 K; (b) density contour at 100 K

Figure 4.17 shows the radial distribution function of bulk liquid argon at a reduced density ( $\rho\sigma^3$ ) of 0.844 and a reduced temperature of  $0.71(k_B T / \varepsilon)$ . Excellent agreement was obtained with the result reported in texts.

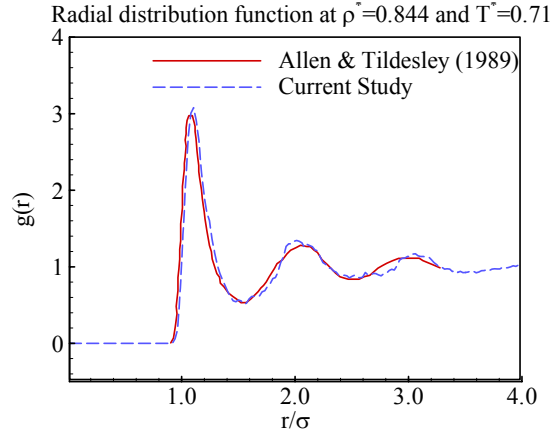


Figure 4.17: Radial distribution functions for liquid argon using NVE simulations

Gaseous phase argon was also simulated at a temperature of 200 K and pressure of 7.5 MPa, using 70304 atoms, and periodic boundary conditions as shown in Figure 4.18. Again the equilibrium pressure, kinetic energy and potential energy were very close to similar studies done in literature (Little, 1996). The total kinetic energy and potential energy obtained in this study were  $2.91\text{E-}16$  J and  $-1.0\text{E-}16$  J respectively. This matches very well with the values of  $2.9\text{E-}16$  and  $-1.06\text{E-}16$  in literature. Thus, the code has been validated by testing it extensively on different phases of argon.

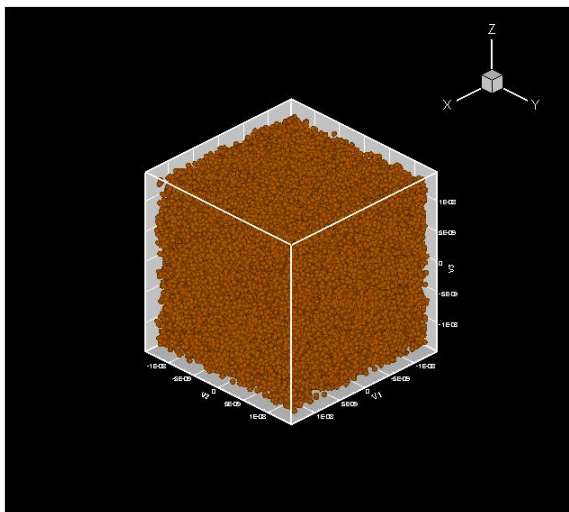


Figure 4.18: Gaseous phase argon at 200K and 7.5 MPa

The overall approach was also examined by comparing the calculated cohesive energies and melting points for both aluminum and alumina against experimental data. Figure 4.19 shows the calculated Al-Al, Al-O, and O-O radial distribution functions for alumina. The inter-atomic distances for peak values for Al-Al, Al-O and O-O coordination are 2.9, 1.58 and 2.65 Å respectively. Good agreement with experimental values is obtained (Miguel et al. 1998; Gutierrez et al., 2001). Figure 4.20 shows  $\text{Al}_2\text{O}_3$ , AlO, and  $\text{Al}_2\text{O}$  fragments coming out of a 5 nm alumina particle when heated beyond 4000 K. The Al and O atoms in the crystal are initially packed in a hexagonal structure, equilibrated at room temperature, and then heated at 800 MPa until decomposition occurs. The decomposition products qualitatively validates that the SM potential can indeed simulate molecular interactions involved in the alumina particle.

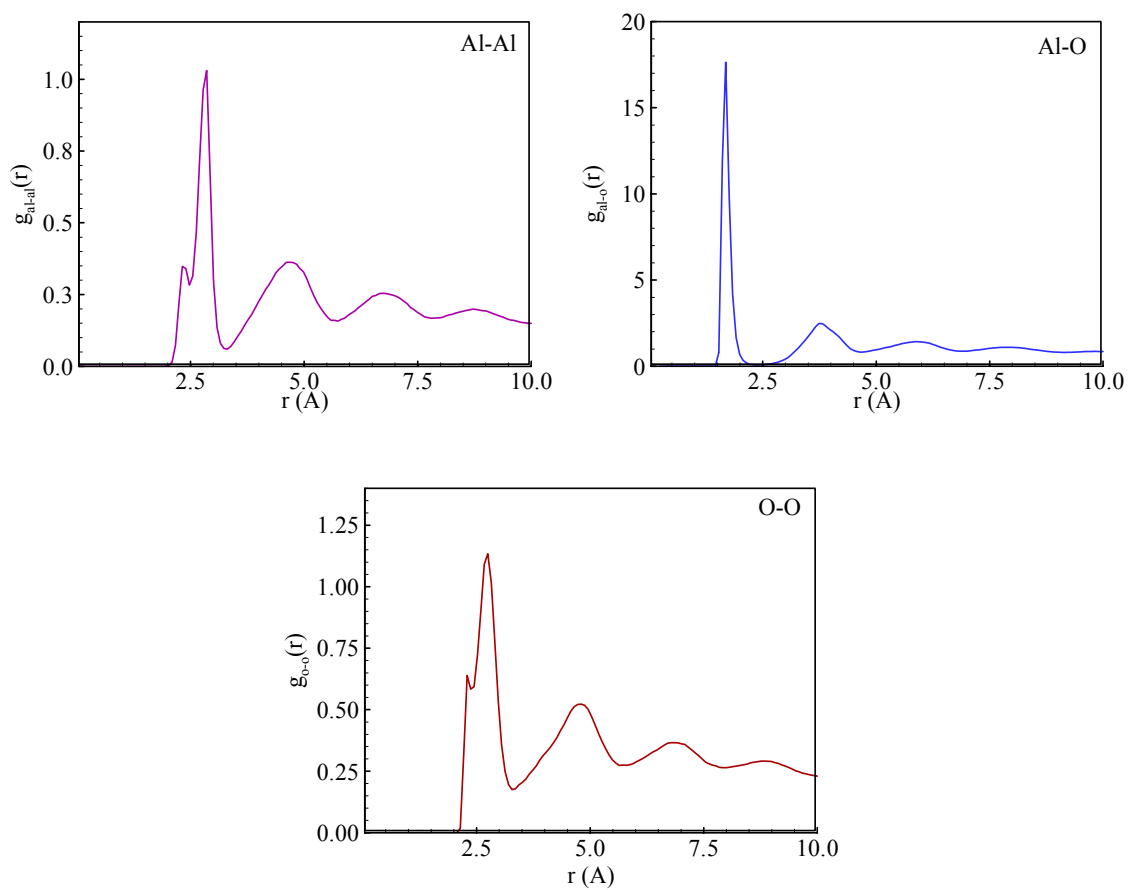


Figure 4.19: Radial distribution functions for Al-Al, Al-O, and O-O interactions

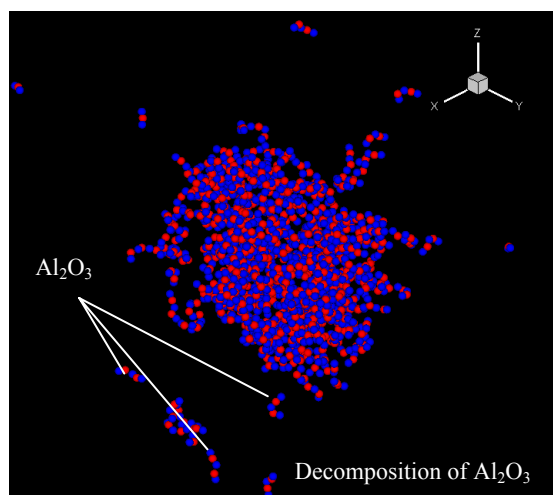


Figure 4.20: Fragmentation and decomposition of  $\text{Al}_2\text{O}_3$  from an alumina particle when heated beyond 4000 K; initial diameter of 5 nm



## Chapter 5

### Thermo-Mechanical Behavior of Pure Aluminum at Nano Scales

#### 5.1 Background

Nano-sized aluminum and other metallic particles have been extensively used in many propulsion and energy-conversion applications due to their unusual energetic properties, such as increased catalytic activity and higher reactivity (Ilyin et al., 2001; Kwon et al., 1996). The excess energy of surface atoms and reduced activation energies for chemical reactions contribute to these extraordinary chemical characteristics (Pivkina et al., 2004; Mench et al., 1998).

Along with these energetic properties, particles at nano scales exhibit many thermo-physical features as well which are distinct from those found at micro scales. As the size decreases beyond a critical value, due to the increase in the surface-to-volume ratio, the melting temperature deviates from the bulk value and becomes a size-dependant property (Alavi et al., 2006). This phenomenon has been studied experimentally by means of transmission electron diffraction by Wronski for nano-sized tin (Wronski, 1967). The apparatus consists of an evaporator attached to a small furnace, and 5-10 nm particles are produced by evaporating tin pellet from the surface and then condensing it on a thin carbon or silicon monoxide substrate. The melting points agree reasonably well with the predictions based on classical theories, which show a non-linear relationship with the reciprocal of the particle size. The melting temperature of tin becomes size-

dependant for particles smaller than 10 nm, reducing from a bulk value of 505 K to 425 K for a 5 nm particle. Eckert et al. synthesized nano-crystalline aluminum powders by mechanical attrition in argon, hydrogen and oxygen atmospheres, and observed a similar reduction in the melting point with decreasing grain size (Eckert et al., 1993). The study was performed for 13-40 nm particles using differential scanning calorimetry (DSC). The melting point increases from 840 K for 13 nm particles, and reaches its bulk value of 940 K for 40 nm particles. In addition to these experimental studies, Alavi et al. performed molecular-dynamics simulations for clusters of aluminum atoms using the Streitz-Mintmire potential and canonical (NVT) ensembles (Alavi et al., 2006). Special attention was given to the structure of the cluster and dynamic coexistence of the liquid and solid phases. However, only clusters up to a size of 3 nm (i.e., 1000 atoms) were considered. Campbell et al. (Campbell et al., 2005) conducted molecular-dynamics simulations for the oxidation of a 20 nm aluminum particle. However, the effect of particle size on the melting and ignition of aluminum was not addressed.

As discussed before, particle size plays a significant role in determining the characteristics of ignition and combustion. For micron-sized and larger aluminum particles, the ignition temperature coincides with the melting point of the surface oxide ( $\text{Al}_2\text{O}_3$ ) layer at 2327K (Bucher et al., 2000). The impervious nature of aluminum oxide inhibits the ignition of aluminum. Once the layer melts, it coalesces to form an oxide cap, and the aluminum core is then exposed to the ambient gases for oxidation. At nano scales (less than 100 nm), the ignition occurs near the melting point of aluminum at 940 K by cracking of the oxide shell, possibly caused by the pressure buildup (Rai et al., 2004; Rozenband and Vaganova, 1992) and/or phase transformations (Dreizin, 2003; Trunov et

al., 2006) inside the shell. According to Rai et al., oxidation of alumina-coated nano-sized aluminum particles is initiated by melting of the aluminum core. The resultant volume dilatation causes a pressure build-up inside the shell formed by the oxide layer. Because of the higher curvature as compared to micron-sized particles, the stress developed due to the pressure becomes unsustainable and the shell subsequently ruptures. This concept was originally introduced by Rozenband (Rozenband and Vaganova, 1992), who developed a model taking into account the mechanical stresses at the metal-oxide interface. Trunov et al. (Trunov et al., 2006) attributed the observed low ignition temperature of nano-sized particles to the transformation from the amorphous to the gamma and alpha phases in the oxide layer. As a consequence of the density variations in different phases, the layer develops cracks, which permit direct oxidation of aluminum in the core.

## 5.2 Objectives

In light of the inconsistency and uncertainties of the various theories concerning the particle behavior at nano scales discussed in section 5.1, fundamental research based on well-calibrated techniques appeared to be imperative, in order to achieve an improved understanding of the effects of particle size on the melting and ignition behavior. Since this was the first of the series of MD studies performed, the purpose of the present work was to study the melting of aluminum particles in the size range of 2-9 nm consisting of 256-23328 atoms. The influence of the surface passivating layer was not considered, and was treated in other studies. This will be discussed in subsequent chapters. The results not only provided basic information about particle behavior at nano scales, but also set the

stage for a study of the ignition and combustion of aluminum particles over a broad range of scales. The melting process was characterized using a combination of structural and thermodynamic parameters, including the potential energy, Lindemann index, translational-order parameter, and radial-distribution functions. Both bulk material and nanoparticles were considered. The dynamic coexistence of the solid and liquid phases was also explored. In addition, the effect of surface charge development on melting was examined using the Streitz-Mintmire potential.

A major assumption involved in any Molecular Dynamics study before using any potential is the Born-Oppenheimer Approximation as discussed in Chapter 4. According to this theory, the nuclear and electronic motion in molecules can be separated and the nuclear motion sees a smeared out potential from the speedy electrons. The potential functions are an approximation to this potential energy surface and are basically fitted to such experimental data as structural, thermodynamic or material properties. Moreover, almost all the potentials considered are fitted to the properties for bulk materials. One of the key issues in nanoparticle or cluster simulations is the size dependence of properties which has been shown in literature. The accuracy of a model can be judged from its ability to simulate properties like size dependence of melting point. An ideal potential to be used for current research should be able to accurately predict thermodynamics, elastic properties, surface energies and surface relaxation of crystalline oxide and aluminum. Hence, the second goal of this work was to compare the existing potentials, most of which have been either fitted to thermodynamic or structural properties for the bulk. Due to the availability of a wide range of potentials, a comparison has been made, using the melting phenomenon for an aluminum nanoparticle as a benchmark. MD simulations

involving a large number of particles are computationally very expensive and a correct choice of the potential can save a lot of computational time. The aim was to select an optimum potential which predicts the aluminum nanoparticle melting to a good level of accuracy and is also computationally not too expensive for nano-sized aluminum particle studies. Five existing potentials (the Lennard-Jones, glue, embedded-atom, Streitz-Mintmire, and Sutton-Chen potentials) were implemented and evaluated.

### 5.3 Results and Discussion

After validation, the general framework described in Chapter 4 was employed to study the melting of nano-sized aluminum particles. Figure 5.1 shows the melting phenomenon of bulk aluminum in a vacuum. The simulation was performed using the glue potential and periodic boundary conditions. An FCC lattice was adopted to calculate the initial position vectors for the known number of aluminum atoms. Melting was observed at a temperature of 1244 K, at which point sharp variations occur in the potential energy, atomic density, translational-order parameter, radial-distribution function, and the Lindemann index.

The melting of nano-sized aluminum particles was examined in the size range of 2-9 nm. The simulations started with solid phase aluminum using an FCC crystal structure in a cubic configuration. Figure 5.2 shows the changes in the same thermodynamic and structural properties for a 4 nm particle consisting of 2048 atoms. Melting occurs at 735 K. Since the potential energy and atomic density vary smoothly at the melting point for a

particle, only the translational-order parameter and Lindemann index are employed to characterize the melting point for the rest of the study.

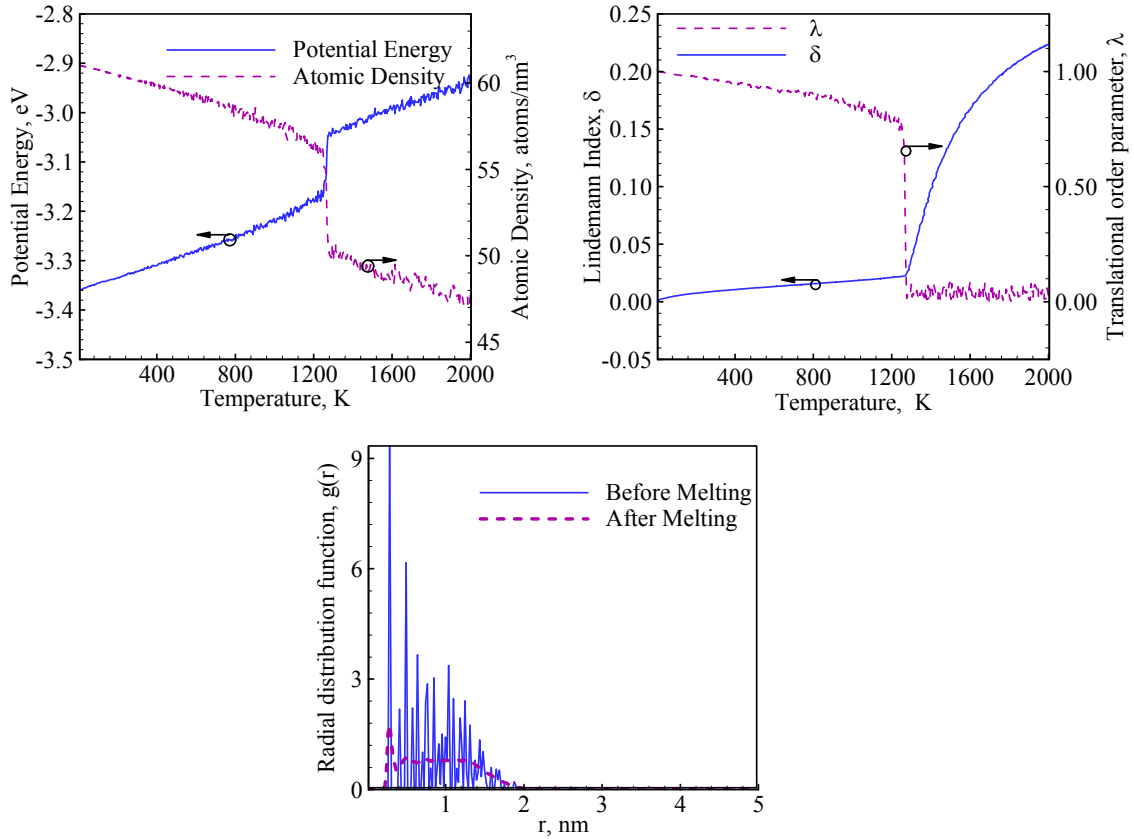


Figure 5.1: Variations of thermodynamic and structural properties during melting of bulk aluminum in vacuum; the glue potential

The phenomenon of surface pre-melting represents a qualitative difference between the calculated bulk-material and particle melting. A bulk solid can be simulated by enforcing periodic boundary conditions in all three spatial directions, whereas a particle is associated with a free surface. In the case of a particle, the surface acts as a nucleation site for the phase transition and propagates to the interior. Hence, the phase change in a particle is manifested by a gradual increase in such properties as the potential

energy and Lindemann index, as opposed to the abrupt variations found in a bulk material.

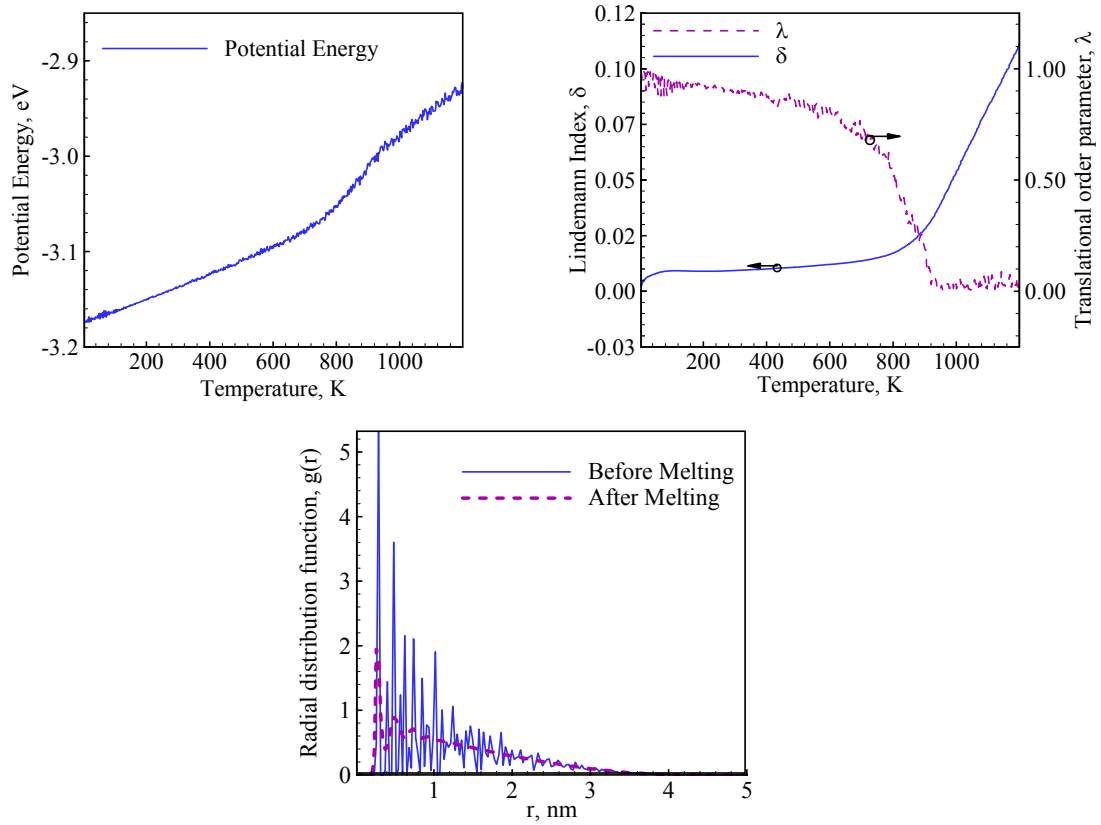


Figure 5.2: Variations of thermodynamic and structural properties during melting of nano-sized aluminum particle; the glue potential

Starting with the FCC aluminum in the solid phase, the nano-sized aluminum particle takes on a spherical shape due to surface tension in the liquid phase after melting. A solid-state spherical nanoparticle can be obtained by cooling the liquid aluminum down to a temperature below the melting point, as shown in Figure 5.3. The density contour can be obtained using the post-processing code, in which the atoms in the computational domain are mapped on a grid and the thermodynamic properties like density are

calculated by averaging the properties in all the cells. The result agrees closely with the density of solid-state aluminum of  $2700 \text{ kg/m}^3$ , further validating the simulations.

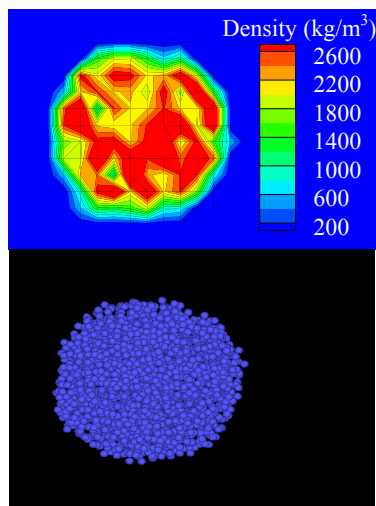


Figure 5.3: A 4 nm aluminum particle in solid state; the glue potential

The calculations using the five potentials were also checked against the cohesive energies of bulk aluminum in the solid state using the micro-canonical ensemble. Table 5.1 shows the comparison of cohesive energies obtained in the current study with those reported in the literature. The calculated energies match exactly the values found in the literature.

Table 5.1: Cohesive energies for bulk aluminum

Potential	Calculated (eV)	Literature (eV)
Lennard-Jones Potential	-3.353	-
Glue Potential	-3.360	-3.360 (Ercolessi and Adams, 1994)
Embedded Atom Potential	-3.385	-
Streitz-Mintmire Potential	-3.385	-3.390 (Streitz and Mintmire, 1994)
Sutton-Chen Potential	-3.312	-3.340 (Sutton and Chen, 1990)



The effect of particle size on melting in vacuum was investigated. Figure 5.4 shows the results using isobaric-isoenthalpic ensembles based on five different potentials. The corresponding numerical values are listed in Table 5.2. The melting temperature increases from 473 K for a 2 nm particle and reaches the bulk value of 937 K for 8 nm and larger-sized particles. Annealing was accomplished with the velocity scaling at a rate of 0.01 K per step. The results obtained in the present study bears a close resemblance to the experimental data of Eckert et al., but cannot be compared quantitatively because of the absence of oxide layer in the simulations (Eckert et al., 1993).

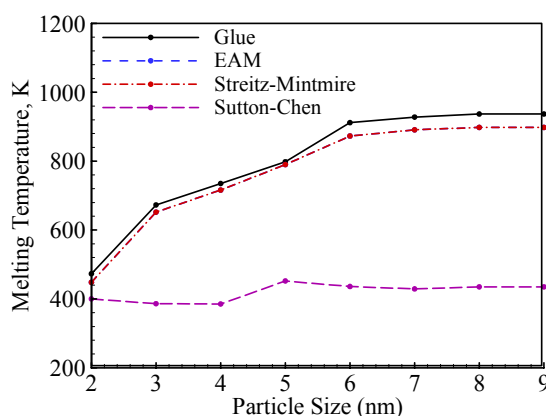


Figure 5.4: Melting point of nano-sized aluminum particle as function of particle size

The two-body Lennard-Jones potential failed to predict the melting point for nano-scale aluminum particles. Even at 1200 K, the particle still remains in the solid state, and only an increase in the vibrational frequency was observed. A similar phenomenon was noted in the simulations for bulk aluminum. The Sutton-Chen potential was found to predict geometrical structures for nano clusters very accurately, but failed to provide an accurate prediction of the melting point for nano-sized aluminum particles. This is an example where a potential fitted to structural properties like elastic constants

and bulk modulus fails to perform well for thermodynamic properties. The glue and Streitz-Mintmire potentials are comparable. The former generally leads to a melting temperature about 50-100 K higher than the latter does. The success of the glue and Streitz-Mintmire potentials in capturing the effect of size on melting of nano-sized aluminum particles once again underlines the importance of many-body potentials for modeling aluminum behavior.

Table 5.2: Melting points of nano-scale aluminum particles as function of particle diameter

Potentials	Particle Size (Atoms)								
	2nm (256)	3nm (864)	4nm (2048)	5nm (4000)	6nm (6912)	7nm (10976)	8nm (16384)	9nm (23328)	Bulk (pbc)
Lennard-Jones	-	-	-	-	-	-	-	-	-
Glue	473	673	735	798	912	928	937	937	1244
Embedded-Atom	448	652	716	790	873	891	898	898	1146
Streitz-Mintmire	448	652	716	790	873	891	898	898	1146
Sutton-Chen	400	386	385	452	436	429	435	435	529

The glue and Streitz-Mintmire potential predict bulk melting points of 1244 K and 1146 K, respectively, which are greater than the thermodynamic melting point by about 18%. According to the study by Lutsko et al. a factor should be introduced between the simulated (structural) and the actual (thermodynamic) melting points when periodic boundary conditions are enforced for bulk materials (Lutsko et al., 1989). The thermodynamic melting point is approximately 0.75-0.85 times its structural counterpart. Applying this factor to obtain the predicted thermodynamic melting point gives a value close to 940 K for bulk aluminum. Since, in the case of particles, the free surface acts as a

nucleation site for melting, the phase change predicted by NPH simulations directly corresponds to the thermodynamic melting and no correction factor is required.

Figure 5.5 shows final spherical shapes attained by aluminum nanoparticles in the size range of 2-9 nm at 1200 K as a result of surface tension. All the simulations commenced with cubic geometries and were based on glue potential.

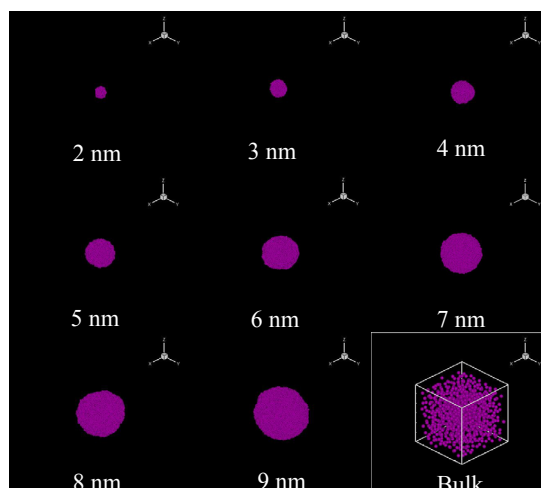


Figure 5.5: Spherical shape assumed by nano-scale aluminum particles after melting

In all the simulations discussed above, the aluminum temperature was increased continuously by means of velocity scaling, and melting was identified based on the variations in the structural and thermodynamic properties. The procedure amounts to the heating of a solid material in vacuum until the transition to a liquid state is achieved. For particles containing 500 atoms or less, uncertainties arise in characterizing the phase transition due to the co-existence of the solid and liquid phases. An alternative approach to obtain the melting point is thus implemented by equilibrating the particle at specific temperatures and calculating the thermodynamic and structural properties for each

respective state. The method is more appropriate for small clusters, although it is computationally more expensive. Figure 5.6 shows the results for a 2 nm particle (256 atoms) from such equilibrium simulations in terms of the variation of potential energy as a function of temperature. The melting was characterized by fluctuations in the potential energy, a phenomenon referred to as dynamic melting by Alavi et al (Alavi et al., 2006). The particle oscillates between the liquid and solid phases in the temperature range of 450-475K, as evidenced by the fluctuations in potential energy. As in the previous simulations, the Lennard-Jones and Sutton-Chen potentials could not predict the dynamic melting behavior accurately. The glue and Streitz-Mintmire potentials, although they produce different magnitudes of equilibrium potential energy, result in the same temperature range for dynamic melting.

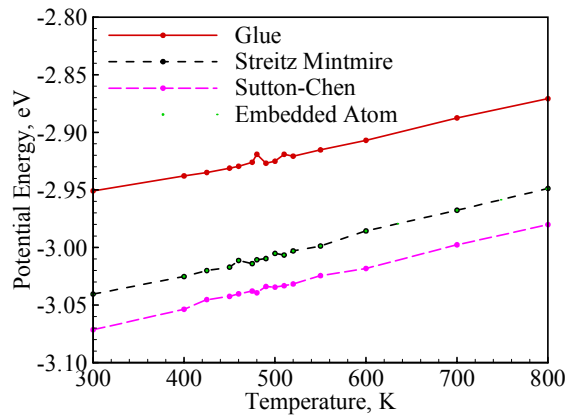


Figure 5.6: Variation of equilibrium potential energy with temperature for 2 nm sized particle (256 atoms)

The effect of surface charges on the melting of a nanoparticle also needs to be investigated, although this phenomenon is often negligible for a bulk material due to the lack of surface. To this end, the results of simulations performed for nanoparticles in the

range of 2-9 nm, using the embedded-atom and Streitz-Mintmire potentials, were analyzed. The two potentials are identical except that the former ignores completely the electrostatic part of the latter. The development of surface charges for 2-9 nm particles appears to be too small to exert a significant influence on the electrostatic part of the Streitz-Mintmire potential, and both potentials result in exactly the same melting point. A similar observation was reported by Alavi et al. based on a simulation of 500 aluminum atoms in an FCC structure. Figure 5.7 shows the final spherical shape with charges for a 3 nm nanoparticle. For particles smaller than 3 nm, the surface charge development plays a negligible role in determining the dynamic melting behavior as well and the results are identical to those from embedded-atom potential.

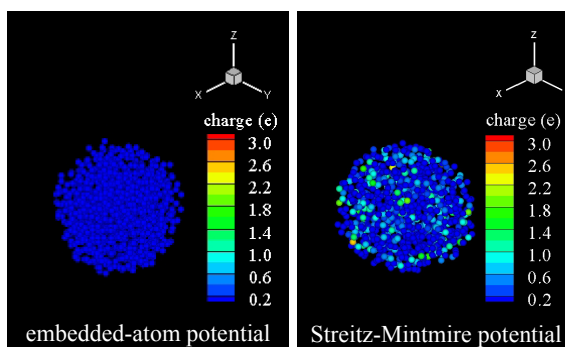


Figure 5.7: Surface charge development for 3 nm aluminum particle using the embedded-atom and Streitz-Mintmire potentials

## 5.4 Conclusions

Molecular-dynamics simulations using isobaric-isoenthalpic (NPH) ensembles have been performed to characterize the melting of nano-sized aluminum particles in the range of 2-9 nm and to investigate the effect of surface charge development on melting.

Five different potentials were implemented. The two-body Lennard-Jones potential failed to predict the melting point. The Sutton-Chen potential, validated against structural properties, also led to erroneous results of the melting phenomenon. The glue and Streitz-Mintmire potentials predicted accurately the size dependence of the melting temperature, but the former generally yielded a melting temperature about 50-100 K higher than the latter did. The difference in the melting behavior between a nanoparticle and a bulk material was investigated. Sharp variations in structural and thermodynamic properties were found across the melting point for a bulk material. In contrast, only smooth changes were observed for nanoparticles, due to the presence of surface pre-melting. The melting temperature of an aluminum particle increases monotonically from 473 K at 2 nm to the bulk value of 937 K at approximately 8 nm. As the size decreases below a critical value, the increased surface-to-volume ratio and associated higher surface energy enhanced vibrational instability. This interface-induced disorder is responsible for the size dependence of particles melting at nano scales. For particle sizes less than 3 nm, the solid and liquid phases were found to coexist. The effect of surface charge development on melting was also explored by analyzing the results from the embedded-atom and Streitz-Mintmire potentials. The two potentials are identical except that the former ignores completely the electrostatic part of the latter. The development of surface charges had negligible effect on the particle melting characteristics.

## Chapter 6

### Effect of Voids and Pressure on Melting of Nano-Particulate and Bulk Aluminum

#### 6.1 Background

After exploring the effect of size dependence on melting of particulate aluminum and investigating the melting characteristics of pure aluminum nanoparticle, effort was applied to improve the understanding of melting of particulate phase at nano scales and the effect of parameters like internal defects (voids) on material properties. From a structural point of view, voids have been the subject of research for both the bulk and particulate phases. Allard et al. reconstructed the images of 5-15 nm palladium particles from electron holograms using a field-emission-transmission electron microscope, and reported for the first time the existence of internal voids in metallic particles (Allard et al., 1994). Yoshiharu et al. discussed the formation of voids in pure aluminum quenched in hydrogen gas (Shimomura and Moritaki, 1981). The number density of voids was found to be proportional to the square root of the partial pressure of hydrogen in the gas. Marian et al. examined nano-void deformation in aluminum subject to cyclic shear deformations (Marian et al., 2005) and the growth of these voids under hydrostatic tensions (Marian et al., 2004). Hyuk et al. developed techniques for preparing colloidal particles with hollow interiors (Hyuk et al., 2005). In parallel, considerable progress has been recently made in molecular self assembly and supra molecular control for synthesizing and assembling nano-structured energetic materials (Online, 2008).

Aluminum nanoparticles manufactured as a result of these efforts may likely contain internal voids of some sort and can affect the melting point.

The term melting point itself has been used in the literature with different definitions. *Experimental melting point* is the temperature for phase transition as observed in an experimental set up. *Thermodynamic* and *structural melting points* are terms used in theoretical and numerical studies. The former,  $T_m$ , ideally should be identical to the experimental melting point for a real solid. It is based on the coexistence of the solid and liquid phases, and theoretically is the temperature at which the solid and liquid Gibbs free energies are equal. Since calculation of free energies is a non-trivial task, in most molecular dynamics studies the bulk is simulated using periodic boundary conditions without any defects. Such a numerical framework produces structural melting,  $T_s$ . The absence of any nucleation sites in a perfect crystal leads to heating the substance beyond  $T_m$ , a phenomenon known as superheating. Structural melting refers to the limit beyond which there is general collapse of lattice structure. Results obtained from a numerical simulation correspond to either structural or thermodynamic melting, depending on the properties of the initial crystal. The theories regarding vibrational instability, lattice shear instability, and catastrophic generation of dislocations are associated with structural melting.

Deliberately introducing clusters of vacancy defects to avoid superheating in a perfect crystal is referred as defect-nucleated melting. The concept was introduced and reported in the numerical studies by Lutsko et al. (Lutsko et al., 1989) and Phillpot et al. (Phillpot et al., 1989) These studies highlighted the fact that the nucleation of the liquid phase at the defect is the dominant initiation mechanism of melting, and hence the



melting of an ideal crystal with periodic boundary conditions takes place at a temperature higher than the experimental melting point. Phillpot et al. investigated the melting characteristics of silicon in the presence of a grain boundary and a free surface (110) using molecular dynamics simulations associated with the Stillinger-Weber potential. Lutsko et al. simulated the high temperature behavior of a grain boundary, free surface and a planar array of voids on (001) plane of copper using the embedded-atom-method potential. The investigation found structural and thermodynamic melting points of 1450 K and 1171 K respectively for copper. Recently, the concept of defect-nucleated melting has been implemented by Solca et al. to determine the theoretical melting curves of argon and neon, as a function of pressure using isobaric-isoenthalpic molecular dynamics and Lennard Jones potentials (Solca et al., 1997; Solca et al., 1998). The structural melting points for an ideal crystal were found to be 20% higher than the thermodynamic melting points for lattices with a defect in the form of a void. The work of Lutsko et al. shows that there exists a constant ratio between the structural and thermodynamic melting points ( $f = T_s / T_m$ ) (Lutsko et al., 1989). For copper and argon the ratios are 1.234 and 1.176, respectively (Lutsko et al., 1989; Solca et al., 1997). Agarwal et al. simulated defect-nucleated melting of argon over a broader range of pressures of 0.094-531.6 kbar (Agarwal et al., 2003). The melting point was found to be independent of the shape and location of the void.

Experimental studies have suggested that small atomic clusters exhibit characteristics different from those of a bulk substance. A decrease of the melting point by 30% has been measured in metallic clusters of diameters of 20-30 Å (Ph. Buffat and Borel, 1976). A modification of surface conditions can depress the melting point or

substantially superheat the solid. An ideal crystal melts at a temperature higher than the experimental or thermodynamic melting point, and imperfections such as voids reduce the melting point. The extent to which these imperfections affect the melting point, however, is very subjective and varies with substance. Since the presence of a surface acts as a nucleation site for melting, an alteration in the surface properties can have a major impact on the melting temperature and related phenomena for the substance.

## 6.2 Objectives

In our earlier work based on molecular dynamics simulations, the effects of particle size and surface charge development on the melting of particulate aluminum were investigated in the range of 2-9 nm (Puri and Yang, 2007) as discussed in Chapter 5. The work involved nano-sized aluminum particles in the range of 2-9 nm. Results indicated that as the particle size decreases below a critical value (8 nm), owing to the increase in the surface-to-volume ratio, the melting temperature becomes a size-dependant property and decreases monotonically with decreasing diameter, from a bulk value of 937 K at approximately 8 nm to 473 K at 2 nm (Puri and Yang, 2007). The finding was found to be consistent with those from other experimental and numerical studies (Alavi et al., 2006; Wronski, 1967; Eckert et al., 1993; Bucher et al., 2000). As an extension of the previous work, this step explores the effect of pressure and defects in the form of voids on the melting characteristics of nano-particulate aluminum in the range of 2-9 nm where bulk properties break down. From pure scientific perspective this also

helps to explore the difference between structural and thermodynamic melting for bulk and particulate phase in case of metals like aluminum.

The present work involves MD simulations using an isobaric-isoenthalpic (NPH) ensemble. The Glue potential is selected to treat the inter-atomic interactions, because of its ability to capture the size dependence of thermodynamic properties for particulate aluminum (Puri and Yang, 2007). A combination of structural and thermodynamic parameters, including the potential energy, Lindemann index, translational-order parameter, and radial-distribution functions, are used to characterize the melting process. For the particulate phase, spherical nanoparticles up to 9.0 nm are considered. Voids of different shapes and sizes are taken into account, and results are compared with perfect particles having no defects. The underlying mechanisms of the entire melting process are examined using snapshots of the time evolution of atomic positions and density contours. For the bulk phase, crystals composed of 864 and 2048 atoms are considered. The structural melting point,  $T_s$  for an ideal crystal is found to be 32% higher than the thermodynamic melting point,  $T_m$  for lattices with a defect.

### 6.3 Results and Discussion

The general framework outlined in Chapter 4 and used in MD study mentioned in Chapter 5 was first applied to study the melting of bulk aluminum with and without defects. The simulations were carried out by arranging atoms in a FCC lattice structure and evolving the system with periodic boundary conditions. Figure 6.1 shows the variations of thermo-mechanical properties with increasing temperature for a perfect

crystal of 864 atoms in a vacuum. Homogeneous melting due to lattice instability was observed at a temperature of 1244 K, as evidenced by abrupt changes in the potential energy, atomic density, Lindemann index, translational order parameter, and radial distribution function. This phenomenon is commonly referred to as structural melting, and the associated transition temperature is greater than the thermodynamic melting point (940 K) by 32%.

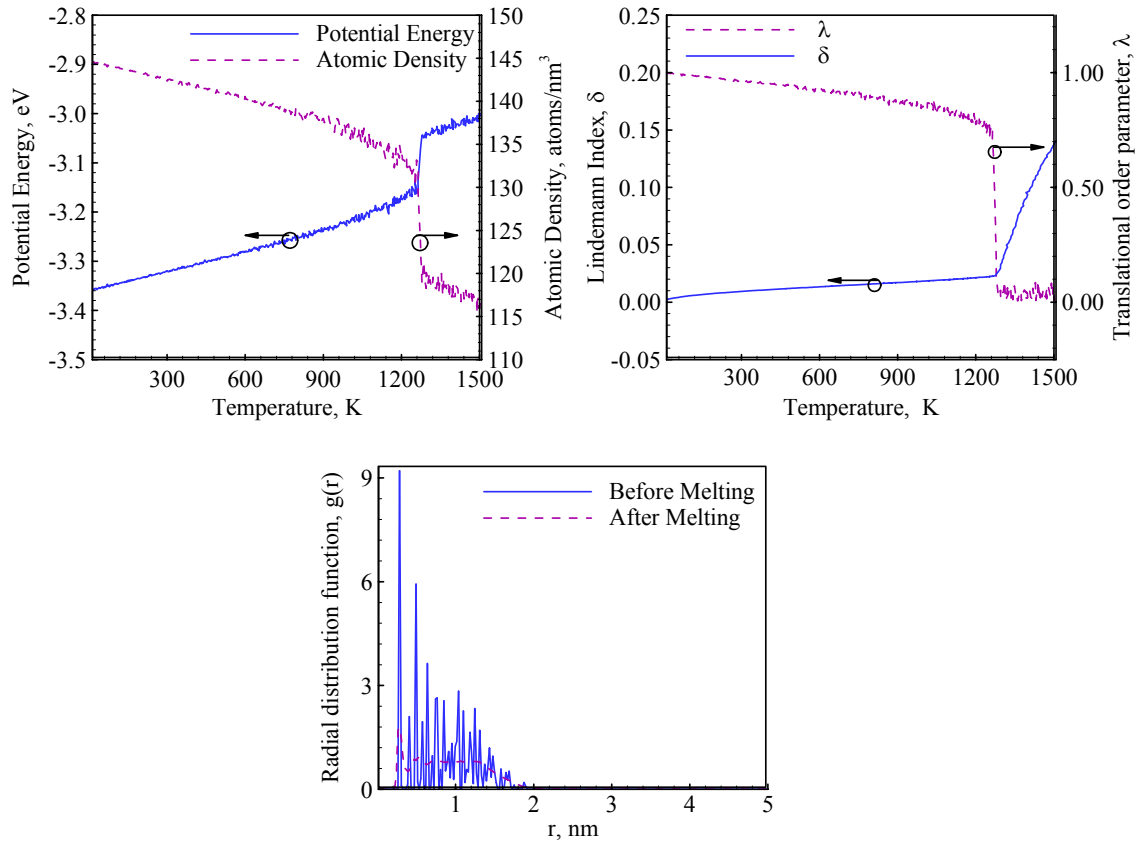


Figure 6.1: Variations of structural and thermodynamic properties during melting of bulk aluminum; perfect crystal of 864 atoms without defects

To obtain the ratio between the structural and thermodynamic melting points, bulk crystals with different void sizes in the range of 0.19-4.0 nm<sup>3</sup> were considered, as shown in Figure 6.2. The procedure followed the same approach adopted in previous studies

(Lutsko et al., 1989; Phillpot et al., 1989; Solca et al., 1997; Solca et al., 1998; Agarwal et al., 2003). The influences of void shape and location were also treated. For example, a void of  $1.05 \text{ nm}^3$  can be implemented by creating either a  $4 \times 2 \times 2 \text{ nm}^3$  or a  $4 \times 4 \times 1 \text{ nm}^3$  void geometry, through the removal of 64 atoms from a crystal of 864 atoms. Voids provide a nucleation site for simulating thermodynamic melting. There, however, exists a range of critical void size for thermodynamic melting. A very small void size is insufficient for nucleation of the liquid phase, and a void size larger than the critical value can cause collapse of the crystal. As compared to 1244 K for a perfect crystal, the melting point for a crystal with voids initially decreases with void size, and then plateaus close to the thermodynamic melting point of aluminum, as seen in Figure 6.3. The situation is consistent with observations made in previous studies on argon and copper (Lutsko et al., 1989; Solca et al., 1997). When the void size exceeds  $1.7 \text{ nm}^3$ , the crystal collapses suddenly, and the phenomenon of phase change cannot be simulated.

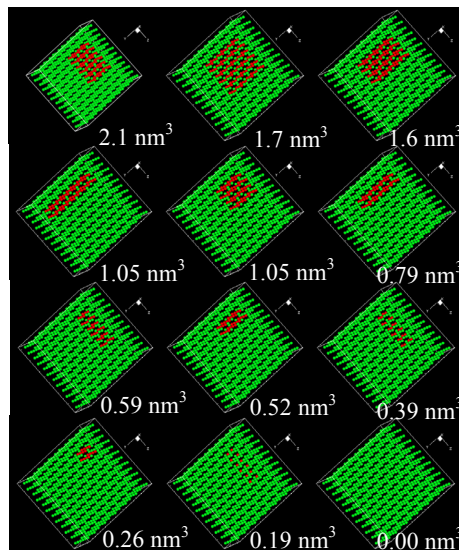


Figure 6.2: Different void geometries considered for bulk aluminum with 864 atoms

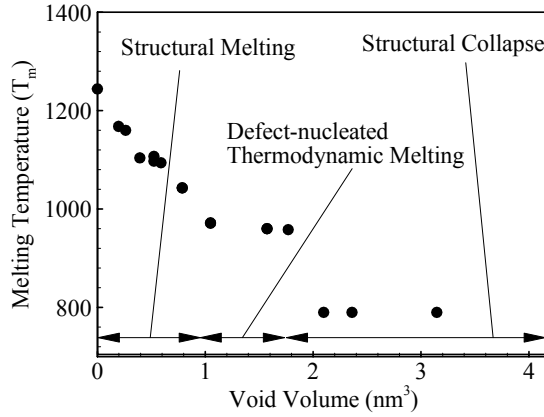


Figure 6.3: Effect of void size on melting of bulk aluminum with 864 atoms

The melting temperature is a function only of the volume of the void, not its shape. For a volume of  $1.05 \text{ nm}^3$ , the two geometries shown in Figure 6.2 produce exactly the same melting point. When the void size falls in the range of  $1.0\text{--}1.7 \text{ nm}^3$ , the void only provides a nucleation site and leads to the same temperature for the phase change, i.e., the thermodynamic melting point, irrespective of the shape of the void. From all these cases, the ratio of 1.32 between the structural and thermodynamic melting points was consistently obtained.

Figure 6.4 shows the case of thermodynamic melting for a  $1.05 \text{ nm}^3$  void. The variations of properties are not as steep as the structural melting because of the nucleation at the void. The situation with a large void size of  $4.0 \text{ nm}^3$  is shown in Figure 6.5, for which the crystal collapses. The potential energy decreases, but the atomic density increases. The trend is opposite to that observed during melting. The whole phenomenon occurs at a temperature (800 K) much lower than the thermodynamic melting point (940 K), indicating the collapse of the crystal and no phase change.

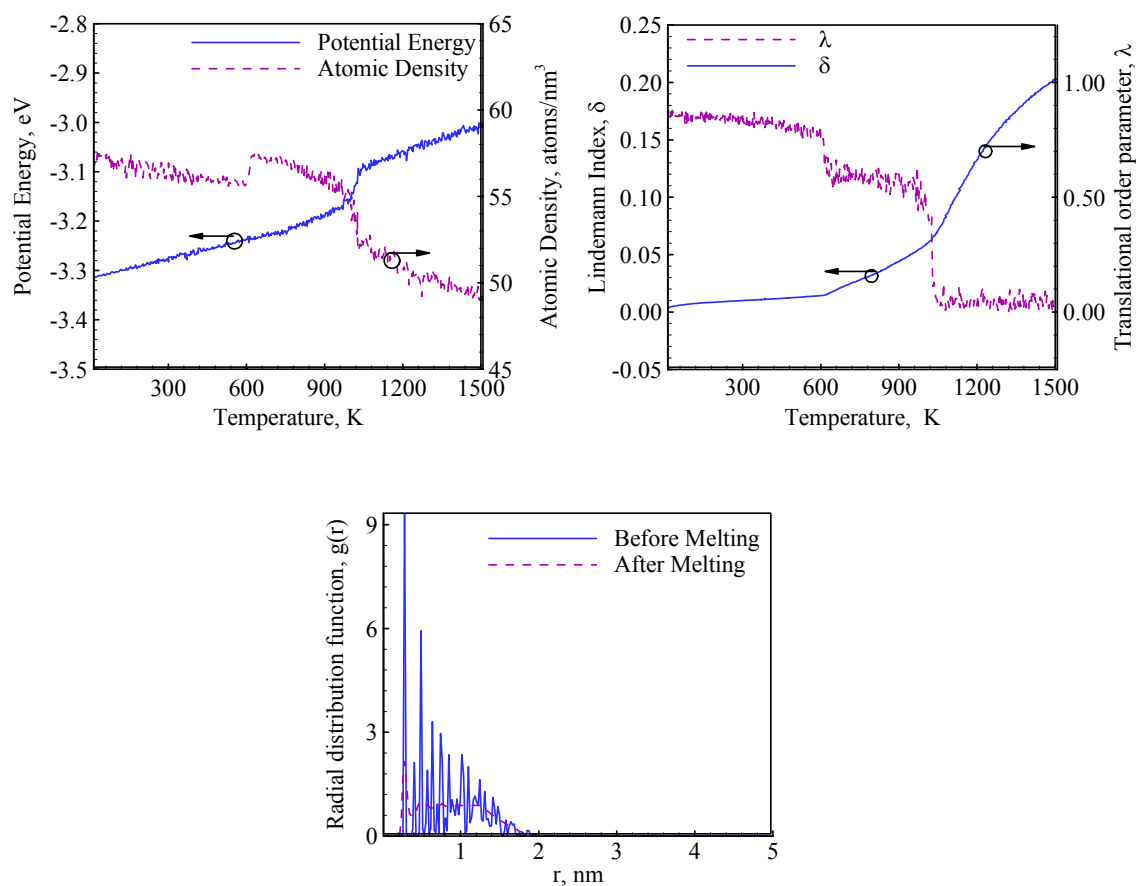


Figure 6.4: Variations of structural and thermodynamic properties during melting of bulk aluminum; crystal of 864 atoms with 1.05 nm<sup>3</sup> void

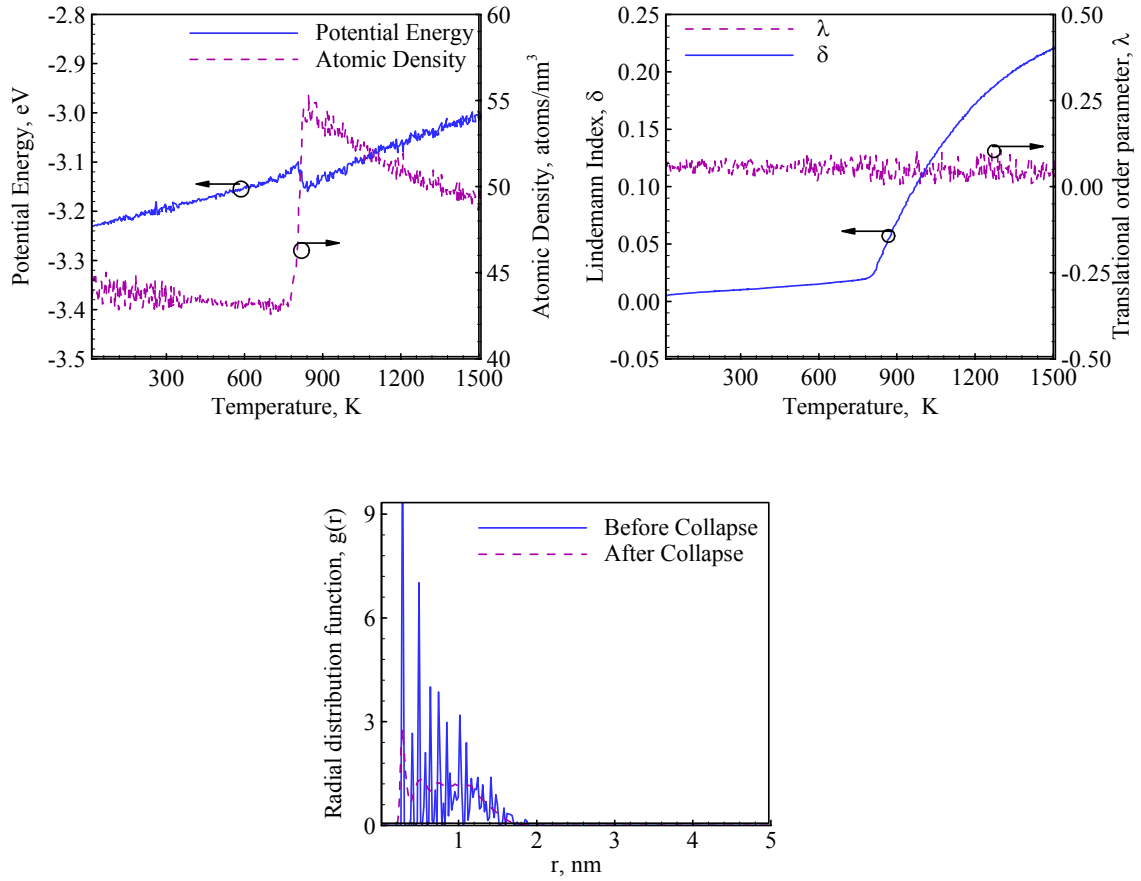


Figure 6.5: Variations of structural and thermodynamic properties of bulk aluminum showing lattice collapse; crystal of 864 atoms with 4.0 nm<sup>3</sup> void

Figure 6.6 shows the temporal evolution of atomic positions, illustrating the difference between the structural melting, thermodynamic melting, and lattice collapse of the crystal. In the case of structural melting, the phase transition is abrupt and homogeneous, as seen in Figure 6.6a. The crystal has solid structure up to 124.2 ps, and a phase change occurs suddenly at 126.9 ps, due to vibrational instability without any nucleation. In the case of thermodynamic melting, however, the nucleation starts near the void, as indicated by the local concentration of atoms around the void, and proceeds to the rest of the crystal. Figure 6.6b shows thermodynamic melting with a void size of 1.05



$\text{nm}^3$ . The nucleation starts near the void at 85.8 ps, and the whole crystal melts by 102.3 ps. If the void size exceeds its critical value, the whole crystal collapses and cannot be put in the category of either thermodynamic or structural melting. The breakdown of the structure with a void of  $4 \text{ nm}^3$  is evidenced in Figure 6.6c, and is comparatively different from the mechanism of melting. At 78.9 ps, when the temperature of the crystal is around 790 K, the atoms close to the void leave their positions and fill up the void space. No phase change is observed in this case.

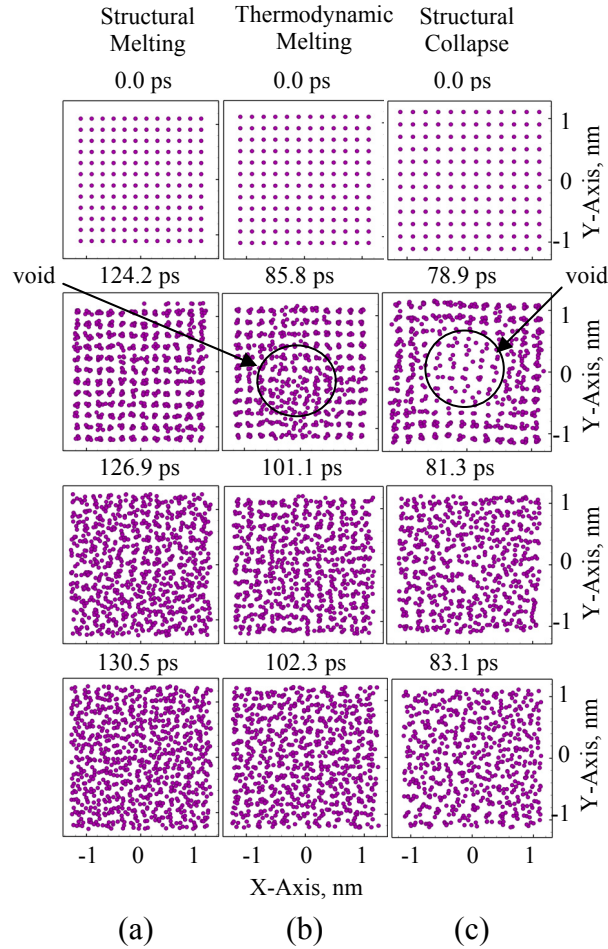


Figure 6.6: Temporal evolution of atomic positions, showing mechanisms of melting and structural collapse for bulk aluminum with 864 atoms (a) without defect, (b) with a void size of  $1.05 \text{ nm}^3$ , and (c) with a large void size of  $4 \text{ nm}^3$

To study the effect of the number of atoms in bulk aluminum on defect-nucleated melting, a similar analysis was performed for a crystal with 2048 atoms. The structural and thermodynamic melting points (plateau region) are the same as those for 864 atoms, i.e., 1244 and 940 K, respectively. Figure 6.7 shows the variation of the melting point as a function of void size for bulk aluminum with 2048 atoms. The structural melting point

for a perfect crystal is observed at 1244 K, and the melting point decreases as the void size increases, showing a trend identical to that of bulk with 864 atoms.

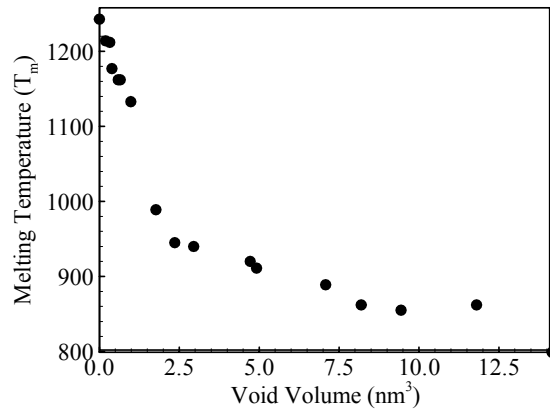


Figure 6.7: Effect of void size on melting of bulk aluminum with 2048 atoms

The range of the void size for defect-nucleated melting increases as the number of atoms considered to represent the bulk phase increases. Figure 6.8 shows the variation of the critical void size for the lattice collapse as a function of bulk volume. For 2048 atoms, a void size on the order of 2-5 nm<sup>3</sup> results in thermodynamic melting, as compared to 1-1.7 nm<sup>3</sup> for 864 atoms. From the study of perfect and defected crystals, it can be concluded that the ratio between the structural and thermodynamic melting points ( $f = T_s / T_m$ ) for aluminum is 1.32, close to the ratio of 1.234 for metals like copper. Copper is known to have stronger cohesive forces than aluminum, and hence should have a higher structural melting point than aluminum. The thermodynamic melting point of copper is 1357 K, and the corresponding structural melting point is 1674 K, compared to 1244 K for aluminum.

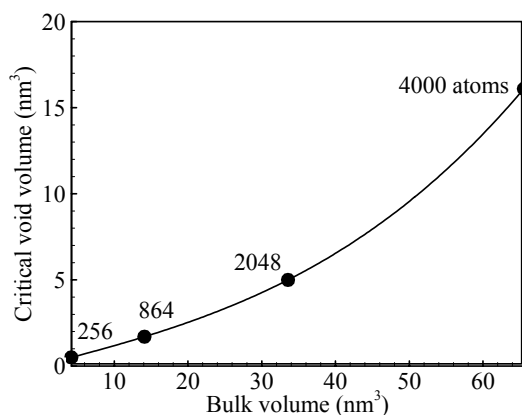


Figure 6.8: Variation of critical void size for lattice collapse as a function of bulk aluminum volume

After establishing the benchmark result for bulk aluminum, effort was applied to explore the melting of nano particulates in the range of 2.0-9.0 nm. The effect of voids with different geometries and sizes were considered. Results were compared for particles with and without voids. Figure 6.9 shows some of the defect configurations treated for a 5.5 nm nanoparticle (5072 atoms). The influence of void size up to  $14.1 \text{ nm}^3$  on the melting temperature is given in Figure 6.10. The melting temperature remains constant at 912 K (Puri and Yang, 2007) for small voids up to  $1 \text{ nm}^3$ . Since the surface is already available for nucleation, the presence of a small void just acts as another nucleation site and exerts little influence on the thermodynamic phase change. The melting point, starts dropping as the void volume increases beyond  $1 \text{ nm}^3$ , due to the increase in forces causing the structural instability. As the void size exceeds  $8 \text{ nm}^3$ , the particle is unable to hold these forces associated with the introduction of the void, and the crystal collapses abruptly at 700 K for a  $10 \text{ nm}^3$  void.

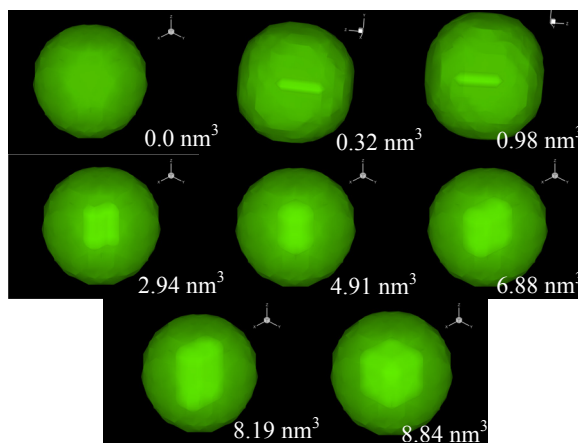


Figure 6.9: Different void geometries considered for a spherical 5.5 nm aluminum particle

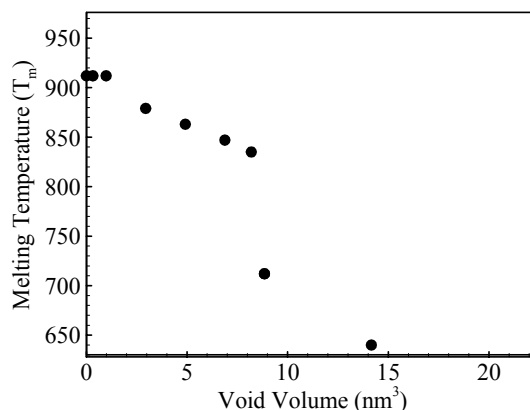


Figure 6.10: Effect of void size on melting for a spherical 5.5 nm aluminum particle

The melting phenomenon is also examined through the evolution of atomic positions and density contours in Figs. 6.11 and 6.12 , respectively. In Figure 6.12a, the nucleation process commences at 97.2 ps and is completed by 108.9 ps for a perfect nanoparticle. In the case with a void size of 0.98 nm<sup>3</sup>, the nucleation starts simultaneously at the surface and void at 92.1 ps. The phase change spreads to the rest of the particle until melting occurs at 107.1 ps, as evidenced in Figure 6.12b. The void size

of  $8.2 \text{ nm}^3$  shown in Figure 6.12c is too big for the particle to retain its structural stability, and the particle starts collapsing at 76.5 ps. The above analysis was conducted in a vacuum. The effect of pressure was investigated at 1, 5, 10, 50, 100 and 300 atm. The influence was found to be negligible, and the same melting temperature was observed for all the pressures considered.

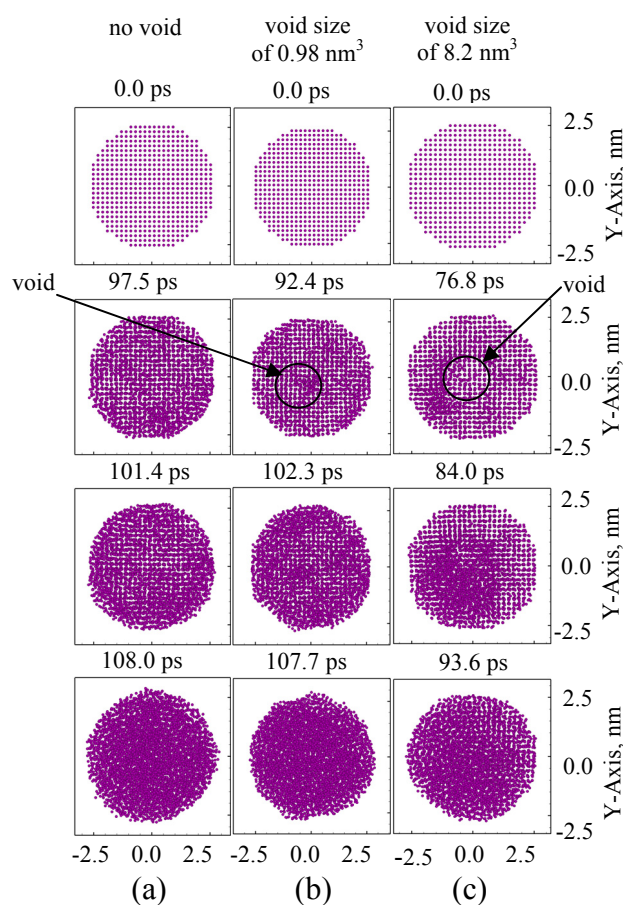


Figure 6.11: Time evolution of atomic positions, showing mechanism of melting for a 5.5 nm nanoparticle (a) without defect, (b) with a void size of  $0.98 \text{ nm}^3$ , (c) with a large void size of  $8.2 \text{ nm}^3$

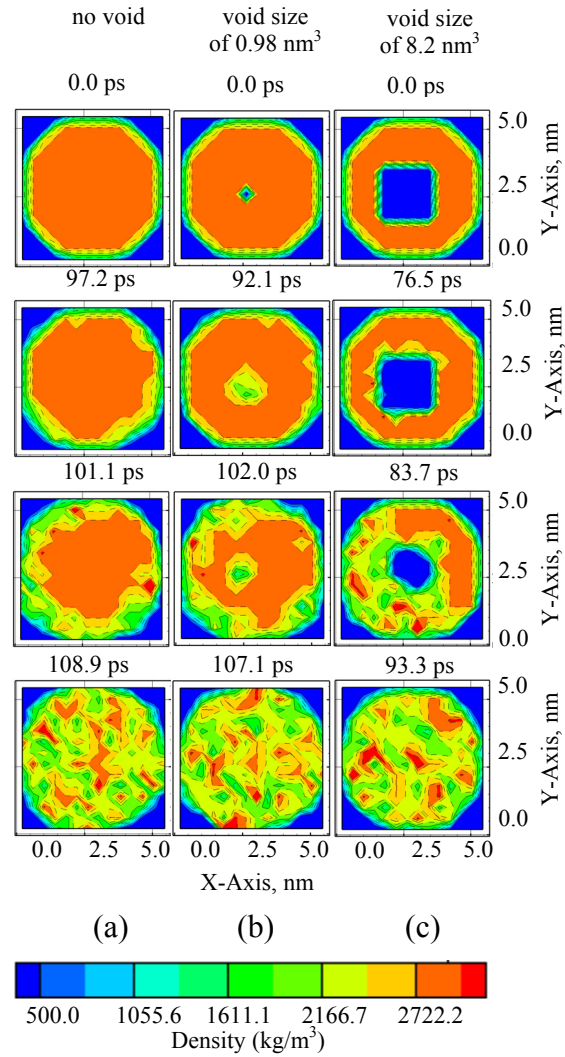


Figure 6.12: Time evolution of density contours, showing mechanism of melting for a 5.5 nm nanoparticle (a) without defect, (b) with a void size of 0.98 nm<sup>3</sup>, (c) with a large void size of 8.2 nm<sup>3</sup>

A similar phenomenon was observed for a 8.5 nm particle, as shown in Figure 6.13. Thermodynamic melting occurs at 940 K, which is in agreement with the previous result (Puri and Yang, 2007). There is no variation in the melting point by introduction of a void up to 5 nm<sup>3</sup>. The deviation from the thermodynamic melting point then occurs due to the effect of nucleation near the void. As the void size increases, the

lattice stability decreases, further lowering the melting point. The lattice structure of the particle collapses when the void size becomes around  $20 \text{ nm}^3$ . The melting mechanism can also be explored by the temporal evolution of atomic positions and density contours shown in Figs. 6.14 and 6.15, respectively. For a perfect particle, the phase change proceeds from the surface to the interior, as evidenced in Figs. 6.14a and 6.15a. For the void size of  $5 \text{ nm}^3$ , nucleation starts at both the void and surface at 92 ps, as shown in Figs. 6.14b and 6.15b. For a large void size of  $20 \text{ nm}^3$  exceeding the critical value, lattice collapse occurs directly at 57.4 ps, and no phase change is observed, as indicated in Figs. 6.14c and 6.15c.

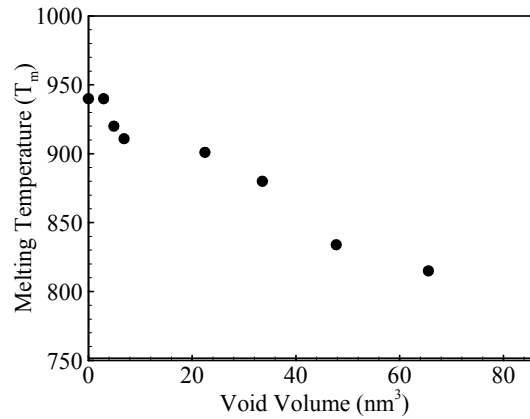


Figure 6.13: Effect of void size on melting of a spherical 8.5 nm aluminum nanoparticle



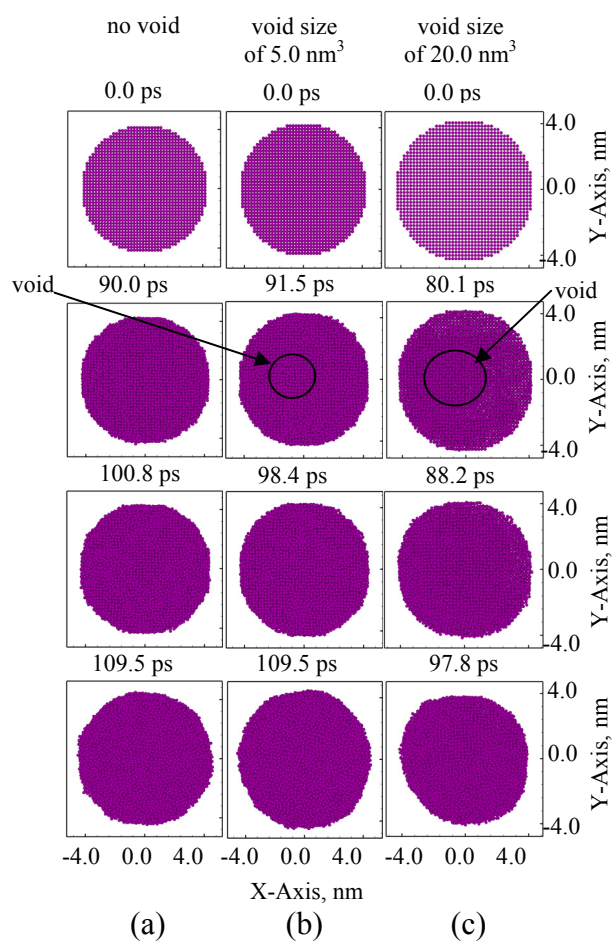


Figure 6.14: Time evolution of atomic positions, showing mechanism of melting for a 8.5 nm nanoparticle (a) without defect, (b) with a void size of 5.0 nm<sup>3</sup>, (c) with a large void size of 20.0 nm<sup>3</sup>

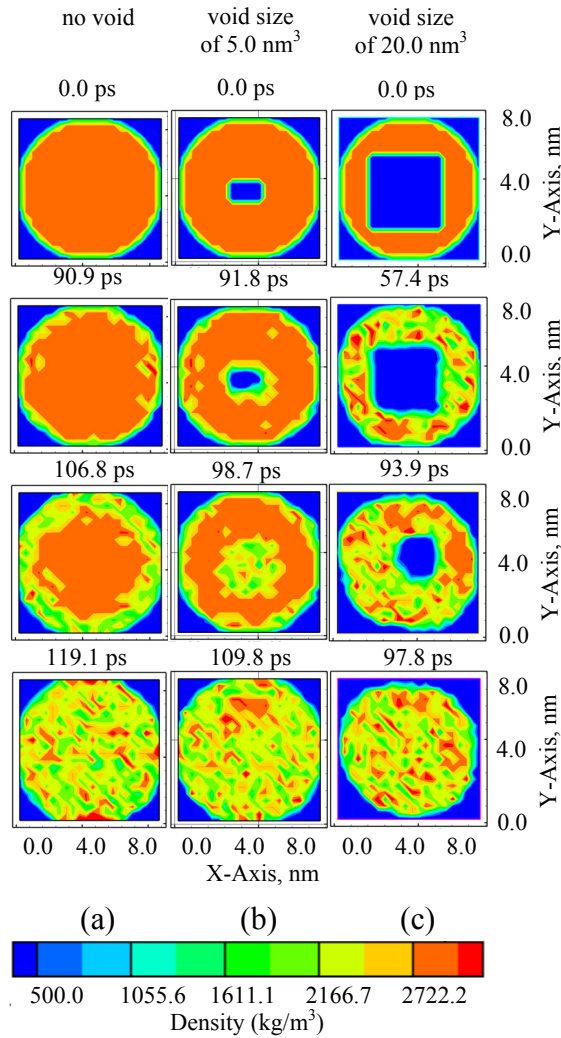


Figure 6.15: Time evolution of density contours, showing mechanism of melting for a 8.5 nm nanoparticle (a) without defect, (b) with a void size of 5.0 nm<sup>3</sup>, (c) with a large void size of 20.0 nm<sup>3</sup>

## 6.4 Conclusions

The effect of defects in the form of voids on the melting of bulk aluminum and aluminum nano-particulates in the size range of 2-9 nm has been studied using isobaric-

isoenthalpic (NPH) ensembles. A variety of void shapes and sizes were treated, and results were compared with perfect materials. Detailed mechanisms dictating the melting phenomenon were explored. For nanoparticles, nucleation occurs simultaneously at both the surface and void. Void becomes effective only if its size exceeds a critical value, which increases with increasing size of the particle. For 5.5 nm and 8.5 nm particles, the critical void sizes are 1 and 5 nm<sup>3</sup>, respectively. The effect of pressure on the melting of nano-particulate aluminum was found to be insignificant in the range of 1-300 atm. For bulk aluminum, the structural melting of aluminum takes place at a temperature of 1244 K. The ratio between the structural and thermodynamic melting points was found to be 1.32, independent of the void shape and size. This ratio was comparable to the result obtained for other metals like copper.

## Chapter 7

### Thermo-Mechanical Behavior of Nano Aluminum Particles with Oxide Layers

#### 7.1 Background

Nano aluminum particles are associated with higher specific surface area, higher reactivity, potential ability to store energy in surface defects, lower melting points, and smaller characteristic times for mass and energy transport. The work discussed in this chapter explores some of the fundamental issues concerning the behaviors of nano-sized aluminum particles with oxide layers, with emphasis placed on their thermo-mechanical properties during melting. Aluminum particles are usually covered with a passivating oxide layer ( $\text{Al}_2\text{O}_3$ ) with a thickness of the order of 2-5 nm (Bucher et al., 2000), which protects the particle from further oxidation and has a significant bearing on the thermodynamic and chemical properties of the particle. When introduced in a high temperature environment, the particle melts. The phenomenon involves solid-solid phase transformations, diffusion of cations and anions, and cracking within the oxide layer. Each of these processes plays an important role in determining the characteristics of particle ignition and combustion over a broad range of scales.

Particle size, in addition to material properties and ambient conditions, dictates the physiochemical behaviors of particles in various oxidizing environments. For micron-sized and larger aluminum particles, the ignition temperature coincides with the melting point of the surface oxide layer at 2327 K. The impervious nature of aluminum oxide

inhibits the ignition of aluminum. Once the layer melts, it coalesces to form an oxide cap. The aluminum core is then exposed to the ambient gases for oxidation. At nano scales (less than 100 nm), ignition occurs near the melting point of aluminum at 940 K through cracking of the oxide shell, possibly caused by the pressure buildup and/or phase transformations inside the shell. The primary objective of this work is to analyze these phenomena using Molecular Dynamics (MD) simulations.

In the previous study, the melting behavior of a pure nano aluminum particle was studied in the size range of 2-9 nm by means of molecular dynamics (MD) simulations (Puri and Yang, 2007). Five different potential functions (the Lennard-Jones, glue, embedded-atom, Streitz-Mintmire, and Sutton-Chen potentials) were implemented, and isobaric-isoenthalpic (NPH) ensembles were used. The melting temperature of a pure nanoparticle increases monotonically with increasing size, from 473 K at 2 nm to a bulk value of 937 K at approximately 8 nm. Among the five potentials considered, only the many-body glue and Streitz-Mintmire potentials accurately predicted the melting temperature as a function of particle size. A subsequent study was performed to investigate the effect of void size and pressure on the melting temperatures of bulk and nano-particulate aluminum (Puri and Yang, 2007b). Alavi and Thompson (Alavi et al., 2006) performed MD simulations for clusters of pure aluminum up to 1000 atoms, focusing on the cluster structure and dynamic coexistence of melting. Alavi et al. further explored the structure and charge distributions of bulk crystalline  $\text{Al}_2\text{O}_3$ , a surface slab of  $\text{Al}_2\text{O}_3$ , and an isolated  $\text{Al}_2\text{O}_3$  nanoparticle (Alavi et al., 2005). Campbell et al. simulated the oxidation of naked aluminum with a size of 20 nm (Campbell et al., 2005).

The aforementioned studies have provided much information about the melting behavior of pure aluminum particles at nano scales. Detailed knowledge for particles coated with oxide layers, however, is not available. The present study addresses this issue based on MD simulations.

## 7.2 Objectives

The Streitz-Mintmire potential was selected because of its ability to capture the size dependence of thermodynamic properties, and to handle interactions between aluminum and oxygen atoms. The work treats a spherical aluminum core in the face-centered cubic (FCC) structure covered with an oxide shell in both amorphous and crystalline (corundum) forms, as shown in Figure 7.1. Various fundamental processes involved in particle melting are explored over an appropriate range of particle size and oxide-layer thickness.

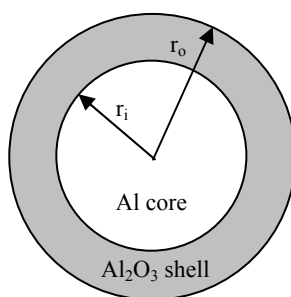


Figure 7.1: Schematic of a spherical nanoparticle with aluminum core and oxide shell

Isobaric-isenthalpic (NPH) and micro canonical (NVE) ensembles are employed to model the melting of bulk and nano-particulate aluminum. In NPH ensembles, a system of  $N$  atoms is coupled to an external source by introducing additional variables

into the Lagrangian using volume as an extra degree of freedom through mechanical coupling (Anderson, 1980) as discussed in Chapter 4. The equations of motion for NPH and NVE ensembles are numerically integrated using a fifth-order predictor-corrector and the Verlet algorithm, respectively. An optimum heating rate of 0.1 K per femto-second is employed based on the tradeoff between computational efficiency and resolution of calculated thermodynamic and structural properties. The macroscopic thermodynamic properties are derived from the instantaneous values using the equation of state and statistical mechanics. The Lindemann index measures the vibrational motion of particles, and is calculated as a function of the distance between atoms (Zhuo et al., 2002). The translational-order parameter is indicative of the ordered structure in any phase (Gezelter et al., 1997). It has a value of approximately unity for a solid state, and drops to nearly zero for a liquid state. A separate post-processing code is also developed to superimpose the numerical grid on the geometry under consideration, and to analyze the results based on the contours of various thermodynamic properties.

### 7.3 Results and Discussion

The theoretical and numerical framework summarized in the preceding section has been applied to study the particle melting behavior in the size range of 5-10 nm. The simulation commences with a spherical aluminum particle in an FCC crystal structure covered with either a crystalline or an amorphous oxide layer. The oxide thickness is 1-2.5 nm. Figure 7.2 shows the structures of nanoparticles under consideration at room temperature. A hexagonal crystal structure is chosen to treat crystalline  $\text{Al}_2\text{O}_3$ . In the case

of an amorphous layer, the shell is pre-heated to a temperature higher than the melting point of  $\text{Al}_2\text{O}_3$  (2327 K) and cooled to room temperature. The approach follows the standard technique of simulating amorphous  $\text{Al}_2\text{O}_3$  layer in literature (Hoang et al., 2005; Gutierrez et al., 2002; Chang et al., 2004).

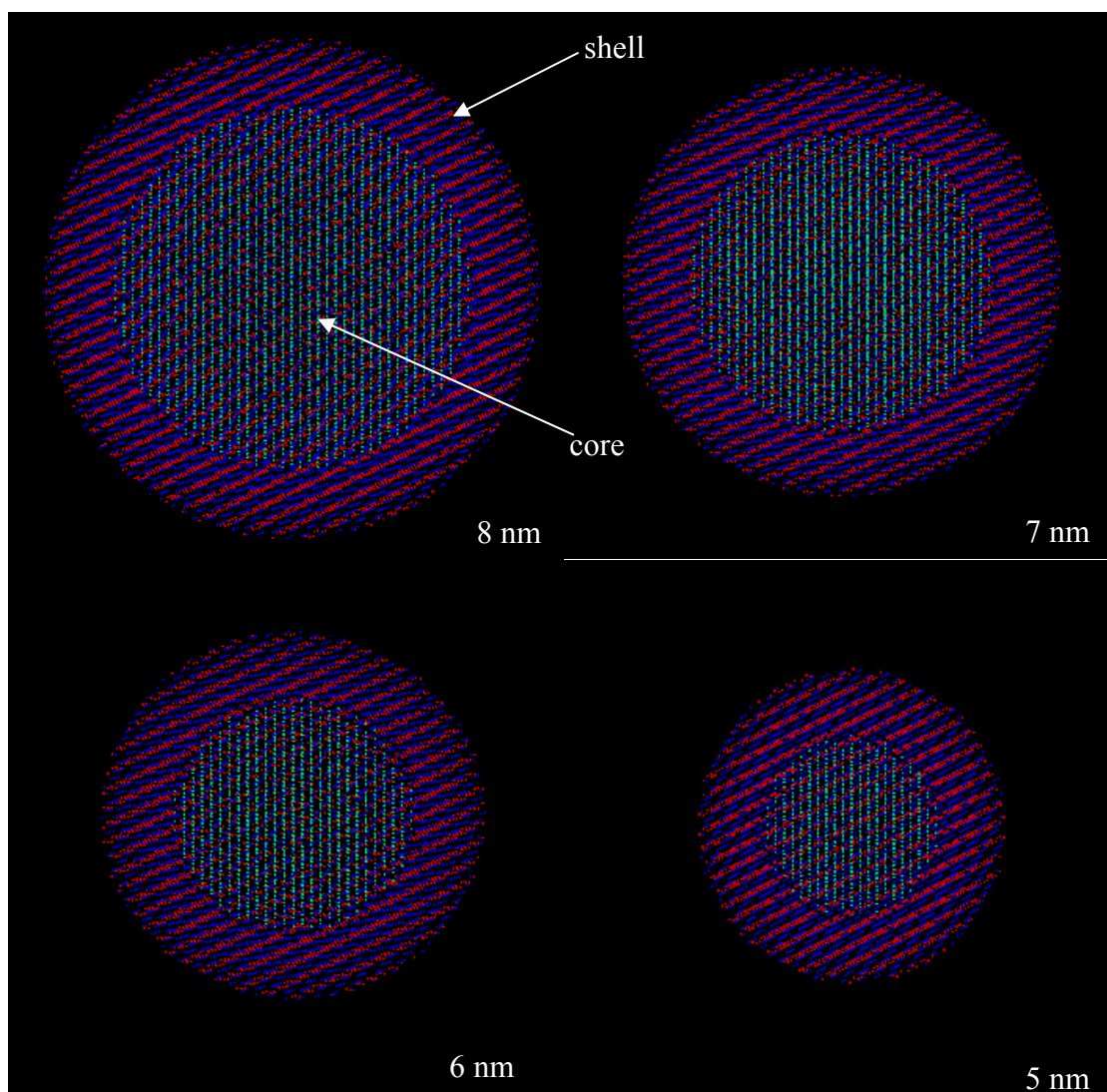


Figure 7.2: Aluminum nanoparticles with crystalline oxide layer at room temperature



The aluminum core and oxide layer are equilibrated at room temperature for a minimum of 15,000 time marching steps, using a micro-canonical ensemble. Figure 7.3 shows the variation of the Lindemann index during the equilibration calculation for a 5 nm particle (3 nm of core diameter and 1 nm crystalline oxide thickness). The index is initially set to zero. After a transient phase, it stabilizes at constant values of 0.028 and 0.012 for the core and oxide layer, respectively. The particle is then heated at a rate of 0.1 K per femto-second.

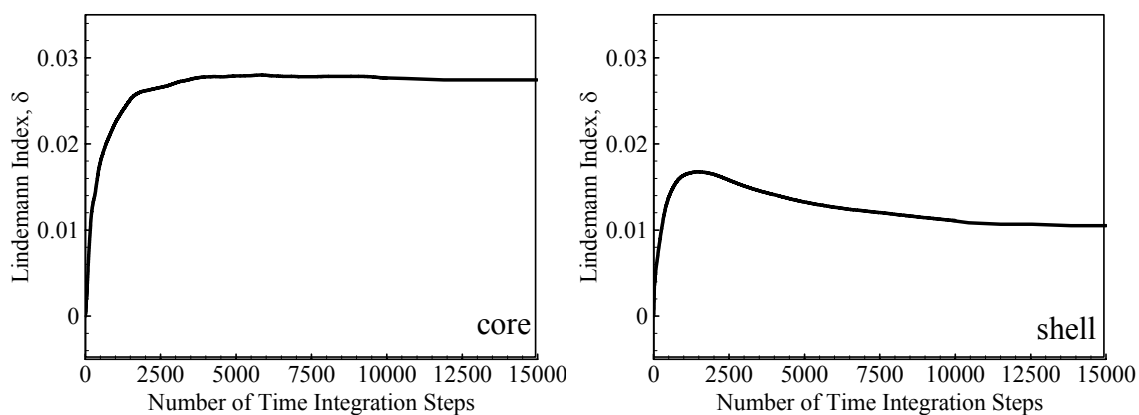


Figure 7.3: Equilibration calculations for 5 nm particle (3 nm core diameter and 1 nm crystalline oxide thickness)

Figure 7.4 shows the evolution of the Lindemann indices for both the aluminum core and oxide shell. Figure 7.5 shows the density contours for the particle at different temperatures. The phase transition in various stages is clearly observed. As the particle is heated, the Lindemann index for the aluminum core increases and reaches an inflection point at 0.03, at which point nucleation for the solid-liquid phase transition occurs at 650 K (see Fig. 7.5c). The density of the core drops from  $2700 \text{ kg/m}^3$  in the solid state to  $2400 \text{ kg/m}^3$  in the liquid state. The Lindemann index of the oxide shell drops due to the

solid-solid phase transition, after an initial increase to a peak value of 0.018 at 500 K during the transient phase.

Alumina is known to exist in six different polymorphs (corundum,  $Rh_2O_3$ ,  $Pbnm$  perovskite,  $R3c$ -perovskite,  $A$ -type rare earth sesquioxide, and  $B$ -type rare earth sesquioxide) (Duan, 1998). The initial structure studied here is corundum, which transforms to one of the other five denser polymorphs. The contour plot at 550 K, shown in Fig. 7.5b, indicates a density change from 3890 to 4050  $kg/m^3$  as a result of such a phase transition. In the crystalline structure of  $Al_2O_3$ , aluminum atoms occupy tetrahedral or octahedral voids in the lattice formed by oxygen atoms. When these aluminum atoms change their coordination from six to a higher value, a solid-solid transition to a denser crystalline structure occurs (Duan, 1998). As the temperature continues to increase, the shell melts at 1129 K, where the inflection point appears in the Lindemann-index profile. The situation is similar to that for the aluminum core. The density of the oxide shell decreases to 3010  $kg/m^3$  in the liquid state, as shown in Fig. 7.5d.

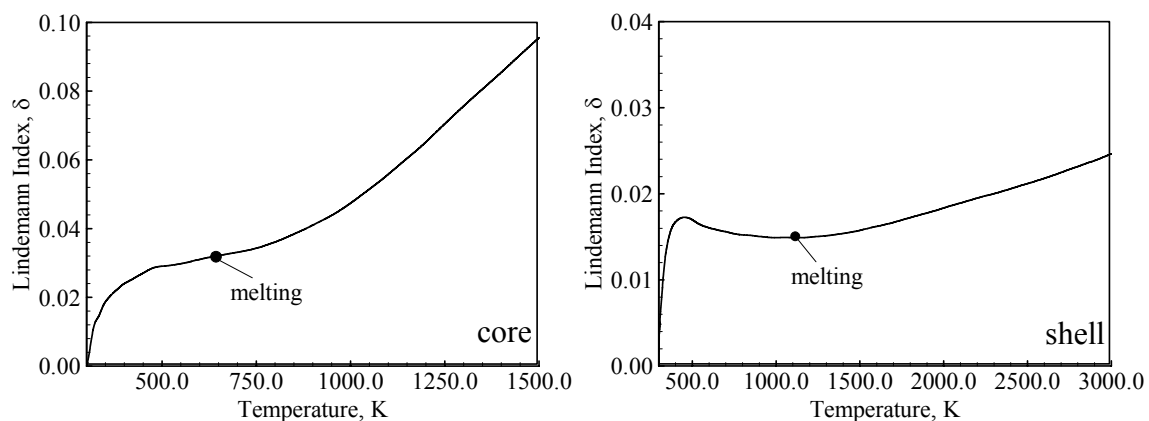


Figure 7.4: Evolution of Lindemann indices for aluminum core and crystalline oxide layer; 5 nm particle (3 nm core diameter and 1 nm oxide thickness)

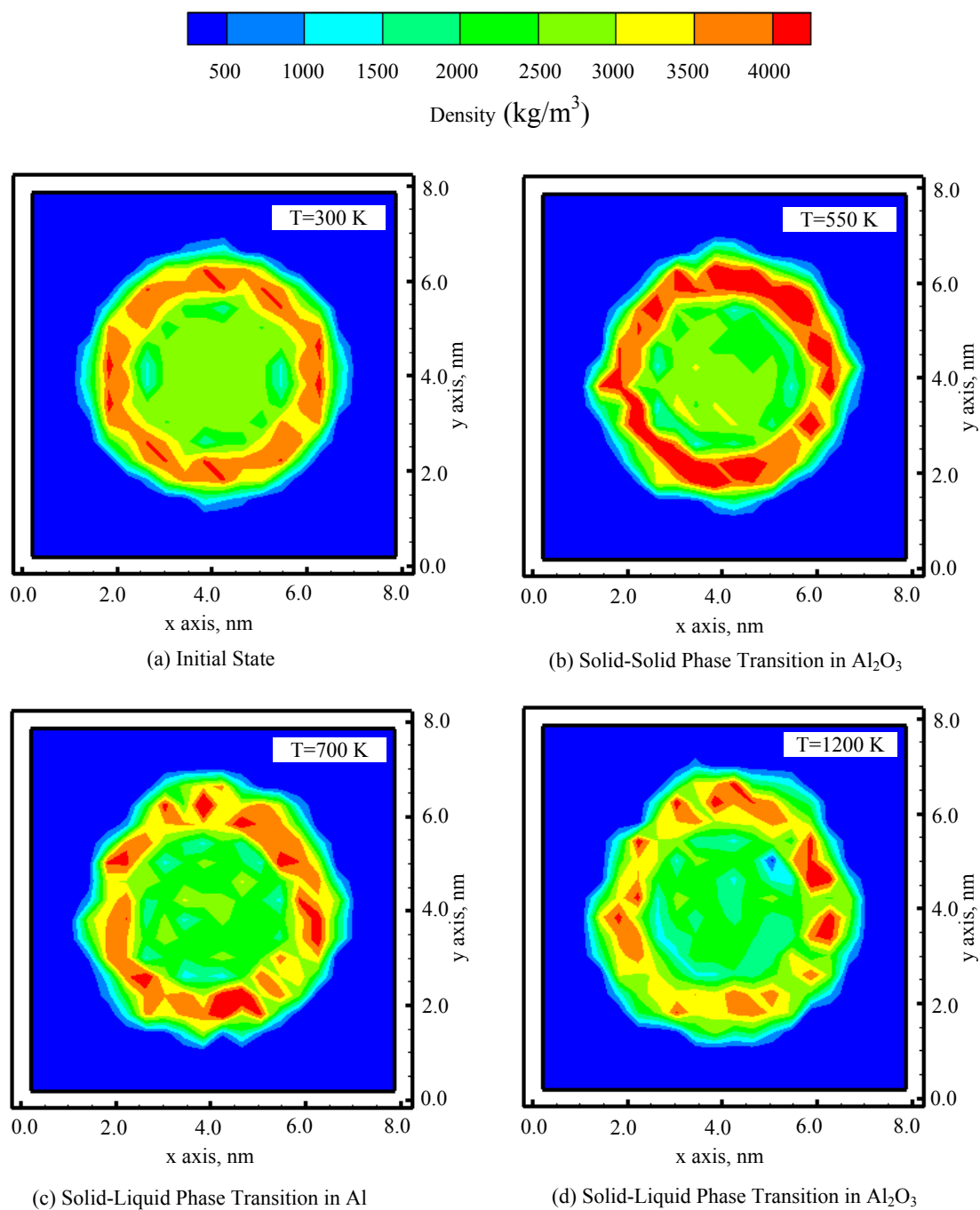


Figure 7.5: Density distributions at various temperatures during heating of 5 nm particle

The size dependence of the melting phenomenon is examined in the range of 5-10 nm. In each case, the thickness of the oxide layer remains at 1 nm. Figure 7.6 shows the evolution of the Lindemann indices for the aluminum core and oxide shell as a function of temperature. The core melts at a temperature considerably lower than its bulk value of 940 K. The oxide layer melts at 1047, 1100 and 1159 K, respectively, for particle sizes of 6, 7 and 8 nm. Nucleation of the liquid phase takes place at relatively lower temperatures of 986 and 1008 K for 9 and 10 nm particles. These temperatures are substantially lower than the counterpart for bulk alumina which is 2327 K. The size dependence of the melting behavior for pure aluminum was reported in the first previous study. The results from the present study indicate an identical trend for both the aluminum core and oxide shell. This phenomenon can be attributed to the increase in the specific surface area as the particle size decreases.

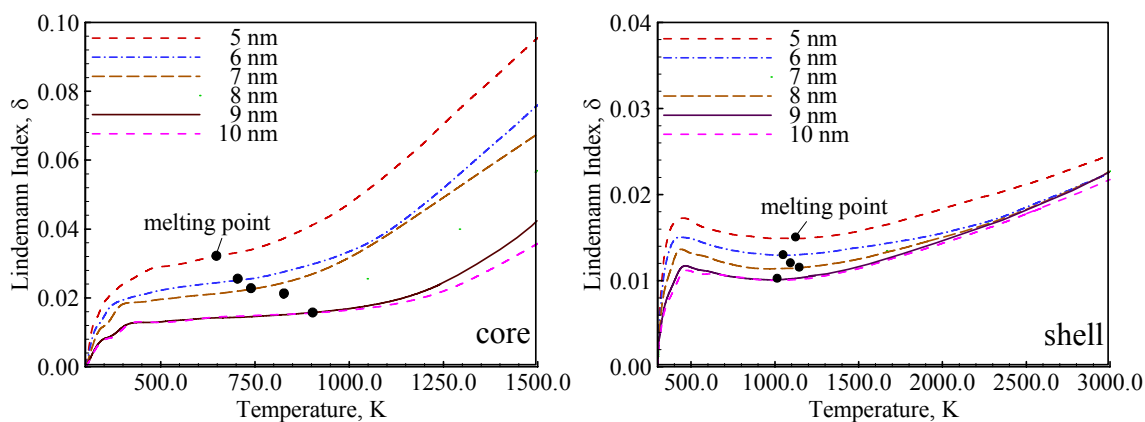


Figure 7.6: Evolution of Lindemann indices for aluminum core and crystalline oxide layer; particle size of 5-10 nm (3-8 nm core diameter and 1.0 oxide thickness)

The effect of the oxide-shell thickness on particle melting is explored in the range of 1.0-2.5 nm. The core diameter is fixed at 5 nm. Figure 7.7 shows the evolution of the

Lindemann index. The melting point of the oxide layer increases, from 1130 K for 1.0 nm to 1313 K for 2.5 nm thickness. The overall melting temperature results are summarized in Fig. 7.8.

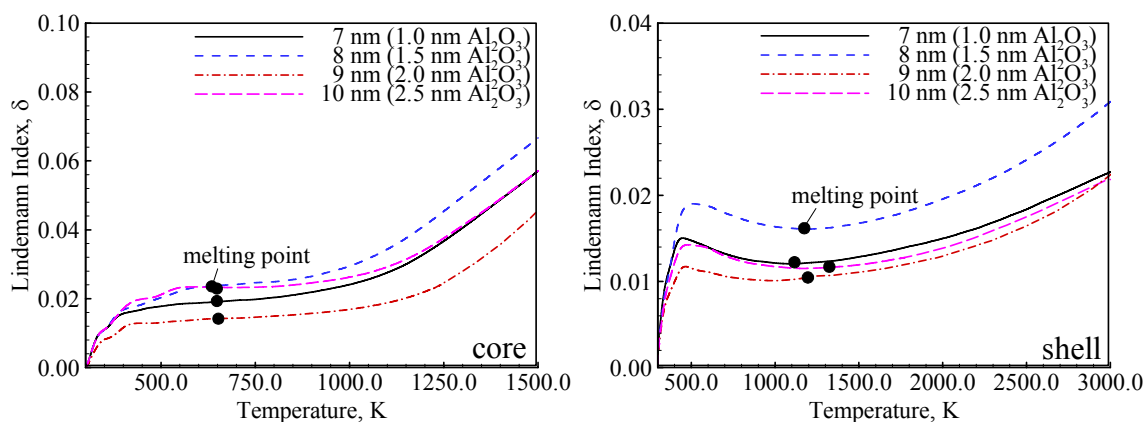


Figure 7.7: Evolution of Lindemann indices for aluminum core and crystalline oxide layer; particle size 7-10 nm (5 nm core diameter and 1.0-2.5 nm oxide thickness)

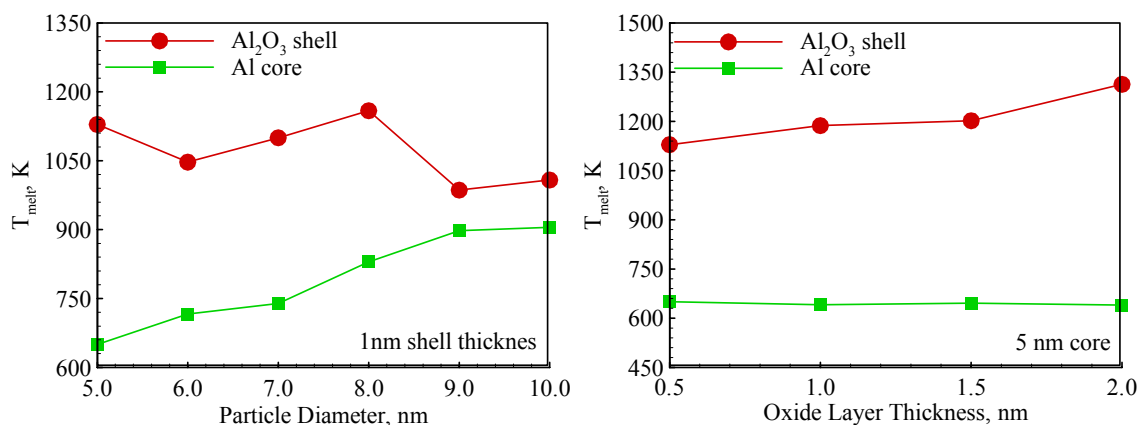


Figure 7.8: Variation of melting points as function of core size and oxide layer thickness

To further understand the size dependence of alumina melting, a simulation was performed for a pure alumina nanoparticle with a diameter of 5 nm. The evolution of the Lindemann index shown in Fig. 7.9 indicates a melting temperature of 1284 K. This value is consistent with that of alumina with an embedded aluminum core, which falls in

the range of 986-1313 K. The Lindemann index also bears a close resemblance to the case with an aluminum core. It increases rapidly in an initial transient phase, reaches a peak at 0.025, and then decreases, because of the phase transformation to a denser phase. The inflection point at 1284 K marks the transition from the solid to the liquid state.

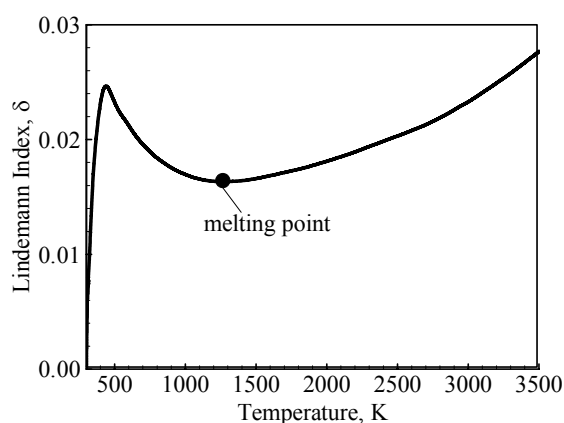


Figure 7.9: Evolution of Lindemann index during heating of 5 nm pure crystalline alumina particle

In addition to the crystalline structure, the situation with an amorphous oxide layer was investigated. To accomplish this, the crystalline structure was heated to a temperature greater than its melting point and then rapidly cooled to 300 K to obtain an amorphous layer. The resulting nanoparticle was heated afterwards to allow examination of its thermo-mechanical behavior during the melting process. Figure 7.10 shows the evolution of the Lindemann indices for a 5 nm particle covered with either a crystalline or an amorphous oxide layer. The core melts at almost the same temperature for both cases. The sharp variation of the Lindemann index for the crystalline structure, however, is not observed in the case with the amorphous shell. For a change to the beta or the gamma form, a minimum of 4 nm thick amorphous layer would be required (Trunov et

al., 2005). Since the present study only considers oxide layers up to 2.5 nm thick, the transformation from the amorphous to the gamma phase does not take place. The solid-to-liquid phase change is also absent in the case of the amorphous oxide shell.

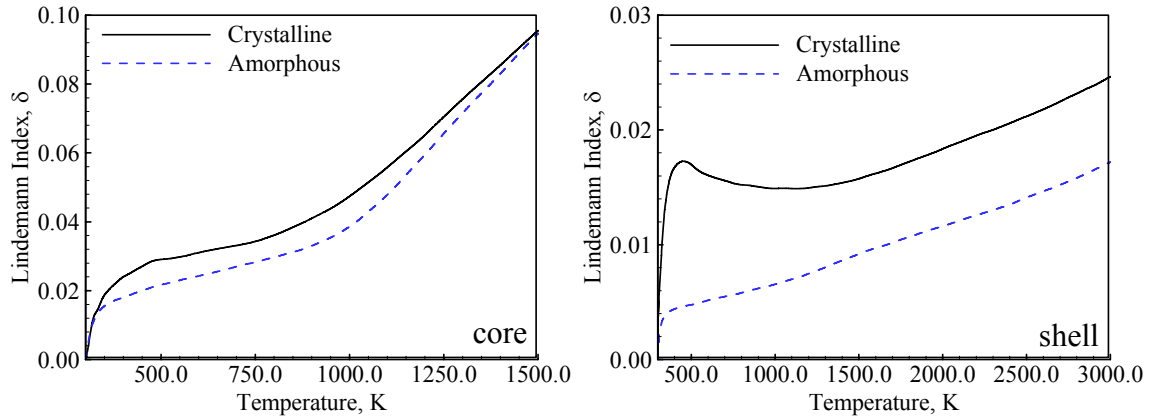


Figure 7.10: Evolution of Lindemann indices during heating of 5 nm particles with crystalline and amorphous oxide layers (3 nm core diameter and 1 nm oxide thickness)

During the particle melting, the density of the aluminum core decreases from 2700 to 2400 kg/m<sup>3</sup>, an 11.1% change. The associated volume dilatation exerts a significant influence on the stress development in the oxide shell. The whole process can be theoretically treated as pressure build-up in a spherical shell. For the aluminum core, the bulk modulus,  $K$ , is 76 GPa. The pressure developed inside the shell becomes 8.4 GPa, based on the relation  $K = -\rho \partial p / \partial \rho$ . Following basic theories in solid mechanics, the stresses in spherical coordinates under an equilibrium condition can be obtained from the following equation (Ragab, 1999)

$$\sigma_r = p_i \left( \frac{r_o^3 - r_i^3}{r^3} \right) \left( \frac{r_i^3}{r_o^3 - r_i^3} \right) \quad (7.1)$$

$$\sigma_\theta = \sigma_\phi = p_i \left( 1 + \frac{r_o^3}{2r^3} \right) \left( \frac{r_i^3}{r_o^3 - r_i^3} \right) \quad (7.2)$$

where  $p_i$  is the pressure exerted on the shell due to the volume expansion of the core,  $r$  the radial coordinate, and  $\sigma_r$ ,  $\sigma_\theta$ ,  $\sigma_\phi$  the stresses in the radial, azimuthal and polar directions, respectively. The subscripts  $i$  and  $o$  denote the inner and outer radii of the oxide shell, respectively, as illustrated in Fig. 7.1. The maximum stress occurs at the interface. Table 7.1 lists the stress values for different particle sizes. The tensile strength of alumina is 0.2552 GPa at room temperature and decreases by an order of magnitude when the temperature exceeds 1300 K (Shackelford, 2000). Since the stresses in the shell caused by the core melting are an order of magnitude higher than the tensile strength, the shell should crack. In the present MD study, however, the shell remains intact. This may be attributed to the fact that the rate of the solid-to-liquid phase transition in the shell is too fast to allow for any substantial stress development in the solid phase.

Table 7.1: Stresses developed inside the oxide shell due to melting

Core Diameter (nm)	Oxide Thickness (nm)	Particle Diameter (nm)	$\sigma_\theta, \sigma_\phi$ (GPa)	$\sigma_r$ (GPa)
4.0	1.0	6.0	9.505	8.4
5.0	1.0	7.0	11.424	8.4
5.0	1.5	8.0	8.269	8.4
5.0	2.0	9.0	6.807	8.4
5.0	2.5	10.0	6.000	8.4
6.0	1.0	8.0	13.394	8.4
7.0	1.0	9.0	15.396	8.4
8.0	1.0	10.0	17.419	8.4

Several experimental studies on aluminum substrates and films have revealed that when an aluminum particle coated with an oxide layer is heated from room temperature, the oxide layer grows due to diffusion of aluminum cations through the layer and bonding with oxygen atoms at the surface (Jeurgens et al., 2002). It is instructive to consider whether a similar phenomenon occurs for nanoparticles in the present research. Before



heating, the core consists of aluminum atoms arranged in a FCC structure, and the shell contains  $\text{Al}_2\text{O}_3$  atoms arranged in a hexagonal structure. The phenomenon of diffusion of aluminum cations for cases with different core size and thickness is shown in Figs. 7.11 and 7.12 respectively. These show snapshots of particle structures with crystalline shells. The core diameter is fixed at 5 nm, and the shell thickness varies from 1 to 2 nm. The diffusion of aluminum cations through the shell is evident, especially for smaller particles. For an amorphous shell, the diffusion of cations proceeds much faster, as shown in Figure 7.13. The potential gradient caused by the positive and negative charges gives rise to the movement of cations and the ensuing growth of the shell. Once the charge gradient is nullified due to the diminished diffusion of cations, the shell stops growing. This commonly happens when the shell thickness reaches 5 nm, a typical oxide-layer thickness reported in the literature (Jeurgens et al., 2002). Since the present study focuses on thermo-mechanical behavior, all the simulations were carried out for nanoparticles in a vacuum. If the particle were exposed to oxygen, these aluminum cations would combine to form species like  $\text{AlO}$ ,  $\text{Al}_2\text{O}$ , which would then deposit on the surface and increase the oxide thickness.

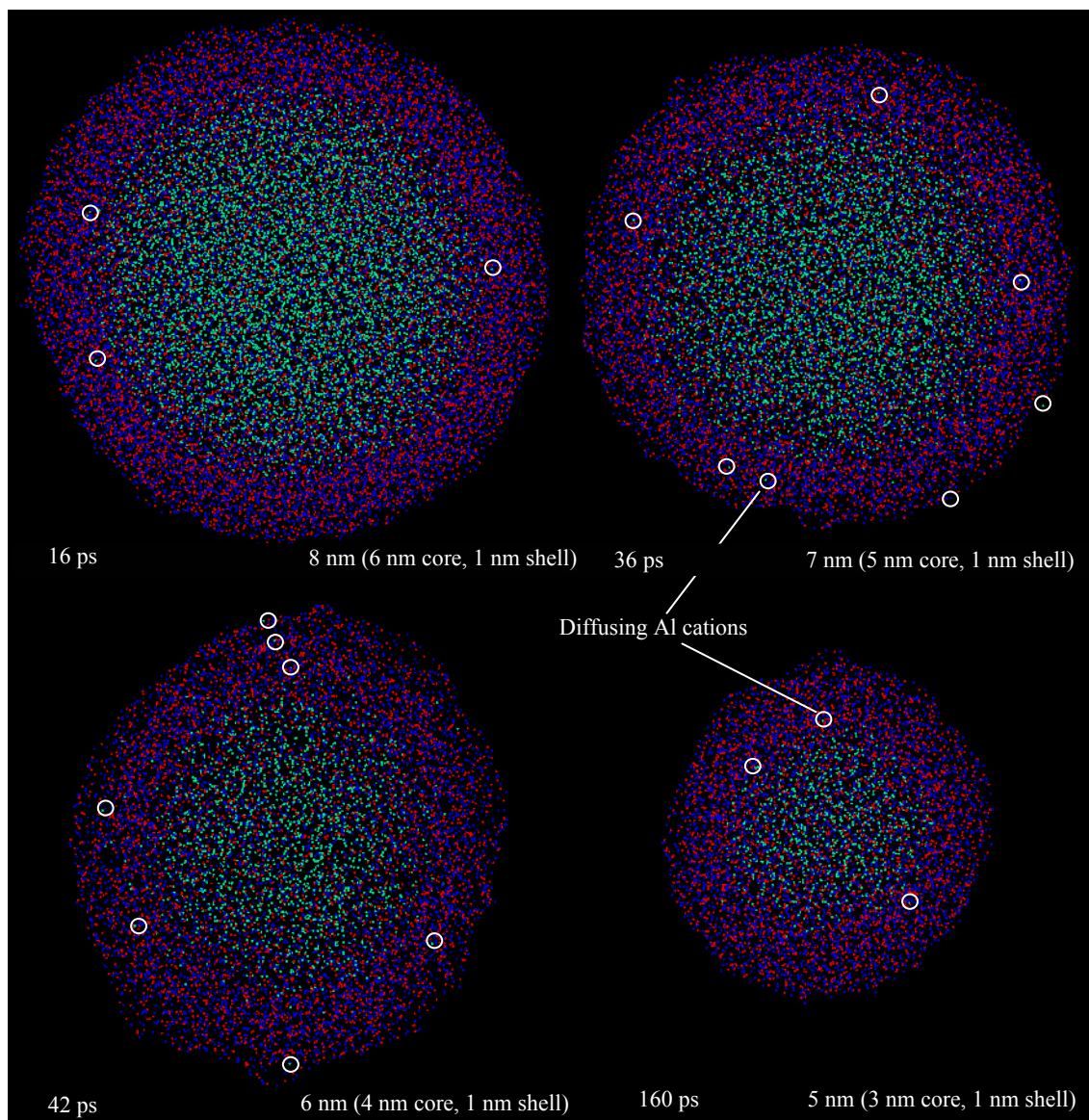


Figure 7.11: Snapshots of 5-8 nm nano aluminum particles with crystalline oxide layer, showing diffusion of aluminum cations (core size of 3-6 nm and oxide thickness of 1 nm)

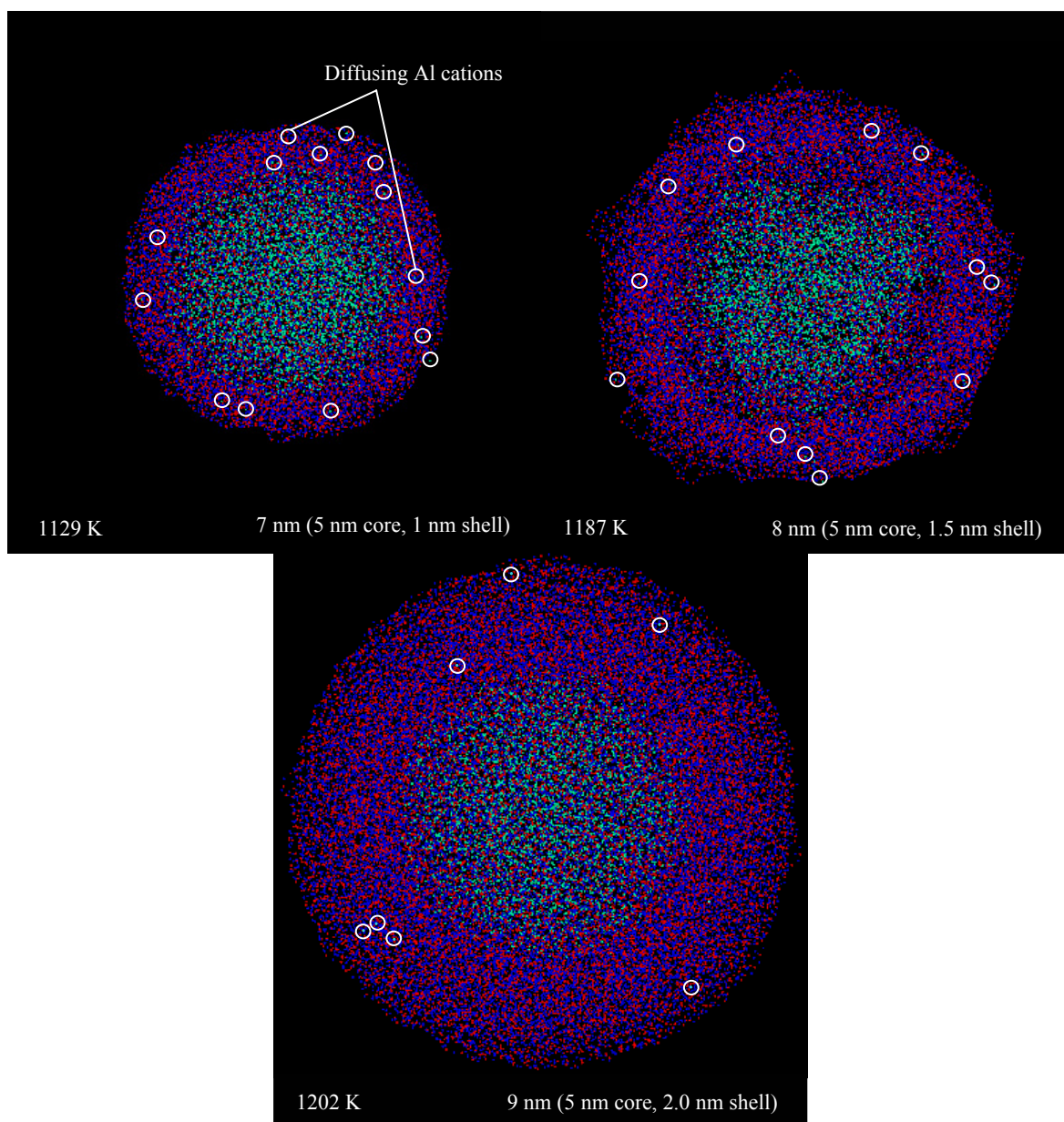


Figure 7.12: Snapshots of 7-9 nm nano aluminum particles with crystalline oxide layer, showing diffusion of aluminum cations (core size of 5 nm and oxide thickness of 1-2 nm)

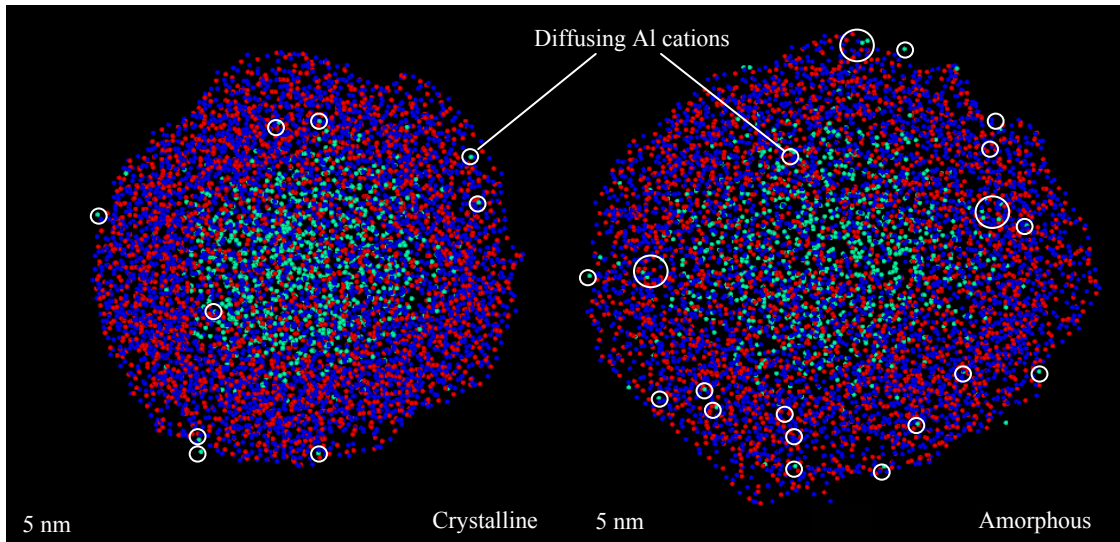


Figure 7.13: Snapshot showing diffusion of aluminum cations in crystalline and amorphous oxide layers for 5 nm particle (oxide thickness of 1 nm)

Molecular dynamics simulations provide exclusive insight into the atomistic mechanisms involved for smaller nanoparticles which can't be explained by continuum laws. From kinetic gas theory, the mean free path of oxygen molecules can be calculated using Eqn. 7.3.

$$\lambda = R_u T / \sqrt{2} \pi d^2 N_A P \quad (7.3)$$

where  $R_u$  is the universal gas constant,  $T$  the temperature,  $P$  the pressure,  $N_A$  the Avogadro's number and  $d$  the diameter of the gas molecule. Assuming the diameter of oxygen molecules to be 0.37 nm, at 300 K and 1 atm pressure, the mean free path of oxidizer species is 67 nm. As a result, continuum laws cannot be applied to particles smaller than 67 nm. Knudsen number, defined as the ratio of molecular mean free path to the representative physical length scale can be expressed as in Eqn. 7.4

$$Kn = \lambda / L \quad (7.4)$$

Using calculations of mean free path and Knudsen number, different regimes for particle combustion can be determined at different temperatures and pressures as shown in Figure 7.14. At high temperatures and low pressures, continuum laws fail to predict the thermo-mechanical phenomena at nano scales. In the regime with Knudsen number greater than one, molecular dynamics simulations need to be used to explore various phenomena. In the continuum limit with low Knudsen numbers, a careful study of length scales and time scales can be performed to determine the mode of ignition and combustion which is discussed in detail in next chapter.

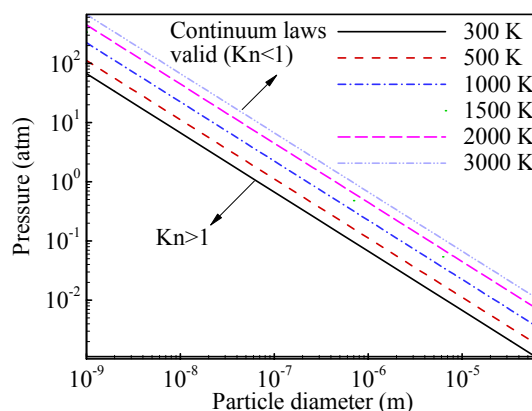


Figure 7.14: Domain for application of continuum laws based on particle diameter and Pressure

Using the results of this particular work and previous simulations, a multi-scale theory for the ignition and combustion of particulate aluminum is being proposed covering a broad range of scales in Chapter 9. Based on the various thermo-mechanical phenomena going on within the core and the shell, the whole time history from ignition till particle burnout has been divided into five stages, which explain the behavior of nano as well as micron-sized particles. A thermodynamic explanation for the observed

thickness of the oxide layer based on phase diagrams has also been provided. An attempt has been made to explore the effect of pressure, temperature, oxidizer, oxide thickness and particle diameter on ignition and oxidation. Characteristics like heterogeneous vs. homogeneous combustion, diffusion vs. kinetically controlled mechanism, mode of ignition etc. have been discussed in context of the unified model. All the phenomena are closely coupled and the exclusive combinations of length and time scales determine the six different modes of ignition.

## 7.4 Conclusions

A molecular-dynamics study was performed to examine the thermo-mechanical behavior of nano aluminum particles coated with oxide layers in both the crystalline and amorphous forms. The size dependence of the melting phenomenon was first examined for particles in the range of 5-10 nm, with the oxide thickness fixed at 1 nm. In each case, the oxide layer melted at 986-1159 K, substantially lower than the bulk value melting point of 2327 K. The effect of the oxide-shell thickness was explored in the range of 1.0-2.5 nm, with the core diameter fixed at 5 nm. The melting point of the oxide layer increased from 1130 K for 1.0 nm to 1313 K for 2.5 nm thickness. The results were compared with the case of a pure 5 nm alumina nanoparticle, for which melting was observed at 1284 K. The Lindemann-index curve showed qualitatively the same trend as that seen for the oxide layer with an aluminum core.

For a crystalline oxide layer, melting was preceded by a solid-solid phase transition to a denser polymorph, characterized by a decrease in the Lindemann index, as

the particle was heated. This phenomenon, however, was absent in the case of amorphous layers. A structural analysis indicated that the stresses in the shell, caused by the volume dilatation in the aluminum core during melting, were an order of magnitude higher than the tensile strength. The shell may therefore crack if it melts at a rate slow enough to allow stress development in the solid phase. Diffusion of aluminum cations through the oxide shell was also investigated.

The present study has shed much insight into the various thermo-physical processes involved in the melting of nano aluminum particles. The results provide a basis for the development of a multi-scale theory for the ignition and combustion of nanoparticulate aluminum.



## Chapter 8

### Pyrophoricity of Aluminum at Nano Scales

#### 8.1 Background

Pyrophoricity has been the subject of various theoretical and experimental studies, especially in the area of metal dust explosion since 1960s. The term pyrophoricity refers to the tendency of a substance to burn spontaneously in the presence of an oxidizing medium without any ignition source. With increasing interest in nanotechnology, and distinct physical and chemical characteristics at such scales, nano particulates present more handling difficulties as compared to their micron-sized counterparts. Finer particles are more prone to ignition, and their dust clouds can even lead to violent explosion. At nano scales, the reduced ignition temperature, high specific surface area, and high transport rate substantially enhance the pyrophoricity of the substance. Among metals, platinum, iron, titanium, magnesium, cobalt, nickel, and aluminum are considered highly pyrophoric. Powders can be classified into three categories based on the degree of explosion hazard. The first group is considered extremely explosive including aluminum and magnesium, the second average explosive including iron, and the third slightly explosive (Buoik, 1954).

For nano aluminum particles, serious safety concerns are raised not only for storage and usage, but also for manufacturing (Kondis, 1976; Kondis, 1976b). Particulate aluminum is prepared through the milling technique either in an inert atmosphere of



hydrocarbons, or in an environment with an appropriate oxygen concentration to form a protective coating on the new surfaces as fine particles are formed. As the particle size decreases, the reactivity increases due to the increase in the specific surface area and the decrease in the diffusion time scale. Particulates then favor welding over comminution once the particle size falls below a critical value. Moreover, the dried powders produced from such milling processes can cause explosions or fires initiated by exposing nascent (un-oxidized) mass to the atmosphere. Particles of the order of less than 1 micron thus produced are considered an explosive hazard (Kondis, 1976b). Reliable measurements of the critical particle size that can lead to explosion are required during manufacturing. On the other hand, pyrophoricity, if controlled, can be employed for some useful applications like decoy flare (Baldi and Alfonso, 1991). Such applications require sound knowledge of pyrophoricity limits of aluminum.

Glassman et al. (Glassman et al., 1992) defined the conditions for metal particles to be pyrophoric, and made a distinction between pyrophoricity and explosivity. Pyrophoricity occurs when the energy release from the formation of the oxide shell on a nascent particle is sufficient to heat the metal to its boiling point and to vaporize it. A simple lump-parameter analysis based on a quasi-steady model was performed to obtain the critical ratio of the shell thickness to the core size,  $(\delta/R)_{cr}$ , for pyrophoricity. A universal value of  $(\delta/R)_{cr} = 0.175$  was found. The work ignored heat losses to ambient gases and the transient development within the particle during the energy-release process. Furthermore, bulk material properties were employed in the analysis. At nano scales, particles exhibit many behaviors distinct from their counterparts at micro or larger scales.

The physiochemical properties become size-dependent, and the thermodynamic melting and boiling points, heats of fusion, vapor pressure, and ignition temperature are substantially changed from their bulk values (Eckert et al., 1993; Alavi et al., 2006; Jiang et al., 2002; Liang et al., 2003; Zhang et al., 1999; Panda and Pratsinis, 1995; Puri and Yang, 2007). In addition, the growth of the oxide layer is characterized by heterogeneous surface reactions, phase transformations within the oxide layer, diffusion of Al cations and O anions through the layer, and direct attack at the aluminum core surface by oxidizer atoms (Jeurgens et al., 2000). All these processes are transient in nature, as a result of the small characteristic length and time scales involved.

The purpose of the present study is to develop an improved theory of pyrophoricity by incorporating various distinct features of nano materials. Since the combustion mode switches from homogeneous gas-phase reactions to heterogeneous surface reactions as the particle size reduces to nano scale, the condition for pyrophoricity is now defined by the critical size for which the heat released during the growth of oxide is sufficient to melt the core, and subsequently rupture the oxide shell. Both nascent and oxide-coated (passivated) nano-particulate aluminum is explored over a range of limiting oxide thickness of practical concern.

## 8.2 Size Dependence of Properties at Nano Scales

### 8.2.1 Thermodynamic Properties

Particles at nano scales show strong size dependence of properties due to high specific surface area and reactivity. A recent molecular dynamics (MD) study by Puri and Yang (Puri and Yang, 2007) indicated that the melting temperature of nascent particulate aluminum decreases monotonically with decreasing diameter, from a value of 937 K at approximately 8 nm to 473 K at 2 nm. The same trend occurs for the alumina shell, for which the melting temperature may decrease substantially to 1100 K, compared to its bulk value of 2327 K (Puri and Yang, 2008d).

These findings are consistent with those from other experimental and numerical studies by Eckert et al. (Eckert et al., 1993) and Alavi et al. (Alavi et al., 2006), respectively. Eckert et al. synthesized nano aluminum powders coated with crystalline oxide by mechanical attrition in argon, hydrogen, and oxygen atmospheres. A significant reduction in the melting point with decreasing grain size was observed by means of differential scanning calorimetry (DSC) in the size range of 13-40 nm (Eckert et al., 1993). The melting point decreases from its bulk value of 940 K at 40 nm to 840 K at 13 nm. The melting temperature and enthalpy of fusion vary linearly with the reciprocal of the particle size, as follows

$$T_m = 977.4 - 1920 / D, \quad 13 \leq D \leq 40 \text{ nm} \quad (8.1)$$

$$L_{fus} = 14.705 - 177.49 / D \quad 13 \leq D \leq 40 \text{ nm} \quad (8.2)$$

where  $T_m$  is the melting point in K,  $L_{fus}$  the latent heat of fusion in  $kJ/mol$ , and  $D$  the particle diameter in  $nm$ . The relation is valid in the size range of 13-40 nm, with the oxide thickness of 2-5 nm.

In a recent model proposed by Jiang et al. (Jiang et al., 2002; Liang et al., 2003), variations in the melting temperature and heat of fusion for nano-sized metal particles were correlated based on the Lindemann criterion of melting, taking the following general functional forms.

$$T_m = T_{m,b} \exp\left(-\left(2L_{fus,b}/3RT_{m,b}\right)/\{(D/6l)-1\}\right) \quad (8.3)$$

$$L_{fus} = L_{fus,b} \exp\left(-\left(2L_{fus,b}/3RT_{m,b}\right)/\{(D/6l)-1\}\right)\left[1-1/\{(D/6l)-1\}\right] \quad (8.4)$$

where  $T_{m,b}$  and  $L_{fus,b}$  are the bulk values for the melting temperature and heat of fusion, respectively,  $l$  the length of  $Al-Al$  atomic bond and  $R_u$  the universal gas constant. A similar expression can be written specifically for aluminum in simplified form using Mott's equation for the melting entropy (Zhang et al., 1999)

$$\frac{L_{fus}(R)}{L_{fus,b}} = \frac{T_m(R)}{T_{m,b}} \left[1 - \frac{1}{(R/R_0 - 1)}\right] \quad (8.5)$$

$$\frac{T_m(R)}{T_{m,b}} = \exp\left(-\frac{\alpha - 1}{R/R_0 - 1}\right) \quad (8.6)$$

For aluminum, the critical radius,  $R_0$  has the value of 0.9492. The material constant,  $\alpha$ , takes the form

$$\alpha = \frac{2L_{fus,b}}{3R_u T_{m,b}} + 1 \quad (8.7)$$

where  $R_u$  is 8.314 J/mol/K, and  $\alpha$  is 1.9186 for aluminum. Figure 8.1 shows the melting temperature and enthalpy of fusion as a function of particle size, calculated from Eqns.

**8.5** and **8.6**. For comparison the thermo-physical properties for bulk aluminum and alumina are listed in Table **8.1**.

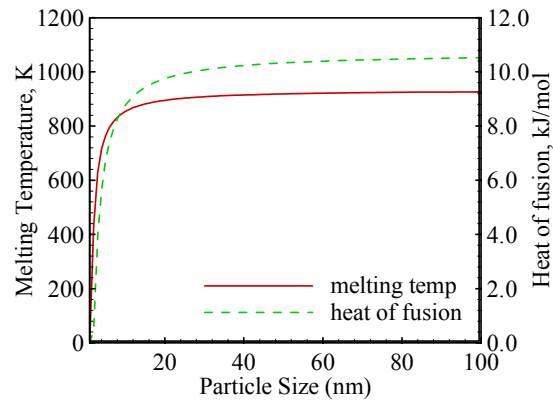


Figure **8.1**: Size dependence of melting point and heat of fusion for nano-particulate aluminum

Table **8.1**: Thermo physical properties of bulk aluminum and alumina

Properties	Aluminum	Alumina
Vaporization Temperature (1atm)	2740 K	4000 K
Density	2700 kg/m <sup>3</sup> (Solid) 2377 kg/m <sup>3</sup> (Liquid)	3050 kg/m <sup>3</sup> (Amorphous) 3050 kg/m <sup>3</sup> (Gamma) 3900 kg/m <sup>3</sup> (Alpha) 3010 kg/m <sup>3</sup> (Liquid)
Heat of fusion	10.7 kJ/mol	-
Heat of vaporization	293.4 kJ/mol	-

The vapor pressure,  $p_D$ , of aluminum near the surface of a liquid aluminum droplet can be calculated using the Kelvin equation as (Panda and Pratsinis, 1995)

$$p_D = p_0 \exp(4\sigma v_1 / k_B T D) \quad (8.8)$$

where  $v_1$  is the monomer volume calculated using the bulk density of aluminum. The vapor pressure of aluminum over a flat surface,  $p_0$ , and the surface tension,  $\sigma$  of aluminum, can be calculated using the following formulae, (Hultgren et al., 1973; Rhee, 1970) respectively.

$$P_0 = \exp\left(13.07 - \frac{36373}{T}\right) atm \quad (8.9)$$

$$\sigma = 948 - 0.202T \text{ Dyne/cm} \quad (8.10)$$

For a given ambient pressure and particle diameter, the above three correlations can be solved iteratively to calculate the vaporization temperature. Consequently the effect of particle size on vaporization temperature at different ambient pressures can be obtained, as shown in Figure 8.2.

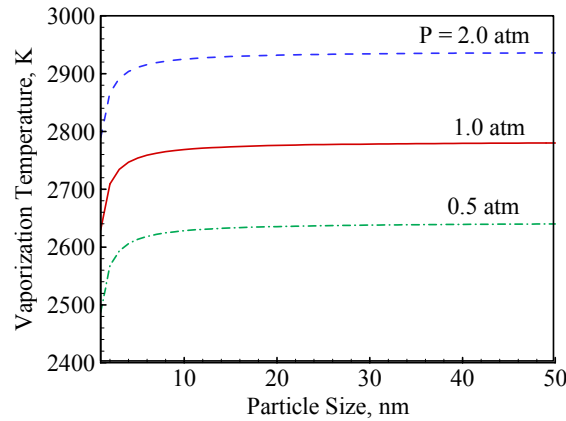


Figure 8.2: Size dependence of vaporization temperature for nano-particulate aluminum

### 8.2.2 Ignition Characteristics

Figure 3.13 summarized the ignition temperatures of aluminum as a function of particle diameter, compiled from various experimental studies. Micron-sized and larger particles ignite around the melting point of alumina (2327 K), and burn with a detached flame front through the vaporization of aluminum (Glassman, 1977; Glassman, 2001; Yetter and Dryer, 2001). When the particle size decreases to one micron or smaller, ignition temperatures become scattered between 940-2327 K. A further decrease of the particle size to 100 nm renders ignition at the melting temperature of aluminum core (940 K), or even less. A major factor contributing to this phenomenon is the heterogeneous surface reactions either due to direct attack of oxidizer molecules through the cracks in the oxide layer, or due to diffusion of ions through the oxide layer. Both mechanisms need to be considered to provide a more complete description of particle pyrophoricity.

### 8.3 Pyrophoricity of Nascent Aluminum Particles

The Glassman theory of pyrophoricity assumes homogeneous reactions in the gas phase (Glassman et al., 1992). The flame structure and associated energy release process are diffusion controlled (Glassman, 2001). At nano scales, the situation becomes fundamentally different. Ignition may occur at a temperature corresponding to the melting point of the aluminum core (Rai et al., 2004). Much energy is released at the surface through heterogeneous reactions. The process is pre-dominantly kinetics-controlled. Under this condition, metal particle can thus be said to be pyrophoric if the heat released during the formation of an oxide shell with a specified thickness is

sufficient to melt the core and rupture the oxide shell. Heterogeneous reactions involving direct oxidation at the surface then take over and consume the metal. The whole process is shown schematically in Figure 8.3.

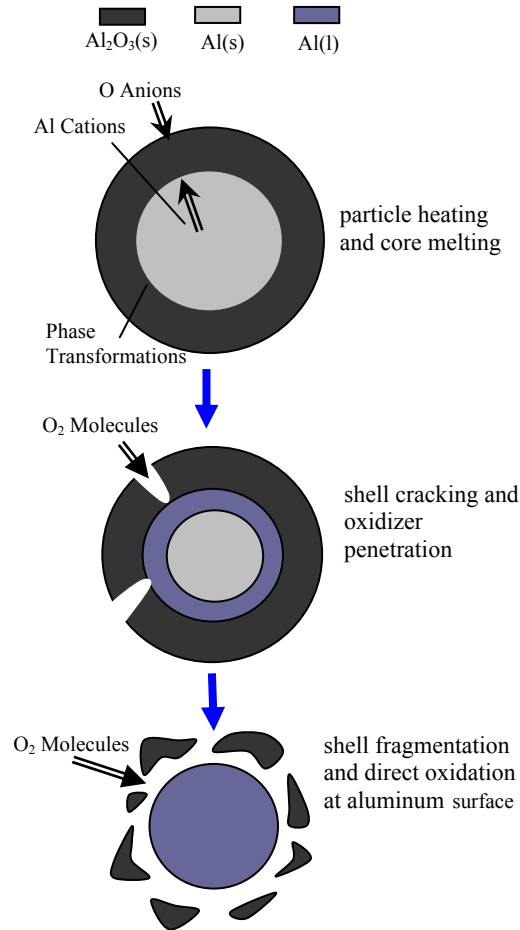


Figure 8.3: Pyrophoricity at nano scales with melting of aluminum core as primary mechanism of ignition

The energy equation used to solve for temperature of the particle can be expressed as

$$\frac{d(m_{Al}c_{Al}T_p + m_{Al_2O_3}c_{Al_2O_3}T_p)}{dt} = \dot{m}_{Al,ox}H_{ox} - \dot{q}_{heat,mol} \quad (8.11)$$



where  $c$  is the specific heat,  $T$  the temperature,  $m$  the mass,  $t$  the time,  $H_{ox}$  the heat release by oxidation, and  $q$  the heat loss. The heat loss in all the simulations is incorporated using the following correlation in the molecular limit (Filippov et al., 2000).

$$\dot{q} = \alpha \pi R^2 \frac{p_g \sqrt{8k_B T_g / \pi m_g}}{2} \left( \frac{\gamma^* + 1}{\gamma^* - 1} \right) \left( \frac{T_p}{T_g} - 1 \right) \quad (8.12)$$

where  $T_p$  is the temperature at the surface of the aluminum core,  $T_g$  the gas temperature,  $p_g$  the gas pressure,  $m_g$  the mass of oxygen molecule,  $\gamma^*$  the average value of adiabatic constant,  $k_B$  the Boltzmann's constant,  $R$  the particle radius, and  $\alpha$  the accommodation coefficient. The expression for  $\dot{m}_{Al,ox}$  is obtained from different correlations appropriate for the phenomenon under consideration. The mass and energy conservation equations are simultaneously solved to obtain the temperature profiles, thickness of the oxide layer and size of the aluminum core.

Once a nascent aluminum particle is introduced in air at room temperature, the direct oxide attack can be formulated using inward Stefan's flow correlation (Trunov et al., 2006)

$$\dot{m}_{O_2}^{ox} = -\ln \left( 1 - \chi \frac{\mu_{O_2}}{\mu_{gas}} \right) \frac{8\pi \mu_{Al_2O_3}}{3\mu_{O_2}} \rho_{gas} D_{O_2} R_p f \quad (8.13)$$

where,  $\dot{m}_{O_2}^{ox}$  is the rate of increase in mass of the oxide layer,  $\chi$  the molar fraction of oxygen in gaseous environment,  $\mu$  the molecular mass,  $\rho_{gas}$  the density of the oxidizer,  $D_{O_2}$  the diffusion coefficient of oxygen in air,  $R$  the radius of the particle, and  $f$  the fraction of the surface exposed to oxidizer. The rate of growth can be used to calculate

the corresponding increase in oxide thickness and reduction in aluminum core radius. Assuming that  $R_1$  and  $\delta_1$  are the initial core size and thickness of the oxide shell respectively and  $R_2$  and  $\delta_2$  are the values after growth of oxide layer, mass conservation between the two states can be written as

$$\frac{4}{3}\pi\left\{(R_1 + \delta_1)^3 - R_1^3\right\}\rho_{Al_2O_3} + \frac{4}{3}\pi R_1^3 \rho_{Al} = \frac{4}{3}\pi\left\{(R_2 + \delta_2)^3 - R_2^3\right\}\rho_{Al_2O_3} + \frac{4}{3}\pi R_2^3 \rho_{Al} \quad (8.14)$$

Eqns. 8.11 to 8.14 can be solved simultaneously and Figure 8.4 shows the results. For an aluminum particle of size 5 nm, the heat released melts the core and vaporizes aluminum instantaneously in 0.4 nanoseconds. A 14 nm particle reaches the melting temperature, and the heat released is sufficient to melt the core too. Hence it is pyrophoric. Using a parametric analysis, the critical particle size in the limiting case was found to be 20 nm. Particles larger than 20 nm are stable and a case of non-pyrophoricity is also shown in Figure 8.4 for illustration. The temperature rises to around 650 K but drops off as the rate of heat losses become dominant.

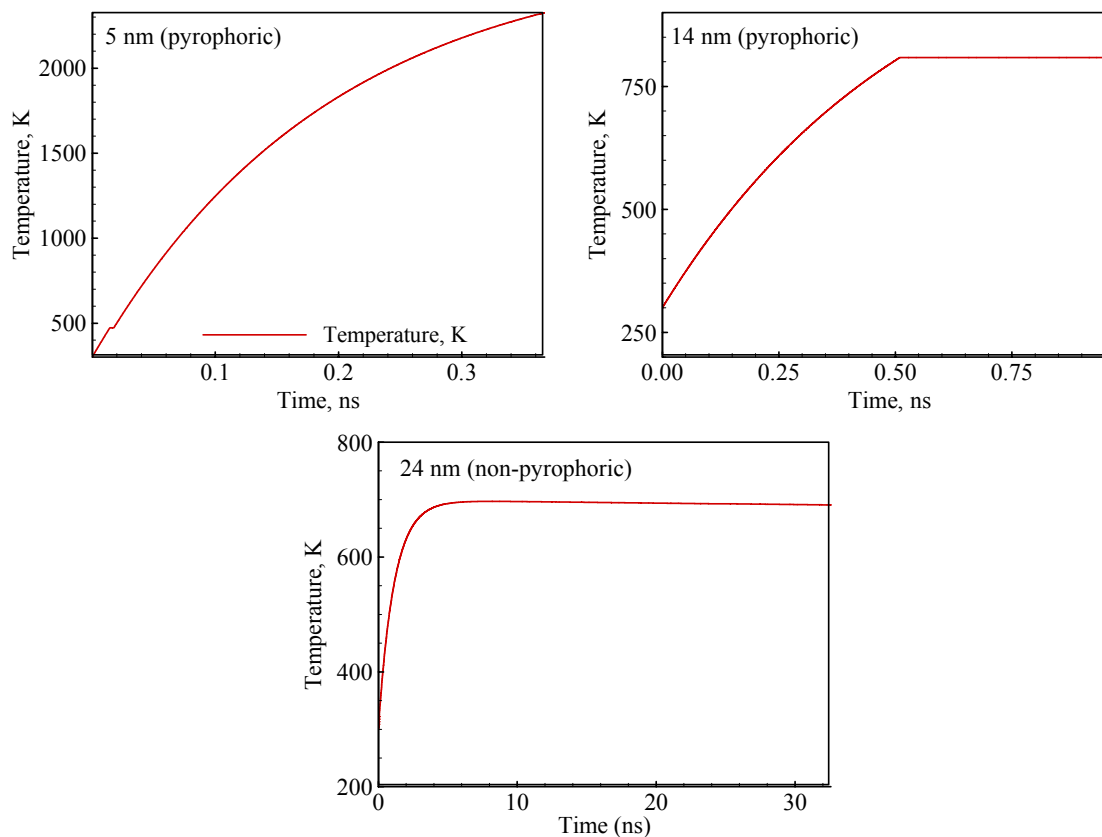


Figure 8.4: Time evolution of temperature for nascent aluminum particles

## 8.4 Pyrophoricity of Oxide-Coated Aluminum Particles

### 8.4.1 Particles with Thin Oxide Shell

It is also a well known fact that aluminum particles are covered with an oxide coating of the order of 0.3-5 nm. So far the effort has been applied to nascent aluminum particles. To apply the theory at nano scales, the initial effect of oxide coating also needs to be considered. Jeurgens et al. studied the thermodynamic stability of amorphous oxide films on aluminum and concluded that in the temperature range of up to 873 K, the

amorphous layers stabilize up to 0.5, 2.5 and 5.0 nm for 111, 100, and 110 crystallographic faces (Jeurgens et al., 2000). In another study by Puri and Yang (Puri and Yang, 2008d) it was observed that at nano scales aluminum cations can diffuse through the oxide layer, reacting with the oxidizer ions. This would eventually increase the thickness of the layer and simultaneously consume the aluminum core. This implies that an aluminum particle with a coating of few nanometers, can be oxidized up to the limiting oxide thickness and if this heat release is sufficient to melt the core and subsequently crack the oxide coating, the small particles can explode/burn pyrophorically.

The rate of growth is limited by the diffusion of ions and can be calculated theoretically using Mott's potential. The mathematical equation governing the process is given by (Jeurgens et al., 2000)

$$\frac{dx}{dt} = \Omega n \nu \exp\left(\frac{-U + qaE_0}{kT}\right) \quad (8.15)$$

where  $\Omega$  is the volume of oxide formed per cation,  $n$  the number of cations per unit area which may jump the energy barrier  $U$ ,  $\nu$  the attempt frequency of cation jump,  $q$  the charge of migrating cation,  $2a$  the distance from potential minimum to next potential minimum,  $k$  the Boltzmann constant,  $T$  the temperature,  $E_0$  the electric field due to Mott's potential  $V_M$  and  $x(t)$  denotes the oxide film thickness at time  $t$ . The constants are given in detail in work by Jeurgens et al. In non-adiabatic conditions the rate of ion transport is not enough to generate sufficient heat to overcome heat loss and particles remain stable as shown in Figure 8.5. Even a thickness of 0.5 nm is sufficient to protect the particle from getting consumed. In other cases for 5-50 nm particle size, the

temperature increases for a maximum of 50-100 K but ultimately rate of heat loss brings the particle temperature down to 300 K.

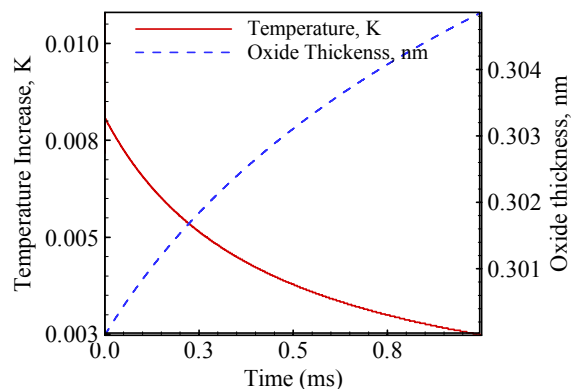


Figure 8.5: Time evolution of temperature and oxide thickness for particle with 10 nm core diameter and 0.3 nm oxide thickness using ion transport in non-adiabatic conditions

In an adiabatic case with initial thin shells, due to the faster rate of ion transport, a growth rate of 1-10 nm/s is sufficient to cause self-heating of the aluminum core to its melting point and subsequently melt it. However the growth rate being dependent on oxide thickness drops significantly for an initial oxide thickness greater than 0.4 nm and is not sufficient to cause pyrophoricity if kept at room temperature. Figure 8.6 shows the result for three different initial oxide thicknesses. The rate of temperature increase significantly drops as the thickness is increased. The rate of oxide growth due to ion transport, however, becomes dominant at temperatures much higher than the temperature in ambient conditions considered for pyrophoricity studies.

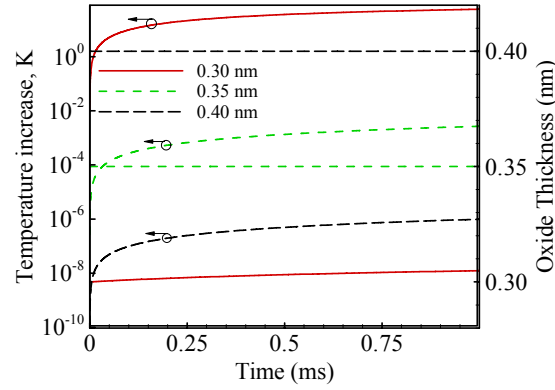


Figure 8.6: Time evolution of temperature and oxide thickness using ion transport for particle with 10 nm core diameter and 0.3-0.4 nm oxide thickness in adiabatic conditions

#### 8.4.2 Particles with Thicker Oxide Shell

Pyrophoricity of particles with thicker oxide shells was also explored. This involves growth of amorphous layer, and phase transformations using the correlations obtained by Trunov et al. (Trunov et al., 2006). However, the rate of increase in the thickness of a particular phase of oxide and its transformation to other phases can be computed by fitting experimental data to Arrhenius type expressions. For phase transformations, the rate of mass increase,  $\dot{m}_{(i-1) \rightarrow i}^{tr}$  of the oxide phase  $i$  transformed from oxide phase  $i-1$  can be described as

$$\dot{m}_{(i-1) \rightarrow i}^{tr} = 4\pi R_{i-1}^2 \rho_i F_{i-1 \rightarrow i} T_p \left\{ 1 - \exp\left(-\frac{K_{i-1 \rightarrow i} h_{i-1}}{R_u T_p}\right) \right\} \exp\left(-\frac{E_{i-1 \rightarrow i}}{R_u T_p}\right) \quad (8.16)$$

where  $T_p$  is the temperature of the particle,  $\rho$  the density,  $h$  the oxide thickness,  $R$  the radius,  $R_u$  the universal gas constant, and  $F$ ,  $K$ , and  $E$  experimentally determined constants as shown in Table 8.2 below.

Table 8.2: Kinetic parameters determined for phase transformations

Kinetic Parameter	Value
$E_{am \rightarrow \gamma}$	458 kJ/mol
$E_{\gamma \rightarrow \alpha}$	394 kJ/mol
$K_{am \rightarrow \gamma}$	$1 \times 10^{12}$ J/mol-m
$K_{\gamma \rightarrow \alpha}$	$1 \times 10^8$ J/mol-m
$F_{am \rightarrow \gamma}$	$2 \times 10^{15}$ m/s-K
$F_{\gamma \rightarrow \alpha}$	$5 \times 10^6$ m/s-K

The following relation for growth of layer in each phase is proposed with constants in the Table 8.3 below.

$$m_i^{ox} = \frac{C_i \exp(-E_i / RT_p)}{r_{i-1}^{-1} - r_i^{-1}} \quad (8.17)$$

Table 8.3: Constants used in expression for growth of oxide layer

Kinetic Parameter	Value
$E_{am}$	120 kJ/mol
$E_{\gamma}$	227 kJ/mol
$E_{\alpha}$	306 kJ/mol
$C_{am}$	$5.098 \times 10^{-8}$ kg/m-s
$C_{\gamma}$	$4.0784 \times 10^{-3}$ kg/m-s
$C_{\alpha}$	$2.3791 \times 10^{-2}$ kg/m-s

The numerical code simulates the growth of oxide layer, melting of core, temperature rise and the results match with the observations reported in work by Trunov

et al. (Trunov et al., 2006). However, there was no significant growth of oxide layer while simulating particles of the order of nanometers. At such low temperatures, the rate of increase in mass of alumina was of the order of  $10^{-32}$  and  $10^{-49}$  g/s and not sufficient to cause any substantial increase in the oxide thickness. As a result, the rate of heat loss was significantly higher than the rate of heat release and particles remained at 300 K. Figure 8.7 shows the evolution of temperature and oxide thickness for a 10 nm core diameter and 0.5 nm oxide thickness.

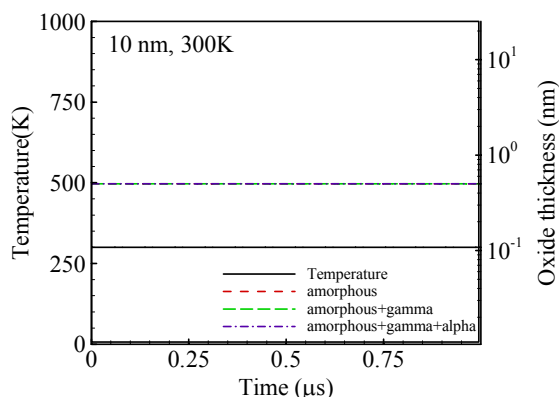


Figure 8.7: Evolution of temperature and oxide thickness for particle with 10 nm core diameter and 0.5 nm oxide thickness

### 8.5 Glassman's Criterion for Pyrophoricity

According to Glassman et al. (Glassman et al., 1992), the critical condition for pyrophoricity can be determined by equating the heat released through the oxidation to the sum of the energy needed to heat the oxide coat and metal to the boiling point of metal and also vaporize the metal. Estimation was thus made for the size of metal



particles in their nascent stage that becomes pyrophoric, based on the following four assumptions:

1. The problem was considered to be time independent.
2. Heat losses from the particle were ignored.
3. The oxide layer formed was assumed to grow up to a limiting value as observed in the experiments.
4. The densities of metal and oxide were calculated at room temperature.

The condition for pyrophoricity for a particle of radius  $R$  and oxide thickness  $\delta$  can be expressed as

$$\frac{\left(1 - \left(\delta/R\right)_{cr}\right)^3}{\left\{1 - \left(1 - \left(\delta/R\right)_{cr}\right)^3\right\}} = \frac{\rho_{Al_2O_3} \left\{ \left(-H_{ox}^o\right) - \left(H_{bpt\ of\ Al}^o - H_{298}^o\right) \right\}_{Al_2O_3}}{\rho_{Al} \left( H_{bpt\ of\ Al}^o - H_{298}^o + L_{vap} \right)_{Al}} \quad (8.18)$$

where  $\rho$  is the density,  $H_{ox}^o$  the heat release during the oxidation of aluminum,  $L_{vap}$  the enthalpy of vaporization, and  $H$  the enthalpy at a given temperature. The material properties can be obtained from the JANAF tables, listed in Table 8.4 (JANAF, 1981).

Table 8.4: Properties used in determination of pyrophoricity

Property	Value
Density of alumina, $\rho_{ox}$	3890 kg/m <sup>3</sup>
Density of aluminum, $\rho_{Al}$	2700 kg/m <sup>3</sup>
Heat release during oxidation, $\left(-H_{298}^o\right)_{ox}$	1675 kJ/mol
$\left(H_{bpt}^o - H_{298}^o\right)$	454 kJ/mol
$\left(H_{bpt}^o - H_{298}^o + L_v\right)$	381.67 kJ/mol
Bulk aluminum melting point	940 K
Bulk aluminum boiling point	2740 K
Bulk alumina melting point	2327 K
Bulk alumina volatilization temperature	4000 K

After relaxing the assumptions in this model, the present research predicts a value of 20 nm which is smaller than the size of 27.6 nm predicted by Glassman for an oxide growth up to 2.5 nm.

## 8.6 Conclusions

Pyrophoricity/explosivity of nano-particulate aluminum has been explored using the size dependence of properties like melting temperature, vaporization temperature, heat of fusion and heat of vaporization at nano scales. In the context of unified theory at nano scales, the limiting condition for pyrophoricity is modified from vaporization of aluminum to melting of core and subsequent rupture of the oxide layer. The critical particle size is evaluated using the modified criterion is found out to be 20 nm. Pyrophoricity has so far been defined for pure aluminum particles. The study also explored the limits for oxide coated nano aluminum particles for given values of particle size and thickness of oxide layer. In adiabatic conditions and very thin oxide layer of the order of 0.30-0.35 nm the diffusion of ions is sufficient enough to lead to pyrophoricity. In non-adiabatic conditions, the particles remain stable. The phase transformations and subsequent growth of a thick oxide layer greater than 1 nm is not enough to generate sufficient heat to overcome heat loss and particles in this case also remain stable.

## Chapter 9

### Unified Theory of Aluminum Particle Combustion

#### 9.1 Ignition and Combustion at Multi Scales

As discussed in Chapter one, nanoparticles are associated with increased catalytic activity, higher reactivity, higher specific surface area, potential ability to store energy in surface defects, lower melting points, and smaller characteristic times for mass and energy transport as compared to their micro counterparts (Ilyin et al., 2001; Kwon et al., 1996). The excess energy of surface atoms and reduced activation energies for chemical reactions contribute to these extraordinary chemical characteristics (Pivkina et al., 2004). These highly desirable traits of aluminum are also responsible for the difference in combustion characteristics at nano scales.

Chapter 2 and 3 discussed the observations of various experimental and numerical studies at micro and nano scales respectively. It was seen that particle size plays the most significant role in determining the characteristics of ignition and combustion. For micron-sized and larger aluminum particles, the ignition temperature coincides with the melting point of the surface oxide ( $\text{Al}_2\text{O}_3$ ) layer at 2327 K (Bucher et al., 2000). The impervious nature of aluminum oxide inhibits the ignition of aluminum. Once the layer melts, it coalesces to form an oxide cap, and the aluminum core is then exposed to the ambient gases for oxidation. At nano scales (less than 100 nm), the ignition occurs near the melting point of aluminum at 940 K by cracking of the oxide shell, possibly caused by

the pressure buildup (Rai et al., 2004; Rozenband and Vaganova, 1992) and/or phase transformations (Dreizin, 2003; Trunov et al., 2006) inside the shell. According to Rai et al. (Rai et al., 2004), oxidation of alumina-coated nano-sized aluminum particles is initiated by melting of the aluminum core. The resultant volume dilatation causes a pressure build-up inside the shell formed by the oxide layer. Because of the higher curvature as compared to micron-sized particles, the stress developed due to the pressure becomes unsustainable and the shell subsequently ruptures. This concept was originally introduced by Rozenband et al. (Rozenband and Vaganova, 1992), who developed a model taking into account the mechanical stresses at the metal-oxide interface. Trunov et al. (Trunov et al., 2006) attributed the observed low ignition temperature of nano-sized particles to the transformation from the amorphous to the gamma and alpha phases in the oxide layer. As a consequence of the density variations in different phases, the layer develops cracks, which permit direct oxidation of aluminum in the core.

Prior to performing any full multiscale simulation of the generation, transport, and combustion of nano-sized energetic materials in flow environments, a good understanding of the combustion of single particles in quiescent medium is required. Many other fundamental issues concerning the combustion characteristics at nano and micro scales like mode of combustion also remain to be clarified. After performing a comprehensive review of work done on aluminum particles at the micro and nano scales and in the light of inconsistencies and uncertainties of the various theories concerning the particle behavior (Rai et al., 2004; Rozenband and Vaganova, 1992; Dreizin, 2003; Trunov et al., 2006), fundamental research based on well-calibrated techniques appeared

to be imperative. It would help to achieve an improved understanding of the effects of particle size on the melting and ignition behavior.

Both experimental and numerical studies have tried to explore the size dependence of thermodynamic properties at nano scales (Alavi et al., 2006; Wronski, 1967; Eckert et al., 1993). As the size decreases beyond a critical value, due to the increase in the surface-to-volume ratio, the melting temperature deviates from the bulk value and becomes a size-dependant property (Alavi et al., 2006). Wronski and Eckert et al. have investigated tin and nano-crystalline aluminum respectively. Wronski observed a reduction from a bulk value of 505 K to 425 K for 5-10 nm tin particles using transmission electron diffraction (Wronski, 1967). Eckert et al. performed a similar study for 13-40 nm particles using differential scanning calorimetry (DSC) and observed a similar reduction in the melting point with decreasing grain size (Eckert et al., 1993). Theoretical studies also predict a drop in melting temperature, heat of fusion and even vaporization temperature as a function of particle size (Jiang et al., 2002; Liang et al., 2003; Zhao and Jiang, 2004; Zhang et al., 1999; Panda and Pratsinis, 1995).

From a theoretical standpoint, theories applied at micro scales cannot be used to predict the ignition behavior for particles of size less than a critical value. From kinetic gas theory, the mean free path of oxygen molecules can be calculated using

$$\lambda = R_u T / \sqrt{2} \pi d^2 N_A P \quad (9.1)$$

where  $R_u$  is the universal gas constant,  $T$  the temperature,  $P$  the pressure,  $N_A$  the Avogadro's number and  $d$  the diameter of the gas molecule. Knudsen number, defined as

the ratio of molecular mean free path to the representative physical length scale can be expressed as

$$Kn = \lambda/L \quad (9.2)$$

Using calculations of mean free path and Knudsen number, two different regimes for particle combustion can be determined at different temperatures and pressures as shown in Figure 7.14. For high temperatures and low pressures, continuum laws fail to predict the thermo-mechanical phenomena at nano scales. In the regime with Knudsen number greater than one, molecular dynamics simulations need to be used to explore various phenomena leading to ignition and combustion.

Comprehensive studies based on molecular-dynamics (MD) simulations have been performed to explore the thermo-mechanical behaviors of nano aluminum particles (Puri and Yang, 2007; Puri and Yang, 2007b; Puri and Yang, 2008d). Molecular dynamics simulations provide exclusive insight into the atomistic mechanisms involved for nanoparticles which can't be explained by continuum laws. In previous studies, the melting behavior of a pure nano-sized aluminum particle was studied in the size range of 2-9 nm. Five different potential functions (the Lennard-Jones, glue, embedded-atom, Streitz-Mintmire, and Sutton-Chen potentials) were implemented (Puri and Yang, 2007). The melting temperature of a pure nanoparticle increased monotonically with increasing size, from 473 K at 2 nm to a bulk value of 937 K at approximately 8 nm. The effect of pressure and internal defects in the form of voids on the melting of bulk and nano-particulate aluminum in the size range of 2-9 nm, was investigated through molecular dynamics simulations using isobaric-isoenthalpic (NPH) ensembles (Puri and Yang,

2007b). The main objectives were to determine the critical interfacial area required to overcome the free energy barrier for the thermodynamic phase transition, and to explore the underlying mechanisms for defect-nucleated melting. The presence of voids did not impact the melting properties due to the dominance of nucleation at the surface, unless the void size exceeds a critical value beyond which lattice collapse occurs. The effect of pressure on the particulate melting was found to be insignificant in the range of 1-300 atm.

Finally, the thermo-mechanical behavior of nano aluminum particles coated with crystalline and amorphous oxide layers during melting was studied. The effect of particle size in the range of 5-10 nm with oxide thickness in the range of 1-2.5 nm was investigated. Various fundamental processes, including structural changes, stress development, and phase transformations in both the aluminum core and the oxide shell, were examined and quantified systematically. The diffusion of aluminum cations through the oxide layer was also explored. In addition, a structural analysis was applied to determine the stress field in the oxide shell due to the volume dilatation in the aluminum core. In the particle-size range considered, the oxide layer melted at  $\sim 1100$  K, substantially lower than the value for bulk alumina (2327 K). The oxide thickness exerted a weak influence on the melting temperature of the shell. All these studies provided valuable input towards the development of a multi-scale theory for the ignition and combustion of nano-particulate aluminum.

Using the results of these simulations and theoretical correlations, a multi-scale theory for the ignition and combustion of particulate aluminum is being proposed covering a broad range of scales. Based on the various thermo-mechanical phenomena

going on within the core and the shell, the whole time history from ignition till particle burnout has been divided into five stages, which explain the behavior of nano as well as micron-sized particles. A thermodynamic explanation for the observed thickness of oxide layer based on phase diagrams has also been provided. An attempt has been made to explore the effect of pressure, temperature, oxidizer, oxide thickness and particle diameter on ignition and oxidation. Characteristics like heterogeneous vs. homogeneous combustion, diffusion vs. kinetically controlled mechanism, mode of ignition etc. have been discussed in context of the unified model. All the phenomena are closely coupled and the exclusive combinations of length and time scales determine the six different modes of ignition.

## **9.2 Stages of aluminum oxidation**

An aluminum particle introduced to an oxidizing environment at a pre-specified temperature and pressure, is always covered with a layer of aluminum oxide. The thickness of this oxide layer depends on manufacturing processes and acts as a passivation layer, protecting the particle from getting ignited. During ignition, it either cracks or melts and hence, the thickness of this layer becomes important.

It has been reported that the oxide thickness is always of the order of 3-5 nm. The concept of limiting oxide thickness can be explained on the basis of ion movement within the shell. The potential gradient caused by the positive and negative charges gives rise to the movement of cations and ensuing growth of the shell. Once the charge gradient is nullified due to the diminished diffusion of cations, the shell stops growing. This



commonly happens when the shell thickness reaches 5 nm, a typical oxide-layer thickness reported in the literature (Jeurgens et al., 2002). However, a good estimate of the thickness of the initial oxide layer formed during manufacturing can also be obtained using phase equilibrium analysis in terms of Gibbs free energy. It is assumed that during the solidification of aluminum from liquid state, oxygen dissolves in liquid aluminum resulting in Al-O the equilibrium solution. The amount of oxygen dissolved and the rate of cooling determines the amount of  $\text{Al}_2\text{O}_3$  and Al phase that solidify, hence the thickness of the shell. For deriving an expression for the oxide thickness, a Al-O phase diagram (Figure 9.1) has been adapted from literature (Goldsmith et al., 1960).

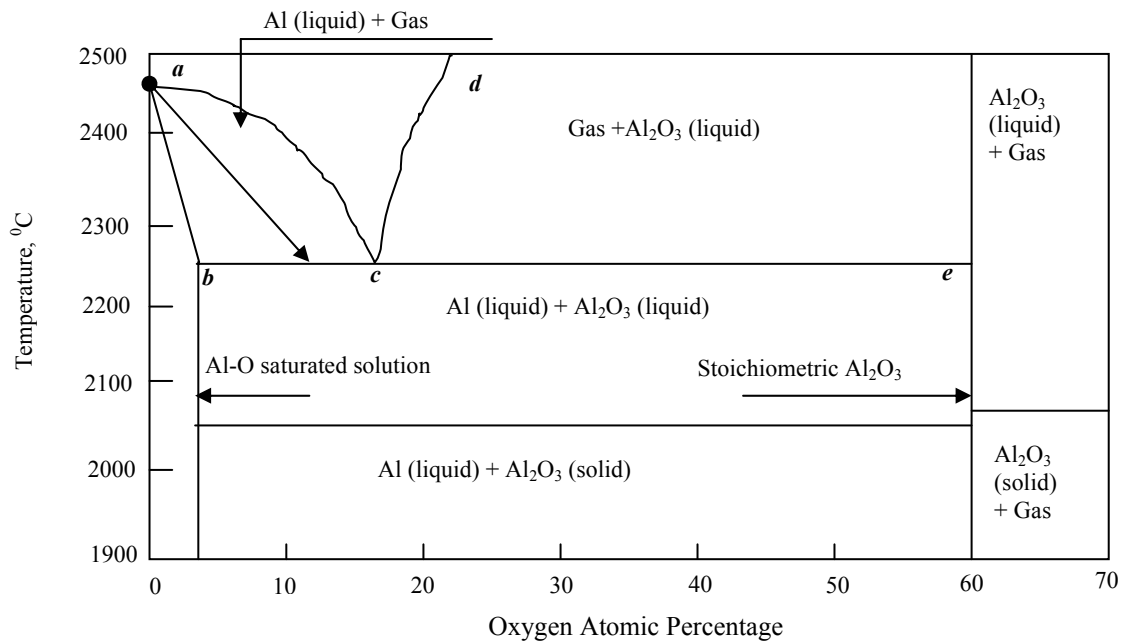


Figure 9.1: Al-O phase diagram (Goldsmith et al., 1960)

Starting from the pure boiling aluminum, a quasi steady system with oxygen would follow line  $ab$  and  $ac$  as shown in Figure 9.1. The phase diagram shown in the figure has

the atomic percentage of oxygen which has been converted to percentage by weight for analysis. Line  $ab$  indicates the limiting oxygen concentration that can reach in a liquid when dissolution occurs rapidly i.e. 0.1% (0.06% by mass). The oxygen content is always greater than the line  $ab$  but is limited by  $ac$ , with maximum concentration corresponding to point  $c$ , i.e. 14% (8.8% by mass). Similarly, in the second phase of aluminum oxide, the maximum concentration of oxygen is given by 60% (47.1% by mass). If an excess of oxygen around molten aluminum is assumed during fabrication, the maximum oxygen dissolution in molten aluminum reaches 8.8%. When it is rapidly quenched, two different phases of solid aluminum and solid aluminum oxide separate out. To find relative mass fractions of these two phases in the limiting case, a simple lever rule can be applied to obtain  $m_{Al_2O_3}/m_{Al} = 0.228$  and  $V_{Al_2O_3}/V_{Al} = 0.1539$ . Thus, the volume fraction occupied by oxide layer would be 0.133. Using this analysis we can relate the oxide thickness to the size of particle as shown in Figure 9.2 to obtain  $\delta = 0.046R_{out}$ .

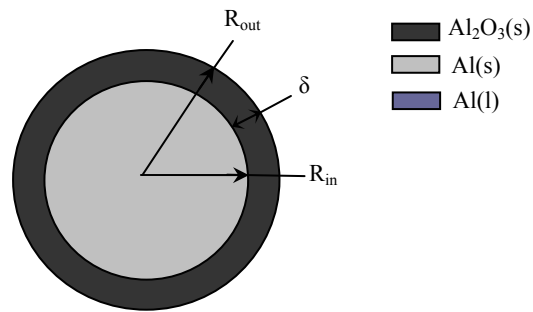


Figure 9.2: A schematic showing aluminum oxide thickness on a nanoparticle

This analysis predicts a thickness of the order of 2.3 nm and 4.6 nm for particles of sizes 50 and 100 nm, respectively. In most of the experimental literature, a thickness of the order 3-5 nm has been reported for particles in the range 50-100 nm. The oxide-layer

thickness can also be computed from the results of Eisenreich et al. (Eisenreich et al., 2004) This gives the fraction occupied by aluminum oxide as 0.12, which is in agreement with 0.133, assuming experimental uncertainties.

Table 9.1 lists the properties of aluminum and its oxide that will be frequently referred to in the discussion of the five stages. The values for nano phase have been obtained using molecular dynamics simulations and theoretical correlations like Lindemann index for melting. Figure 9.3 shows schematically the five-stage theory which aims to describe the particle behavior, from the time it is introduced in an oxidizing environment till the complete burn-out.

Table 9.1: Thermo-physical properties of aluminum and alumina

Substance	Melting Temperature	Vaporization Temperature (@ 1 atm)	Density
Bulk Aluminum	940 K	2740 K	Solid: 2700 kg/m <sup>3</sup>
			Liquid: 2377 kg/m <sup>3</sup>
Nano Aluminum	448-940 K	2629-2740 K	-
Bulk Alumina	2327 K	4000 K	Amorphous: 3050 kg/m <sup>3</sup>
			Gamma: 3660 kg/m <sup>3</sup>
			Alpha: 3900 kg/m <sup>3</sup>
			Liquid: 3010 kg/m <sup>3</sup>
Nano Alumina Shell (1-3 nm)	986-1313 K	-	-

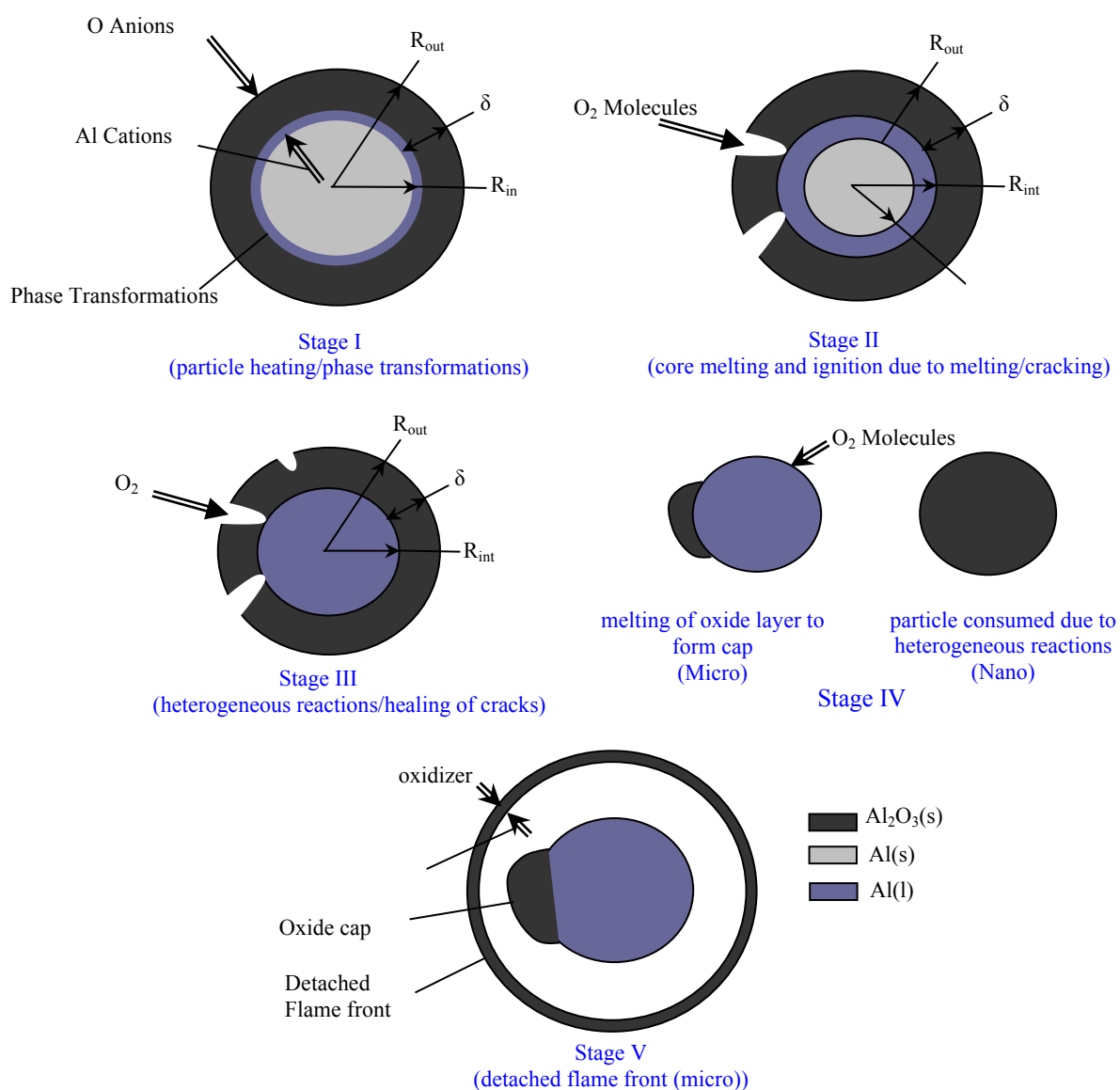


Figure 9.3: Various Stages of Aluminum Particle Ignition and Combustion

### 9.2.1 Stage I

The first stage involves simple heating of the aluminum core coated with amorphous oxide layer, until the melting point of aluminum is reached. This stage is also

characterized by phase transformations inside the oxide layer. The concept of phase transformations has been proposed by Trunov et al. (Trunov et al., 2006). The growth of the three phases of alumina namely, amorphous,  $\gamma$  and  $\alpha$  and their transformations from one form to the other start in Stage I. The growth of natural amorphous alumina layer is controlled by the outward diffusion of Al cations. The diffusion process has been proposed in the theoretical studies (Jeurgens et al., 2002) and was observed through MD simulations as well (Puri and Yang, 2008d). The energy of oxide metal interface stabilizes the oxide only up to a critical thickness of about 5 nm. When the temperature is sufficiently high, the amorphous oxide transforms to  $\gamma$  phase. If prior to phase change, the thickness of the amorphous layer is less than 5 nm, gamma alumina no longer forms a continuous layer covering the surface due to its higher density. As a result oxidation rate increases rapidly because of direct oxidation. These openings heal gradually and the oxidation rate decreases. The growth of  $\gamma$  alumina is limited by inward grain boundary diffusion of oxygen anions. This is also accompanied by transformations from  $\gamma$  phase to  $\theta$  and  $\delta$  phases, which do not affect the oxidation rate significantly. This  $\gamma$  phase alumina finally transforms to coarse and dense  $\alpha$  phase alumina. The rate of increase in the thickness of a particular phase of oxide and its transformation to other phases can be computed by fitting experimental data to Arrhenius type expressions (Trunov et al., 2006). For phase transformations, the rate of mass increase,  $\dot{m}_{(i-1) \rightarrow i}^{tr}$  of the oxide phase  $i$  transformed from oxide phase  $i-1$  can be described as

$$\dot{m}_{(i-1) \rightarrow i}^{tr} = 4\pi R_{i-1}^2 \rho_i F_{i-1 \rightarrow i} T_p \left\{ 1 - \exp\left(-\frac{K_{i-1 \rightarrow i} h_{i-1}}{R_u T_p}\right) \right\} \exp\left(-\frac{E_{i-1 \rightarrow i}}{R_u T_p}\right) \quad (9.3)$$

where  $T_p$  is the temperature of the particle,  $\rho$  the density,  $h$  the oxide thickness,  $R$  the radius,  $R_u$  the universal gas constant, and  $F$ ,  $K$ , and  $E$  experimentally determined constants as shown in Table 9.2 below.

Table 9.2: Kinetic parameters determined for phase transformations

Kinetic Parameter	Value
$E_{am \rightarrow \gamma}$	458 kJ/mol
$E_{\gamma \rightarrow \alpha}$	394 kJ/mol
$K_{am \rightarrow \gamma}$	$1 \times 10^{12}$ J/mol-m
$K_{\gamma \rightarrow \alpha}$	$1 \times 10^8$ J/mol-m
$F_{am \rightarrow \gamma}$	$2 \times 10^{15}$ m/s-K
$F_{\gamma \rightarrow \alpha}$	$5 \times 10^6$ m/s-K

Using these experimental constants values and properties of different phases, the rate of mass increase for amorphous to  $\gamma$  phase, and  $\gamma$  to  $\alpha$  phase at 450 K for a particle of size 10 nm coated with an oxide of 2.5 nm thickness are found to be of the order of  $10^{-48}$  and  $10^{-53}$  kg/s respectively.

Simpson provided direct correlations for growth of oxide layer thickness due to phase transformations as a function of temperature (Simpson et al., 1998)

$$\dot{h}_{am \rightarrow \gamma} = 1.549 \times 10^{20} \exp(-4.3858 / k_B T) \quad (9.4)$$

$$\dot{h}_{\gamma \rightarrow \alpha} = 3.16 \times 10^{18} \exp(-5.117 / k_B T) \quad (9.5)$$

The experiments were conducted by performing time resolved reflectivity measurements on thin films deposited on sapphire substrate. These give growth rates of the order of 0.01 to 1.0 mm/s in the temperature range of 873 to 1123 K for the case of amorphous to  $\gamma$  phase transition. Similarly, a growth rate of 0.001 to 1.0 mm/s is

observed in the temperature range of 1193 to 1313 K for the case of  $\gamma$  to  $\alpha$  phase transition. Merzhanov et al., provided characteristic times associated with such phase transformations by studying ignition of fine 50 micron aluminum wires subjected to electrical heating in different oxidizers (Merzhanov et al., 1977). Amorphous to  $\gamma$  phase transition has characteristic time given by

$$\tau_{am \rightarrow \gamma} = 10^7 \exp(40000 / R_u T) \quad (9.6)$$

Similarly, for  $\gamma$  to  $\alpha$  phase transition

$$\tau_{\gamma \rightarrow \alpha} = 5.5 \times 10^{-16} \exp(100,000 / R_u T) \quad (9.7)$$

Here  $R_u$  has units of *cal/mol K* and time scale,  $\tau$  in *seconds*. In the temperature range, 873 to 2073 K,  $\tau_{am \rightarrow \gamma}$  is of the order of  $10^2$  to  $10^{-3}$  seconds. In the temperature range 1473 to 2073 K,  $\tau_{\gamma \rightarrow \alpha}$  is of the order of 0.3 to  $10^{-5}$  seconds.

The oxide layer in Stage I and subsequent Stage II can also grow due to the diffusion of anions and cations through the oxide layer. The rate of growth is limited by the diffusion of ions and can be calculated theoretically using Mott's potential. The mathematical equation governing the process is given by (Jeurgens et al., 2002)

$$\frac{dx}{dt} = \Omega n \nu \exp\left(\frac{-U + qaE_0}{k_B T}\right) \quad (9.8)$$

where  $\Omega$  is the volume of oxide formed per cation,  $n$  the number of cations per unit area which may jump the energy barrier  $U$ ,  $\nu$  the attempt frequency of cation jump,  $q$  the charge of migrating cation,  $2a$  the distance from potential minimum to next potential minimum,  $k_B$  the Boltzmann constant,  $T$  the temperature,  $E_0$  the electric field due to

Mott's potential  $V_M$  and  $x(t)$  denotes the oxide film thickness at time  $t$ . The constants are given in detail in work by Jeurgens et al. The rate of increase of thickness obtained from the constants at 450 K for 0.5 nm thickness, is of the order of  $10^{-15}$  m/s. The rate is a very strong function of oxide thickness and increases exponentially for a comparatively thinner oxide layers.

In the quantum regime, characteristic time scales for electron transport under diffusion,  $\tau_D$  and convection,  $\tau_C$  can also be calculated as  $R^2/D$  and  $R^2/\mu V_0$  respectively. Here,  $R$  is the characteristic length scale,  $D$  the diffusivity,  $\mu$  the mobility, and  $V_0$  is the electric potential (Rode et al., 1992). Using the values given in Rode et al., 1992, the values for a 2.5 nm thick layer are  $8 \times 10^{-13}$  seconds and  $2 \times 10^{-14}$  seconds respectively. The corresponding time scales associated with the layer growth can be calculated using  $2\rho_{ox}\tau_D/C_0M_{ox}$  and  $2\rho_{ox}\tau_C/C_0M_{ox}$ . Here,  $\rho$  is the density,  $C$  the volumetric concentration and  $M$  is the molecular mass of the species. These come out to be of the order of  $5.1 \times 10^{-8}$  and  $1.27 \times 10^{-9}$  seconds in case of diffusion or convection dominated growth respectively.

The above analysis implies that diffusion of ions is one of the prominent mechanisms in this stage along with particle heating because of thin oxide layer. The phase transformations become prominent at higher temperatures and thicker layers i.e. Stage II.



### 9.2.2 Stage II

The second stage begins when the melting point of aluminum core is reached. The phase transformations continue in this stage as well and become one of the dominant mechanisms. The melting temperature can be much lower than the bulk melting point of aluminum based on the core size. From the previous detailed study of thermo-mechanical behavior of oxide layers using MD simulations (Puri and Yang, 2008d), the oxide layer can also exhibit phase transition from solid to liquid at temperatures much lower than the bulk melting temperature of 2327 K. Existing studies on combustion of micron-sized aluminum indicate that ignition coincides with melting of the oxide layer. However, for nano-sized particles, ignition takes place either in Stage II or Stage III. In Stage II ignition is due to cracking of the oxide shell. Cracking itself can occur, either due to the pressure buildup inside the shell as a result of core melting or due to phase transformations at the surface. As a result at nano scales, the particles get ignited at a much lower temperature which for some particles is near the melting point of Al i.e. ~933 K.

The ratio of energy conducted to that rate of energy stored by the layer (in the form of a spherical shell) is directly proportional to the surface area to volume ratio and can be written as

$$\frac{E_{cond}}{E_{stored}} \propto \frac{kA\Delta T / \Delta r}{\rho c V \Delta T / \Delta t} \propto \frac{k}{\rho c} \frac{A \cdot \Delta t}{V \cdot \Delta r} \quad (9.9)$$

where  $k$  is the conductivity,  $A$  the surface area,  $V$  the volume,  $c$  the specific heat,  $\rho$  the density,  $\Delta t$  the time scale, and  $\Delta r$  the length scale associated with the process. As the

particle size decreases to nano scales, this ratio increases and hence, the shell conducts heat easily. This eventually melts the aluminum core before the shell melts and results in rupture at around 933 K. In case of a micro-sized particle, the energy stored is more compared to conduction. This high thermal resistance to conduction results in rapid heating and eventual melting of the shell before the solid core. This Fourier number analysis and characteristic time scales can be used to explain the high correlation between core melting and oxide layer cracking at nano scales as shown in Figure 9.4. A characteristic time scale of the order of picoseconds falls in the range of heating time scales associated with some experimental studies performed for nano-sized particles involving laser flash heating (Wang et al., 2005).

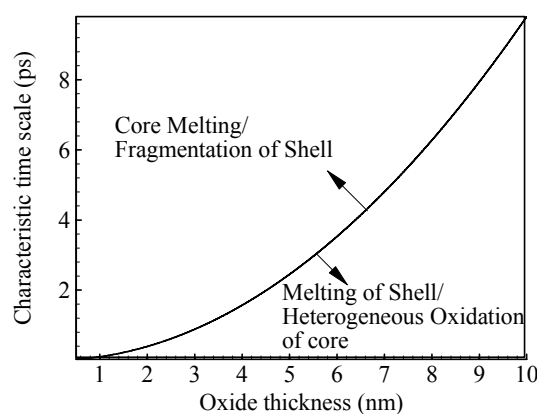


Figure 9.4: Fourier Analysis based on characteristic time and length scales associated with oxide layer

However, there always is a parallel process of direct oxidation at these crack sites which heal the layer. Theoretically this is the fastest oxidation rate and can be calculated using (Friedlander, 2000)

$$\frac{dN_{O_2}}{dt} = \frac{P_{O_2} \pi D_p^2}{\sqrt{2\pi m k_B T}} \quad (9.10)$$

where  $P$  is the partial pressure of oxygen in gas,  $D$  the particle diameter,  $k_B$  the Boltzmann's constant,  $T$  the temperature, and  $N$  is the number of molecules. This gives a characteristic time of the order of  $10^{-12}$  seconds for a particle size of the order of 50 nm with pressure and temperature of 0.3 MPa and 1373 K respectively. Looking at other time scales, the characteristic times for heating and melting for the core are given by (Faeth, 1977)

$$\tau_{heat} = \frac{D^2}{\alpha_f} \quad (9.11)$$

$$\tau_{melt} = \frac{D^2 h_{fg}}{c_p \Delta T \alpha_f} \quad (9.12)$$

where,  $D$  is the particle diameter,  $\alpha_f$  the thermal diffusivity, and  $h_{fg}$  the heat of fusion. These are of the same order of magnitude as that of the characteristic time scale obtained using Equation 9.10. The characteristic heat transfer from the particle in the molecular limit can be defined as (Filippov et al., 2000)

$$\tau_{heat,mol} = \left( \frac{\rho_p c_p m_g}{\alpha \rho_g k_B} \frac{D}{\sqrt{8 k_B T_g / \pi m_g}} \right) \quad (9.13)$$

where,  $\rho_p$  is the density of the aluminum core,  $\rho_g$  the gas density,  $c_p$  the specific heat of aluminum core,  $m_g$  the mass of oxygen molecule,  $k_B$  the Boltzmann's constant,  $T_g$  the gas temperature,  $D$  the particle diameter, and  $\alpha$  the accommodation coefficient. At room temperature the characteristic time scale for a 10 nm particle is of the order of  $10^{-7}$

seconds. This is two orders of magnitude larger than the characteristic time scales obtained using continuum relations.

The characteristic time for diffusion of heat through gas phase is 1000 times more than condensed phase and hence can be ignored. If the characteristic time scale for the growth of layer through direct oxidation is small as compared to that of melting and cracking, then the oxidation for the rest of time can be modeled as that of diffusion through the layer. Otherwise, the oxidation process has to be modeled as the direct attack of oxygen on aluminum surface, with cracks exposing the surface. It is this comparison between characteristic times of healing and cracking and Fourier number which explains ignition due to cracking or melting for nano or micro-particles respectively. The stage continues till the melting of aluminum core is complete.

### **9.2.3 Stage III**

The healing and formation of cracks continues in stage three. The surface reactions take place with the diffusion of oxygen through the oxide shell as the rate-limiting step. This stage is characterized by oxidation at the interface, heating up of the regressing liquid aluminum core, and growth of solid aluminum oxide layer until the melting point of aluminum oxide is reached, subsequently ending Stage III.

### 9.2.4 Stage IV

At this point, the oxide layer melts and forms a cap under the effect of surface tension, covering a portion of the surface for a micron-sized particle (Stage IV). This is followed by heterogeneous reactions at the surface or homogeneous gas phase reactions. The aluminum oxide formed, continues to melt, and adds to the oxide cap. Pressure and particle diameter play a very important role in determining the particle behavior in the stage IV through their influence on the characteristic diffusion time relative to kinetic times. For diffusion controlled mechanism the combustion time can be derived as

$$t_{b,diff} = \frac{\rho_p D_p^2}{8\rho D \ln(1 + \nu Y_{O,\infty})} \quad (9.14)$$

where  $D_p$  is the initial particle diameter,  $\rho_p$  the particle density,  $\rho$  the gas density,  $D$  the gas mass diffusivity,  $\nu$  the mass stoichiometric fuel-oxidant ratio, and  $Y$  is the mass fraction. In case of a kinetically controlled mechanism the mass consumption rate is given by

$$\frac{\dot{m}}{4\pi r_p^2} = MW_p k P X_{O,s} \quad (9.15)$$

where,  $X_o$  is the oxidizer mole fraction, and  $k$  the surface reaction rate with the oxidizer.

This on integration gives a characteristic time of

$$t_{b,kin} = \frac{\rho_p D_p}{2MW_p k P X_{O,\infty}} \quad (9.16)$$

To determine the dominant combustion mechanism the Damkohler number, Da, for surface reaction is defined as (Yetter and Dryer, 2001)

$$Da = \frac{t_{b,diff}}{t_{b,kin}} = \frac{MW_p k P D_p X_{o,\infty}}{4 \rho D \ln(1 + \nu Y_{o,\infty})} \quad (9.17)$$

This implies that small particles at low pressures generally burn under kinetically controlled conditions as shown in Figure 9.5. Similarly, larger particles at high pressures may undergo a diffusion- controlled mechanism. It is also speculated that because of the geometry of nano-sized particles, the oxidizer species need not diffuse across a relatively large distance before reaching the particle surface. This results in significantly shorter diffusion times and would lead to a chemical-kinetic-controlled situation. Till the end of stage four, a nano-sized particle will be fully consumed, whereas a micron-sized particle will enter the final fifth stage. The boiling point of aluminum is reached, and instead of heterogeneous reactions at the surface, homogeneous reaction takes place with a detached flame (Stage V).

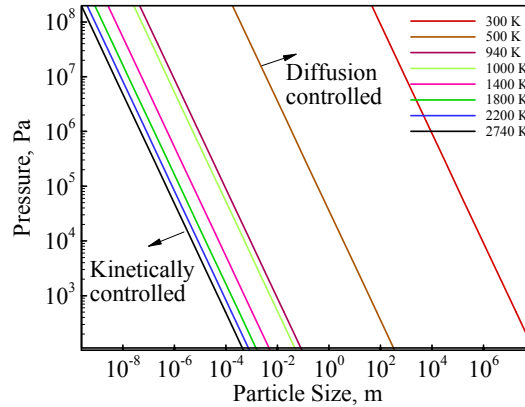


Figure 9.5: Regimes of Diffusion vs. Kinetically controlled mechanism as a function of different pressures and particle size

To obtain the kinetics of oxidation, various oxidation laws have been observed experimentally (Medvedev et al., 1982; Gurevich et al., 1978; Grigor'ev et al., 1973;

Grigor'ev et al. 1979). The process of growth of oxide layer can be described by a generalized expression (Fedorov and Kharlamova, 2003)

$$\frac{dh}{dt} = KC_{ox}^m \exp(-E/RT) \exp(-h/h_0) \quad (9.18)$$

where  $h$  is oxide thickness,  $h_0$  the initial oxide thickness,  $K$  the pre-exponent in oxidation law,  $C_{ox}$  the oxidizer concentration near particle surface, and  $m$  the oxidizer concentration in terms of oxidizer. Another frequently used equation to describe kinetics is of the form

$$\frac{dh}{dt} = \frac{KC_{ox}^m}{h^n} \exp(-E/RT) \quad (9.19)$$

For  $n = 1$ , parabolic oxidation rate law is assumed, which is valid if the oxidation rate is limited by the diffusion through the oxide film. The kinetics for reaction between oxygen and aluminum in the temperature range 1873 to 2273 K, following the parabolic rate law can be expressed as (Merzhanov et al., 1977)

$$\frac{dh}{dt} = \frac{1.9 \times 10^{-5}}{h} \exp(-17,000 / R_u T) \quad (9.20)$$

where,  $R_u$  is in  $cal/mol K$  and  $dh/dt$  is in  $cm/s$ . The growth rate calculated using Eqn. 9.20 is of the order of 1.54 cm/s at 1000 K. The relation was obtained through electro-thermo-graphic method by heating aluminum wire through constant power electric current in oxygen. For  $n = 0$ , the rate law can be expressed as

$$\frac{dh}{dt} = 18 \times 10^5 \exp(-20,000 / R_u T) \quad (9.21)$$

where,  $R_u$  is in  $\text{cal/mol K}$  and  $dh/dt$  is in  $\text{cm/s}$ . This gives a growth rate of  $8.17 \text{ cm/s}$  at  $1000 \text{ K}$ . Roberts et al. ignited micron-sized particles in 99% oxygen and 1% nitrogen atmospheres at high temperatures and pressures and obtained the following surface reaction rate law (Roberts et al., 1993)

$$k_s = A \exp(-E_a / RT_p) \quad (9.22)$$

Here,  $A$  is the pre-exponential coefficient with value of  $200 \text{ kg/m}^2\text{s}$ ,  $E_a$  the activation energy with value of  $22800 \text{ cal/mol}$ ,  $T_p$  the particle surface temperature and  $R_u$  the gas constant in  $\text{cal/mol K}$ .

Bergsmark et al. (Bergsmark et al., 1989) studied the oxidation of molten aluminum in oxygen at different particle pressures in the temperature range  $1073$  to  $1223 \text{ K}$ . They observed parabolic rate constants of the order of  $10^{-11}$  to  $10^{-12} \text{ cm}^2/\text{s}$ . These values are consistent with results of Fedorov et al.

Suvaci et al. studied the oxidation kinetics of aluminum powder in air and concluded that beyond a critical temperature, the oxidation rate changes from parabolic to linear rate law (Suvaci et al., 2000). The linear oxidation rate is faster than the parabolic rate. The growth rate can be expressed as  $1.1 \times 10^{-16} \exp(-238,000/R_u T) \text{ g}^2/\text{cm}^4\text{s}$  and  $7.4 \times 10^{-11} \exp(-128,000/R_u T) \text{ g/cm}^2\text{s}$  for growth of amorphous and  $\gamma$  layer respectively.

Trunov proposed the following relation for growth of layer in each phase

$$m_i^{ox} = \frac{C_i \exp(-E_i / RT_p)}{r_{i-1}^{-1} - r_i^{-1}} \text{ with constants in the Table 9.3 below. These give oxidation rates}$$

of the order of  $10^{-38} \text{ kg/s}$ .



Table 9.3: Constants used in expression for growth of oxide layer

Kinetic Parameter	Value
$E_{am}$	120 kJ/mol
$E_{\gamma}$	227 kJ/mol
$E_{\alpha}$	306 kJ/mol
$C_{am}$	$5.098 \times 10^{-8}$ kg/m-s
$C_{\gamma}$	$4.0784 \times 10^{-3}$ kg/m-s
$C_{\alpha}$	$2.3791 \times 10^{-2}$ kg/m-s

### 9.2.5 Stage V

In stage five, the particle burns just like the way it has been discussed in the literature for micron-sized particles, with a detached flame front and an oxide cap. For a micron-sized particle, as the temperature rises, aluminum melts first, and then the oxide melts and coalesces, allowing the aluminum vapor to diffuse to a gas phase flame. Thus, aluminum burns in the gas phase, and the flame front is detached from the droplet surface. The hot oxide products diffuse outward;  $\text{Al}_2\text{O}_3$  condenses and forms a smoke cloud that emits thermal radiation at a temperature of 3800 K. At nano scales, due to extremely small length scales, the reactions are always heterogeneous at the particle surface. The whole particle is consumed by the time when the aluminum boiling point is reached, due to heterogeneous reactions with oxidizer either diffusing through the layer or directly reacting at the surface. This is the reason causing the absence of a detached flame front for a nanoparticle.

### 9.3 Modes of ignition

Based on combinations of length and time scales defined in Stage I-III, six different modes of ignition can be identified as summarized in Table 9.4

Table 9.4: Various regimes of particle behavior during ignition

Phenomenon			Time Scale	Length Scale		Remarks	Mode
Core melts	Shell melts	Shell Heals		Oxide	Core		
Y	Y	N	$t_{melt,core} \approx t_{melt,shell}$ $t_{reac} \gg t_{melt,core}, t_{melt,shell}$	thin	small	Ignition by melting at smaller scales very early in Stage II	<b>I</b>
Y	N	Y	$t_{melt,core} \approx t_{reac}$ $t_{melt,shell} \gg t_{melt,core}, t_{reac}$	thick	small	Oxide Cracks and Heals, Stage III prominent, Nano self consumed in Stage IV, Micron sized particle reaches Stage V	<b>II</b>
N	Y	Y	$t_{reac} \approx t_{melt,shell}$ $t_{melt,core} \gg t_{reac}, t_{melt,shell}$	thin	large	Oxide melts and Heals, Stage IV prominent, Nano self consumed, Micron sized particle reaches Stage V	<b>III</b>
Y	N	N	$t_{melt,core} \ll t_{reac}, t_{melt,shell}$	thick	small	Ignition by crack and oxide fragmentation, no coating formed. Core small, shell thick and kinetic rates such that reaction scale is slow to heal, Stage II/III ignition	<b>IV</b>
N	N	Y	$t_{reac} \ll t_{melt,core}, t_{melt,shell}$	thick	large	Phase transformations, heals very fast so always protected, shell is still not melting. No early ignition in Stage II/III. Nano particle self consumed in Stage IV, Micron sized particle reaches Stage V.	<b>V</b>
N	Y	N	$t_{melt,shell} \ll t_{melt,core}, t_{reac}$	thin	large	Ignition by melting at larger scales, shell melts doesn't heal in time and core also intact. Shell is thin enough to melt compared to large core, unique case of very thin shells	<b>VI</b>
N	N	N				No ignition, condition not met	

Depending on the unique combination of pressure, temperature, core size, and thickness of the layer, there is a time scale associated with phenomena like core melting, shell melting and healing of the shell and this determines the mode of ignition. Figure 9.6 shows all these different modes. First three cases (I-III) deal with situation where two phenomena have time scales of the same order of magnitude and the third one has little affect. The later three cases (IV-VI) deal with the situation where one of the phenomena dominates the other two and hence determines the overall mode of ignition. Previous MD simulations have already shown that at nano scales core and shell melt at a much lower temperature compared to the bulk (Puri and Yang, 2007; Puri and Yang, 2007b; Puri and Yang, 2008d).

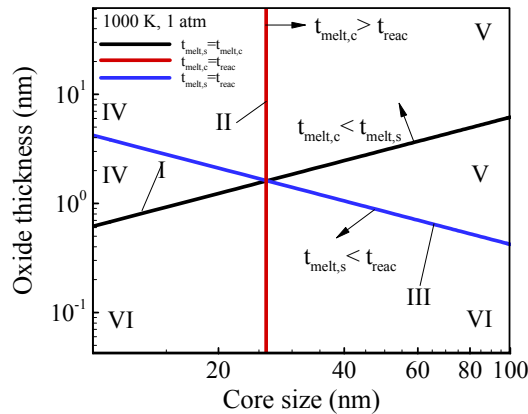


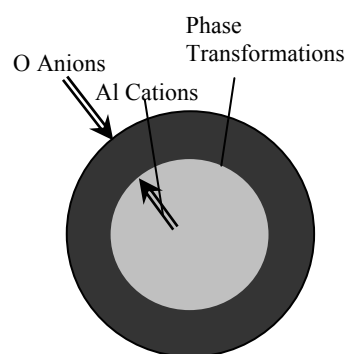
Figure 9.6: Different modes of ignition based on length and time scales

If the particle size is very small and is covered with a thin layer, it can result in similar time scales for melting of the core as well as the shell. If the time scales associated with healing of the shell is large compared to these, the ignition can happen very early in Stage II by peeling of the oxide shell as shown in Figure 9.7 as Mode I.

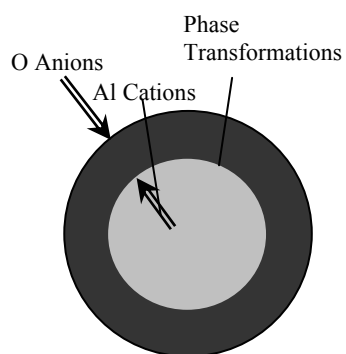
Figure 9.7 also shows the mode of ignition (II) if a small core is covered with a much thicker oxide shell. In such a scenario, the time scales for melting of the core and healing are of the same order and shell remains intact. Stage III in the five stage theory becomes the prominent stage in time history of aluminum particle.

If on the contrary, the melting of the shell and heterogeneous reactions happen simultaneously and melting of the core is slow, the oxide melts, nanoparticle is completely consumed and micron sized particle reaches Stage V. This is shown as Mode III in Figure 9.7.

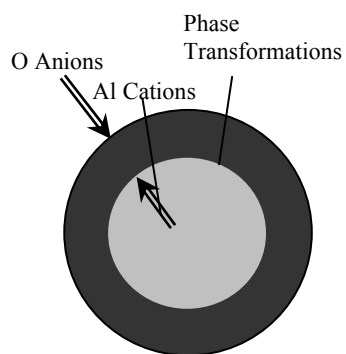
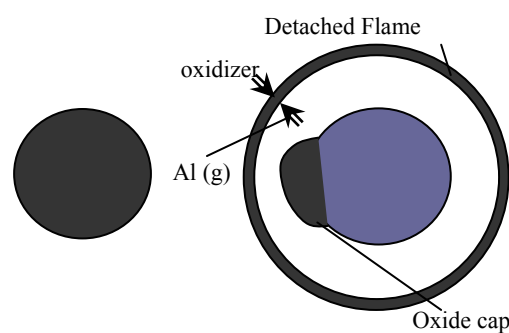
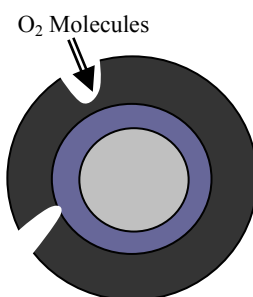
In addition of above three modes, there can be three additional modes which are characterized by one prominent phenomenon as compared to two competing processes. If the core melting is very prominent, which happens in case of thick shell and small cores, the ignition happens due to fragmentation and there is no healing either, because of slow kinetic rates (Mode IV). If the heterogeneous reactions are the prominent mechanism, phase transformations are the only process that continues and there is no ignition until Stage IV. Nano-sized particle is totally self-consumed and micro stage particle reaches stage V and burns in detached flame front fashion (Mode V). If time scales associated with the melting of the shell is most prominent, the ignition occurs by melting at larger scales, shell melts doesn't heal in time and core also remains intact. This is a unique case of very thin shells where shell is thin enough to melt compared to large core (Mode VI).



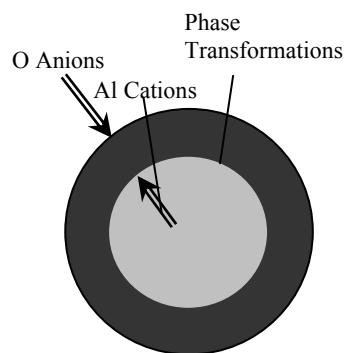
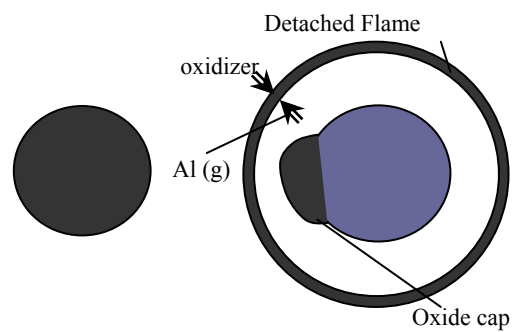
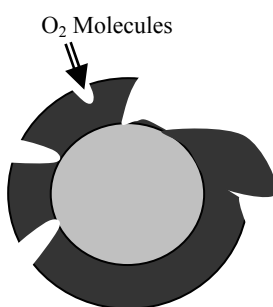
MODE-I



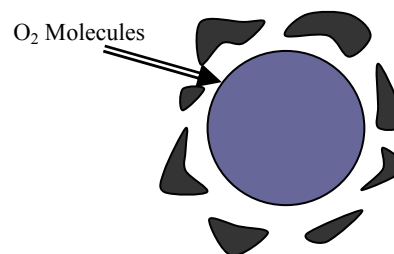
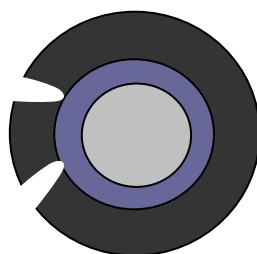
MODE-II



MODE-III



MODE-IV



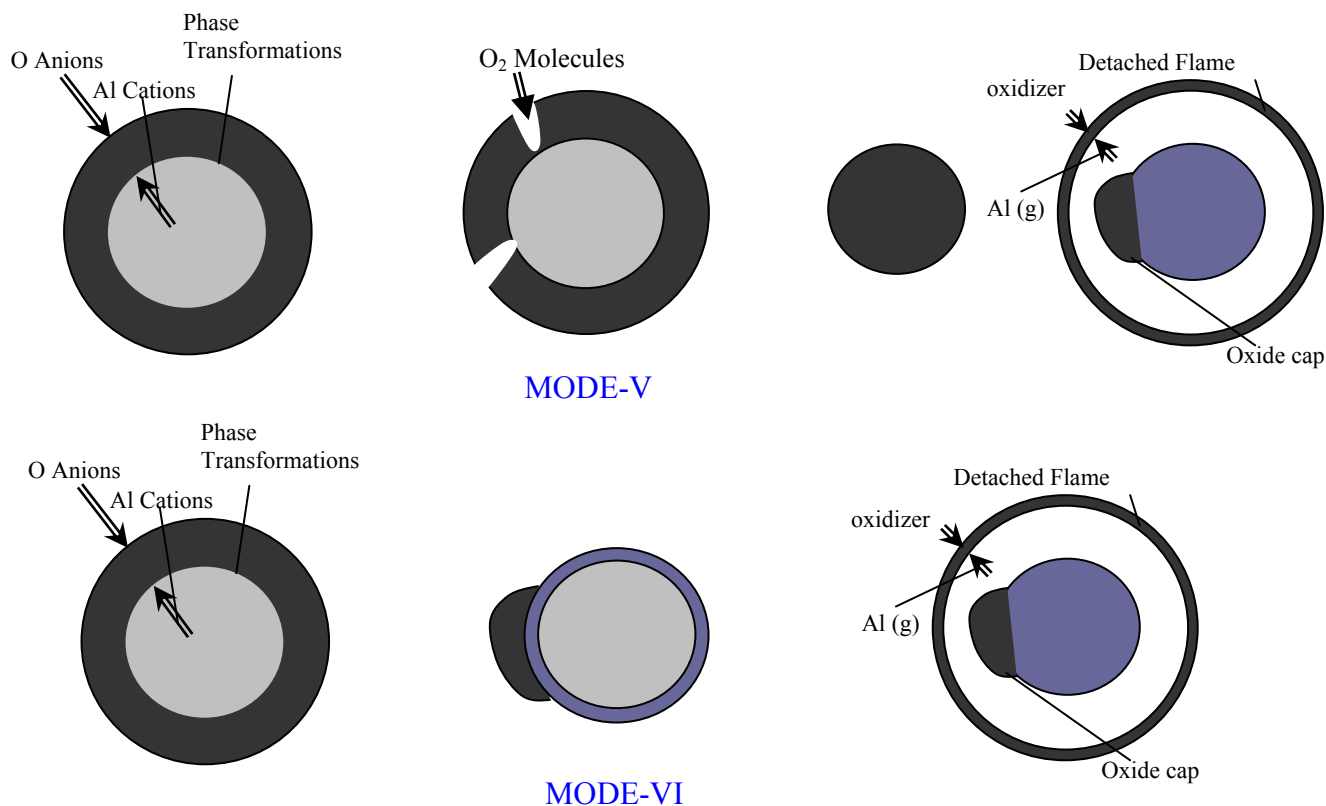


Figure 9.7: Schematic of different modes of ignition for oxide coated aluminum particles

The plot shown in Figure 9.6 is at 1000 K and 1 atm. Temperature and pressure also play a key role in determining probability of different mode of ignition. Figure 9.8 and 9.9 show the effect of increase in pressure and temperature respectively on different modes. As pressure increase it does not affect melting time scales but it does affect the reaction time scales. As pressure increases, the characteristic time scales associated with healing of layer reduces, and hence stage V and VI become more prominent. The core is virtually always covered with oxide shell and hence a nano-sized particle is consumed in a heterogeneous way and a micron-sized particle enters Stage V. As temperature is increased the characteristic time scales for direct attack of oxygen on particle increases and hence the effect is opposite to that of an increase in pressure as shown in Figure 9.9.

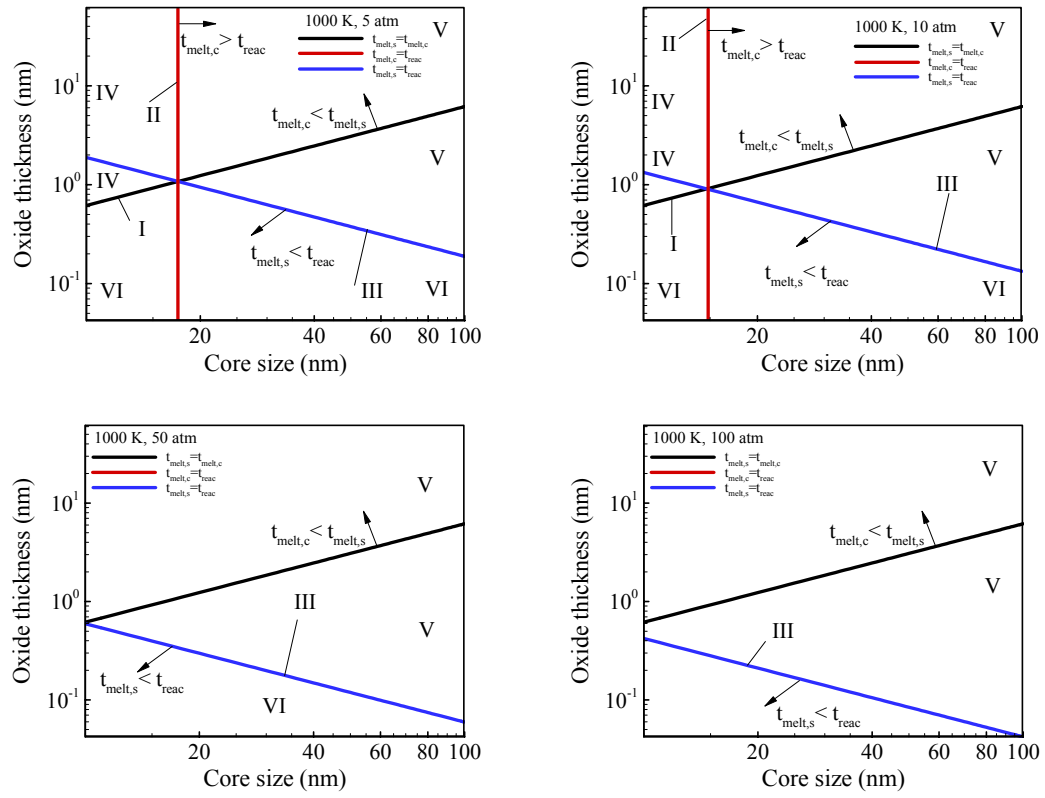


Figure 9.8: Effect of Pressure on Characteristic Time Scale Study

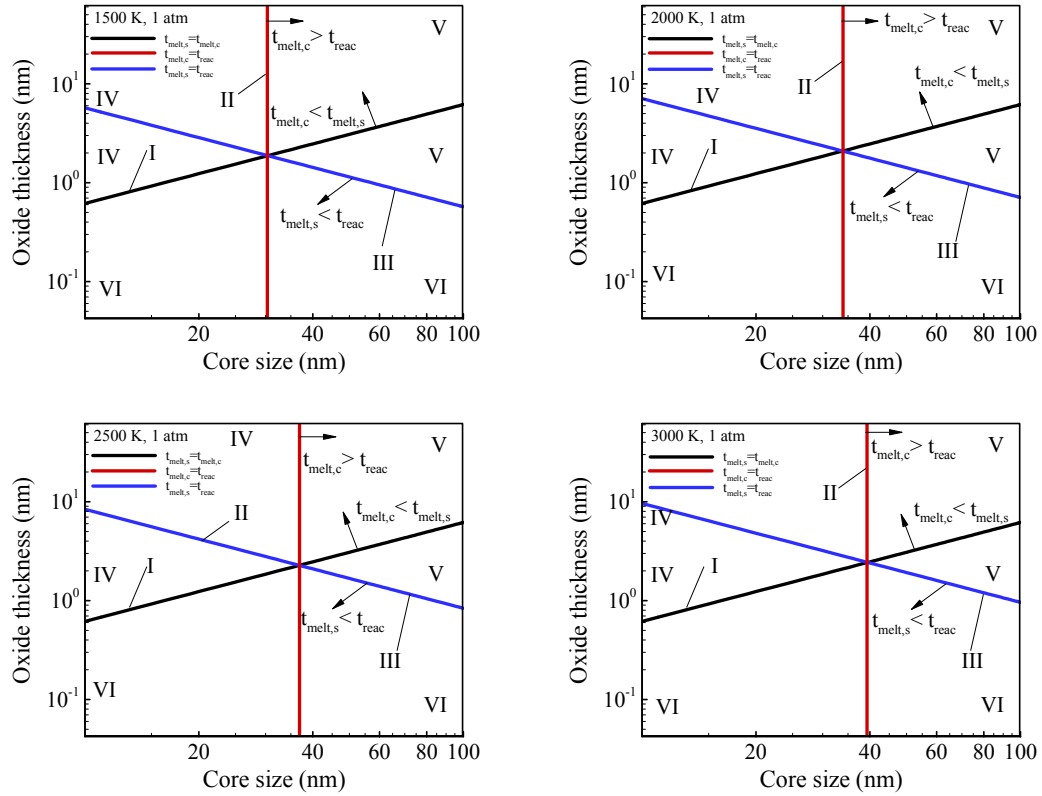


Figure 9.9: Effect of Temperature on Characteristic Time Scale Study

#### 9.4 Ignition Formulation using Phase Transformations

An attempt has been made to reproduce the work done by Dreizin so that this phase transformation stage can be incorporated into the numerical codes. Some results obtained from this model are shown below. Figure 9.10 shows the evolution of temperature and layer growth at 1250 K for a 100nm particle. The temperature increases rapidly in the stage when  $\gamma$  phase is forming due to direct oxidation. The combustion could not be attained because after reaching a peak of about 2100 K, the temperature starts falling off due to heat loss. This was an interesting phenomenon. It was realized



that due to large surface to volume ratio, a nanoparticle will have higher heat loss too. So, if a particle has very high thermal conductivity it will loose heat quickly too and might not ignite.

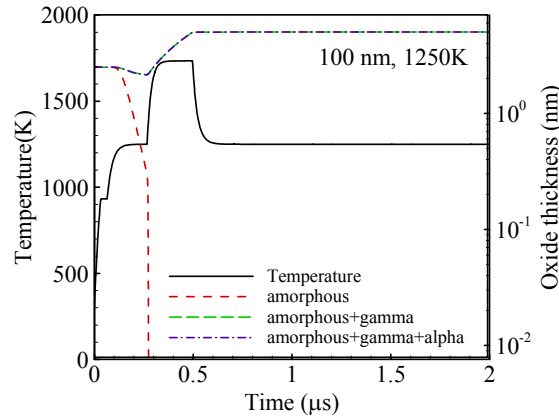


Figure 9.10: Predicted temperature histories and overall thickness of oxide layers for 100 nm particle introduced in air at 1250 K

Figure 9.11 shows the behavior of a 500nm particle at 1650 K. The particle could ignite at 1650 K. Figure 9.12 shows the case of a 5  $\mu\text{m}$  particle at 2100 K. Larger particles need a higher ambient temperature to ignite. Since the bigger particle takes longer to ignite, the higher fraction of  $\alpha$  phase thickness as compared to smaller particles is clearly seen. Further work needs to be done to fully reproduce and validate Dreizin's work, so that it can be incorporated into the numerical code for flame propagation studies.

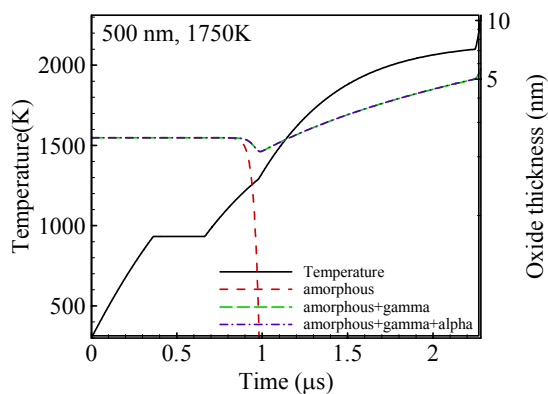


Figure 9.11: Predicted temperature histories and overall thickness of oxide layers for 500 nm particle introduced in air at 1750 K

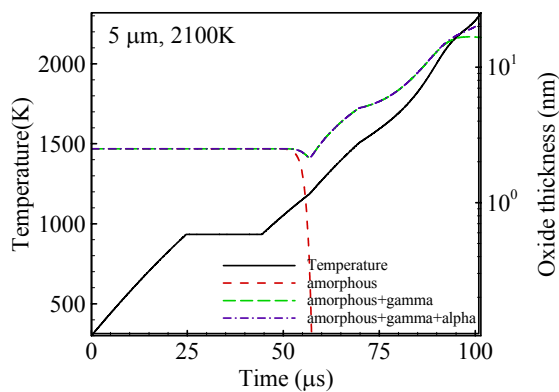


Figure 9.12: Predicted temperature histories and overall thickness of oxide layers for 5  $\mu\text{m}$  particle introduced in air at 2100 K

## 9.5 Conclusions

From the existing literature it can be concluded that the modeling for nano aluminum is still in nascent stages. Ignition and Combustion at Nano scales is much

different from the one at micro scales. In case of direct oxidation at nano scales, the process is kinetically controlled due to small diffusion scales involved. The heterogeneous oxidation through the oxide layer is a diffusion controlled mechanism due to the slow diffusion of aluminum cations or oxygen anions. However, oxidation in the last stage through direct oxygen can be kinetically or diffusion controlled based on Damkohler numbers.

For nano-sized particles the ignition stage always starts with heterogeneous reactions and phase transformations and is observed at relatively lower temperatures as compared to micro-scale. Cracking in oxide layer can occur either due to phase transformation of aluminum oxide or thermal expansion caused by melting of solid core. Due to fast rate of heterogeneous reactions, the nanoparticles are totally consumed in a pure heterogeneous fashion till the time the boiling point of aluminum is reached and there is no detached flame front formation. All the phenomena are closely coupled and are associated with characteristic time scales which help in explanation of different modes of ignition at both scales.

## Chapter 10

### Summary and Future Work

#### 10.1 Summary

In the present research work, a comprehensive study based on molecular-dynamics (MD) simulations has been performed to explore the thermo-mechanical behavior of nano aluminum particles covered with oxide layers (Puri and Yang, 2007; Puri and Yang, 2007b; Puri and Yang, 2008d). In addition, a unified theoretical model and numerical scheme has been established to investigate the ignition and combustion of aluminum particles at different length scales (Puri and Yang, 2008c; Puri and Yang, 2008). The entire framework accommodates all the processes and mechanisms involved at micro- and nano scales, and can be conveniently applied to a variety of metal particulates. A comprehensive review is currently being prepared summarizing the state of knowledge in this topical area (Puri and Yang 2008b). The research results (modeling techniques and research findings) will be transferred to ARL and other DoD laboratories to maximize the utilization of nano metal particles in the formulation of advanced energetic materials.

Chronologically, a comprehensive review on the ignition and combustion of aluminum particles at micro and nano scales was first performed. Various processes and mechanisms involved were identified. Research focus was then placed on the continued development of a unified theory of particle ignition and combustion, and on the

establishment of a Molecular Dynamics (MD) simulation tool to handle the problems at nano scales. With the theoretical and computational tools already established the main objective was then to investigate the thermo-mechanical behaviors of bulk and nanoparticulate aluminum by means of MD simulations. The general computational framework developed in the current molecular-dynamics study can handle micro-canonical (NVE), isobaric-isenthalpic (NPH), and isobaric-isothermal (NPT) ensembles using both Verlet and predictor-corrector algorithms. These algorithms have been parallelized using the atomic decomposition method. A separate post-processing code has also been developed to superimpose the grid on the geometry under consideration, and to analyze the results using the contours of various thermodynamic properties. The code has the capability of handling multi-atom simulations and can treat liquid and solid phases.

Nano-sized aluminum particles in the range of 2-9 nm are studied in the first study. Five different potential functions are implemented, and the results are evaluated using the particle-size dependence of the melting phenomenon as a benchmark. A combination of structural and thermodynamic parameters, including the potential energy, Lindemann index, translational-order parameter, and radial-distribution functions, are used to characterize the melting process. The dynamic coexistence of the solid and liquid phases is also explored. In addition, the effect of surface charge development on melting is examined using the Streitz-Mintmire potential.

To investigate the effect of voids and surfaces on melting, bulk materials are considered in addition to the particulate phase. For the study of bulk materials, crystals composed of 864 and 2048 atoms were treated; for the particulate phase, spherical nanoparticles up to 8.5 nm (20736 atoms) were considered. Simulations are carried out

by arranging atoms in an FCC lattice structure and evolving the system with periodic boundary conditions for the bulk phase. The phenomenon of defect nucleated melting is studied using voids of different shapes and sizes. Results are compared with pure crystals with no voids. The entire melting process is examined using snapshots of time evolution of atomic positions and density contours.

Finally, molecular-dynamics study has been performed to examine the thermo-mechanical behavior of nano aluminum particles coated with oxide layers. The size dependence of the melting phenomenon was first examined in the range of 5-10 nm, with the oxide thickness fixed at 1 nm. In each case, the oxide layer melted at temperatures substantially lower than the bulk value. The melting temperatures obtained varied between 986 and 1159 K. The effect of the oxide-shell thickness on the particle melting was explored in the range of 1.0-2.5 nm, with the core diameter fixed at 5 nm. The melting point of the oxide layer increased, from 1130 K for 1.0 nm to 1313 K for 2.5 nm thickness. The results were compared by simulating a pure 5 nm alumina nanoparticle. Melting was observed at 1284 K and the Lindemann index curve qualitatively showed the same trend as seen for the oxide layers with aluminum core.

Melting for oxide layers was also preceded by solid-solid phase transition to denser polymorphs, characterized by a decrease in Lindemann index for few picoseconds. The phenomenon was only observed for crystalline layers and was absent in the case of amorphous layers. A detailed structural analysis indicated that the shell stresses caused by the core melting were an order of magnitude higher than the tensile strength. The shell should have cracked under such a condition. However, in the present MD study, the shell

remained intact. This was attributed to the fact that the shell does not remain in a pure solid state and undergoes solid-to-solid and solid-to-liquid phase transitions.

The phenomenon of diffusion of aluminum cations through the shell was also investigated. The diffusion was faster and more prominent in the case of amorphous as compared to the crystalline layer. With insight into the behavior of aluminum particles at nano scales, the present research is an important milestone towards the development of a multi-scale theory for the ignition and combustion of nano-particulate aluminum.

In the end the condition for pyrophoricity/explosivity of nano-particulate aluminum is also analyzed. The size dependence of thermodynamic properties at nano scales, including melting and, vaporization temperatures, heat of fusion and heat of vaporization are considered and incorporated into the existing theories developed for micro and larger scales. In the context of unified theory at nano scales, the limiting condition for pyrophoricity is modified from the vaporization of aluminum to the melting of core and subsequent rupture of the oxide layer. The critical particle size is evaluated using the modified criterion and is found to be highly pyrophoric. The study also explores the explosive tendency for oxide coated nano aluminum particles for given values of particle size and thickness of oxide layer.

Finally, a phenomenological theory for ignition and combustion of aluminum particles has been proposed. The whole time history from ignition till particle burnout is divided into five stages. An attempt has been made to explore different modes of ignition based on the effect of pressure, temperature, oxidizer, oxide thickness and particle diameter and is investigated using time and length scales involved during ignition and combustion.

## 10.2 Recommendations for Future Work

### 10.2.1 Ignition Behavior of Metal-Coated Aluminum Particles

Having investigated nano-particulate aluminum and its oxides in detail, we propose to build a more complex system containing binary compositions like aluminum coated with other metal or even involving doping. Low energy electron diffraction (LEED) and scanning tunneling microscopy (STM) have shown that two metals interacting on a surface can form compounds with structures not seen in bulk alloys (Rodriguez, 1996). Many novel phenomena related to the kinetics of metals on metals have been discovered. The knowledge gathered in this area provides a solid basis for the synthesis of new materials with applications in areas of catalysis, electro-chemistry, microelectronics and nano energetics. Metals such as platinum (Pt), palladium (Pd) or nickel (Ni) have been recently considered for coating on aluminum to enhance the ignition characteristics and energetics.

The isothermal oxidation performance for the Pt-Al system at 1473 K has been found to be similar to that of Ni-Al. Both Pt-Al and Ni-Al oxidize at approximately the same rate showing nearly parabolic reaction kinetics, and Zr-doped alloys have been observed to oxidize at different rates (Dickey et al., 1999). Doping can also be used to control the outward diffusion of ions in  $\text{Al}_2\text{O}_3$  in an oxide-coated nano aluminum particle. The segregation of these dopants is believed to alter the cation transport in the  $\text{Al}_2\text{O}_3$  scale (one of the prominent mechanisms at nano scales) and thereby change the oxidation mechanism (Pint et al., 1993). Partially oxidized aluminum substrates have been obtained at different oxidation conditions in the study of Pd/AlOx/Al samples prepared in situ



through X-ray photoelectron spectroscopy (XPS) and low energy ion scattering (LEIS) (Sedlacek et al., 2004). For aluminum particles coated with a thin layer of metal like nickel, ignition can be achieved at a considerably lower temperature due to the highly exothermic inter-metallic reactions. This type of particles is also less subject to agglomeration (Babuk et al., 2001). Several experimental studies have been conducted to explore the structural and thermal behaviors of these inter-metallics. The ignition mechanisms of such systems, however, are not completely understood (Andrzejak et al., 2007). It is not clear if the inter-metallic reactions or oxidation with ambient gases are responsible for the observed changes in ignition characteristics and flame development. Furthermore, the behavior of some of these systems at nano scales is completely unexplored in the field of energetics.

The proposed work will proceed in three steps. First, a phenomenological theory will be established to describe and analyze the various physio-chemical processes involved in the ignition and combustion of single aluminum particles coated with different metals (e.g., Pt, Pd, and Ni) at nano scales. The key phenomena of concern include inter-metallic reactions, phase transformations of aluminum core and coated-metal layer, oxidation, and energy transport at different length and time scales. Results will provide basic theoretical insights into the mechanisms involved. In the second step, an appropriate inter-metallic system will be selected for further study based on the impact to the Army's needs and coordination with other members of the MURI team. The final step will involve detailed MD simulations of the particle behavior in the size range up to 20 nm. The study will extend the general framework established in the present MURI program by considering inter-metallic interactions. State-of-the-art potential functions

will be employed (Eck et al., 2002). Priority will be given to those which have been specially developed for describing inter-atomic interaction forces of transition metals and have been used reliably for modeling metal systems (Sutton and Chen, 1990). All the calculations will be performed on a distributed computing facility recently upgraded at PSU, so that sweeping results can be acquired in a timely fashion. The combined modeling and computational capabilities will provide unique and quantitative insights into the atomistic mechanisms involved in the heating and subsequent reactions of metal-coated aluminum particles.

### **10.2.2 Oxidation of Aluminum in Flow Environments**

The ultimate goal of this research is to study the behavior of nano-energetic particles. The emphasis will be placed on aluminum particles and their collective behavior in different flow environments. A solid foundation has been laid in this direction by examining the single particle behavior.

For the flow environment study, the first step will be to establish a general analysis accommodating particle and thermo-fluid dynamics for two phase flow interactions. Efforts will be devoted to the combustion of nano aluminum particles in gaseous environments with different compositions and flow conditions. The physical configurations to be considered can be a premixed flame propagation or ignition in a constant area duct. The formulation for the gas phase dynamics will be based on the complete conservation equations for a multi-component chemically reacting system in three dimensions. Turbulence closure will be achieved by means of large eddy simulation

(LES) techniques, in which grid resolved scales will be calculated explicitly. The unresolved small scales and their effects on resolved scales will be modeled either analytically or empirically.

### **10.2.3 Flame Speed Calculations in Particle Laden Flows**

The combustion of nanoparticles has been studied previously in a well characterized laminar particle laden flow by means of both numerical and theoretical approaches. However, there were a lot of assumptions involved and the particles were treated as large molecules, which is a limiting case when particle size goes to zero. The particle laden flow has been modeled as one dimensional, laminar, steady flow of premixed gas mixture. The formulation has been numerically solved using CHEMKIN software. The results obtained in this PhD work can be used to relax some of those assumptions and improve the model.

### **Bibliography**

- Alavi, S., and Thompson, D. L., "Molecular Dynamics simulations of melting of aluminum nanoparticles," *Journal of Physical Chemistry A*, Vol. 110, No. 4, 2006, pp. 1518
- Alavi, S., Mintmire, J. W., and Thompson, D. L., "Molecular Dynamics Simulations of Oxidation of Aluminum Nano Particles," *Journal of Physical Chemistry B*, Vol. 109, 2005, pp. 209

- Alder, B. J., and Wainwright, T. E., "Phase Transition for a Hard Sphere System," *Journal of Chemical Physics*, Vol. 27, 1957, pp. 1208
- Alekseev, A. G., Barlas, R. A., Tsidelko, T. I., and Shapoval, A. F., "Effect of Particle Size on the Combustibility and Explosion Parameters of Dispersed Aluminum and Magnesium Powders," in *V. V. Nedin (Ed), Preduprezhdenie Vnezapnykh Vzryvov Gazodispersnykh Sistem*, 1971, pp. 66 (in Russian)
- Allard, L. F., Voelkl, E., Kalakkad, D. S., and Datye, A. K., "Electron holography reveals the internal structure of palladium nano-particles," *Journal of Material Science*, Vol. 29, 1994, pp. 5612
- Allen, M. P., and Tildesley, D. J., *Computer simulation of liquids*, Second Edition, Clarendon Press, Oxford, 1989
- Anderson, H. C., "Molecular dynamics simulations at constant pressure and/or temperature," *Journal of Chemical Physics*, Vol. 72, No. 4, 1980, pp. 2384-2393
- Agarwal, P. M., Rice, B. M., and Thompson, D. L., "Molecular dynamics study of the effects of voids and pressure in defect-nucleated melting simulations," *Journal of Chemical Physics*, Vol. 118, No. 21, 2003, pp. 9680-9688
- Andrzejak, T., Shafirovich, E., and Varma, A., "Ignition Mechanism of Nickel-Coated Aluminum Particles," *Combustion and Flame*, Vol. 150, 2007, pp. 60-70
- Assovskiy, I. G., Zhigalina, O. M. and Kolesnikov-Svinarev, V. I., "Gravity Effect in Aluminum Droplet Ignition and Combustion," *5th International Microgravity Combustion Workshop*, 18-20 May 1999 Cleveland, USA, NASA, 1999
- Assovskiy I. G., "Nano particles in aluminum combustion," *Proceedings of 29th International Pyrotechnics Seminar*, Westminster, Colorado, IPS, 2002, pp.219-226
- Babuk, V. A., Vassiliev, V. A., and Sviridov, V.V., "Propellant Formulation Factors and Metal Agglomeration in Combustion of Aluminized Solid Rocket Propellant," *Combustion Science and Technology*, Vol. 163, 2001, pp. 261-289
- Babuk, V. A., Vassiliev, V. A., and Sviridov, V. V., "Formation of Condensed Combustion Products at the Burning Surface of Solid Rocket Propellant," *Solid Propellant Chemistry, Combustion and Motor Interior Ballistics*, Chapter 2.21, edited by V. Yang, T.B. Brill and W.Z. Ren, Progress in Astronautics and Aeronautics, AIAA, Vol. 185, 2000, pp. 749-774
- Baldi, and Alfonso L., *Patent 5028385*, "Treatment of metals for coating or activation," July 1991, <http://www.freepatentsonline.com/5028385.html>

- Bartlett, R. W., Ong J. N., Fassell W. M., and Papp C. A., "Estimating Aluminum Particle Combustion Kinetics," *Combustion and Flame*, Vol. 7, 1963, pp. 227-234
- Beckstead, M. W., "A Summary of Aluminum Combustion," Internal Aerodynamics in Solid Rocket Propulsion," *von Karman Institute for Fluid Dynamics, Lecture Series*, Belgium, May, 2002
- Belyaev, A. F., Frolov, Yu. V., and Korotkov, A. I., "Combustion and Ignition of Particles of Finely Dispersed Aluminum," *Fiz. Goreniia Vzryva*, Vol. 4, 1968, pp. 323 (in Russian)
- Bergsmark, E., Simensen, C. J., and Kofstad, P., "The oxidation of Molten Aluminum," *Materials Science and Engineering*, A120, 1989, pp. 91-95
- Bhatia, R., and Sirignano, W., "Metal Particle Combustion with Oxide Condensation," *Combustion Science and Technology*, 1993
- Boiko, V., Lotov, V., and Papyrin, A., "Ignition of gas suspensions of metallic powders in reflected shock waves," *Combustion, Explosion, and Shock Waves*, Vol. 25, 1989, pp. 67-74,
- Born, M., and Oppenheimer, R., "On the Quantum Theory of Molecules," *Annalen der Physik*, Vol. 84, 1927, pp.457-484
- Brewer, L., "The Thermodynamic Properties of the Oxides and Their Vaporization Processes," *Chemical Reviews*, Vol. 52, No. 1, 1953, pp. 36-40
- Brooks, K. P., and Beckstead, M. W., "Evaluation of a Flame Model with a Rijke Burner," *28th JANAF Combustion Meeting*, Vol. II, CPIA 573, 1991, pp.509-517
- Brooks, K. P., and Beckstead, M. W., "Dynamics of Aluminum Combustion," *Journal of Propulsion and Power*, Vol. 11, No. 4, pp. 769-780, 1995
- Brossard, C., Ulas, A., Yen, C. L., and Kuo, K. K., "Ignition and Combustion of Isolated Aluminum Particles in the Post-Flame Region of a Flat-Flame Burner," *16th International Colloquium on the Dynamic of Explosions and Reactive Systems*, Krakow, Poland, 3-8 August, 1997
- Brousseau, P., and Anderson, C. J., "Nanometric Aluminum in Explosives," *Propellants, Explosives and Pyrotechnics*, Vol. 27, 2002, pp.300-306
- Brzustowski, T., and Glassman, I., "Spectroscopic Investigation of metal combustion," *Heterogeneous Combustion*, Progress in Aeronautics and Astronautics, AIAA, New York, Vol. 15, 1964a, pp. 41-63
- Bucher, P., Yetter, R. A., Dryer, F. L., Vicenzi, E. P., Parr, T. P., and Hanson, D. M., "Flame Structure Measurement of Single Measurement of Single Isolated

Aluminum Particles Burning in Air,” *Twenty-Sixth Symposium (International) on Combustion*, Naples, Italy, 1996, pp. 2-25

Bucher, P., Yetter, R. A., Dryer, F. L., Vicenzi, E. P., Parr, T. P., and Hanson, D. M., “PLIF Species and Ratio metric Temperature Measurements of Aluminum Particle Combustion in  $O_2$ ,  $CO_2$ , and  $N_2O$  Oxidizers, and comparison with Model Calculations,” *Twenty-Seventh Symposium (International) on Combustion*, The Combustion Institute, 1998, pp. 2421-2429

Bucher, P., Yetter, R. A., Dryer, F. L., Vicenzi, E. P., Parr, T. P., and Hanson, D.M., “Condensed-phase Species Distributions about Aluminum Particles Reacting in Various Oxidizer,” *Combustion and Flame*, Vol. 117, 1999, pp. 351-361,

Bucher, P., Yetter, R. A., Dryer, F. L., Vicenzi, E. P., Parr, T. P., and Hanson, D. M., “Detailed Studies on the Flame Structure of Aluminum Particle Combustion,” *Solid Propellant Chemistry, Combustion and Motor Interior Ballistics*, Chapter 2.19, edited by Yang, V., Brill, T. B., and Ren, W. Z., Progress in Astronautics and Aeronautics, AIAA, Reston, VA, Vol. 185, 2000, pp. 689-722

Bulian, C. J., Kerr, T. T., and Puszynski, J. A., “Ignition Studies of Aluminum and Metal Oxide Nanopowders,” in *F. J. Schelling (Ed), IPSUSA Seminars, Inc., 31st International Pyrotechnics Seminar*, Fort Collins, CO, 12-14 July, 2004, pp. 327

Buoik, A., Safety Engineering in Powder Metallurgy [in Russian from the Polish], *Hutnik (Stalingrod)*, Vol. 8, 1954

Campbell, T., Kalia, R. K., Nakano, A., Vashishta, P., “Dynamics of Oxidation of Aluminum Nanoclusters using Variable Charge Molecular-Dynamics Simulations on Parallel Computers,” *Physical Review Letters*, Vol. 82, No. 24, 1999, pp. 4866-4869

Campbell, T. J., Aral, G., Ogata, S., Kalia, R. K., Nakano, A., and Vashishta, P., “Oxidation of aluminum nanoclusters,” *Physical Review B*, Vol. 71, 2005, pp. 205413

Catorie, L., *Private Communication*, December 2004

Chang, H., Choi, Y., Kong, K., Ryu, B. H., “Atomic and electronic structures of amorphous  $Al_2O_3$ ,” *Chemical Physics Letters*, Vol. 391, 2004, pp. 293-296

Cleri, F., and Rosato, V., “Tight binding potentials for transition metals and alloys,” *Physical Review B*, Vol. 48, No. 1, 1993, pp. 22-33

Cousins, C. S. G., “The corundum structure: internal strain tensors and cluster configurations under stress,” *Journal of Physics: Solid State Physics*, Vol. 14, 1981, pp. 1508-1602

- Davis, A., "Solid Propellants: The Combustion of Particles of Metal Ingredients," *Combustion and Flame*, Vol. 7, 1963, pp. 359-367
- Daw, M. S., and Baskes, M. I., "Embedded-atom method: Derivation and application to impurities, surfaces, and other defects in metals," *Physical Review B*, Vol. 29, No. 12, 1984, pp. 6443-6453
- Daw, M. S., "Model of metallic cohesion: The embedded-atom method," *Physical Review B*, Vol. 39, No. 11, 1989, pp. 7441-7452
- Daw, M. S., Foiles, S. M., and Baskes, M. I., "The Embedded Atom Method: A review of theory and applications," *Materials Science Reports*, 1993, pp. 251-310
- Derevyga, M. E., Stesik, L. N., and Fedorin, E. A., "Study of the Ignition and Combustion of Aluminum and Zinc in Air," *Combustion Explosion and Shock Waves*, Vol. 13, 1977, pp. 722
- Dickey, E. C., Pint, B. A., Alexander, K. B., and Wright, I. G., "Oxidation Behavior of Platinum-Aluminum Alloys and the Effect of Zr doping," *Journal of Materials Research*, Vol. 14, No. 12, 1999, pp. 4531
- Dreizin, E. L., "Surface Phenomena in Aluminum Combustion," *Combustion and Flame*, Vol. 101, 1995, pp. 378-382
- Dreizin, E. L., "Experimental Study of Stages in Aluminum Particle Combustion in Air," *Combustion and Flame*, Vol. 105, 1996, pp. 541-556
- Dreizin, E. L., "On Mechanism of Asymmetric Aluminum Particle Combustion," *Combustion and Flame*, Vol. 117, 1999, pp. 841-850
- Dreizin, E. L., "Experimental Study of Aluminum Particle Flame Evolution in Normal and Micro-Gravity," *Combustion and Flame*, Vol. 116, 1999, pp. 323-333
- Dreizin, E.L., "Phase Changes in Metal Combustion," *Progress in Energy and Combustion Science*, Vol. 26, 2000
- Dreizin, E. L., "Effect of Phase Changes on Metal-Particle Combustion Process," *Combustion, Explosion, and Shock Waves*, Vol. 39, No. 6, 2003, pp. 681-693
- Duan, W., Wentzcovitch, R. M., and Thomson, T., "First principles study of high-pressure alumina polymorphs," *Physical Review B*, Vol. 57, No. 17, 1998
- Eck, B., Kurtulus, Y., Offermans, and W., Dronskowski, R., "Atomistic Simulations of Solid-State Materials Based on Crystal-Chemical Potential Concepts: Application for Compounds, Metals, Alloys, and Chemical Reactions," *Journal of Alloys and Compounds*, Vol. 338, 2002, pp. 142

- Eckert, J., Holzer, J. C., Ahn, C. C., Fu, Z., and Johnson, W. L., "Melting Behavior of Nanocrystalline Aluminum Powders," *Nano Structured Materials*, Vol. 2, 1993, pp. 407
- Eisenreich, N., Fietzek, H., Lorenzo, M., Kolarik, V., Koleczko, A., and Weiser, V., "On the mechanism of low temperature oxidation for aluminum particles down to the nano-scale," *Propellants, Explosives, Pyrotechnics*, Vol. 29, 2004
- Ercolessi, F., and Tosatti, E., "Au (100) Surface Reconstruction," *Physical Review Letters*, Vol. 57, No. 6, 1986, pp. 719-722
- Ercolessi, F., Parrinello, M., and Tosatti, E., "Simulation of gold in the glue model," *Philosophical Magazine A*, Vol. 58, No. 1, 1988, pp. 213-226
- Ercolessi, F., and Adams, J. B., "Interatomic Potentials from First principles Calculations: the Force-Matching Method," *Europhysics Letters*, Vol. 26, No. 8, 1994, pp. 583-588
- Ermakov, V. A., Razdobreev, A. A., Skorik, A. I., Pozdeev, V. V., and Smolyakov, S. S., "Temperature of Aluminum Particles at the Moments of Ignition and Combustion," *Fiz. Goreniya Vzryva*, Vol. 18, 1982, pp. 141 (in Russian)
- Ermakova, E., Solca, J., Huber, H., and Welker, M., "Argon in condensed phase: Quantitative calculations of structural, thermodynamic, and transport properties from pure theory," *Journal of chemical Physics*, Vol. 102, No. 12, 1995, pp. 4942-4951
- Evans, D. J., and Hoover, W. G., "Flows far from equilibrium via molecular Dynamics," *Annual Rev. Fluid Mech.*, Vol. 18, 1986, pp. 243-264
- Faeth, G. M., "Current Status of Droplet and Liquid Combustion," *Progress in Energy and Combustion Science*, Vol. 3, 1977, pp. 191-224
- Fedorov, A. V., and Kharlamova Y. V., "Ignition of an Aluminum Particle," *Combustion, Explosion, and Shock Waves*, Vol. 39, No. 5, 2003, pp. 544-547
- Fedoseev, V. A., "Combustion of Magnesium and Aluminum Particles in Different Media," *Fizika Aerodispersnykh Sistem*, Vol. 3, 1970, pp. 61 (in Russian)
- Filippov, A. V., and Rosner, D. E., "Energy transfer between an aerosol particle and gas at high temperature ratios in the Knudsen transition regime," *International Journal of Heat and Mass Transfer*, Vol. 43, 2000, pp. 127-138
- Finnis, M. W., and Sinclair, J. E., "A simple empirical N-body potential for transition metals," *Philosophical Magazine A*, Vol. 50, No. 1, 1984, pp. 45-55



- Foelsche, R. O., Burton, R. L., and Krier, H., "Ignition and Combustion of Aluminum Particles in H<sub>2</sub>/O<sub>2</sub>/N<sub>2</sub> Combustion Products," *Journal of Propulsion and Power*, Vol. 14, No. 6, 1998, pp. 1001-1008
- Foiles, S. M., "Calculation of the surface segregation of Ni-Cu alloys with the use of the embedded-atom method," *Physical Review B*, 1985, Vol. 32, No. 12, pp. 7685-7693
- Foiles, S. M., Baskes, M. I., and Daw, M. S., "Embedded-atom-method functions for the fcc metals Cu, Ag, Au, Ni, Pd, Pt, and their alloys," *Physical Review B*, Vol. 33, No. 12, 1986, pp. 7983-7991
- Foiles, S. M., and Daw, M. S., "Application of the embedded atom method to Ni<sub>3</sub>Al," *Journal of Materials Research*, Vol. 2, 1987, pp. 5-15
- Foiles, S. M., and Daw, M. S., "Calculation of the thermal expansion of metals using the embedded-atom method," *Physical Review B*, Vol. 38, No. 17, 1988, pp. 12643-12644
- Foiles, S. M., and Adams, J. B., "Thermodynamic properties of fcc transition metals as calculated with the embedded atom method," *Physical Review B*, Vol. 40, No. 9, 1989, pp. 5909-5915
- Fontijn, A., and Felder, W., "HTFFR kinetics studies of Al+CO<sub>2</sub>=AlO+CO from 300 to 1900K, a non-Arrhenius reaction," *The Journal of Chemical Physics*, Vol. 67, No. 4, 1977, pp. 1561-1569
- Fowler, R.F., "The identification of a droplet in equilibrium with its vapor", CCP5 Quaterly, 13, pp.58-62, 1984
- Frenkel, D., and Smit, B., *Understanding Molecular Simulation: From Algorithms to Applications*, Second Edition, Academic Press, New York, 2002
- Friedlander, S. K., *Smoke, Dust and Haze*, Second Edition, Oxford University Press, New York, 2000
- Friedman, R., and Maeck, A., "Ignition and Combustion of Aluminum Particles in Hot Ambient Gases," *Combustion and Flame*, Vol. 6, 1962, pp. 9-19
- Friedman, R., and Maeck A., "Combustion Studies of Single Aluminum Particles," *Ninth Symposium (International) on Combustion*, 1963, pp. 703-709
- Gall, M. L., Huntz, A. M., Lesage, B., and Monty, C., "Self-diffusion in alpha-Al<sub>2</sub>O<sub>3</sub> and growth of alumina scales formed by oxidation: Effect of Y<sub>2</sub>O<sub>3</sub> doping," *Journal of Materials Science*, Vol. 30, 1995, pp. 201-211

- Gezelter, J. D., Rabani, E., and Berne, B. J., "Can Imaginary Instantaneous Normal Mode Frequencies Predict Barriers to Self-Diffusion?," *Journal of Chemical Physics*, Vol. 107, No. 12, 1997, pp. 4618-4627
- Glassman, I., *Combustion*, First Edition, Academic, New York, 1977
- Glassman, I., Papas, P., and Brezinsky, K., "A new definition and Theory of Pyrophoricity," *Combustion Science and Technology*, Vol. 83, 1992, pp. 161-165
- Glassman, *Combustion*, Third edition, Academic Press, 1996
- Girifalco, L. A., and Weizer, V. G., "Application of the Morse Potential Function to Cubic Metals," *Physical Review*, Vol. 114, No. 3, 1959, pp. 687-690
- Goldsmith, A., Hirschhorn, H. J., and Waterman, T. E., *Thermo-physical Properties of Solids*, WADC Technical Report 58-76, Vol. III, US Air Force Wright-Patterson AF Base, OH, 1960
- Gremyachkin, V. M., Istratov, A. G., and Leipunskii, O. I., "Effect of immersion in a flow on Metal Droplet Combustion," *Combustion Explosion and Shock Waves*, Vol. 15, No. 1, 1979, pp. 26-29
- Grigor'ev, Y. M., Galchenko, Y. A., and Merzhanov, A. G., "Investigation of the rate of the high temperature reaction between aluminum and oxygen using the ignition method," *Combustion, Explosion and Shock Waves*, Vol. 9, No. 2, 1973, pp. 162-167
- Grigor'ev, Y. M., and Vakina, Z. K., "Critical Ignition Conditions for Metals with a Logarithmic Oxidation Law," *Combustion, Explosion and Shock Waves*, Vol. 15, No. 1, 1979, pp. 51-53
- Gutierrez, G., Taga, A., and Johansson, B., "Theoretical structure determination of  $\text{Al}_2\text{O}_3$ ," *Physical Review B*, Vol. 65, 2001, pp. 012101
- Gutierrez, G., and Johansson, B., "Molecular dynamics study of structural properties of amorphous  $\text{Al}_2\text{O}_3$ ," *Physical Review B*, Vol. 65, 2002, pp. 104202
- Gurevich, M. A., Ozerov, E. S., and Yurinov, A. A., "Effect of an oxide film on the inflammation characteristics of aluminum," *Combustion, Explosion and Shock Waves*, Vol. 14, No. 4, 1978, pp. 448-451
- Halicioglu, T., and Pound, G. M., "Calculation of Potential Energy parameters from Crystalline State Properties," *Physica Status solidi (a)*, Vol. 30, 1975, pp. 619-623
- Hartman, K. O., "Ignition and Combustion of Aluminum Particles in Propellant Flame Gases," *Eighth JANAF Combustion Meeting*, Vol. 1, 1971, pp. 1-24

- Hasnaoui, A., Politano, O., Salazar, J. M., Aral, G., Kalia, R. K., Nakano, A., Vashishta, P., "Molecular dynamics simulations of the nano-scale room-temperature oxidation of aluminum single crystals," *Surface Science*, Vol. 579, 2005, pp. 47-57
- Hoang, V. V., Oh, S. K., "Annealing effects on structure in amorphous  $\text{Al}_2\text{O}_3$  models," *Physica B*, Vol. 364, 2005, 2125-232
- Hoagland, R. G., Daw, M. S., Foiles, S. M., and Baskes, M. I., "An atomic model of crack tip deformation in aluminum using an embedded atom potential," *Journal of Materials Research*, Vol. 5, No. 2, 1990, pp. 313-324
- Hoover, W. G., "Canonical dynamics: Equilibrium phase-space distributions," *Physical Review A*, Vol. 31, 1985, pp. 1695
- Huang, Y., Risha, G. A., Vigor, Y., and Yetter, R. A., "Analysis of Nano-Aluminum Particle Dust Cloud Combustion in Different Oxidizer Environments," *43rd Aerospace Sciences Meeting and Exhibit*, Reno, Nevada, 2005
- Huang, Y., Risha, G. A., Vigor, Y., and Yetter, R. A., "Flame Propagation in Bimodal Nano/Micro-Sized Aluminum Particles/Air Mixtures," *44th Aerospace Sciences Meeting and Exhibit*, Reno, Nevada, 2006
- Huang, Y., Risha, G. A., Yang, V., and Yetter R. A., "Combustion of bimodal nano/micron-sized aluminum particle dust in air," *Proceedings of the Combustion Institute*, Vol. 31, 2007, pp. 2001-2009
- Hultgren, R., Desai, P. D., Hawkins, D. T., Gleiser, M., and Kelley, K. K., Selected Values of Thermodynamic Properties of the Elements, *American Society for Metals*, 8th Edition, Metal Parks, Ohio, 1973
- Hyuk, I., Jeong, U., and Xia, Y., "Polymer hollow particles with controllable holes in their surfaces," *Nature Materials*, Vol. 4, 2005, pp. 671
- Ilyin, A. P., Gromov, A. A., Vereshchagin, V. I., Popenko, E. M., Surgin, V. A., and Lehn H., "Combustion of Agglomerated Ultrafine Aluminum Powders in Air," *Combustion Explosion and Shock Waves*, Vol. 37, 2001, pp. 664
- Ivanov, G. V., and Tepper, F., "Activated Aluminum as a Stored Energy Source for Propellants," *Fourth International Symposium on Special Topics in Chemical Propulsion*, Challenges in Propellants and Combustion 100 Years after Nobel, Stockholm, Sweden, 27-28 May, 1996, pp. 636-644
- JANAF Thermodynamic Tables*, 3rd Edition, American Chemical Society, 1981

- Jiang, Q., Yang, C. C., and Li, J. C., "Melting enthalpy depression of nanocrystals," *Materials Letters*, Vol. 56, 2002, pp. 1019-1021
- Jeurgens, L. P. H., Sloof, W. G., Tichelaar, F. D., and Mittemeijer, E. J., "Determination of thickness and composition of aluminum-oxide overlayers on aluminum substrates," *Applied Surface Science*, Vol. 144-145, 1999, pp. 11-15
- Jeurgens, L. P. H., Sloof, W. G., Tichelaar, F. D., and Mittemeijer, E. J., "Thermodynamic stability of amorphous oxide films on metals: Application to aluminum oxide films on aluminum substrates," *Physical Review B*, Vol. 62, No. 7, 2000, pp. 4707-4719
- Jeurgens, L. P. H., Sloof, W. G., Tichelaar, F. D., Borsboom, C. G., and Mittemeijer, E. J., "Determination of total primary zero loss intensities in measured electron emission spectra of bare and oxidized metals Application to aluminum oxide films on aluminum substrates," *Applied Surface Science*, Vol. 161, 2000, pp. 139-148
- Jeurgens, L. P. H., Sloof, W. G., Tichelaar, F. D., and Mittemeijer, E. J., "Growth kinetics and mechanisms of aluminum-oxide films formed by thermal oxidation of aluminum," *Journal of Applied Physics*, Vol. 92, No. 3, 2002, pp.1649-1656
- Jeurgens, L. P. H., Sloof, W.G., Tichelaar, F. D., and Mittemeijer, E. J., "Structure and morphology of aluminum-oxide films formed by thermal oxidation of aluminum," *Thin Solid Films*, Vol. 418, No. 2, 2002, pp. 89-101
- Jeurgens, L.P.H., Sloof, W.G., Tichelaar, F.D., and Mittemeijer, E.J., "Composition and chemical state of the ions of aluminum-oxide films formed by thermal oxidation of aluminum," *Surface Science*, Vol. 506, 2002, pp. 313-332
- Johnson, C., Parr, T., Hanson-Parr, D., Hollins, R., Fallis, S., and Higa, K., "Combustion and Oxidation of Metal Nanoparticles and Composite Particles," *Proceedings of 37<sup>th</sup> JANNAF Meeting*, 13-17 Nov, 2000, pp. 539
- Johnson, R. A., "Analytic nearest neighbor model for fcc metals," *Physical Review B*, Vol. 37, No. 8, 1988, pp. 3924-3931
- Johnson, R. A., "Alloy models with the embedded-atom method," *Physical Review B*, Vol. 39, No. 17, 1989, pp. 12554-12559
- Jones, H. D., "Theory of the Thermodynamic Properties of Liquid Metals," *Physical Review A*, Vol. 8, No. 6, 1973, pp. 3215-3226
- Joswig, J. O., and Springborg, M., "Genetic algorithms search for global minima of aluminum clusters using a Sutton-Chen potential," *Physical Review*, Vol. 68, No. 8, 2003, pp. 085408

- Keffer, D. J., and Mintmire, J. W., "Efficient Parallel Algorithms for Molecular Dynamics Simulations Using variable Charge Transfer Electrostatic Potentials," *International Journal of Quantum Chemistry*, Vol. 80, 2000, pp. 733-742
- King, M., "Modeling of Single Particle Aluminum Combustion in CO<sub>2</sub>-N<sub>2</sub> Atmospheres," *17th Symposium (International) on Combustion*, The Combustion Institute, Pittsburg, 1977, pp. 1317-1328
- Kondis, Thomas J., *Patent 3986674*, "Monitoring activation of particulate aluminum," October 1976, <http://www.freepatentsonline.com/3986674.html>
- Kondis, Thomas J., *Patent 3963482*, "Large size aluminum particle containing aluminum oxide therein," June 1976, <http://www.freepatentsonline.com/3963482.html>
- Konning, M., Antonelli, A., and Yip, S., "Single simulation determination of phase boundaries: A dynamic Clausius-Clapeyron integration method," *Journal of Chemical Physics*, Vol. 115, No. 24, 2001, pp. 11025-11035
- Kudryavtsev, V., Sukhov, A., Voronetskii, A., and Shpara, A., "High Pressure Combustion of Metals (Three-Zone Model)," *Combustion Explosion and Shock Waves*, Vol. 15, No. 6, 1979, pp. 731-737
- Kwon Y. S., Gromov, A. A., Ilyin A. P., Popenko E. M., and Rim G. H., "The mechanism of combustion of superfine aluminum powders," *Combustion and Flame*, Vol. 133, 2003, pp. 385
- Law, C. K., "A simplified Theoretical Model for Vapor Phase Combustion of Metal Particles," *Combustion Science and Technology*, Vol. 7, 1973, pp. 197-212
- Law, C. K., and Williams, F., "On a Class of Models for Droplet Combustion," *12th Aerospace Sciences Meeting*, Washington, D.C., *AIAA Paper 74-147*, 1974
- Liang, L. H., Li, J. C., and Jiang, Q., "Size-dependant melting depression and lattice contraction of Bi nanocrystals," *Physica B*, 2003, pp. 49-53
- Little, J. K., "Simulation of droplet evaporation in supercritical environments using parallel molecular dynamics," *Ph.D Dissertation*, Department of Mechanical Engineering, The Pennsylvania State University, PA, 1996
- Lokenbakh, A., Zaporina, N., Knipele, A., Strod, V., and Lepin, L., "Effects of heating conditions on the agglomeration of aluminum powder in air," *Combustion, Explosion, and Shock Waves*, Vol. 21, pp. 73-82, 1985
- Long, L. N. L., Micci, M. M., Wong, B. C., "Molecular dynamics simulations of droplet evaporation," *Computer Physics Communications*, Vol. 96, 1996, pp. 167-172

- Lutsko, J. F., Wolf, D., Phillpot, S. R., and Yip, S., "Molecular Dynamics study of lattice-defect nucleated melting in metals using an embedded-atom-method potential," *Physical Review B*, Vol. 40, No. 5, 1989, pp. 2841-2855
- Maeck, A., "Fundamentals of Combustion of Single Aluminum and Beryllium Particles," *Eleventh Symposium (International) on Combustion*, 1967, pp. 203-217
- Mallard, W. G., Westley, F., and Hampson, R. F., *NIST Chemical Kinetics Database Version 6.0*, NIST Standard Reference Data, Gaithersburg, MD, 1994
- Marian, J., Knap, J., and Ortiz, M., "Nanovoid Cavitation by Dislocation Emission in Aluminum," *Physical Review Letters*, Vol. 93, 2004
- Marian, J., Knap, J., and Ortiz, M., "Nanovoid deformation in aluminum under simple shear," *Acta Materiala*, Vol. 53, 2005, pp. 2893
- Marion M., and Gokalp I., "Studies on the Ignition and Burning of Aluminum Particles," *AIAA 95-2861*, 1995
- Marion M., and Gokalp I., "Studies on the Ignition and Burning of Aluminum Particles," *Combustion Science and Technology*, Vol. 116, 1996, pp. 369-390
- Matyushov, D. V., and Schmid, R., "Calculation of Lennard-Jones energies of molecular fluids," *Journal of Chemical Physics*, Vol. 104, No. 21, 1996, pp. 8627-8638
- McClean, R., Nelson, H., and Cambell, M., "Kinetics of Reaction  $\text{Al}+\text{H}_2\text{O}$  over an extended temperature range," *Journal of Physical Chemistry*, Vol. 97, 1993, pp. 9673-9676
- Meda, L., Marra, G., Galfetti, L., Inchingalo, S., Severini, F., and De Luca, L., "Nano-composites for rocket solid propellants," *Composites Science and Technology*, v 65, n 5 SPEC. ISS., April, 2005, pp. 769-773
- Medvedev, A. E., Fedorov, A. V., and Fomin, V. M., "Mathematical modeling of metal particle ignition in the high temperature flow behind a shock," *Combustion, Explosion and Shock Waves*, Vol. 18, No. 3, 1982, pp. 261-264
- Melcher, J. C., Burton R. L., and Krier, H., "Combustion of Aluminum Particles in Solid Rocket Motor Flows," *36th JANAF Combustion Meeting*, Vol.1,CPIA#691,1999, pp. 249-258
- Melcher, J., Burton, and R., Krier, H., "Formation of Condensed Combustion Products at the Burning Surface of Solid Rocket Propellant," *Solid Propellant Chemistry, Combustion and Motor Interior Ballistics*, Chapter 2.20, edited by V. Yang, T.B. Brill and W.Z. Ren, Progress in Astronautics and Aeronautics, AIAA, Vol. 185, 2000, pp. 723-748

- Melchionna, S., Ciccotti, G., Holian, B.L., "Hoover NPT Dynamics for systems varying in shape and size", *Molecular Physics*, Vol. 78, No. 3, pp. 533-544
- Mench, M., Yeh, C. L., and Kuo, K., "Propellant Burning Rate Enhancement and Thermal Behavior of Ultra-Fine Aluminum Powders (Alex)," *29th International Annual Conference of ICT*, Karlsruhe, Germany, June 30-July 3, 1998, pp. 30/1
- Merzhanov, A. G., Grigorjev, Y. M., and Galchenko, Y. A., "Aluminum Ignition," *Combustion and Flame*, Vol. 29, 1977, pp. 1-14
- Mei J., and Davenport, J. W., "Free-energy calculations and the melting point of Al," *Physical Review B*, Vol. 46, No. 1, 1992, pp. 21-25
- Micheli, P. L., and Schmidt, W. G., "Behavior of Aluminum in Solid Rocket Motors," Aerojet Solid Propulsion Co., *AFRPL-TR-76-58*, Sacramento, CA, 1977
- Miguel, M. A. S., and Sanz, J. F., "Molecular dynamics simulations of liquid aluminum oxide," *Physical Review B*, Vol. 58, No. 5, 1998, pp. 2369-2371
- Morse, P. M., "Diatomic molecules according to the wave mechanics II. Vibrational levels," *Physical Review*, Vol. 34, 1929, pp. 57-64
- Nose, S., "A unified formulation of the constant temperature molecular dynamics methods," *Journal of Chemical Physics*, Vol. 81, 1984, pp. 511
- Nose, S., "A molecular dynamics method for simulations in the canonical ensemble," *Molecular Physics*, Vol. 52, 1985, pp. 255
- Nose S., and Yonezawa, F., "Isothermal-isobaric computer simulations of melting and crystallization of a Lennard-Jones system," *Journal of Chemical Physics*, Vol. 84, No. 3, 1986, pp. 1803-1814
- Olsen, S. E., and Beckstead M. W., "Burn time measurements of Single Aluminum Particles in Steam and Carbon-di-oxide mixtures," *Journal of Propulsion and Power*, Vol. 12, No. 4, 1996, pp. 662-671
- Orlandi, O., and Fabignon, Y., "Numerical simulation of the combustion of a single droplet in propellant gas environment," *2nd European Conference on Launcher Technology, Space Solid Propulsion*, Rome, November 21-24, 2000
- Ortega, A., "The kinetics of solid-state reactions toward consensus - Part I: Uncertainties, failures, and successes of conventional methods," *International Journal of Chemical Kinetics*, Vol. 33, 2001, pp. 343-353
- Panda, S., and Pratsinis, S. E., "Modeling the synthesis of aluminum particles by evaporation-condensation in an aerosol flow reactor," *Nanostructured Materials*, Vol. 5, No. 7, 1995, pp. 755-767

- Park, K., Lee, D., Rai, A., Mukherjee, D., and Zachariah, M. R., "Size-resolved Kinetic Measurements of Aluminum Nanoparticle Oxidation with Single Particle Mass Spectrometry," *Journal of Physical Chemistry*, Vol. 109, 2005, pp.7290-7299
- Ph. Buffat, and Borel, J. P., "Size effect of the melting temperature of gold particles," *Physical Review A*, Vol. 13, 1976, pp. 2287
- Phillpot, S. R., Lutsko, J. F., Wolf, D., Yip, S., "Molecular dynamics study of lattice-defect-nucleated melting in silicon," *Physical Review B*, Vol. 40, 1989, pp. 2831
- Pint, B. A., Martin, J. R., and Hobbs, L. W., "O/SIMS Characterization of the Growth Mechanism of Doped and Undoped  $\alpha$ -Al<sub>2</sub>O<sub>3</sub>," *Oxidation of Metals*, Vol. 39, 1993, pp. 167
- Pivkina, A., Ulyanova, P., Frolov, Y., Zavyalov, S., and Schoonman, J., "Nanomaterials for Heterogeneous Combustion," *Propellants, Explosives, Pyrotechnics*, Vol. 29, No. 1, 2004, pp. 39-48
- Plimpton, S., "Fast parallel Algorithms for short range Molecular Dynamics," *Journal of Computational Physics*, Vol. 117, No. 1, 1995, pp. 1-19
- Powles, J. G., Fowler, R. F., Evans, W. A. B., "The surface thickness of simulated microscopic liquid drops", *Physics Letters*, 98A, 1983, pp. 421-425
- Powles, J. G., Fowler, R. F., Evans, W. A. B., "A new method for computing surface tension using a drop of liquid," *Chemical Physics Letters*, Vol. 96, No.3, 1983, pp.289-292
- Powles, J.G., Fowler, R.F., Evans, W. A. B., "The dielectric constant of a polar liquid by the simulation of microscopic drops," *Chemical Physics Letters*, Vol. 7, No. 3, 1984, pp.280-283
- Powles, J.G., Rickayzen, G., Williams, M.L., "A curious result concerning the Clasiuss virial," *Journal of Chemical Physics*, Vol. 83, 1985, pp. 293-296 Text
- Prentice, J. L., "Combustion of Pulse Heated Single Particles of Aluminum and Beryllium," *NWC TP 5162*, Naval Weapons Center, China Lake, CA, 1971
- Prentice, J. L., "Combustion of Laser-Ignited Aluminum Droplets in Wet and Dry Oxidizers," *AIAA 12th Aerospace Science Sciences Meeting*, AIAA Paper No. 74-146, 1974
- Price, E. W., Christensen, H. C., Knipe, R. H., Drew, C. M., Prentice, J. L., and Gordon, A. S., "Aluminum Particle Combustion Progress Report," *NOTS-TP-3916*, Naval Ordnance Test Station, China Lake, Ca, 1966



- Price, E. W., and Sigman, R. K., "Combustion of Aluminized Solid Propellants," *Solid Propellant Chemistry, Combustion and Motor Interior Ballistics*, Chapter 2.18, edited by V. Yang, T.B. Brill and W.Z. Ren, *Progress in Astronautics and Aeronautics*, AIAA, Vol. 185, 2000, pp. 663-687
- Puri, P., Yang, V., "Effect of Particle Size on Melting of Aluminum at Nano Scales," *Journal of Physical Chemistry C*, Vol. 111, 2007, pp. 11776
- Puri, P., and Yang, V., "Molecular Dynamics Simulations of Effects of Pressure and Void Size on Melting of Aluminum," *43<sup>rd</sup> AIAA/ASME/SAE/ASEE Joint Propulsion Conference & Exhibit*, Cincinnati, July 2007
- Puri, P., and Yang, V., "A multi-scale theory of ignition and combustion of particulate aluminum," *in preparation*, 2008
- Puri, P., and Yang, V., "Ignition and Combustion of Aluminum Particles at Micron and Nano Scales," *in preparation for Progress in Energy and Combustion Science*, 2008
- Puri, P., and Yang, V., "Pyrophoricity of Aluminum at Nano Scales," *to be submitted to Combustion and Flame*, 2008
- Puri, P., and Yang, V., "Thermo-Mechanical Behavior of Nano Aluminum Particles with Oxide Layers," AIAA Paper 2008-938, *to be submitted to Physical Review*, 2008
- Ragab, A., and Bayouni, S. E., *Engineering Solid Mechanics Fundamentals and Applications*, CRC Press, New York, 1999
- Rahman, A., "Correlations in the motion of Atoms in Liquid Argon," *Physical Review*, Vol. 136, No. 2A, 1964, pp. 405
- Rai, A., Lee, D., Park, K., and Zachariah, M. R., "Importance of Phase Change of Aluminum in Oxidation of Aluminum Particles," *Journal of Physical Chemistry*, Vol. 108, No. 9, 2004, pp.14793-14795
- Rai, A., Lee, D., Park K., and Zachariah, M.R., "Size Resolved Measurements and Theory of Aluminum Nanoparticle Oxidation Kinetics," *Combustion Institute Meeting*, 2005
- Rappe, A. K., and Goddard, W. A., "Charge Equilibration for Molecular Dynamics Simulations," *Journal of Physical Chemistry*, Vol. 95, No. 8, 1991, 3358-3363
- Rhee, S. K., "Wetting of Ceramics by Liquid Aluminum," *Journal of American Ceramic Society*, Vol. 53, No. 7, 1970, pp. 386-389

- Risha G. A., "Enhancement of Hybrid Rocket Combustion Performance using Nano-Sized Energetic materials" *Ph.D Dissertation*, Department of Mechanical Engineering, The Pennsylvania State University, PA, 2003
- Risha, G. A., Huang, Y., Yetter, R. A., and Yang, V., "Experimental Investigation of Aluminum Particle Dust Cloud Combustion," *43rd Aerospace Sciences Meeting and Exhibit*, Reno, Nevada, 2005, Reno, Nevada, AIAA 2005-739
- Risha, G. A., Huang, Y., Yetter, R. A., and Yang, V., "Combustion of Aluminum Particles with Steam and Liquid Water," *44th AIAA Aerospace Sciences Meeting and Exhibit*, Reno, Nevada, 2006, AIAA 2006-1154
- Risha, G. A., Son, S. F., Yetter, R. A., and Yang, V., Tappan, B.C., "Combustion of nano-aluminum and liquid water," *Proceedings of Combustion Institute*, 31, 2007, pp. 2029-2036
- Roberts, T. A., Burton R. L., and Krier H., "Ignition and Combustion of Aluminum/Magnesium Alloy particles in O<sub>2</sub> at High pressures," *Combustion and Flame*, 92, 1993, pp. 125-143
- Rode, H., Hlavacek, V., Viljoen, H. J., and Gatica, J. E., "Combustion of Metallic Powders: A Phenomenological model for the Initiation of Combustion," *Combustion Science and Technology*, Vol. 88, pp. 153-175
- Rodriguez, J. A., "Physical and Chemical Properties of Bimetallic Surfaces," *Surface Science Reports*, 24, 1996, pp. 223
- Roohatan, C. C. J., "A study of Two-Center Integrals Useful in Calculations on Molecular Structure I," *Journal of Chemical Physics*, Vol. 19, No. 12, 1951, pp. 1445-1458
- Rozenband, V. I., and Vaganova N. I., "A Strength Model of Heterogeneous Ignition of Metal Particles," *Combustion and Flame*, Vol. 88, 1992, pp. 113
- Sebetci, A., and Guvenc, Z. B., "Global minima of Al<sub>N</sub>, Au<sub>N</sub> and Pt<sub>N</sub>, N<80 clusters described by the Voter-Chen version of embedded-atom potentials," *Modeling and Simulation in Materials Science and Engineering*, Vol. 13, 2005, pp. 683-698
- Sedlacek, L., Matolinova, I., Veltruska, K., and Matolin, V., "Study of Pd-Al Interactions on Pd/AlO<sub>x</sub>/Al Systems during CO Adsorption and Desorption Cycles: XPS and LEIS," *Surface Science*, Vol. 556, 2004, pp. 1035
- Shackelford, J.F., and Alexander, W., *CRC Materials Science and Engineering Handbook*, CRC Press, Third Edition, 2000

- Shimomura, Y., and Moritaki, Y., "On the Important Effect of Water Vapor in the Atmosphere on Void Formation in Quenched Pure Aluminum," *Japanese Journal of Applied Physics*, Vol. 20, 1981, pp.1781
- Simpson, T. W., Wen, Q., Yu, N., and Clarke, D. R., "Kinetics of the Amorphous  $\rightarrow \gamma \rightarrow \alpha$  transformations in Aluminum Oxide: Effect of Crystallographic orientation," *Journal of American Ceramic Society*, Vol. 81, No. 1, 1998, pp. 61-66
- Solca, J., Anthony, J. D., Steinebrunner, G., Kircher, B., and Huber, H., "Melting curve for argon calculated from pure theory," *Chemical Physics*, Vol. 224, No. 2, 1997, pp. 253-261
- Solca, J., Dyson, A.J., Steinebrunner, G., Kirchner, B., and Huber, H., "Melting curves for neon calculated from pure theory," *Journal of Chemical Physics*, Vol. 108, No. 10, 1998, pp. 4107-4111
- Song, X., and Morris, J. R., "Accurate method to calculate liquid and solid free energies for embedded atom potentials," *Physical Review B*, Vol. 67, 2003, pp. 092203
- Streitz, F. H., and Mintmire, J. W., "Electrostatic Potentials for metal-oxide surfaces and interfaces," *Physical Review B*, Vol. 50, No. 16, 1994, pp. 11996-12003
- Sturgeon, J. B., and Laird, B. B., "Adjusting the melting point of a model system via Gibbs-Duhem integration: Application to a model of aluminum," *Physical Review B*, Vol. 62, No. 22, 2000, pp. 14720-14727
- Sutton, A. P., and Chen, J., "Long Range Finnis-Sinclair Potentials," *Philosophical Magazine Letters*, 61, 1990, pp. 139
- Suvaci, E., Simkovich, G., and Messing, G. L., "The Reaction-Bonded Aluminum Oxide Process: I, The Effect of Attrition Milling on the Solid-State Oxidation of Aluminum Powder," *Journal of American Ceramic Society*, Vol. 83, No. 2, 2000, pp. 299-305
- Tatum, D., and Kuo, K., "Physicochemical Considerations in Modeling Ignition and Combustion of Highly Non-Spherical Nano-Sized Aluminum Particles," *39th AIAA/ASME/SAE Joint Propulsion Conference and Exhibit*, Huntsville, Alabama, 20-23 July, 2003
- Thompson, S. M., Gubbins, K. E., Walton, J. P. R. B., Chantry, R. A. R., and Rowlinson, J. S., "A molecular dynamics study of liquid drops," *Journal of Chemical Physics*, Vol. 81, No. 1, 1984, pp. 530-542

- Tomar, V., and Zhou, M., "Classical molecular dynamics potential for the mechanical strength of nanocrystalline composite fcc Al + Fe<sub>2</sub>O<sub>3</sub>," *Physical Review B*, Vol. 73, 2006, pp. 174116
- Trunov, M. A., Schoenitz, M., Zhu, X., and Dreizin, E. L., "Effect of polymorphic phase transformations in Al<sub>2</sub>O<sub>3</sub> film on oxidation kinetics of aluminum powders," *Combustion and Flame*, 2005, pp 310-318
- Trunov, M. A., Schoenitz, M., and Dreizin, E. L., "Ignition of Aluminum Powders Under Different Experimental Conditions," *Propellants Explosives and Pyrotechnics*, Vol. 30, 2005, pp. 36-43
- Trunov, M.A., Schoenitz, M., Dreizin, E. L., "Effect of polymorphic phase transformations in alumina layer on ignition of aluminum particles," *Combustion Theory and Modeling*, Vol. 10, 2006, pp. 603
- Trunov, M. A., Umbrajkar, S. M., Schoenitz, M., Mang, J. T., and Dreizin, E. L., "Oxidation and Melting of Aluminum Nanopowders," *Journal of Physical Chemistry B*, 110 No. 26, 2006, pp. 13094-13099
- Turns, S. R., Wong S. C., and Ryba, E., "Combustion of Aluminum based Slurry Agglomerates," *Combustion Science and Technology*, Vol. 54, 1987, pp. 299-318
- Turns, S.R., *An Introduction to Combustion*, Second Edition, McGraw Hill, 1996,
- Vashishta, P., Kalia, R. K., Nakano, A., "Multimillion atom molecular dynamics simulations of nanostructures on parallel computers," *Journal of Nanoparticle Research*, Vol. 5, 2003, pp. 119-135
- Vorter, A., and Chen, S. F., "Accurate Interatomic Potentials for Ni, Al and Ni<sub>3</sub>Al," *Materials Research Society symposia proceedings*, Vol. 82, No. 175, 1987, pp. 175-180
- Wang, S., Yang, Y., Yu, H., and Dlott, D. D., "Dynamical Effects of the Oxide Layer in Aluminum Nano energetic Materials," *Propellants, Explosives, Pyrotechnics*, Vol. 30, No. 2, 2005
- <http://www.neem.psu.edu/>, 2008
- Widener, J. F., Liang, Y., and Beckstead, M. W., "Aluminum Combustion Modeling in Solid Propellant Environments," AIAA 99-2629, *35th AIAA/ASME/SAE/ASEE Joint Propulsion Conference and Exhibit*, 1999
- Wilson, R. P., and Williams F. A., "Experimental Study of Combustion of Single Aluminum Particles in O<sub>2</sub>/Air," *Thirteenth Symposium (International) on Combustion*, The Combustion Institute, Pittsburg, PA, 1971, pp. 833-845

- Wong, S. C., and Turns S. R., "Ignition of Aluminum Slurry Droplets," *Combustion Science and Technology*, Vol. 52, 1987, pp. 221-242
- Woon, D. E., "Accurate modeling of interatomic forces: a systematic Moller-Plesset study of the argon dimer using correlation consistent basis sets," *Chemical Physics Letters*, Vol. 204, No 1, 1993, pp. 29-35
- Wronski C. R. M., "The size dependence of the melting point of small particles of tin," *British Journal of Applied Physics*, Vol. 18, 1967, pp. 1731
- Yetter, R. A., and Dryer, F. L., "Metal Particle Combustion and Classification," *Microgravity Combustion: Fire in Free Fall*, Academic Press, pp. 419-478, 2001
- Yuasa, S., Zhu, Y., and Sogo, S., "Ignition and Combustion of Aluminum in Oxygen/Nitrogen Mixture Streams, Effects of Oxygen Concentration on Combustion of Aluminum in Oxygen/Nitrogen Mixture Streams," *Combustion and Flame*, Vol. 108, 1997, pp.387
- Zenin, A. A., Kusnezov, G., and Kolesnikov, V., "Physics of Aluminum Particle Combustion at micro gravity," *AIAA-90-0696*, 1999
- Zenin, A. A., Kusnezov, G., and Kolesnikov, V., "Physics of Aluminum Particle Combustion at convection," *AIAA-2000-0849*, 2000
- Zha, C. S., Boehler, R., Young, D. A., Ross, M., "The argon melting curve to very high pressures," *Journal of Chemical Physics*, Vol. 85, No. 2, 1986, pp. 1034-1036
- Zhang, Z., Lu, X. X., and Jiang, Q., "Finite size effect on melting enthalpy and melting entropy of nanocrystals," *Physica B*, 1999, pp. 249-254
- Zhao, M., Jiang, Q., "Melting and surface melting of low-dimensional in crystals," *Solid State Communications*, 2004, pp. 37-39
- Zhu, Y., and Yuasa, S., "Effects of Oxygen Concentration on Combustion of Aluminum in Oxygen/Nitrogen Mixture Streams," *Combustion and Flame*, Vol. 115, No. 3, 1998, pp. 327
- Zhou, Y., Karplus, M., Ball, K. D., and Berry, R. S., "The distance fluctuation criterion for melting: Comparison of square well and Morse potential modes for clusters and homo polymers," *Journal of Chemical Physics*, Vol. 116, No. 5, 2002, pp. 2323-2329
- Zik, O., Olami, Z., and Moses, E., "Fingering instability in combustion," *Physical Review Letters*, Vol. 81, 1998, pp 3868

## **VITA**

### **Puneesh Puri**

Puneesh Puri was born in Rohtak, India on January, 16 1982. He received his B. Tech. degree in Mechanical Engineering from Indian Institute of Technology, Delhi in 2003. He joined the Department of Mechanical and Nuclear Engineering at The Pennsylvania State University in August, 2003 to conduct full time research at Propulsion Engineering Research Center (PERC) in the area of ignition and combustion of micro and nano aluminum particles. He has been a research assistant in combustion area since then, working on injector dynamics, combustion wave ignition systems with focus on ignition characteristics of JP-7 fuel in particular, and managing the high performance computing facility for large scale CFD and MD calculations.